

eman ta zabal zazu



Universidad  
del País Vasco

Euskal Herriko  
Unibertsitatea

**FIVE-AXIS MILLING OF ROUGH AND PBF-LB PARTS  
WITH FREE-FORM SURFACES USING BALL-END AND  
CIRCLE-SEGMENT END MILLS**

Presented by  
**Felipe Marin**

Thesis advisors  
**Dr. Luis Norberto López de Lacalle**  
**Dr. Adriano Fagali de Souza**

**2024**

(c) 2024 Felipe Marin



*One step at a time*



## Acknowledgements

I would like to dedicate these lines to all those who, with their collaboration and support, have made the completion of this Ph.D thesis possible.

First and foremost, I am deeply indebted to my thesis advisors, Dr. Luis Norberto López de Lacalle Marcaide and Dr. Adriano Fagali de Souza; thanks for the support, motivation, and resources provided. I also want to express my gratitude to the rest of the University of the Basque Country employees, who contributed somehow to the conclusion of this Ph.D. thesis. Special thanks to Aitzol, Amaia, Adrian, Asier, Haizea, Iñaki, Izaro, Naiara, Octavio, Rober, Silvia, and Soraya crucial people for developing projects and providing infrastructures at the Aeronautics Advanced Manufacturing Centre – CFAA.

I would also like to thank my colleagues and friends from the University of the Basque Country, who supported my work and made this journey possible and enjoyable. Without your thoughts and ideas, this work will not be the same. Also, thanks for the support in using the university's infrastructure, improving my Spanish, and listening to my problems. It was lucky and a pleasure to know you guys – Alejandro, Aner, Aizpea, Ander, Exequiel, Fran, Gaizka, Guillermo, Gonzalo, Ibon, José David, Magdalena, Marta, Mario, Oihane, Olaia, Pablo, Patricia, Robson, Sara, and Sarvesh.

This thesis could not have been possible without the support of the Research Group on Computer-Aided Manufacturing (GPCAM) of the Federal University of Santa Catarina, with special thanks to Nicolas, Rodrigo K, Rodrigo V, Taiue, and Vitor, besides professors Adriano and Helton. Thanks for your knowledge, Dr. Mikowski from the Federal University of Santa Catarina, Dr. Basso, and Dr. Roger Rodrigues from the University of São Paulo. I also thank the National Council for Scientific and Technological Development (CNPq).

Finally, in the personal realm, the support of my family and close friends has been essential. Father and Mother, all my achievements are also yours. The efforts put in me since the first days of my life made it possible to accomplish this beautiful journey. Thanks for encouraging me to fight for what I want. I mainly thank my sister, who was always available and supported my evolution. Thank you to all the others who made my journey enjoyable and provided strength and motivation to continue.

Kindly thank all for the support. I am deeply grateful.



eman ta zabal zazu



Universidad  
del País Vasco

Euskal Herriko  
Unibertsitatea

**FIVE-AXIS MILLING OF ROUGH AND PBF-LB PARTS  
WITH FREE-FORM SURFACES USING BALL-END AND  
CIRCLE-SEGMENT END MILLS**

Presented by  
**Felipe Marin**

Thesis advisors  
**Dr. Luis Norberto López de Lacalle**  
**Dr. Adriano Fagali de Souza**

**2024**





## Summary

This Ph.D. thesis investigates the manufacturing processes of complex geometrical shapes, focusing on the milling process of free-formed surfaces with ball-end tooltips. This kind of surface is commonly present in high-value-added products like turbofan blades and BLISK components, and manufacturing deviation can decrease durability and performance, making the prediction of the surface texture and dimensional errors important. This work covered several topics related to finishing components containing free-form surfaces. The influences of the material, cutting contact, cutting parameters, equipment, and tooltip influence are investigated.

In the first part of the thesis, a detailed review of the state-of-the-art was conducted to identify the scientific and industrial gaps. A review of the application of free-form surfaces in the aeronautical field, the definition of free-form surfaces, and a detailed review of manufacturing processes of complex parts by milling were conducted, aiming the finishing process understanding with conventional ball-end tooltip and new circle segment end mills, providing tools and the required contextualization for the Ph.D. thesis. Also, a new manufacturing process to produce near-net shape parts with internal microstructures is revised, followed by methods for inspection and evaluation.

Then, the results related to the preliminary manufacturing process investigation are presented. An initial assessment of the machine response time (MRT) in multi-axis milling allowed the identification of possible defects related to feed-oscillation and the response of the angular axis in comparison to the linear axis of the NC machine. The effect of the engagement of the tooltip with the surface together with the effect of the milled material, was evaluated using a representative workpiece of free-form milling. After that, a preliminary investigation on machining a thin-walled blade component on a multitasking machine was carried out, followed by the study of the tool deflection according to the tool tilting. Finally, clamping issues and other related problems in the manufacture of big-sized, thin-walled components were addressed. Where identified the main sources of form errors and recommendations for improving the manufacturing process of such kinds of geometries were made. These upper-cited investigations were used to guide the research line in the direction of surface texture for reliable parts and the understanding of the topography produced in the finishing process by ball-end tooltips.

After that, it was identified that the current commercial CAD/CAM software can not properly predict the finishing texture of the ball-end milling process, which can make the manufacturing process of free-form surfaces difficult. So, the process was modelled to suppress this limitation. To obtain a generic model of the finishing process of free-form

surfaces, a discretization of the complex process into instantaneous positions was carried out. To do so, a methodology to extract the cutter location (CL), cutter contact (CC) points, and relative instantaneous vectors of the tool and surface was developed and implemented on software with an open interface. Then, the geometrical modelling of the ball-end tooltip is integrated using the infinitesimal approach to predict the surface texture. Lastly, the method is evaluated on a thin-walled part machined in 5-axis with a conventional ball-end tooltip and a lens-shaped barrel tool, allowing the evaluation of aspects of the milled surface, such as crisp height and roughness on the feed direction.

Finally, the manufacturing process using powder bed fusion laser beam (PBF-LB) is investigated to produce near-net-shape parts containing free-form surfaces and internal microstructures. First, a study case identifying limitations and the properties of samples manufactured by PBF-LB is conducted, aiming to produce reliable parts with improved functional design for industrial application. By changing the PBF-LB manufacturing parameters, it was possible to obtain different mechanical properties, and the investigation of the internal porosity distribution by computer tomography allowed statistical identification of the fragile ductile compartment change, supporting the industrial application of this kind of process in critical areas like the aeronautical sector. After that, a blade with internal microstructures is manufactured by PBF-LB, and the effect of the geometry on the finishing process by ball-end milling using conventional and lens-shaped barrel tooltips is evaluated. The internal microstructure of the blades increased the specific rigidity, improving the part's mechanical properties and producing a finished surface with lower deviations and roughness.

To sum up, this Ph.D. thesis delves into the manufacturing process of complex parts, focusing on the finishing process of free-form surfaces, a complex and multidisciplinary theme. The research contributions allowed a better understanding of machine dynamics, highlighting the effect of the feed-rate oscillation, the selection of parameters, and the geometrical features involved in the finishing process with the ball-end tooltip. By taking into account the influence of the tooltip engagement, the effect of its centre, and the machined material, it was possible to get insights into the cutting force influence, tool deflections, and other related problems that damage the surface. Furthermore, the developed API in high-end CAD/CAM software with an open interface and the integration of a geometrical model considering different types of ball-end tooltips facilitates the understanding of the manufacturing process of free-form surfaces, knowledge also applied to finishing parts manufactured by PBF-LB, which allows the design and manufacture of high-performance parts, with internal functional features, under tolerance and surface finishing, contributing to both academic and industrial field.

## Resumen

La presente tesis doctoral profundiza en los procesos de fabricación de formas geométricas complejas, con un enfoque específico en el proceso de acabado de superficies mediante el fresado con herramientas de punta esférica, tanto convencionales como de doble radio. Las superficies complejas, también conocidas como superficies de forma libre y no desarrollables, se encuentran comúnmente en diversos productos de alto valor añadido en distintos sectores productivos.

Uno de estos sectores es el aeronáutico, donde estas superficies pueden hallarse en el fuselaje, estabilizadores y en varios componentes del motor, como los álabes de los turboventiladores, las carcasas y los Discos Integrados de Álabes. En estos componentes, las desviaciones en el proceso de fabricación pueden tener un impacto considerable en la durabilidad y el rendimiento final del producto, lo que requiere la aplicación de estrictas tolerancias, haciendo que el proceso de diseño y fabricación sea especialmente desafiante.

Además de esto, la predicción precisa de la rugosidad superficial y los errores dimensionales inherentes de los procesos de fabricación se convierten en aspectos cruciales. En este contexto, la presente tesis doctoral aborda diversos temas relacionados con el acabado de componentes que contienen superficies complejas, examinando la influencia de varios factores como el material utilizado, las modificaciones de diseño, los procesos productivos empleados para la obtención del componente semiacabado, la máquina herramienta utilizada en el acabado, así como los parámetros específicos de corte y la orientación de la herramienta. También se estudia el contacto entre la herramienta y la pieza durante el proceso de corte, teniendo en cuenta la propia geometría de las herramientas y el filo de corte.

En la primera parte de la tesis, se presenta una breve contextualización del sector junto con las motivaciones y objetivos generales y específicos. En el segundo capítulo de la tesis doctoral se realiza una exhaustiva revisión del estado del arte con el fin de identificar tanto las brechas científicas como las industriales existentes en el campo, además de consolidar los conocimientos necesarios para el entendimiento de los capítulos subsiguientes. Se lleva a cabo un análisis detallado de la aplicación de superficies de geometría compleja en la industria aeronáutica, seguido por la definición del concepto de superficies de geometría compleja, materiales empleados que cumplen con las condiciones operacionales extremas de los componentes del motor, y los procesos de fabricación de las piezas que hacen posible la producción de componentes de alto rendimiento para la industria aeronáutica.

Se hace hincapié particular en el proceso de mecanizado por remoción de material, con un enfoque especial en el fresado y los procesos de acabado con herramientas de bola. Se recapitulan características clave tanto de fresas de punta esférica convencionales como de las nuevas fresas de segmento circular, proporcionando así las herramientas conceptuales necesarias para comprender el proceso de acabado de piezas de alto valor añadido. Esto hace factible el desarrollo de herramientas para la predicción de la superficie mecanizada, como se realiza en la presente tesis doctoral.

Además, se revisa un nuevo proceso de fabricación diseñado para producir piezas con formas casi finales, específicamente la manufactura aditiva por fusión por lecho de polvo con haz láser. Este proceso permite diseñar y fabricar piezas con microestructuras internas que optimizan el producto tanto mecánica como funcionalmente. Finalmente, también se lleva a cabo la revisión de métodos para la inspección y evaluación no destructiva de dichas piezas.

En el tercer capítulo se presentan los resultados obtenidos tras las investigaciones preliminares del proceso de fabricación, realizadas con el propósito de orientar la línea de investigación. El primer estudio aborda la evaluación inicial del tiempo de respuesta de la máquina (TRM) en el fresado multieje, considerando el movimiento simultáneo en cuatro ejes. La metodología propuesta y validada permitió identificar limitaciones en la velocidad de avance tanto en los ejes angulares como en los lineales de las máquinas de control numérico. Estas limitaciones, derivadas de restricciones mecánicas, cinemáticas y saturación del lazo de control, pueden generar oscilaciones en el avance y, por ende, marcas no deseadas en la superficie acabada.

En el segundo estudio presentado en el tercer capítulo, se evaluó el efecto del contacto de la fresa de bola con la superficie y su impacto en el radio efectivo de corte. Para ello, se desarrolló una metodología que utiliza la geometría proporcionada por el software CAD y las coordenadas calculadas por el CAM para determinar el punto de contacto sobre una orientación específica de la herramienta y el radio efectivo de corte.

En el tercer estudio se continuó evaluando el contacto de la fresa de bola con la superficie, considerando además el efecto del material a fresar. Para este fin, se diseñó una pieza representativa y robusta, y se fabricaron tres muestras utilizando materiales con diferentes propiedades mecánicas. Además, se modeló el proceso para entender la formación de la viruta, cuantificar las energías acumuladas en los procesos y cómo esto afecta la superficie final generada. Esto permitió evaluar la respuesta de diferentes orientaciones de la herramienta y las propiedades mecánicas de los materiales en el

fresado de distintas superficies inclinadas, simulando diferentes condiciones que ocurren en el fresado de un componente con geometría compleja.

El cuarto estudio presentado evalúa la deflexión de las nuevas fresas de segmento circular, analizando diferentes orientaciones y condiciones de corte. Para ello, se realizaron ensayos de mecanizado en un bloque de material de difícil mecanizado y suficientemente rígido, lo que indujo altas fuerzas de corte y aumentó los efectos de la deflexión. Así, se evaluaron estadísticamente la influencia de los parámetros de corte y la orientación de la herramienta, junto con los resultados de fuerza y rugosidades obtenidos en la deformación de este tipo de herramienta. Además, los datos de fuerza de corte medidos en el proceso fueron utilizados para simular la deflexión teórica de la herramienta y cuantificar su influencia en la deformación final medida.

El quinto estudio presentado en el tercer capítulo abordó problemas de diseño, fijación y manufactura en componentes de gran tamaño y pared delgada. La inspección del componente permitió identificar las influencias de algunos de sus elementos y configuraciones de fijación en los errores de forma, y se propusieron recomendaciones para mejorar el proceso de fabricación de este tipo de geometrías. Además, se cuantificaron los tiempos reales de mecanizado y se evaluaron las diferencias con los previstos por el software CAM, lo que permite mejorar la previsibilidad del proceso de fabricación de piezas de gran tamaño.

El último estudio preliminar llevó a cabo una investigación sobre el mecanizado de un componente de pala con pared delgada y superficie compleja en una máquina multitarea. Se evaluó la superficie final obtenida con distintos ángulos de orientación de herramientas de bola y se cuantificaron los defectos y limitaciones en su fabricación para posteriormente emplearlos en estudios más completos considerando diferentes geometrías de herramienta, materiales y condiciones de corte. Esto proporcionó una idea general para una evaluación más exhaustiva de esta geometría en los estudios subsiguientes.

Estas investigaciones preliminares fueron utilizadas para orientar la línea de investigación hacia el estudio de la textura superficial con el objetivo de obtener piezas más fiables, así como para comprender la topografía producida en el proceso de acabado utilizando fresas de punta esférica. Además, se identificó que los actuales software CAD/CAM comerciales no son capaces de predecir adecuadamente la textura de acabado del proceso de fresado con fresas de punta esférica, lo que puede dificultar el proceso de fabricación de superficies complejas. Por lo tanto, se procedió a modelar este proceso con el fin de superar esta limitación.

En el capítulo cuatro se presenta el desarrollo matemático e implementación del modelo en un software de arquitectura abierta. Con el fin de obtener un modelo genérico del proceso de acabado de superficies de geometría compleja, se realizó una discretización del proceso en posiciones instantáneas utilizando pequeños planos infinitesimales. Para ello, se desarrolló e implementó una metodología para extraer la ubicación de la punta de la herramienta y el punto de contacto con la superficie, además de los vectores instantáneos relativos a la herramienta y la superficie. Luego, se integró el modelado geométrico de la punta de bola utilizando el enfoque infinitesimal para predecir la textura superficial. Finalmente, se evaluó el método en una pieza con geometría compleja y pared delgada que fue mecanizada en 5 ejes utilizando tanto una fresa de punta esférica como una herramienta con punta de segmento circular, tipo barril frontal. Esto permitió la evaluación de aspectos de la superficie mecanizada, como la altura de la cresta y la rugosidad en la dirección de avance.

En el capítulo cinco de la tesis se presenta la investigación del proceso de fabricación utilizando la fusión en lecho de polvo con haz láser, una técnica de manufactura metálica que permite producir piezas semiacabadas con superficies complejas y microestructuras internas. En este capítulo se presentan dos estudios. El primero se llevó a cabo con el objetivo de identificar limitaciones y las propiedades de las muestras fabricadas mediante este proceso, con la intención de producir piezas mecánicamente fiables y con diseño funcional mejorado para aplicación industrial. Para ello, se modificaron los parámetros de fabricación, se realizaron ensayos mecánicos y se evaluó la distribución de porosidad obtenida mediante tomografía computarizada. Esto permitió la identificación estadística del cambio en el comportamiento de ductilidad frágil, respaldando así la aplicación industrial de este tipo de proceso en áreas críticas como el sector aeronáutico.

Posteriormente, se presenta el estudio de la fabricación de una pala con microestructuras internas mediante fusión en lecho de polvo con haz láser, donde se evaluó el efecto de la geometría en el proceso de acabado mediante fresado de punta esférica utilizando tanto herramientas convencionales como la herramienta de barril frontal. Los resultados obtenidos indicaron que el diseño del álabe con microestructura interna permitió un aumento de su rigidez específica, mejorando las propiedades mecánicas de la pieza y produciendo una superficie acabada con menores desviaciones y rugosidad.

En resumen, esta tesis doctoral profundiza en el proceso de fabricación de piezas complejas, centrándose en el acabado de sus superficies. Las contribuciones de la investigación permitieron una mejor comprensión de la dinámica de la máquina,

destacando el efecto de la oscilación de la velocidad de avance, la selección de parámetros y las características geométricas involucradas en el proceso de acabado con herramientas de punta de bola. Al considerar la influencia de la región de contacto de la herramienta de corte, el efecto de su centro y el material mecanizado, fue posible obtener información sobre problemas que pueden afectar la calidad de la superficie mecanizada.

Además, se ha desarrollado una aplicación en software CAD/CAM con interfaz de programación abierta, junto con la integración de un modelo geométrico que considera diferentes tipos de herramientas de corte, facilitando la comprensión y optimización del proceso de fabricación de superficies de geometría compleja. Este conocimiento también se aplicó al acabado de piezas fabricadas mediante fusión en lecho de polvo con haz láser, lo que permite el diseño y la fabricación de piezas de alto rendimiento con características internas funcionales, utilizando el proceso de fresado de bola para garantizar un acabado superficial adecuado y dentro de tolerancias especificadas, contribuyendo tanto al ámbito académico como al industrial.





---

## Main Index

### Chapter I. Introduction and contextualization ..... 3

I. 1. Introduction .....	3
I. 2. Context and motivation.....	3
I. 3. Objectives .....	8
I. 3. 1. General Objectives .....	8
I. 3. 2. Specific Objectives.....	8
I. 4. Memory organisation .....	9

### Chapter II. State-of-the-art of the manufacture of free-form surfaces ..... 13

II. 1. Aeronautical engine components.....	13
II. 1. 1. Design and operation .....	13
II. 1. 2. Materials of turbofan engines .....	15
II. 1. 3. Engine parts containing free-form surfaces .....	21
II. 2. Free-form surfaces definition .....	22
II. 3. Computational tools for manufacturing .....	24
II. 3. 1. Software classification.....	25
II. 3. 2. Programming interface with CAD software .....	26
II. 4. Manufacture of free-form surfaces.....	28
II. 4. 1. Manufacturing by removing material .....	28
II. 4. 2. Milling .....	29
II. 4. 3. Finishing free-form surfaces by milling .....	32
II. 4. 4. Tool contact changes in complex surface milling.....	33
II. 4. 5. Multi-axis milling and tool orientation.....	37
II. 4. 6. Toolpath strategies for finishing free-form surfaces .....	38
II. 4. 7. Tools for finishing complex surfaces .....	41
II. 4. 8. Milling tools materials.....	44
II. 4. 9. Tool wear .....	45

---

II. 4. 10. Lubri-coolant systems .....	47
II. 4. 11. Signatures of free-form milled surfaces .....	49
II. 4. 12. New manufacturing processes .....	54
<i>II. 5. Modelling of the milling process.....</i>	<i>60</i>
II. 5. 1. Geometrical modelling .....	61
II. 5. 2. Force estimation .....	63
II. 5. 3. Deflection.....	68
II. 5. 4. Modelling of the machined surface and the cutting energy .....	73
<i>II. 6. Inspection of components.....</i>	<i>80</i>
II. 6. 1. Confocal microscopy .....	80
II. 6. 2. Computed tomography.....	81
<b>Chapter III. Investigation of finishing processes for complex shapes .....</b>	<b>85</b>
III. 1. Introduction .....	85
III. 2. Machining kinematics – movements and tool orientation .....	85
III. 2. 1. Machine response time with 4-axis .....	85
III. 2. 2. Dynamic calculation of the effective cutting radius and implementation in CAD/CAM software.....	91
III. 2. 3. Remarks of the Sub-section .....	98
III. 3. Study of the contact on the finishing .....	98
III. 3. 1. Influences of the workpiece material and the tool-surface engagement on surface finishing in ball-end milling.....	98
III. 3. 2. Ball-end tooltip deflection according to CWE .....	112
III. 3. 3. Remarks of the Sub-section .....	124
III. 4. Milling complex shapes .....	125
III. 4. 1. Manufacture of big-size thin-walled component.....	125
III. 4. 2. Blade manufacture in multitasking centre.....	132
III. 4. 3. Remarks of the Sub-section .....	139
<b>Chapter IV. Ball-end milling - surface prediction .....</b>	<b>143</b>

IV. 1. Introduction .....	143
IV. 2. Overview of the proposed methodology .....	145
IV. 3. Routine for data collection.....	145
IV. 4. Geometrical modelling of the tooltip .....	147
IV. 4. 1. Single radius tooltip .....	147
IV. 4. 2. Double radius tooltips .....	148
IV. 4. 3. Run-out in ball-end tooltips .....	149
IV. 5. Toolpath data treatment .....	150
IV. 5. 1. Instantaneous position.....	151
IV. 5. 2. Adjustment of the angular position with the feed.....	152
IV. 6. Surface prediction .....	153
IV. 6. 1. Scallop height considering instantaneous positions of the tool.....	154
IV. 6. 2. Surface prediction using the mesh data cloud.....	155
IV. 7. Developed routine and modelling outputs .....	155
IV. 7. 1. Routine outputs .....	155
IV. 7. 2. Data treatment and model outputs.....	156
IV. 8. Study Case 1 – Conventional ball-end tooltip.....	158
IV. 8. 1. Materials and Methods .....	158
IV. 8. 2. Results and modelling evaluation .....	159
IV. 8. 3. Conclusions.....	165
IV. 8. 4. Future works.....	166
IV. 9. Study Case 2 – Comparison of the surface finishing with different tooltips ...	167
IV. 9. 1. Materials and Methods .....	167
IV. 9. 2. Results and Discussions.....	169
IV. 9. 3. Conclusions.....	179
IV. 9. 4. Future works.....	180

## **Chapter V. Manufacture of blades by PBF-LB containing microstructures ..... 183**

V. 1. Introduction .....	183
--------------------------	-----

*Main Index*

---

V. 2. Evaluation of the PBF-LB process for manufacturing critical engineering components.....	183
V. 2. 1. Materials and methods .....	184
V. 2. 2. Results and discussion .....	190
V. 2. 3. Conclusions.....	201
V. 3. Manufacture of a blade with Lattice structures .....	202
V. 3. 1. Materials and methods .....	202
V. 3. 2. Results analysis procedure.....	205
V. 3. 3. Conclusions.....	211
<b>Chapter VI. Contributions and future works.....</b>	<b>215</b>
VI. 1. Contributions.....	215
VI. 2. Future works .....	220

---

## List of Figures

<i>Figure I-1. Manufacture of complex parts by milling. ....</i>	<i>3</i>
<i>Figure I-2 Fuel price against crude oil price (USD/barrel).....</i>	<i>5</i>
<i>Figure I-3. Requirements of the modern aeronautical industry and subareas of research interest.....</i>	<i>5</i>
<i>Figure II-1. Turbofan components and materials.....</i>	<i>13</i>
<i>Figure II-2. Brayton cycle and stages.....</i>	<i>14</i>
<i>Figure II-3. Cross section of UltraFan turbojet engine, adapted from Rolls-Royce (2023). .....</i>	<i>15</i>
<i>Figure II-4 . Evolution of turbine materials (Miller, 1996). ....</i>	<i>16</i>
<i>Figure II-5. Inconel® 718 TTT diagram, adapted from Xie et al. (2005).....</i>	<i>19</i>
<i>Figure II-6. a) Time-Temperature-Hardness of Inconel® 718 (Xie et al., 2005). b) Variation in hardness of Inconel® 718 with a temperature (Liao et al., 2008).....</i>	<i>20</i>
<i>Figure II-7. Examples of free-form parts of the turbofan: a) Monolithic fan blade (Rolls-Royce, 2023); b) BLISKs (Meinzer and Seume, 2020); c) Medium-size casing manufactured in martensitic stainless steel. ....</i>	<i>21</i>
<i>Figure II-8. Free-form curve and surface representation. ....</i>	<i>23</i>
<i>Figure II-9. Referencing a single point of a free-form surface.....</i>	<i>24</i>
<i>Figure II-10. Milling process schematic. ....</i>	<i>30</i>
<i>Figure II-11. Generic HPC Blisk in Inconel® 718 (Klocke et al., 2015). ....</i>	<i>31</i>
<i>Figure II-12. Cause and effect diagram for free-form surface milling (Mali et al., 2021). .....</i>	<i>33</i>
<i>Figure II-13. Alterations of the tool contact and effective cutting radii in 3-axis ball-end milling of a half cylinder (de Souza et al., 2015). ....</i>	<i>34</i>
<i>Figure II-14. Machine control loop, adapted from Coelho et al. (2010). ....</i>	<i>36</i>
<i>Figure II-15. Toolpath strategy influences the surface, machining, and polishing time. Adapted from Souza et al. (2014b). ....</i>	<i>40</i>

## List of Figures

---

Figure II-16. Types of barrel tools and nomenclatures: a) barrel oval shape; b) lens shape; c) conical; d) drum taper; e) barrel; f) half-barrel.....	42
Figure II-17. Surface finishing comparison with a ball-end tooltip and an oval barrel-shaped mill to obtain similar crisp height, adapted from Mitsubishi (2023). .....	43
Figure II-18. Properties versus temperature: a) hardness of tool materials, adapted from Almond (1981); b) Yield strength of aeronautical alloys. ....	44
Figure II-19. Types of tool wear: a) flank wear; b) chipping; c) adhesion; d) notch; e) plastic deformation; f) crater; g) rounding edge; h) built-up edge. Adapted from ISO 6888-2 (1989) and Khatri and Jahan (2018). ....	46
Figure II-20. Wear mechanism in metal cutting tools (Li, 2012). ....	46
Figure II-21. a) Temperature machining Inconel <sup>®</sup> 718 with different cooling conditions, adapted from Kaynak (2014); b) Cooling techniques to reduce machining heat generation and improve chip flow. ....	48
Figure II-22. Signature of milled surface with different tool inclinations (Yao et al., 2018). .....	49
Figure II-23. Zones affected by machining, adapted from Liang and Liu (2017). ....	50
Figure II-24. Tool flank wear and surface roughness progression during face milling of 17-4PH stainless steel (Liu et al., 2016). ....	52
Figure II-25. Most common surface damages when milling HRSA. Adapted from Zhou et al. (2012) and Arunachalam et al. (2004). ....	53
Figure II-26. PBF-LB process schematics. ....	55
Figure II-27. Schematic of the damping mechanisms on lattice structures. ....	58
Figure II-28. Flowchart for modelling free-form milling, inputs, and relations. ....	61
Figure II-29. Mechanistic model of force, adapted from Ochoa (2015). ....	64
Figure II-30. Different approaches of part stocks to control part deflection: a) constant $a_p$ ; b) $a_p$ with a sudden increase; c) $a_p$ with smother increase.....	70
Figure II-31. Tool ICE element under flexion and torsion. ....	72
Figure II-32. Theoretical roughness using ball-end tooltip. ....	73

Figure II-33. Simulation of surface machined by ball-end milling: a) ICE trajectory; b) measured surface; c) predicted surface. Adapted from Arizmendi et al. (2008).....	74
Figure II-34. 5-axis ball-end milling surface topography: a) Simulated; b) measured (Layegh K and Lazoglu, 2017). .....	75
Figure II-35. Surface topography after ball-end milling: a) feed marks; b) chatter marks. Adapted from Wojciechowski et al. (2018). .....	76
Figure II-36. a) Milled surface. B) optical profilometry analysis, c) simulated surface, d) down-milling and up-milling confocal images, and e) Specific pressure versus effective diameter. Adapted from Batista et al. (Batista et al., 2017).....	77
Figure II-37. The stochastic approach to simulate the surface of the ball-end milling process proposed by Denkena et al. (2015).....	78
Figure II-38. Confocal optical microscope; a) Leica DCM 3D; b) working principle. ....	81
Figure II-39. Operation principle of computerized tomography. ....	82
Figure III-1. Feed rate oscillation with different CAM, adapted from de Souza et al. (2019b). .....	86
Figure III-2. Part geometries and 4-axis CAM trajectories used for the evaluation of the proposed method (de Souza et al., 2021). .....	88
Figure III-3. Schematic diagram of the MRT method, adapted from de Souza et al. (2021). .....	89
Figure III-4. Maximum linear feed rate with incremental linear movement (de Souza et al., 2021).....	89
Figure III-5. Maximum feed rate with incremental angular movement (de Souza et al., 2021). .....	90
Figure III-6. Estimated machining time by the CAM software, by the proposed method, and the real milling time (de Souza et al., 2021). .....	91
Figure III-7. Changes in the tool-workpiece contact at different instants during free-form milling. ....	92
Figure III-8. Methodology for calculating the effective cutting radius using software....	93

## List of Figures

---

Figure III-9. Stages of the calculation of surface normal vectors: a) CC, CL, and support points calculated by the routine; b) normal vectors obtained through the routine. ....	94
Figure III-10. Tool position over the trajectory and the NC programs modified, including the instantaneous effective cutting radius. ....	95
Figure III-11. Comparison of the effective cutting radius calculated by the proposed routine with the measured by the CAD/CAM software.....	96
Figure III-12. Customized menu for user interaction.....	97
Figure III-13. Workpiece geometry and tool path; b) tooltip, adapted from Basso et al.(2022). ....	100
Figure III-14. Instantaneous specific and accumulated energy calculation. (a) TSE; (b) uncut chip geometry; (c) components of the cutting force; (d) resultant cutting force; (e) instantaneous specific energy, accumulated energy, and maximum chip thickness. (Basso et al., 2022).....	102
Figure III-15. Maximum uncut chip thickness vs. rotation angle and TSE (Basso et al., 2022). ....	103
Figure III-16. Main effects for $S_z$ roughness when milling: (a) electrolytic copper; (b) annealed; (c) hardened AISI H13 steels (Basso et al., 2022).....	104
Figure III-17. Confocal images and averaged $S_z$ values according to workpiece material, milling mode, and lead angle (Basso et al., 2022).....	105
Figure III-18. Damages identified on the machined surfaces: a) severe plastic deformation; b) side flow; c) cavity; (d) scratch lead angle at down-milling (Basso et al., 2022). ....	107
Figure III-19. Tooltip effect on the surface of brittle and ductile materials (Basso et al., 2022). ....	108
Figure III-20. a) Influence of the ploughing according to the material's hardness (HV) and mean $S_z$ values ;b) Accumulated cutting energy for down-milling mode versus workpiece materials and tool lead angle. Adapted from Basso et al. (2022). ....	109



<i>Figure III-21. Accumulated cutting energy, specific cutting energy, machining force, and maximum uncut thickness versus rotation angle, and scheme for surface generation in (a) down-milling and (b) up-milling. Results for annealed AISI H13 steel milled at 5° lead angle (Basso et al., 2022).</i> .....	110
<i>Figure III-22. Tool and workpiece schematics: a) oval barrel tool; b) tool top view; c) CAM programming schematic; d) workpiece dimensions and milling regions.</i> .....	113
<i>Figure III-23. Milled regions according to cutting parameters schematic and inspection regions.</i> .....	114
<i>Figure III-24. a) CWE according to the tool tilting, b) simulated crisp height.</i> .....	115
<i>Figure III-25. Surface deviation according to cutting parameters and tool tilting.</i> .....	116
<i>Figure III-26. Resultant cutting forces and components according to cutting parameters and tool tilting.</i> .....	116
<i>Figure III-27. Roughness Ra, Rz, Sa, and Sz of each region.</i> .....	116
<i>Figure III-28. Pareto chart response for resultant cutting force, surface deviation, and roughness, and main effect plots of resultant cutting force and surface deviation.</i> ....	119
<i>Figure III-29. Topography of lower and higher surface roughness: a) Region 36); b) Region 71.</i> .....	119
<i>Figure III-30. Simulation of the oval barrel tool deflection considering geometry and measured cutting forces.</i> .....	121
<i>Figure III-31. Deflection pattern according to tool contact by tilting and lateral depth of cut.</i> .....	121
<i>Figure III-32. a) Simulated tool deflection versus measured resultant cutting force blocked by tool tilt and <math>a_e</math>, b) effective cutting radius versus specific stiffness.</i> .....	122
<i>Figure III-33. Procedure for error correction using the force and CWE geometrical data.</i> .....	124
<i>Figure III-34. AISI XM-12 aeronautical casing: a) CAD design; b) manufactured.</i> .....	126
<i>Figure III-35. Toolpath strategy for slot milling of honeycomb triangles.</i> .....	128

List of Figures

---

Figure III-36. Measured sections of the casing: a) external sections; b) internal sections.  
..... 129

Figure III-37. a) Upper flange milling; b) Roundness graph of section S1 (0.087  $\mu\text{m}$ ); c) Roundness graph of section S2 (0.083  $\mu\text{m}$ ); d) Roundness graph of section S3..... 130

Figure III-38. Harmonic response of sections 1, 2, 3, 4, 13, 14, 15 and 16..... 131

Figure III-39. Aluminium blade thickness analysis and milled regions. .... 133

Figure III-40. Milled part after operations: a) roughing, b) semi-finishing; c) finishing. 134

Figure III-41. Magnification of the milled marks due to control loop saturation..... 135

Figure III-42. Measured profile height at each region after face transaction. .... 135

Figure III-43. Surface texture at the centre of concave and convex regions. .... 137

Figure III-44. Measured roughness Ra and Rz at the centre of concave and convex regions..... 137

Figure IV-1. CAM surface prediction. .... 143

Figure IV-2. Flowchart of the proposed methodology for surface prediction. .... 145

Figure IV-3. NX Open routine flowchart and NX Open programming routine..... 146

Figure IV-4. Tool schematics for single and double-radius tooltips..... 147

Figure IV-5. Centre deviation caused by run-out at a generic  $z_i$  plane of the tool. .... 150

Figure IV-6. Schematics of toolpath adjustment for surface prediction using instantaneous positions. .... 151

Figure IV-7. Schematics of toolpath discretization with a constant  $\Delta\theta$  and tilt ponderation.  
..... 152

Figure IV-8. Geometrical rotation and translation procedure applied to tool dome and infinitesimal edge elements..... 153

Figure IV-9. Scallop height of a generic tool shape considering two consecutive cutting steps..... 154

Figure IV-10. Programmed routine for 5-axis data acquisition outputs. .... 156

Figure IV-11. a) Ball-end tool dome and helix edge; b) 5-axis milling on a free-form surface simulated by the cam software; c) Toolpath data treatment for instantaneous

surface modelling and application; d) Toolpath data treatment for ICE trochoidal movement and application. ....	157
Figure IV-12. a) Part model and machining strategies. b) Tool with holder presetting. ....	159
Figure IV-13. Machined blade and topography inspection of the central part. ....	160
Figure IV-14. Roughness and topographical analysis. a) measured roughness profile; b) profile evaluation; c) comparison between simulated and measured with 25° lead angle. ....	161
Figure IV-15. a) Simulation of the ICE trochoidal movement: a) isometric view of 3 passes with 15° lead angle; b) top view and theoretical lateral roughness using two levels of feed-per-tooth; c) lateral tool run-out on six tool heights considering 5, 15, and 25 lead angles. ....	164
Figure IV-16. a) CAM programming and refined data obtained by the routine for a blade profile; b) Simulation of the surface using the treated data; c) ICE trochoidal movement on an infinitesimal plane. ....	165
Figure IV-17. Blade geometry: a) CAM finishing toolpath evaluated; b) semi-finished. ....	168
Figure IV-18. Ball-end tooltips: a) frontal view; b) single radius top view; c) lens shape top view; d) Presetting procedure and cutting edges measures. ....	168
Figure IV-19. Different cutting contact engagements. ....	170
Figure IV-20. Metallographic images of the milled surface with 50x magnification. ...	171
Figure IV-21. Post-processed optical images of the milled surfaces and central region. ....	172
Figure IV-22. The average area of the grains and the equivalent diameter for each region. ....	172
Figure IV-23. Roundness analysis of the grains. ....	172
Figure IV-24. Surface hardness after the milling process on the concave and convex sides. ....	173

## List of Figures

---

Figure IV-25. Surface damage after blade inversion according to the cutting condition. ....	175
Figure IV-26. Roughness Ra and Rz according to the milled region. ....	175
Figure IV-27. Milling texture under different tooltips and tool tilt. ....	177
Figure IV-28. Simulated pattern of the surface texture with different tooltips and tool inclinations. ....	179
Figure V-1. Blade manufactured by PBF-LB with internal microstructures. ....	183
Figure V-2. Corrax <sup>®</sup> powder analysis: a) SEM scan 500x magnify; b) size distribution (Marin et al., 2023). ....	185
Figure V-3. Hybrid samples manufactured by PBF-LB over the PH13-8Mo substrate: a) CAD of the cuboid sample, as-built and indentation schematic; b) tensile test samples as-built and machined (Marin et al., 2023). ....	186
Figure V-4. Porous material representation: a) infinitesimal element; b) hybrid material; c) single pore strain; d) pores without stress concentration; e) pores with stress concentration interaction (Marin et al., 2023). ....	189
Figure V-5. Optical microscopy images of samples manufactured using PBF-LB parameters A, C, and E (Marin et al., 2023). ....	191
Figure V-6. SEM images of regions 1 to 5 of sample E (Marin et al., 2023). ....	192
Figure V-7. Laser scanning speed versus MIZ (Marin et al., 2023). ....	193
Figure V-8. Pore distance to MIZ of samples A, C, and E measured by tomography (left) and SEM scans of regions 1, 2, and 3 (right) (Marin et al., 2023). ....	193
Figure V-9. Hardness profiles of the hybrid samples (Marin et al., 2023). ....	195
Figure V-10. Hardness profiles of the samples D and E solubilized and aged versus as built (Marin et al., 2023). ....	195
Figure V-11. Tensile strength test using ASTM 370 hybrid samples: a) samples A; b) samples C; c) samples E (Marin et al., 2023). ....	196

<i>Figure V-12. Relative density: a) OM image according to scanning speed; b) relation with the scanning speed and the number of pores; c) relation with the average hardness of the samples (Marin et al., 2023).....</i>	<i>197</i>
<i>Figure V-13. Scanning speed porosity relation with tensile strength results: a) Pore number and sphericity; b) toughness modulus and strain; c) UTS and relative density (Marin et al., 2023).....</i>	<i>198</i>
<i>Figure V-14. Porosity analysis of the samples by tomography: a) sample schematic; b) sphericity versus equivalent diameter; c) pore area XY plane (normal to the building direction); d) pore size distribution (Marin et al., 2023).....</i>	<i>199</i>
<i>Figure V-15. Ductile to brittle fracture transition with porosity: a) stress concentrator factor; b) minimum pore distance versus the distance from MIZ (Marin et al., 2023).</i>	<i>200</i>
<i>Figure V-16. Blade with lattice structures and dimensions. ....</i>	<i>202</i>
<i>Figure V-17. Evaluation of the hardness on the blades manufactured by PBF-LB. ...</i>	<i>203</i>
<i>Figure V-18. Manufacturing regions and tool engagement schematics. ....</i>	<i>204</i>
<i>Figure V-19. Power consumption according to blade machining regions (1-8). ....</i>	<i>206</i>
<i>Figure V-20. Hammer test assay: a) Experimental apparatus; b) monoaxial sensors position and excitation points; c) first mode response; d) second mode response; e) static stiffness. ....</i>	<i>207</i>
<i>Figure V-21. Comparison of the surface topography of solid and latticed blades: a) concave; b) convex regions. ....</i>	<i>208</i>
<i>Figure V-22. Roughness Ra and Rz values. ....</i>	<i>209</i>
<i>Figure V-23. Dimensional analysis: a) Solid blade; b) Lattice blade. ....</i>	<i>209</i>
<i>Figure V-24. Blade with internal microstructure SEM analysis and energy spectrum in relation to the alloy composition. ....</i>	<i>210</i>
<i>Figure V-25. Blade with internal microstructure tomography analysis: a) Analysed sections; b) Top section; c) Measured distances; d) Lateral section.....</i>	<i>211</i>



---

## List of Tables

Table II-1. Chemical composition of Inconel <sup>®</sup> 718 (wt%) (Devaux et al., 2008). .....	17
Table II-2. Hardness and tensile results of Inconel <sup>®</sup> 718, adapted from Valle et al. (2013). .....	17
Table II-3. Effect of different cooling lubrication strategies on machining performance, adapted from Jawahir et al. (2016).....	49
Table III-1. Linear segment length used to evaluate the machine (de Souza et al., 2021). .....	87
Table III-2. Angular increments used to evaluate the machine response (de Souza et al., 2021). .....	88
Table III-3. Values of the effective cutting radius calculated and theoretical. ....	96
Table III-4. Experiment control factors and levels (Basso et al., 2022). ....	100
Table III-5. Analysis of Variance (ANOVA) for $S_z$ (Basso et al., 2022). ....	104
Table III-6. Experimental parameters and their levels. ....	114
Table III-7. Analysis of Variance of the Resulting Cutting Force. ....	117
Table III-8. Analysis of Variance of the Surface Deviation. ....	118
Table III-9. Analysis of Variance of the Surface Roughness ( $R_a$ ). ....	120
Table III-10. Maximum deflection and resultant cutting force of the simulated regions. .....	122
Table III-11. Estimated versus real milling time of Casing critical regions. ....	127
Table III-12. Distance in mm from Datum A to each section. ....	130
Table III-13. Measurement data from sections S1 to S20. ....	131
Table III-14. Comparison of the number of NC lines versus the predicted and real milling time for each milled region. ....	136
Table IV-1. Composition of Waspalloy AMS 5706. ....	158
Table IV-2. Surface roughness obtained by confocal microscopy. ....	161
Table IV-3. Lead angle effect on the effective radius and cutting speed ( $a_p$ of 0.4 mm). .....	162

List of Tables

---

Table IV-4. Experimental matrix.....	168
Table IV-5. Variation of the effective cutting speed under different cutting tool tilts. ..	170
Table IV-6. Milling time predicted by the CAM versus real. ....	178
Table V-1. Chemical composition of the substrate and powder (Marin et al., 2023). .	185
Table V-2. Uddeholm Corrax® properties solution treated (Marin et al., 2023). ....	185
Table V-3. Parameters used for the manufacture of the samples (Marin et al., 2023). .....	185
Table V-4. PBF-LB manufacturing parameters.....	203
Table V-5. Chemical composition of the Inconel® 718 powder (in weight %). ....	203
Table V-6. Test definitions and manufacturing parameters. ....	205



## List of Acronyms

2D	Two dimensions
3D	Three dimensions
API	Application programming interface
AM	Additive manufacturing
BCC	Body-centred-cubic
BCT	Body-centred tetragonal
BUE	Built-up edge
CAD	Computer-aided design
CAM	Computer-aided manufacturing
CAE	Computer-aided engineering
CAI	Computer-aided inspection
CBN	Cubic boron nitride
CC	Cutter contact point
CFD	Computational fluid dynamics
CL	Cutter location point
CLSF	Cutter location source file
CNC	Computer numerical control
CMM	Coordinate measuring machines
CT	Computed tomography
CWE	Cutter-workpiece engagement
ECM	Electrochemical machining
EDM	Electro-discharge machining

## *List of Acronyms*

---

FDM	Finite difference method
FEA	Finite element analysis
FCC	Face-centered cubic
FFSM	Free-form surface milling
HPC	High-pressure cooling
HRSA	Heat-resisted Superalloys
IBR	Integrated blade rotor
ICCE	In-cut cutting edge
IPW	In-process workpiece
KBE	Knowledge-based engineering
DED-LB	Laser-based directed energy deposition
PBF-LB	Power bed fusion laser beam
MQL	Minimum quantity lubrication
NDT	Non-destructive testing
NURBS	Non-uniform rational B-spline
MIZ	Melting interface zone
NC	Numerical control
OO	Oriented object
RKT	Revenue kilometres-passenger
RPM	Revolutions per minute
TSE	Tool-surface engagement
TTT	Time-temperature-transformation
UTS	Ultimate tensile strength

---

## List of Symbols

### Roman Letters

Symbol	Units	Description
$a$	[mm]	Pore length
$A$	[mm <sup>2</sup> ]	Cutting area
$a_e$	[mm]	Axial depth of cut
$A_i$	[mm <sup>2</sup> ]	Area of $i$
$A_p$	[mm <sup>2</sup> ]	Area of the pore
$a_p$	[mm]	Depth of cut
$A_{seq}$	[mm <sup>2</sup> ]	Area of the equivalent sphere
$d_b$	[mm]	ICE element height
$c_i$	[mm]	Coordinate centre of the tool radius
$D$	[mm]	Tool diameter
$d$	[mm]	Distance between pores
$d_{seq}$	[mm]	Sphere equivalent diameter
$E$	[J/mm <sup>3</sup> ]	Energy density
$E_c$	[J/mm <sup>3</sup> ]	Cutting energy
$E_s$	[J/mm <sup>3</sup> ]	Shear energy
$E_f$	[J/mm <sup>3</sup> ]	Friction energy
$E_p$	[J/mm <sup>3</sup> ]	Ploughing energy
$F$	[mm/rev]	Feed per revolution
$F$	[N]	External force
$F_a$	[N]	Normal force to the edge
$F_c$	[N]	Cutting force

*List of Symbols*

---

$F_i$	[N]	Force component on $i$ direction
$\hat{f}_i$	[-]	Unitary vector of instantaneous direction
$F_M$	[N]	Resulting cutting force
$F_r$	[N]	Radial cutting force
$F_t$	[N]	Tangential cutting force
$f_z$	[mm/z]	Feed-per-tooth
$\hat{g}_i$	[-]	Unitary vector of instantaneous lateral pass
$h$	[mm]	Hatch spacing
$h_b$	[mm]	ICE element length
$h_c$	[mm]	Crisp height
$h_l$	[mm]	Total cutting length
$h_{max}$	[mm]	Maximum uncut chip thickness
HV	[Pa]	Vickers hardness
HRc	[-]	Rockwell Hardness C
K	[N/m]	Stiffness constant
$k_c$	[N/mm <sup>2</sup> ]	Cutting force coefficient
$k_t$	[-]	Stress concentrator factor
$K_U$	[J/m <sup>2</sup> ]	Modulus of tenacity
L/D	[-]	Slenderness ratio
$l_i$	[mm]	Length in $i$ direction
M	[kg]	Mass
$N_i$	[-]	Pore element
$N_i$	[-]	Number of pores
$O_i$	[m]	Cartesian origin of the $i$ axis

---

P	[W]	Laser power
R	[mm]	Nominal radius of the ball-end mill
R <sup>2</sup>	[-]	Multiple correlation coefficient
R <sub>a</sub>	[μm]	Arithmetical mean of the roughness profile
R <sub>ef</sub>	[mm]	Effective cutting radius
r <sub>i</sub>	[mm]	Radius <i>i</i> of the tool
R <sub>z</sub>	[μm]	Mean roughness depth of the roughness profile
R <sub>t</sub>	[μm]	Total height of the roughness profile
S	[RPM]	Spindle Speed
S <sub>a</sub>	[μm]	Arithmetical mean height
S <sub>z</sub>	[μm]	Maximum height area roughness
t	[mm]	Layer thickness
T	[-]	Tangent condition
u	[J/mm <sup>3</sup> ]	Specific cutting energy
U	[J/mm <sup>3</sup> ]	Total energy
U <sub>a</sub>	[J/mm <sup>3</sup> ]	Accumulated energy
v	[mm/s]	Scanning speed
V <sub>b</sub>	[mm]	Flank wear
V <sub>c</sub>	[m/min]	Cutting Speed
V <sub>chip</sub>	[mm <sup>3</sup> ]	Instantaneous chip volume
V <sub>ef</sub>	[m/min]	Effective cutting Speed
V <sub>fa</sub>	[°/min]	Feed rate for angular movement
V <sub>fl</sub>	[mm/min]	Feed rate for linear movement
V <sub>i</sub>	[mm <sup>3</sup> ]	Volume of <i>i</i>

## List of Symbols

---

$V_p$	[mm <sup>3</sup> ]	Volume of the pore
$z$	[-]	Number of cutting edges of a tool

### Greek Letters

Symbol	Units	Description
$\alpha$	[°]	Helix angle
$\delta$	[-]	Delta phase
$\delta$	[mm]	Deflection
$\varepsilon$	[%]	Elongation
$\theta$	[°]	Tool rotation angle
$\eta_i$	[-]	Normal vector to the reference $i$
$\kappa$	[°]	Axial immersion angle
$\gamma$	[°]	Exit angle
$\gamma'$	[-]	Gamma prime phase
$\gamma''$	[-]	Gamma double phase
$\omega$	[rad/s]	Angular rotation speed
$\psi$	[-]	Sphericity ratio
$\Psi$	[°]	Radial immersion angle
$\phi$	[°]	Cutting edge lag angle
$\sigma$	[Pa]	Nominal stress
$\sigma_{max}$	[Pa]	Maximum stress
$\sigma_{YS}$	[Pa]	Yield strength
$\sigma_{TS}$	[Pa]	Ultimate tensile stress
$\phi_i$	[°]	Angular rotation of flute $i$

---

## **Chapter I. Introduction and contextualization**

---





# Chapter I. Introduction and contextualization

*This chapter will introduce the problem and detail the importance of the study. It presents a detailed contextualization with a clear scope delimitation, specifying the content of this doctoral thesis and its objectives and specific objectives.*

## I. 1. Introduction

This document presents a systematic review of the literature and the methodology developed to investigate the surface signature left by different shapes of ball-end tooltips after the milling process together with vanguard manufacturing processes, to improve parts design. Thus, the manufacture of near-net-shape products and their subsequent finishing is investigated. The work was developed in the Department of Mechanical Engineering of the University of the Basque Country (UPV/EHU) together with the Aeronautics Advanced Manufacturing Centre (CFAA) and the support of the Research Group on Computer-Aided Manufacturing (GPCAM) from the Federal University of Santa Catarina (UFSC). The proposed investigation focuses on investigating the manufacture of complex shapes and methods to evaluate, identify, and predict the signatures left by ball-end tooltips on 5-axis milling of free-form surfaces. Besides, it has investigated methods to minimize defects on the machined surface of critical components.

## I. 2. Context and motivation

The milling process is highly versatile, producing parts in various shapes and sizes with gradual removal of material. However, this versatility also introduces complexity and challenges to the manufacturing process. Figure I-1 contextualizes the intricacies involved in the complex manufacturing process through milling.

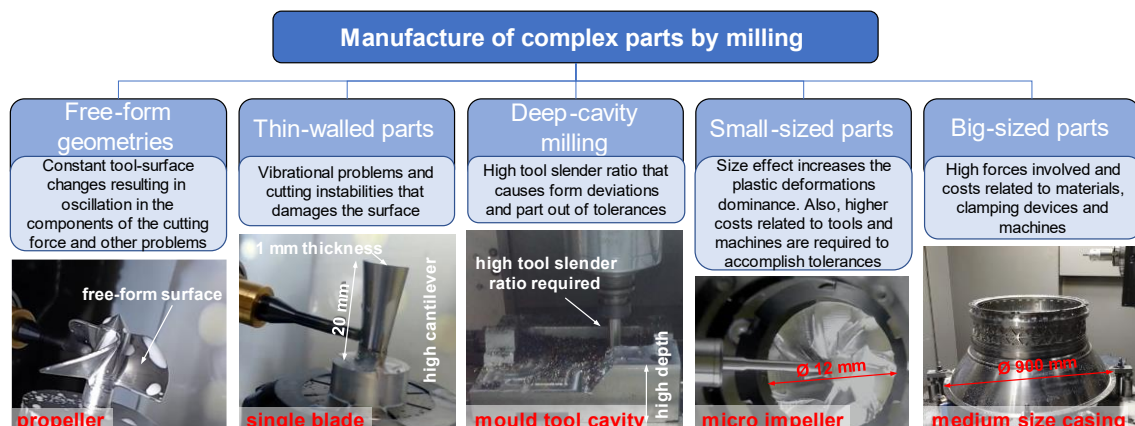


Figure I-1. Manufacture of complex parts by milling.

In the aerospace industry, many of these conditions are present, and manufacturing with high-quality requirements, usually from bulk materials, increases the complexities of the process even more. The constant strive for reliability, safety, and performance in aerospace applications elevates the importance of mitigating issues related to the milling process of components with free-form surfaces, low rigidity, and regions that are difficult to access during the machining process.

Free-form surfaces are one of the most challenging shapes to produce. They are present in several industrial products, such as automotive, medical, military, naval, and dies. However, some sectors, like the aeronautical and aerospace industries, are highlighted due to high added value. In these segments, the quality of the final product is critical, as form errors and high roughness reduce efficiency and impact performance.

The increase in the demand for passenger and goods transportation and climate crisis concerns promoted an exponential growth of civil aviation during the past few decades, along with the development of more efficient aeroplanes. Furthermore, the transporting demand for passengers and goods is expected to increase over the next 20 years by an average of 4.3% per annum. The forecast prediction of The International Civil Aviation Organisation (ICAO, 2023) shows a substantial impact of the increase in cargo traffic in terms of tonnage for the next decades. By the mid-2030s, more than 200,000 flights per day all over the world, increasing concerns about sustainability and availability.

In the same direction, regulatory agencies constantly increase environmental protection standards, limiting nitroxides (NO<sub>x</sub>), carboxides (CO<sub>2</sub>), and noise emissions. This imposes the development of engines with lower weight and improved aerodynamics. Besides, several efforts are being dedicated to accelerating the transition to carbon neutrality (Perea-Moreno et al., 2022). In the best scenarios, using Sustainable Aviation Fuel (SAF), carbon neutrality can be achieved in 2040. However, by the year 2050, obtaining half of the emissions recorded in 2005 will not be possible due to the forecasted demand increase (Abrantes et al., 2021).

Enhancing aircraft efficiency is crucial for achieving a reduction in CO<sub>2</sub> NO<sub>x</sub> emissions. Technological advances like high-performance materials improve the buy-to-fly ratio and engine efficiency, increasing the challenges faced during the manufacturing process of these kinds of components. Besides, the aerodynamics enhancements have already resulted in a substantial 70% decrease in aircraft fuel consumption per passenger-kilometre (RKT). As the passenger's and luggage's weight is an uncontrollable factor, efforts are focused on decreasing the aeroplane part's weight. Consequently, new technologies must come into play to achieve more significant reductions.

The development of engines with reduced weight and enhanced aerodynamics can provide a reduction in emissions by up to 90% and noise by 65% by the year 2050, with over 80% of conventional fuel being replaced by Sustainable Aviation Fuel (SAF) - ACARE's plan 20-50. Furthermore, the Transport Association (IATA, 2023) report shows an increase in the recent costs of commercial aeronautical operations powered by the rise of crude oil (barrel Brent). It can be seen that according to the S&P Global Commodity Index, the price of both crude oil and jet fuel almost doubled (Figure I-2).

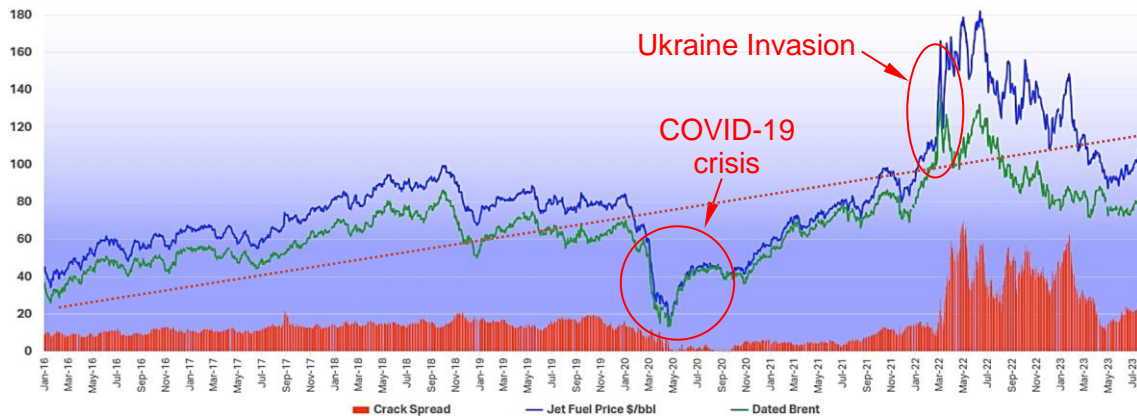


Figure I-2 Fuel price against crude oil price (USD/barrel).

The COVID-19 pandemic resulted in a cumulative loss of over \$180 billion from 2020 to 2022, followed by a bad scenario related to the Ukraine invasion that increased the fuel costs and products related to air transportation to historic heights. Even though, by the end of 2022, aviation emissions reached almost 800 Mt CO<sub>2</sub>, about 80% of the pre-pandemic level, with a share corresponding to fuel consumption of about 25% of the total operational costs. All this justifies the efforts to develop jet engines with lower fuel consumption and emission levels.

The literature review identified that the efforts to optimize the aeronautical industry cover several areas of knowledge. Enhancing aeroplane engines underscores advancements in design and materials with consequent effects on production processes. Figure I-3 presents the requirements of the modern aeronautical industry and subareas of interest.

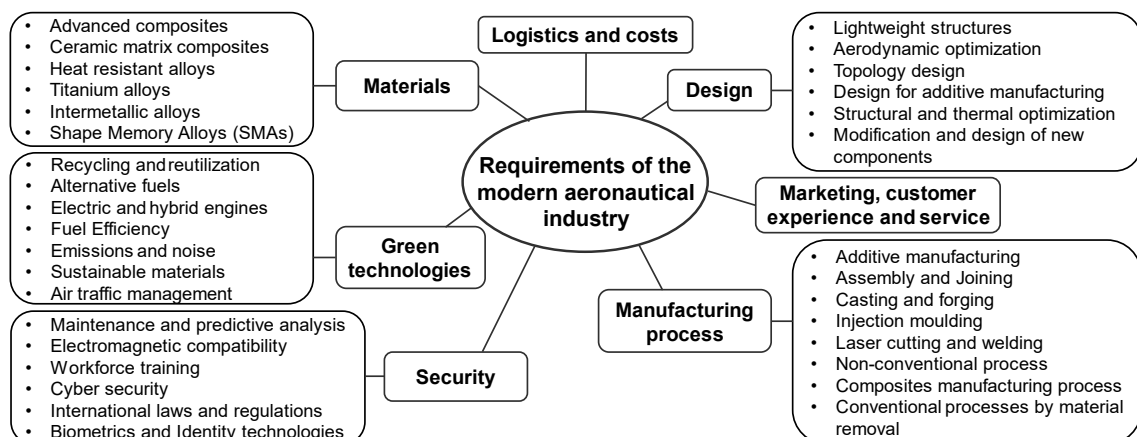


Figure I-3. Requirements of the modern aeronautical industry and subareas of research interest.

In this scenario, additive manufacturing stands out due to freedom in shape, materials, and capacity to produce internal structures. However, concerns about new technologies and technical limitations hold its wide application with challenges on the final surface obtained to the internal micro and meso structures obtained. At the same time, the complexity and flexibility of the additive manufacturing processes increased technical and scientific interest, becoming one of the hottest topics of the last decades. Still, there is no commercial additive process capable of producing surfaces with the standards required for high-performance applications, being the conventional machining processes widely used.

Nowadays, 5-axis milling is the main manufacturing process utilized to finish free-form surfaces. Ball-end tooltips are commonly applied to finish free-form shapes that are not developable surfaces (Tsai and Liao, 2010). Also, numerical control programming with multi-axis is required to guarantee tolerances and improve production (Grešová et al., 2022). This combination allows machining with different tool-part orientations, producing a free-form and smooth surface. However, due to the geometries involved, changes in tool orientation, and the intermittent characteristics of the milling process, it produces crisp waves and marks that increase the roughness, which can compromise performance. The pattern can change according to the cinematic process, wear, or deviations in the tooltips due to clamping or manufacturing.

In the design of blades and blade-integrated disks (BLISKS), also known as integrally bladed rotors (IBR), the shape of the surface can be optimized to improve the aerodynamic flow and weight and then the fuel consumption per weight. Such parts usually require high functional performance, strength, stiffness, and thermal resistance with high precision and accuracy. Besides, hard-to-cut materials and high cutting forces are common in such components, making the finishing process challenging.

The aspect of the surface generated by the milling process significantly impacts the surface integrity and performance of the part. In blades and aerofoil components, form errors and other process signatures can significantly reduce the component's performance; thus, tight design tolerances are applied. Surface integrity also plays an important aspect in the fatigue life of critical parts, and for this reason, it has been extensively investigated in the last decades (Wang et al., 2021a).

The surface roughness effects on aerofoil components are directly dependent on the Reynolds number (dimensionless quantity that represents the ratio of inertial forces to viscous forces on a fluid). The roughness level weakens the flow, provoking low Re separation and higher performance losses. These losses are more significant with the

increase of the Re number, and the surface is rough (Bai et al., 2014). Wang et al. (2021b) investigated the impact of the roughness ( $Ra$ ) and its location on the aerodynamic performance of a subsonic compressor aerofoil ( $Re = 1.5 \times 10^5$ ). The turbulence level increased with the increase of the Roughness  $Ra$ , and the roughness of the leading edge of the aerodynamic profile played an important role in eliminating the laminar separation and improving the aerodynamic performance. Besides, the aerodynamic performance loss was more susceptible to roughness location (up to 30% of the aerodynamical coverage) with a higher roughness magnitude.

To guarantee the position of the tool in 5-axis milling, advanced NC controllers are required together with CAM software capable of developing valid and optimized tool trajectories. Besides, the tolerance band must be carefully adjusted to maintain the process performance with at least a minimum surface quality. Besides, in 5-axis machining, the inverse cinematic of the machine makes the general modelling of the process challenger.

One way to investigate the quality of the manufacturing process is by directly analysing the signature left on the machined surface. The topographic aspect of 5-axis ball-end milling can be estimated using different geometrical models that consider the tool position in space, its diameter, the feed per tooth, the stepover, and the tool run-out. However, in free-form surfaces, the constant contact changes between the tool and the part make this process difficult to predict, even with complex models, resulting in a topic that has been continuously investigated up to now.

Nowadays, commercial CAD/CAM software provides a wide range of tools to aid in the manufacture of free-form surfaces. However, they cannot fully predict free-form milling, cutting forces, tool deflections, and other problems that damage the surface and cause deviation in the final part. Predicting the milled surface texture is limited due to several reasons: i) the simulation does not consider the effect of the material, ii) the cutting edge and relative motion are not taken into account, iii) tool deflection due to machine rigidity is neglected, iv) tool run-out is not considered, and v) the engagement of the tool with the surface is usually estimated by considering the tool dome projection swept between consecutive CC points.

In this regard, supplementary tools (SMART CAM tools) are being developed to fill these gaps along with robust mathematical models to describe cutting phenomena. Additionally, although existing models are capable of predicting some aspects of surface topography, limitations and difficulties in integrating them into software with open architecture persist. These limitations restrict their widespread application in both

commercial and scientific fields. Therefore, more efforts must be made to address these limitations.

As the CAM software does not properly consider the crisp high on the feed direction in the surface prediction on ball-end milling of free-form surfaces, a methodology is proposed based on the discretization of the toolpath. A routine has been developed to obtain modelling information, considering 5-axis milling of free-form surfaces directly from the CAD/CAM software or post-processed NC files. This information is then used to improve process estimations and enhance industrial applications, facilitating future evaluations of more complex problems that require geometrical data of the tool and the surface.

### **I. 3. Objectives**

Considering this scenario, the current thesis proposes to investigate the milling process of complex shapes, addressing topics towards a robust model to predict the texture of free-form surfaces, including material properties, the effective cutting speed of the tooltip, feed rate oscillation, tool run-out, cutting parameters, with a focus on the modelling of ball-end tooltips on free-form surfaces milling for evaluate parts manufactured by machining or printed near-net-shape. Other problems related to manufacturing free-form thin-walled parts by milling are also presented to support understanding the finishing process of such geometries. The global objectives of this thesis are presented in section I.3.1, and the specific objectives are presented in section I.3.2.

#### ***I. 3. 1. General Objectives***

The general objectives of the thesis are: i) Investigate the milling process of free-form surfaces and the finishing process by ball-end tooltips; ii) Propose a method to integrate into CAD/CAM software tools to improve the surface prediction in the 5-axis milling with ball-end tooltips; iii) investigate additive manufacturing processes and design for the manufacture of complex parts with free-form surfaces for mechanical applications; iv) address the use internal microstructures, its effects on the part rigidity and posterior finishing process by ball-end milling.

#### ***I. 3. 2. Specific Objectives***

To achieve the objectives of the doctoral thesis, investigating the milling of free-form surfaces with ball-end tooltips, software implementations, and new manufacturing

processes to improve the design and the process of components, specific objectives were delineated and are stated hereafter.

1. To conduct a detailed state-of-the-art review in manufacturing complex parts with free-form surfaces, identifying applications, challenges, and the main opportunities.
2. To investigate the NC machining response in multi-axis milling.
3. To evaluate the cutting workpiece engagement of ball-end tooltips and develop a programming routine to correlate the cutting location, cutting contact, and respective vectors of the tool and the surface and implement it in CAD/CAM software.
4. To develop a model to predict the free-form surfaces milled with ball-end tooltips.
5. To investigate the influence of the ball-end tooltip centre and workpiece material on the milling process.
6. To study the ball-end tooltip deflection according to tool tilting during milling.
7. To investigate the manufacture of complex thin-walled parts and the effects of the part rigidity and clamping system on the form error.
8. To design and manufacture a part containing free-form surfaces with internal microstructures by PBF-LB and compare performance on the posterior finishing process by milling against a solid one.

## **I. 4. Memory organisation**

This work presents a systematic review of free-form surfaces manufactured by ball-end milling, followed by contributions to modelling the process using CAD/CAM software tools for easy process visualization and improvement. Also, it is presented towards designing complex parts containing free-form surfaces and its effect on the posterior finishing process by milling, contributing to both scientific and industrial fields. The doctoral thesis is organized into a series of chapters, and the content is briefly described below.

**Chapter I** introduces the doctoral thesis, describing the context, the scientific challenges, and the industrial motivation undertaken. In the sequence, the scope of the investigation and aims are presented in detail with a clear statement of the objectives and specific objectives. Finally, the structure of the thesis and memory organisation is presented.

**Chapter II** presents an overview of the state-of-the-art research focused on manufacturing free-form surfaces with ball-end tooltips, identifying gaps, and contextualizing the investigation presented in this doctoral thesis. It contemplates a review of critical parts containing free-form surfaces, their definitions, programming methods, machines, resources and tools, characteristic signatures, and limitations

during the manufacturing process. Also, it presents a review of the additive manufacturing processes that allow the manufacture of parts with complex internal structures, as well as inspection procedures and techniques for evaluation of the machined surface and internal structures.

**Chapter III** presents the preliminary studies conducted to evaluate and improve the understanding of the machining process of free-form surfaces, focusing on the finishing process with ball-end mills and difficult-to-manufacture parts. The research presented in this chapter evaluated the machine response time on a multi-axis machine, the contact of the ball-end tooltip and the material effect on the milled surface, challenges on the manufacture of big-size thin-walled components, and the tool deflection variation with tilt when milling with ball-end tooltip. Lastly, a preliminary case study on blade manufacturing is presented, and challenges are discussed.

**Chapter IV** presents the modelling of ball-end tools considering up to 2 radii tooltips, helix angle, and tool run-out. It also presents the developed methodology to obtain modelling data for free-form surface milling using CAD/CAM software with an open interface. Finally, a routine is implemented using the ball-end tooltip model developed, and the routine outputs are used to evaluate the surface texture and roughness of free-form surfaces finished with ball-end mills.

**Chapter V** studies the manufacture of samples by PBF-LB, evaluates the application of internal microstructures on a blade, and compares it with a solid one. Finally, the effects of the part stiffness and capacity to damp vibrations inherent in the milling process are investigated in order to produce functional parts finished by ball-end tooltips with improved surfaces.

**Chapter VI** presents the main contributions of the present doctoral thesis and proposes research lines for future investigations in the field.



---

## **Chapter II. State-of-the-art of the manufacture of free-form surfaces**

---



## Chapter II. State-of-the-art of the manufacture of free-form surfaces

*This chapter presents a bibliographic review of the state-of-the-art in the milling process of complex parts containing free-form shapes. Furthermore, a systematic review of the defects and problems faced while manufacturing high-value-added components using different materials or geometrical shapes is presented.*

### II. 1. Aeronautical engine components

#### II. 1. 1. Design and operation

The propulsion system is the most expensive and important part of the aircraft. Nowadays, in commercial aviation, the jet aircraft fleet is embedded with turbojets due to the balance between performance and acceptable fuel consumption. As shown in Figure II-1 schematics, the main components of the turbofan are the fan, compressor, combustion chamber, turbine, and casing, describing its materials.

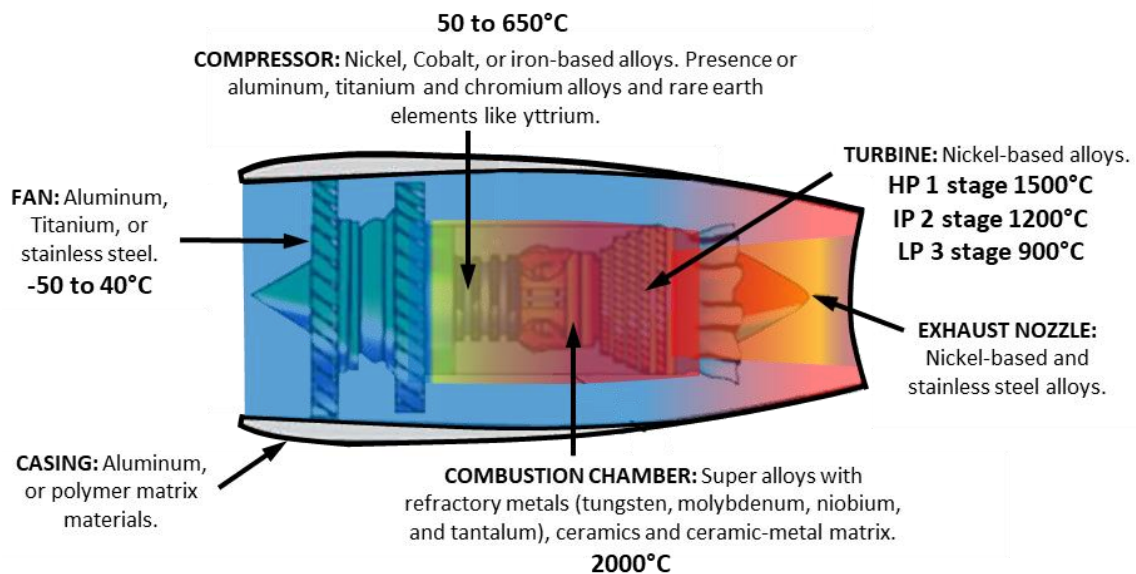


Figure II-1. Turbofan components and materials.

The turbojet engines work by the principle of the Brayton cycle and have higher performance than the Otto cycle commercially utilized in other motors. The operation cycle has four stages, as described in Figure II-2.

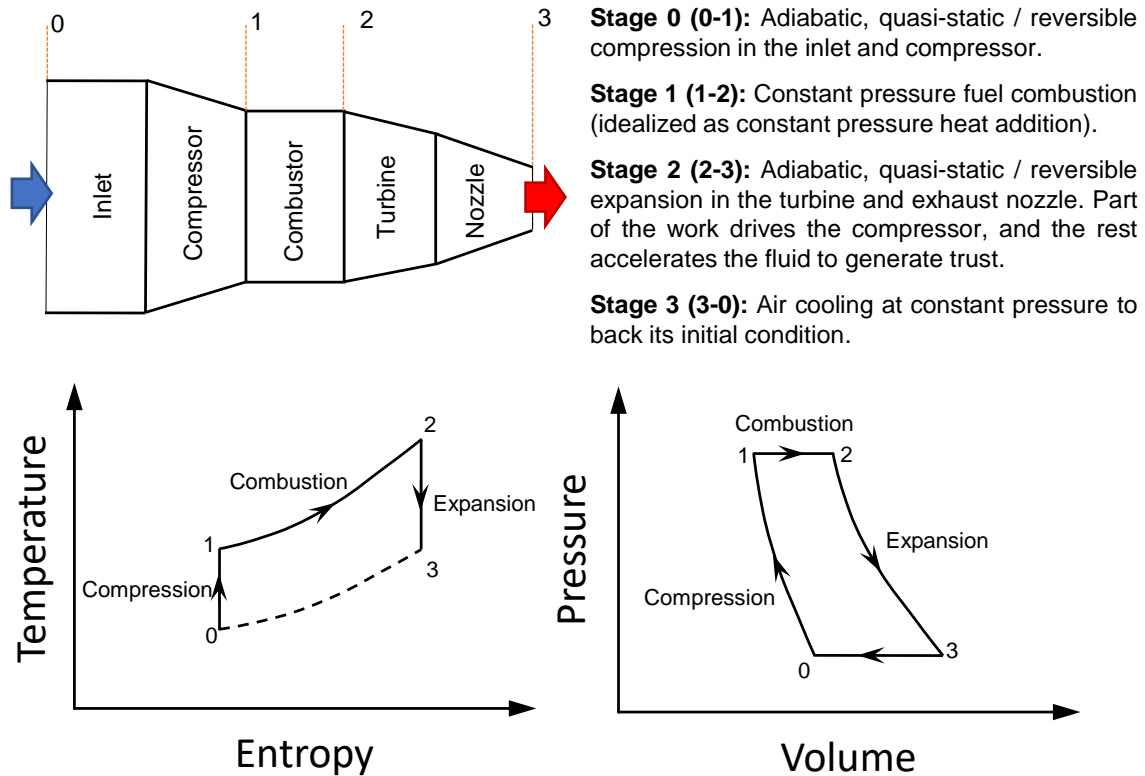


Figure II-2. Brayton cycle and stages.

In the trend of the new generation of turbojets, the Ultrafan architecture is on the spot for application in the 2030s. This new concept delivers greater fuel efficiency, reducing emissions, improving costs, and sustainability. This new concept uses a gearbox (Geared architecture). Applying a gearbox makes it possible to disassociate the fan from the turbine speed rotation, allowing it to operate at the optimized condition for each stage for its global maximum efficiency. It also reduces noise and other associated losses. Furthermore, the modular architecture of UltraFan turbojets enables them to be scaled for various thrust levels, making them suitable for a wide range of aircraft, from regional jets to long-distance aeroplanes, with thrust capabilities ranging from 25,000 lb to over 100,000 lb. So, the design concept of turbofan engines will not change drastically in the near future, maintaining its operation principle and the major part of components.

The latest prototype of UltraFan tested by Rolls-Royce (with a fan nominal diameter of 140 inches, 3556 mm) was capable of delivering 64MW (87,000 horsepower) of power with a 25% fuel burn improvement, 40% less NO<sub>x</sub> emissions, 35% less noise and almost zero nvPM particulates at cruise compared to the actual generation of Trent engines (Rolls-Royce, 2023). Figure II-3 presents the schematic of the UltraFan concept.

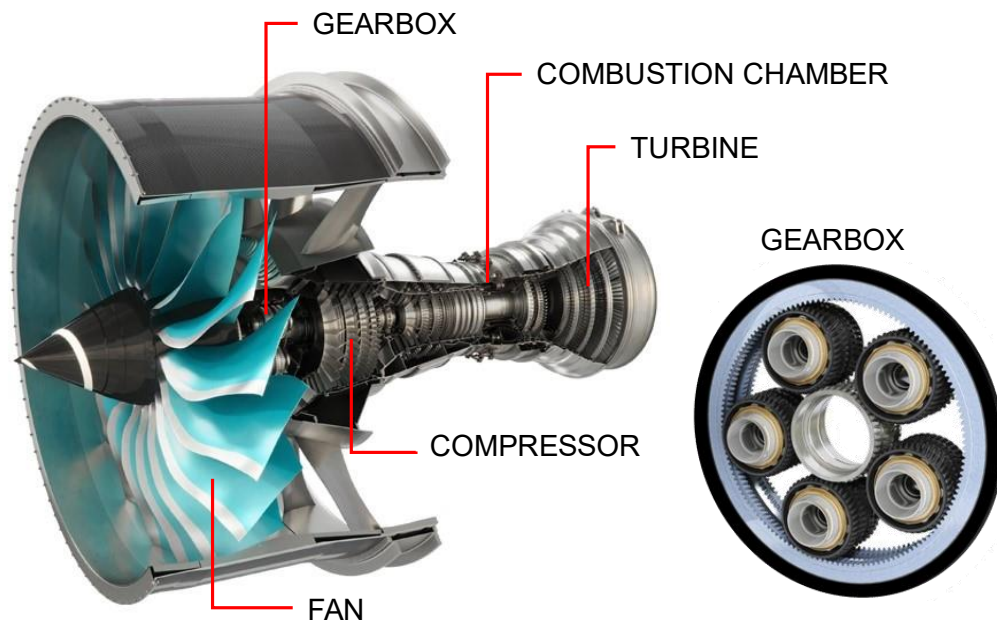


Figure II-3. Cross section of UltraFan turbojet engine, adapted from Rolls-Royce (2023).

### **II. 1. 2. Materials of turbofan engines**

A higher temperature ratio is required to improve the efficiency of turbofan engines, maximizing the operating temperatures. The temperatures in the combustion chamber can reach about 2,300°C. These harsh operational conditions make the region and nearby regions critical for material selection, making the selection of nickel-based superalloys, ceramics, and metal-ceramic matrices commonly used in high-temperature regions.

In the last few decades, to improve the mechanical and physical properties of the components, a lot of effort has been spent researching new materials and alloys with superior properties, like composites, titanium, and nickel-based alloys. However, it also made the manufacturing processes challenging, requiring optimization or the development of new manufacturing processes (Arrazola et al., 2013).

It is estimated that introducing new materials has increased operational temperature by 10°C per annum since the 1950s (Ezugwu, 2005). Some of the mechanical properties that allowed the design of more efficient parts are the strength-to-weight ratio, corrosion resistance, and fatigue resistance (Dwivedi et al., 2021).

Figure II-1 shows turbofan schematics with the most significant materials applied to each region due to temperature requirements. Figure II-4 shows the evolution of the materials used in turbojet engines in terms of their weight.

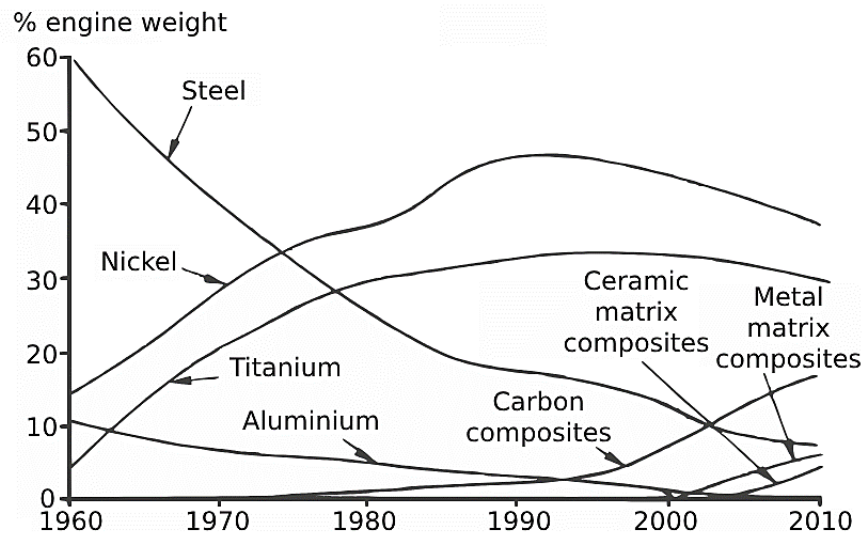


Figure II-4 . Evolution of turbine materials (Miller, 1996).

As presented in Figure II-4, the most significant weight of turbojet engines is composed of nickel-based and titanium alloys. Even increasing the usage of composites, some critical parts of the engine with high or lower operation temperatures can not be replaced due to safety means.

For a long time, stainless steel was the most common alloy in turbofan engines. It has excellent high-temperature corrosion resistance and mechanical properties. With the domain of titanium and superalloys, its lower strength-to-weight ratio reduced its application, as presented in Figure II-4. Nowadays, the parts manufactured in stainless steel are mostly casings, combustor liners, exhaust cones, low-pressure turbine stage blades, bearings, exhaust nozzles, inlet components, and reversers. The tensile strength and hardness for austenitic stainless steel (3XX) go from 515 to 795 MPa and 150 to 220 10HV; for martensitic stainless steel (4XX), they go from 690 to 1,520 MPa and 200 to 600 HV, and duplex stainless steel from 550 to 800 MPa and 200 to 300 HV, respectively. Even though martensitic steel presents higher mechanical properties, austenitic and duplex are preferable for higher corrosion resistance in higher temperature environments.

Titanium alloys are mostly applied on the airframe and engine components due to their exceptional strength and lightweight (high strength-to-weight ratio). The reduction in masses of the components of the fuselage and engine by using lightweight titanium alloys reduces fuel consumption and improves operating efficiency (Uhlmann et al., 2015). Besides, titanium alloys have good performance in high temperatures and corrosion resistance (Zoya and Krishnamurthy, 2000) and have been used in many parts of the turbofan that are subject to low and intermediary temperatures (Figure II-1). The machinability of the titanium due to its chemical reactivity leads to excessive chipping or

breakage and localized shear bands (Hosseini and Kishawy, 2014; Su et al., 2006). Furthermore, also presents a low modulus of elasticity, thermal conductivity, and high strength levels at elevated temperatures, causing premature tool wear and failure, which affects the surface integrity (Ezugwu et al., 2005).

Heat-resisted superalloys (HRSA) are specified in components subject to higher temperatures than titanium alloys due to their more stable mechanical properties. It contains at least 25% Nickel, with many elements forming carbo/nitrides and iron for balance. Nickel-based alloys retain high mechanical and chemical properties, higher strength-to-weight ratio, good toughness, and resistance to thermal fatigue, shock, crack, and corrosion at higher temperatures (Ezugwu et al., 2003). These properties in elevated temperatures (over 600 °C) make them a good option for turbine blade components. However, nickel-based alloys have a higher density than titanium alloys, leading to a weight of about 50% of turbofan (Miller, 1996). Due to the difficulty in machining HRSA, monitoring the machined surface is necessary, especially in high-performance parts with reliability requisites (Arunachalam et al., 2004).

Inconel® 718 is one of the most popular nickel superalloys developed in the 60s. It is widely used in aerospace due to its significant hardening effects and high strain rates. Unfortunately, it also results in difficult-to-cut materials and challenging manufacturing processes. It is associated with short tool life and poor surface integrity, with higher tool wear, flank wear, crater, and breakage, especially in high-speed cutting (Jianxin et al., 2005). The typical composition of the Inconel® 718 is presented in Table II-1, and its mechanical properties in Table II-2.

Table II-1. Chemical composition of Inconel® 718 (wt%) (Devaux et al., 2008).

Ni	Fe	Cr	Nb	Mo	Ti	Al	C	B	Cu	Co	Mn	P
54.2	Bal.	17.9	5.3	2.99	0.97	0.5	0.026	0.003	<0.3	<0.02	<0.02	<0.005

Table II-2. Hardness and tensile results of Inconel® 718, adapted from Valle et al. (2013).

Condition	Phases	Grain size (µm)	Hardness (HV)	$\sigma_{YS}$ (MPa)	$\sigma_{TS}$ (MPa)	$\epsilon$ (%)
As-received	$\delta$ , $\gamma'$ , $\gamma''$ (Nb,Ti)C	30 (ASTM 7)	424.5 ± 4.9	948.3 ± 0.2	1248.4 ± 0.4	30.9 ± 0.8
Ageing 800 °C/6 h	$\delta$ , $\gamma'$ , $\gamma''$ (Nb,T)	29 (ASTM 7)	423.7 ± 6.1	941.3 ± 22	1236.2 ± 11	20.8 ± 1.4
SHT 1050°C / 5 min	(Nb,Ti)C	40 (ASTM 6)	261.7 ± 7.2	336.9 ± 5.6	795.5 ± 5.6	63.9 ± 2.2
SHT 1050°C /10 min	(Nb,Ti)C	59 (ASTM 5)	222.8 ± 11	341.6 ± 13	790.4 ± 13.2	66.3 ± 2.9
SHT 1050 °C / 5 min + ageing 800 °C / 6 h	$\delta$ , $\gamma'$ , $\gamma''$ (Nb,Ti)C	38 (ASTM 6)	426.0 ± 4.6	845.2 ± 8.1	1209.2 ± 2.9	21.7 ± 1.1
SHT 1050 °C/ 10 min + ageing 800 °C / 6 h	$\delta$ , $\gamma'$ , $\gamma''$ (Nb,Ti)C	62 (ASTM 5)	423.7 ± 4.4	846.1 ± 3.3	1208.1 ± 14	20.6 ± 1.0

SHT - Solution heat treatment

The properties of the Inconel® 718 and its temperature increases are directly affected by its constituent phases and compounds. The TTT curve of Inconel® 718 is presented in Figure II-5, where its principal phases and components are:

**Gamma Phase ( $\gamma$ ):** Austenitic matrix of Ni, with high contents of Fe and Cr, presents face-centred cubic (FCC) crystallographic structure with multiple slip systems, high solubility, good ductility, and formability. Solid solution and precipitation hardening are mechanisms used to increase the strength of the phase (Geddes et al., 2010).

**Gamma Prime Phase ( $\gamma'$ ):** Exhibits in crystal structure FCC with ( $\text{Ni}_3\text{Al}$ , Ti); Al and Ti are its primary constituents, with Nb and iron Fe present in low quantities. Other elements, such as Cr, Ti, Nb, and Ta, are present in low quantities (~0 to 1%) that precipitate homogeneously over the matrix, given the stability at elevated temperatures (1100 °C) and also helps to increase the hardness and mechanical strength associated with ageing time and temperature. This phase is necessary for creep resistance and strength at high temperatures of superalloys (Kishawy and Hosseini, 2019).

**Gamma Double Prime Phase ( $\gamma''$ ):** It is a metastable phase with a crystallographic body-centred tetragonal (BCT) structure. This phase is formed by combining Ni with Nb in the presence of Fe and Ti, with the final compound's stoichiometry aligning with the  $\gamma$  matrix,  $\text{Ni}_3\text{Nb}$ . The  $\gamma''$  phase typically precipitates simultaneously with  $\gamma'$ , and its combination results in good mechanical properties over 600°C (Miller, 1996; Raza, 2015).

**Delta Phase ( $\delta$ ):** A thermodynamically stable compound of  $\gamma''$  with an orthorhombic crystal structure that can form during thermomechanical processing, heat treatment, or in service. Similar to the  $\gamma''$  phase, the  $\delta$  phase contains Fe, Ti, Cr, and Mo substituting some Nb atoms increasing alloy mechanical properties.

**Carbides:** Compounds that increase the alloy's strength and are typically present in cubic crystal structures of the MC type [(Nb, Ti)C]. When they dissolve intergranular, they add high-temperature strength by sliding inhibition of grain boundaries. However, depending on the morphology of the carbides and their precipitation along grain boundaries, they reduce the ductility and toughness.

**Nitrides:** The most common nitrides are TiN, followed by NbN; both exhibit an FCC crystal structure. Similar to carbides, nitrides enhance the properties of the matrix. Heat treatment significantly influences nitride formation, and its stability makes it insoluble until it reaches melting points.



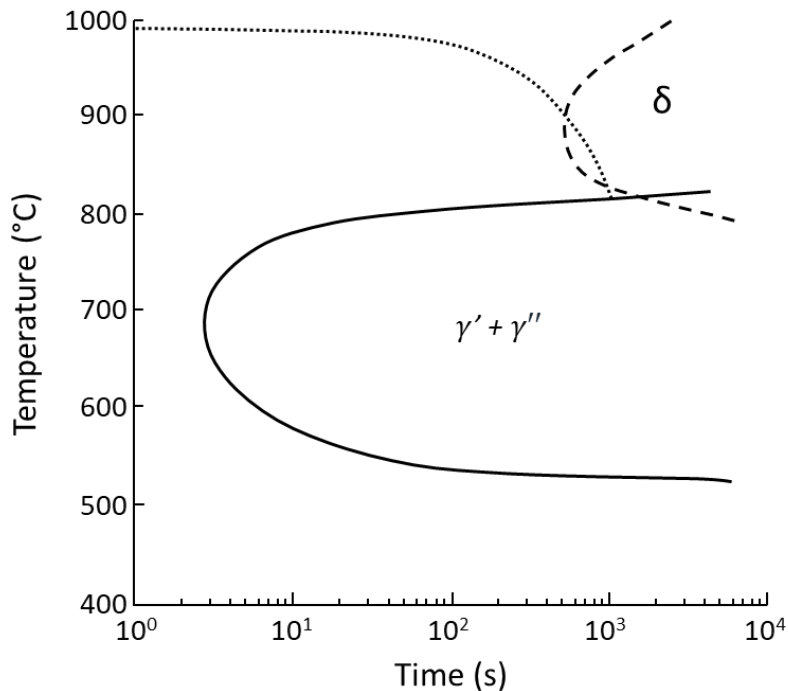


Figure II-5. Inconel® 718 TTT diagram, adapted from Xie et al. (2005).

The precipitation of phase  $\gamma''$  ( $\text{Ni}_3\text{Nb}$ ) is the principal responsible for the mechanical properties increase, which increases the mechanical stability and the hardness. The additional strengthening provided by  $\gamma''$  over  $\gamma'$  comes from a distortion in the c-axis direction of the tetragonal structure of the  $\gamma''$  that coexistence after it precipitates in  $\gamma'$  matrix (Oblak et al., 1974). It is obtained during the forging of the material or during a screw press with a high strain rate forming (Renhof et al., 2005). The precipitation of  $\gamma''$  ( $\text{Ni}_3\text{Nb}$ ) is about 15 % of the volume fraction, while  $\gamma'$   $\text{Ni}_3(\text{Al}, \text{Ti})$  presents about 4%, depending on the material composition (Devaux et al., 2008).

As the temperature increases above 650 °C in nickel-based alloys, the  $\gamma''$  phase starts to decompose to the thermodynamically stable  $\delta$  phase, deteriorating in strength. Increasing the amount of Al and Ti can be used to delay the softening effect. Additionally, to reduce the softening by temperature, several elements are added to the alloy to propitiate carbo-nitrites formation and solid solution strengthening; Co, Cr, Fe, Mo, and W are some of them. This combination of characteristics propitiates great resistance to environmental degradation, complicates the cutting process, and provokes accelerated tool wear (Mignanelli et al., 2017).

During the machining of Inconel® 718, two main reasons for the high temperature at the cutting zone and accelerated tool wear. The first is the high mechanical properties that make it hard to cut. The second is the low thermal conductivity ( $\sim 11 \text{ W/m}^\circ\text{C}$ ) associated with its high chemical stability (Jafarian et al., 2014). Ezugwu et al. (2003) reported the formation of a hardened layer when machining Inconel® 718, attributing it to the high process temperature and low thermal conductivity of the material. Also, the low thermal

conductivity results in a significant heat transfer to the tool, increasing its temperature and promoting the diffusion of elements (Co, W, Ta, Ti, and C) from the tool to the workpiece (Liao and Shiue, 1996).

Usually, with the temperature increase, the materials tend to soften, and the machining process is facilitated; however, due to the upper-cited effect of the hardness of Inconel<sup>®</sup> 718 in machining temperatures from 600 to 800°C still very high, promoting fast tool wear and breakage, making the machining process challenger for most tool materials and coatings. Figure II-6a shows a graph of Time-Temperature-Hardness for the Inconel<sup>®</sup> 718 solution treated at 1040°C for one hour. As can be seen, the temperature increases with the dissolution of the  $\gamma''$ , increasing the hardness with time. The state of thermal softening in Inconel<sup>®</sup> 718 can be achieved during its machining at temperatures above 800°C (Figure II-6b), where a drastic reduction in hardness and strength occurs, decreasing machining forces (Liao et al., 2008). However, the rise in cutting temperature also compromises the machinability, promoting crater wear and flank wear (Bushlya et al., 2013). Hence, a proper selection of process parameters, tool geometry, and tool coatings is necessary for the efficient machining of such material (Mahesh et al., 2021).

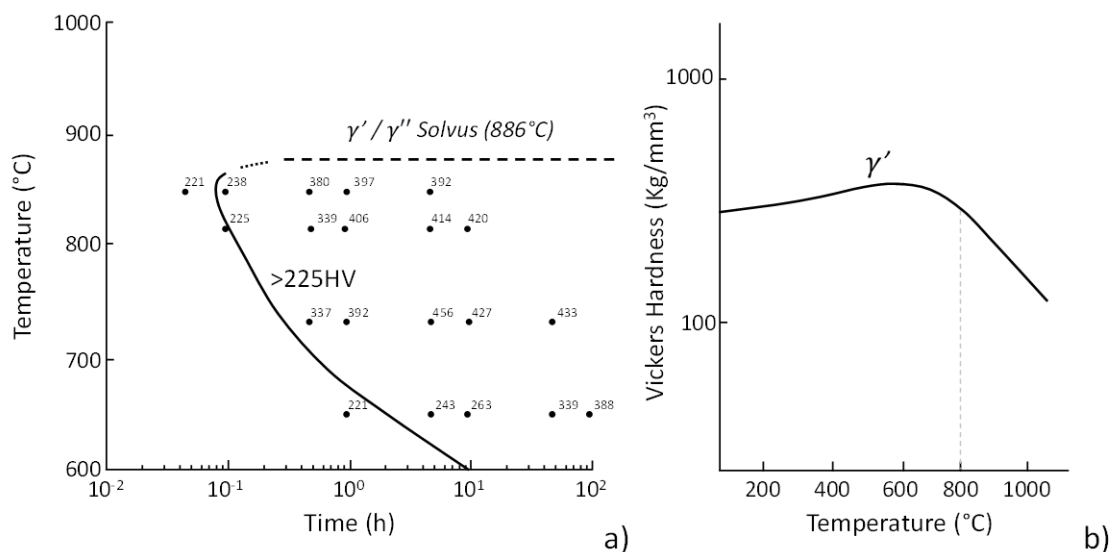


Figure II-6. a) Time-Temperature-Hardness of Inconel<sup>®</sup> 718 (Xie et al., 2005). b) Variation in hardness of Inconel<sup>®</sup> 718 with a temperature (Liao et al., 2008).

Waspaloy is another precipitation hardening Nickel-based alloy that can be applied in critical parts exposed to high temperatures. Even presenting similar properties, it has a higher Yielding (1050 to 1150°C) compared to Inconel<sup>®</sup> 718 (875 to 1090°C). The forming elements on  $\gamma'$  phase of Nickel-based alloys promote  $\sigma$  vs. T curve deviation, reducing yielding. As Inconel<sup>®</sup> 718 produces more  $\gamma''$  than Waspaloy, the second can produce more precipitated carbides or other intermetallic phases, producing more anchoring of the discordances (Guimaraes and Jonas, 1981).

Compared to Inconel<sup>®</sup> 718, Waspaloy presents a high content of Cobalt (~13%) instead of Niobium (~4.5%), modifying its weldability. Polvorosa (2017) compared the machining process of Inconel<sup>®</sup> 718 to Waspaloy at 30 m/min with high-pressure coolant. During the machining of both materials, the main defects observed were crater, notch, and flank wear. However, the better weldability of the Waspaloy favours adhesion, provoking higher tool crater formation and tool-tip chipping that can compromise surface integrity. Vetri Velmurugan et al. (2019) compared the machining process of Waspaloy to Inconel<sup>®</sup> alloy with PVD-coated carbide inserts at  $V_c$  from 50 to 75 m/min. Machining Waspaloy was observed with higher cutting forces due to its twin boundaries, a hardness increase of the first layers of the machined surface, and probably due to thermal softening, a better surface roughness.

Nonetheless, Waspaloy exhibits unstable properties beyond 500°C, concerning its application in harsh environments. The combination of planar glide, carbide precipitation, and oxidation can significantly reduce its fatigue life, producing intergranular failure at 800°C, even in the case of Waspaloy with coarse grains (Lerch et al., 1984).

### II. 1. 3. Engine parts containing free-form surfaces

As can be seen in Figure II-3, an engine turbofan motor contains several parts with free-form surfaces, highlighting turbine blades, also known as fan blades, and blade-integrated disks (BLISKs), also known as integrated blade rotor (IBR), due to difficulties in design and manufacture. Big-size thin-walled parts englobe several manufacturing processes and are also challenging. Figure II-7 presents examples of a blade, an IBR, and a big-sized thin-walled component with free-form surfaces of the turbojet engine.

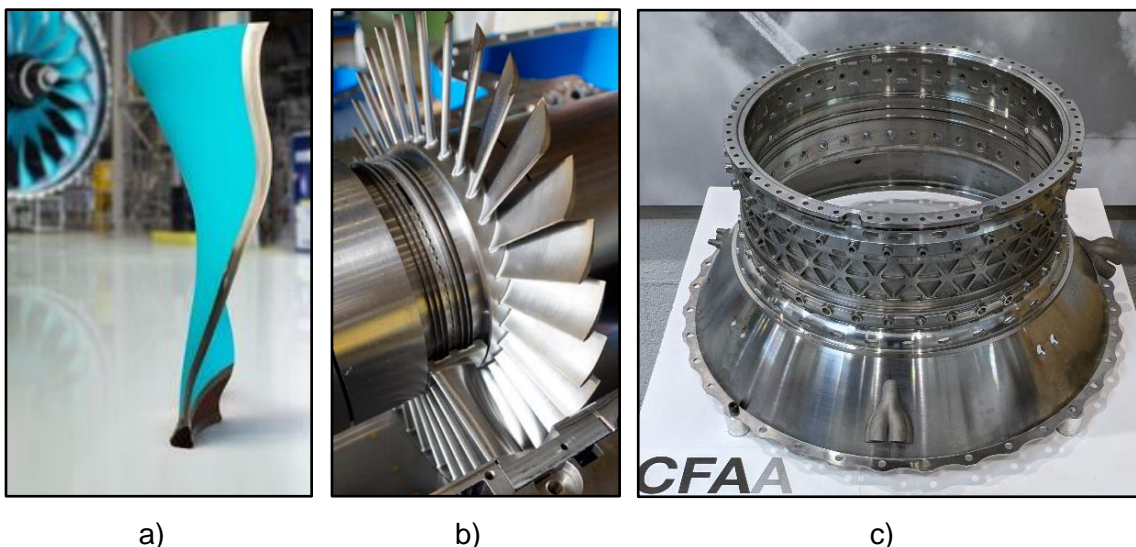


Figure II-7. Examples of free-form parts of the turbofan: a) Monolithic fan blade (Rolls-Royce, 2023); b) BLISKs (Meinzer and Seume, 2020); c) Medium-size casing manufactured in martensitic stainless steel.

The blades for aircraft engines have intrinsic free-form surfaces with several curvature changes along the surface, designed to reach maximum aerodynamic efficiency, helping improve performance while enduring extreme conditions in flight; this is one of the main reasons to attend tight tolerances of manufacture. Combining the blades on a central disk (BLISKs) allows weight reduction and improved durability, performance, and maintenance, being present in a critical region within the engine's compressor section.

The mid-size casing, as presented in Figure II-7c, is located in the intermediary region of the engine, has a structural function on the engine, and separates the high-pressure compressor from the low-pressure compressor. They present a thin-walled structure with complex shapes, usually made in hard-to-cut alloys requiring advanced and improved manufacturing techniques due to several features involved with intricate designs.

The machining of thin-walled parts for turbofans, especially when using special and hard-to-cut alloys, is critical. The manufacture of BLISKs and blades has attributes such as low stiffness and intricate geometries, making them highly susceptible to vibrations and instabilities during manufacturing. Besides, the tight dimensional tolerances increase the process challenges, often leading to special tooling use.

## **II. 2. Free-form surfaces definition**

Free-form surfaces are also known as complex surfaces, and non-developable surfaces can be defined by a tridimensional set of complex curves. A complex curve is all the bi-dimensional curves that can not be represented by the traditional well-defined geometries (lines, arcs, and other forms like circles and ellipsoids). In complex curves and surfaces, the curvature changes non-uniformly along the entity, and for each point of the geometry, a distinct radius of curvature is possible independent of adjacent points. For this reason, it is possible to represent any kind of sculptured shape, being extensively employed in several sectors of the economy, from automotive, aerospace, and military to moulds for plastic goods. Its design is required to meet or improve aesthetic and/or functional requirements (Lasemi et al., 2010).

At the beginning of the 1900s, Bezier developed the first mathematical model to describe a complex curve in only a single segment. The curve was named Bézier curve, Bézier spline, or B-spline and is defined using the extreme points and points of control. The general expression for the Bezier spline of degree  $n$  (order  $n+1$ ) is given by Eq. 1.

$$P(t) = \sum_{i=0}^n B_i(t)P_i \quad \text{Eq. 1}$$

In the Bézier method, a Spline has a degree. The degree of a spline is a mathematical concept that refers to the degree of the polynomial or rational functions used to describe the curve, as the higher the degree of the curve, the higher the curve's smoothness and the closer it passes through the controlling points. Depending on modelling requirements, a higher or a lower number of control points can be used, affecting the spline polynomial degree and compromising computation tasks and global curve alterations. Figure II-8a presents a spline representation where P0 and P3 are the extreme points, and P1 and P2 are the control points that define the spline's polygon of control.

The same concept can be extended to describe a surface. A complex surface can be represented by applying a set of splines, as depicted in Figure II-8c.

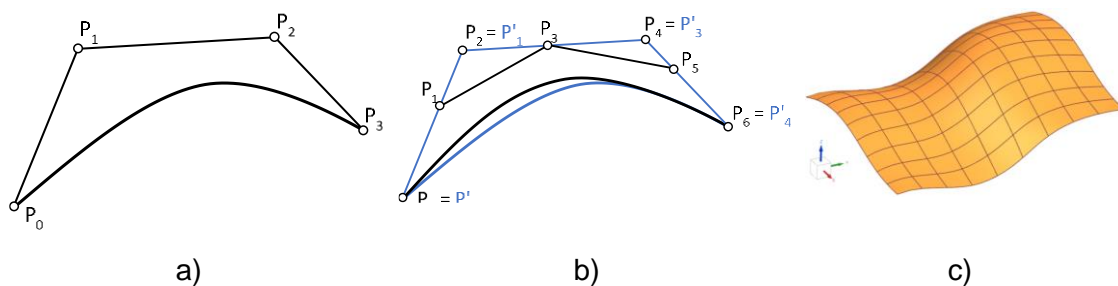


Figure II-8. Free-form curve and surface representation.

Later, new parametric polynomial methods were developed to improve the smoothness of these curves. The non-uniform rational B-spline (NURBS) provides more flexibility to geometrical representations (de Souza and Coelho, 2007).

Nowadays, every software house uses its own spline-based model to design smooth curves and surfaces. The high number of investments in the development of these mathematics makes it difficult to know both the mathematical models employed and the adjustments made by each one. It results in problems related to inter-software data exchange and limits data for modelling. So, standard models for data interchange are usually used, and it is also possible to use Euclidian positions of the space (referencing points) for modelling.

To obtain a relation of a point on a given free-form surface  $S(u, v)$  at a Euclidean space  $R^3$ , it is necessary to have at least 2 points, as depicted in Figure II-9. For a referencing point  $q$ , there is a point  $p$  with a minimum distance driven by a unitary vector  $\hat{n}$ , as mathematically described in Eq. 2. The calculus of the distance of the reference point to point  $p$ , is given by Eq. 3. These mathematical definitions were recurred at the development of the mathematical model. It is used by the CAM software in the toolpath generation and has been part of the developed routine – Chapter IV.

$$\|p - q\| = \min_{x \in S(u, v)} \|p - x\| \quad \text{Eq. 2}$$

$$d(p) = (p - q)\hat{n} \quad \text{Eq. 3}$$

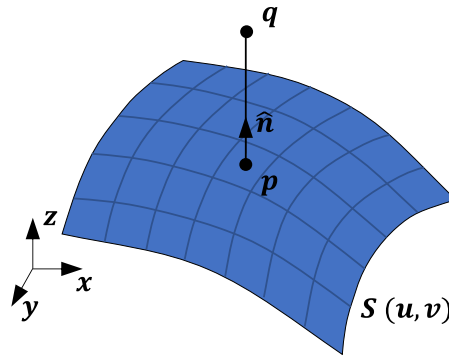


Figure II-9. Referencing a single point of a free-form surface.

## II. 3. Computational tools for manufacturing

Computational tools aid the development and manufacture of free-form surfaces together with NC machinery. Producing complex parts fulfilling specifications and tolerances is almost impossible without its use. Among the computational tools utilized in the manufacturing of free-form surfaces, highlight the CAx technologies, especially CAD (Computer Aided Design), CAM (Computer Aided Manufacturing), CAE (Computer Aided Engineering), and CAI (Computer Aided Inspection).

CAD (Computer Aided Design) is a generic term that describes the software used to create 2D or 3D models of parts and components. These models can be used to create simple sketches or detailed models, allowing the visualization of the object to be produced or its virtual representation.

CAM (Computer Aided Manufacturing) is a term that refers to any computational tool that is used to program, optimize, or assist manufacturing processes. CAM software is dependent on the mathematical information of the CAD model. They will receive the model information and, together with other inputs, compute instructions for moving accurately the CNC (Computer Numerical Control) machines. Some of the operations assisted are milling, turning, drilling, EDM, grinding, laser or plasma beams (cutting, welding cells, LMD, PBF-LB, among others.), and water-jetting.

CAE (Computer-Aided Engineering) comprehends various software tools for virtual testing and assessment of designs or mechanical phenomena. By employing modelling discretization or analytical models together with techniques such as Finite Element Analysis (FEA) or Finite Difference Method (FDM), complex engineering problems can be solved. Computational Fluid Dynamics (CFD), thermal analysis, mechanical loading

(static and cyclic), metal forming, welding, vibration, dynamic of bodies, injection, and casting processes are some of the most known. This tool enables performance evaluations under diverse conditions, facilitating process optimization and reducing the manufacturing number of physical prototypes and design iterations, thus improving product development efficiency.

Finally, CAI (Computer-aided Inspection) software uses computational tools to enhance and automate manufacturing and quality control processes and can be applied to all stages of the manufacturing process. It controls CNC machinery to, in general, perform non-destructive testing, providing quality control data, manufacturing inputs, or even models using reverse engineering techniques to the manufacturing chain.

### ***II. 3. 1. Software classification***

Several CAD software are available in the market, with a wide range of options, tools, and capacities. Besides the distinction of CAD software into solid modelling, surface modelling, and hybrid modelling, they are classified into entry-level, mid-end, and high-end, depending on the embedded tools that software houses incorporates. The more incorporated tools, the more flexible the software is, but less user-friendly. Also, depending on its implementation, the final user will require different abilities to perform more complex or simple tasks. So, the software choice will depend on the complexity of the industry projects, the employee's skills, and the budget.

Entry-level or low-end software is recommended for beginners or institutions that need basic 2D drafting and simple 3D modelling capabilities. With economic licenses (and maintenance) and a user-friendly and intuitive interface, they are suitable for small-scale projects, small institutions, and students.

Mid-range software offers more advanced features compared to entry-level options. They provide more robust 3D modelling capabilities, rendering tools, and additional free-form modelling and assembly tools. They usually present parametric modelling and other tools that make substantial changes to the project easier. It can include simulation tools and a macro interface with external communication to a spreadsheet or programming languages. These programs suit autonomous professionals and a wide range of institutions that work on more complex projects.

High-end software is used for the most demanding projects that require intricate designs and sophisticated simulations. These tools often include specialized modules for specific industries and offer advanced capabilities like generative design, complex simulations, data management, and process integration, allowing the development of more complex

products. For example, Siemens NX, besides a powerful surface modelling mathematics, has special modules for surface evaluation, reverse engineering, manufacturing turbomachinery components, design for additive manufacturing (lattice structures), additive manufacturing (DED-LB), and convergent modelling using polygons, among others.

By including AM modules, high-end software allows the programming of hybrid processes by adding and removing materials. In hybrid manufacturing, the synergy of CAD/CAM/CAI and sometimes CAE software is necessary to obtain valid and efficient toolpath strategies (Dávila et al., 2020), directing the use of high-end software.

### ***II. 3. 2. Programming interface with CAD software***

Different levels of programming can be used in CAx software, from macros inside the software (high-level programming) to more complex interfaces using external languages and programming packs (low-level programming). High-end and more modern CAD systems present programming languages and an open interface that allows the creation of applications to aid in developing several tasks. It can automate the design, assist CAM programming, or modify the CAM outputs to optimize the process or improve machined part quality (Käsemödel et al., 2020).

Since the 1970s, oriented object (OO) programming has been helping the software interact with others to solve problems. In the 1980s, the development of knowledge-based engineering (KBE) propitiated parametric modelling of geometrical shapes and automated the design of products using databases. KBE also allows functional programming on CAD software, embedding design rules, and engineering knowledge, making the multidisciplinary design optimization (MDO) methodology possible. Furthermore, it allows the development of software libraries, modules, platforms of solutions, and intra-software exchange (Lobov and Tran, 2020; Rocca, 2012).

The software Siemens NX (previously Unigraphics NX) has an API extension called NX Open that simplifies product development and analysis. The language is compatible with standard programming languages C#, C++, Java, Python, and Visual Basic, allowing the programming of tasks and external application development to extend the software capacities. By modelling physical properties directly in the CAD environment, higher control of the design process can be achieved, including access to data from features of the core of the software, which is unknown and protected by the software houses.

The high demand for solutions not embedded into commercial CAD/CAM software led to several API developments. Solutions for modelling, CAM, and inspection optimization



are the most common. Tikhomirov (2019) developed an API for Siemens NX using C++ programming language to automate fillet workpiece edges according to the angles between faces. González et al. (2022) developed a CAM module directed for DED-LB process to simulate the final geometry obtained considering a mass balance geometric model, the processing parameters and the laser toolpath.

Käesemodel et al. (2020), by considering the contact change problem present in 3-axis free-form milling with a ball-end tooltip developed in Visual Basic, an API for the Software Siemens NX to modify the outputs of the NC code. By calculating the effective diameters for each position of the NC code, it was possible to adjust the spindle speed and the feed rate line by line, keeping the cutting speed more constant. The result was an improvement in productivity and surface quality.

Chung and Ma (2018) developed three modules for CAM manufacturing in Siemens NX. A toolpath planning module that intelligently identifies workpieces and prescribes suitable operations and processing strategies. A cutting tool API that uses a MySQL database to automate select cutting parameters based on the tool selection. The third is an API to calculate the stability lobe diagram to assist the manufacturing processes and chatter problems, enhancing precision and efficiency in the manufacturing process.

YaoAn et al. (2014) proposed an API to generate an iso-scallop tool path for five-axis machining with barrel tools. An iterative process calculates a new tool path with a tolerance imposed by the user to maintain the scallop height formed by adjacent tool paths as constant. The code was only validated by simulation in the software VeriCut®, which means that machine dynamics and the final surface were not evaluated.

Pechenin et al. (2018) developed a module to compensate radial errors of probe tips during measurement in CNC machines or coordinate measuring machines (CMM). The API was integrated into the CAM module of the software Siemens NX to assist the manufacturing processes and reduce errors associated with part positioning and referencing besides measurement inspections. With the same scope, Lee et al. (2019) made an API in NX for error compensation that measures the points after the semi-finishing and uses them to compensate for the cutting tool path of the finishing operation.

Lu et al. (2019) developed a multi-criteria tool path generation that minimized axis movements (with gauges avoidance) and maximized machining width when milling BLISKS with barrel-shaped tools. The authors programmed in C++ and implemented Siemens NX software through its API (NX Open), modifying the tool path. The comparison of the trajectories was made by simulation on the software Vericut®.

The limits of open interface programming are almost infinite, and the development of modules is still necessary to predict the surface signatures, force, and deviation more accurately for both commercial and academic purposes.

## **II. 4. Manufacture of free-form surfaces**

This section presents a revision of the manufacturing process of free-form surfaces and new techniques like additive manufacturing to produce metallic parts near net shape and with internal microstructures.

The manufacture of any component undergoes a series of distinct stages, even when the part is produced near the final shape. Different manufacturing processes can be used to achieve the final shape during the manufacture of free-form surfaces, depending on parts requirements. Nowadays, the most common processes to manufacture free-form metallic parts are casting, forging, electro-discharge machining (EDM), Electrochemical Machining (ECM), additive processes, water jetting and machining (turning, milling, and combined processes like turn-milling and mill-turning).

In the specific case of high-end aeronautical parts like turbofan components, the parts are usually manufactured from monolithic bulks and machined to the final dimensions due to tight requirements linked to safety and reliability, leading to a high buy-to-fly ratio. Besides, it directly increases the resources involved and manufacturing times. In most parts like blades and frames, the material removed can reach more than 90%, modifying part stiffness and increasing the complexity of the process (Wang et al., 2005).

In this context, many efforts have been put into developing manufacturing processes of parts with shapes closer to their final form, known as the manufacturing of near-net-shape. In this scenario, power bed fusion laser beam highlights allow the manufacture of parts with over 99.9% density and high freedom in shape (external and internal) (Narasimharaju et al., 2022). However, as a new process, serious concerns remain about its usage on commercial aeroplane parts, especially in parts prone to cycling fatigue (Gupta et al., 2022). Nevertheless, this process can not achieve the high level of surface finishing of many sectors, presenting a surface with a granular aspect, recurring to conventional finishing processes like milling (Pratheesh Kumar et al., 2021).

### ***II. 4. 1. Manufacturing by removing material***

Manufacturing by removing material or subtractive manufacturing is a category of manufacturing process that involves subtracting or removing material from a solid workpiece.

In manufacturing parts from monolithic or forged blocks to obtaining better mechanical properties like safety requirements and reliability of the critical parts of the turbofan engine, subtractive processes like machining, laser cutting, water jetting, Electrical Discharge Machining (EDM), and Electrochemical Machining (ECM) are required. It highlights machining due to precision, versatility, material compatibility, good surface finishing, material removal rate, and repeatability. For these reasons, it is one of the most important manufacturing processes for parts containing free-form surfaces. It includes operations like milling, turning, drilling, and grinding, where the material is removed using cutting tools.

EDM and ECM are classified as non-conventional or unconventional manufacturing processes using different material removal principles. EDM uses electrical discharges to erode and remove material from the workpiece. This principle propitiates machining hard and electrically conductive materials like hardened steels. Even though it is capable of producing intricate and complex shapes with high precision, it induces stresses on the surface and white layer formation, which is not recommended for many applications. ECM uses an electrolyte solution (usually salt or acid-based) to provoke a controlled electrochemical dissolution of the workpiece material (anode). It is often used to machine complex shapes or hard-to-cut materials like Nickel-based and titanium alloys, which are present in many aeronautical components. It can achieve high precision and excellent surface finishes without inducing mechanical stresses. However, both processes present a low material removal rate.

Turning is one of the processes with the highest removal rates between the manufacturing processes within chip formation. It presents continuous removal of material that results in lower forces oscillations, contributing to a good finishing of the surface and precision. It can be a good solution to produce big cylindrical shapes like the present in casings or for pre-form shapes of BLISKs. Some special techniques in turning englobe special tool geometries, like Sandvik Coromant Primeturning™, for high feed turning and removal rate in hard-to-cut materials like Inconel® 718 and to turning more complex shapes (Amigo et al., 2023). However, this process can not produce complex parts with 3D contour or free-form surfaces (Kishawy and Hosseini, 2019). More versatile processes like milling are required to manufacture this kind of geometry.

#### ***II. 4. 2. Milling***

Milling is one of the most versatile manufacturing processes capable of producing an infinite number of shapes, including free-form surfaces, facilitated by the use of multi-axis CNC machines. In this process, a rotational cutting tool is employed (with one or

more cutting edges), and the result of the engagement of the tool results in intermittent material removal of the workpiece. Figure II-10 presents the schematic of an end-milling process and the parameters and features involved.

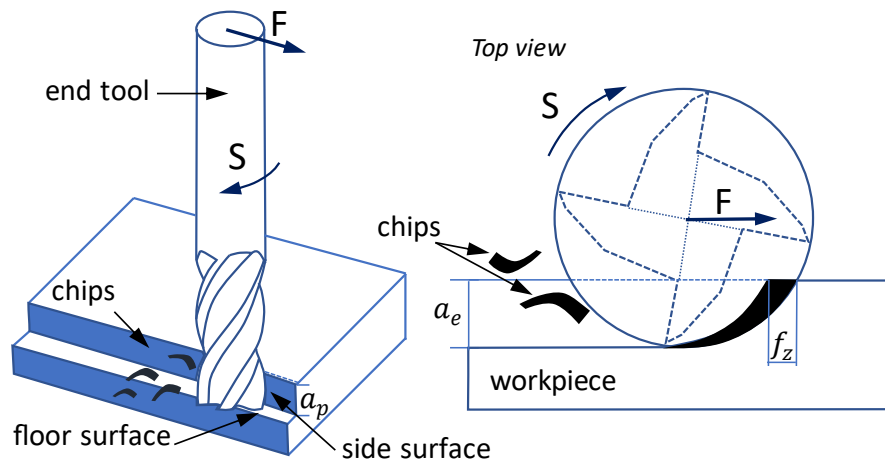


Figure II-10. Milling process schematic.

The milling process allows tight tolerances and good surface integrity to be obtained by gradually removing the material. In the manufacturing process of monolithic parts by milling, a series of steps are followed, from roughing and semi-finishing to finishing, changing tool geometries, cutting parameters, and programmed stocks. In the programming of the machining operations, many times, it is not possible to leave a constant stock for the following operation, leading to dynamic problems related to cutting force oscillation (de Oliveira et al., 2018). Thus, taking into consideration the stages before the finishing process is also necessary to minimize form error and tolerance violations (Ryu and Chu, 2005). The clean-up machining (roughing and semi-finishing) also plays an important role in reducing the machining time of free-form surfaces (Ren et al., 2004).

In manufacturing almost all complex monolithic parts, the milling process is used for at least one stage. In aeronautical components and dies manufactured from monolithic substrates, the material must be gradually removed to minimize problems that come from the variation of the engagements and cause undesirable deviations or surface quality. For aeronautical parts, these deviations can not exceed 50  $\mu\text{m}$  (Klocke et al., 2015). Figure II-11 shows the manufacturing process of a BLISK by material removal and its stages.

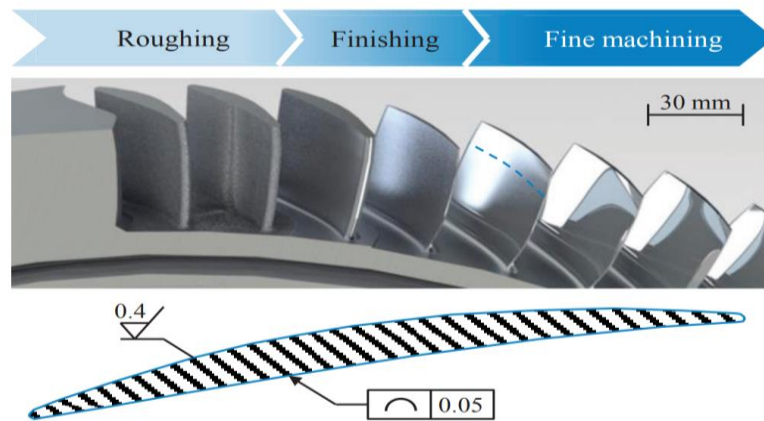


Figure II-11. Generic HPC Blisk in Incone® 718 (Klocke et al., 2015).

The process conditions and tool geometrical requisites that classify the roughing, semi-finish, and finishing operations are:

**Rough Milling:** The initial stage of material removal involves removing a significant amount of material quickly to get closer to the desired shape. For this reason, tools with the largest diameter possible are selected, typically end tools with inserts with some rounding edge to avoid catastrophic breakage of the corner due to high loads.

**Semi-Finishing:** The geometry is maintained, but the diameter decreases to reduce the number of regions with no-tool access and fillets (regions with excessive material). The depth of cut and multiple sizes of tools can be used to minimize the machining steps that provoke forces oscillation and dimensional error in the finishing operation.

**Finishing:** Ball-end tooltips are usually used to finish free-form shapes due to contract changes. As one of the focuses of this doctoral thesis, a detailed review is presented with more details in the next subsection.

The parameters involved in the milling process will depend on the geometrical shapes of tools, workpieces, and materials, as seen in Figure II-10. The main features involved are:

**Workpiece and material:** The type of material and geometrical shape of the workpiece are usually immutable variables. The workpiece will guide the manufacturing process, from the selection of the machine, tool, and clamp systems to the parameters and milling strategies.

**Tool geometry and material:** Different machining parameters are used according to cutting tool geometry and material. The geometrical features of the tool include the helix angle number and shape of cutting edges, among others. The material and coatings from which the cutting tools are made aiming to improve their performance are deeply discussed in subsection II. 4. 8. The geometrical features of the tools can be classified into the tool envelope, used on CAD/CAM systems to generate the NC code (tool trajectory), and the cutting edge (flutes). The geometry of the flutes usually follows a helix

shape with an incidence surface and a secondary surface for chip detachment, like in oblique turning. The helix can present a variable pitch; however, it is more common for constant helix angles ranging from 15 to 60 degrees. The cutting-edge geometry is important for evaluating the dynamics of the milling process, the chip formation, and the cutting forces (Budak et al., 1996; Engin and Altintas, 2001).

**Lubri-coolant solutions:** Coolants and lubricants are often used to dissipate heat and improve the machining processes. It helps reduce tool wear, improve surface finish, and prolong tool life. Types and details of its usage are discussed in subsection II. 4. 10.

The process parameters involved in the milling process are:

**Cutting Speed ( $V_c$ ):** refers to the speed that moves the cutting tool over the workpiece. It considers rotational and linear movements, typically measured in meters per minute.

**Feed per revolution ( $F$ ):** indicates the distance that the tool advances in one complete rotation during turning or milling, usually measured in millimetres per revolution.

**Feed Rate ( $f$ ):** is the rate at which the cutting tool advances into the workpiece, typically measured in millimetres per minute.

**Depth of Cut ( $a_p$ ):** the distance of immersion of the tool.

**Axial depth of Cut ( $a_e$ ):** the axial distance of immersion of the tool.

**Feed-per-tooth ( $f_z$ ):** represents the linear distance the tool advances in each tooth engagement with the workpiece, typically measured in millimetres per tooth.

**Spindle Speed ( $S$ ):** refers to the rotational speed of the spindle of the machine that holds the cutting tool, usually measured in revolutions per minute (RPM).

The spindle speed, cutting speed, and feed per tooth are critical parameters that affect tool life, surface finish, and material removal rate and can be correlated to the tool diameter ( $d$ ) and tooth number ( $z$ ), Eq. 4 and Eq. 5.

$$V_c = \frac{\pi D S}{1000} \quad \text{Eq. 4}$$

$$f_z = \frac{f}{n z} \quad \text{Eq. 5}$$

### **II. 4. 3. Finishing free-form surfaces by milling**

Despite the availability of other finishing processes such as sanding, electropolishing, grinding, SAM (Super Abrasive Machining), shot peening, blasting, and laser ablation, the ball-ending milling or just ball copying process is widely employed to ensure dimensional tolerances before these processes or even for the final product.

Besides its high capacity to produce tight tolerances, the finishing process of free-form surfaces faces a series of challenges related to the oscillation of the components of the cutting force. Due to the intermittent characteristics of the process and several cutting contact changes, complex problem problems of vibration and chatter, accelerated tool wear, and surface irregularities occur. Mali et al. (2021) highlight several key elements that affect free-form surface milling (FFSM): the tool-workpiece contact changes according to the surface parameters and toolpath strategies, materials, influences of the machining parameters, and geometrical features of the tool. Figure II-12 presents a fishbone diagram of the most relevant factors for the accuracy of FFSM.

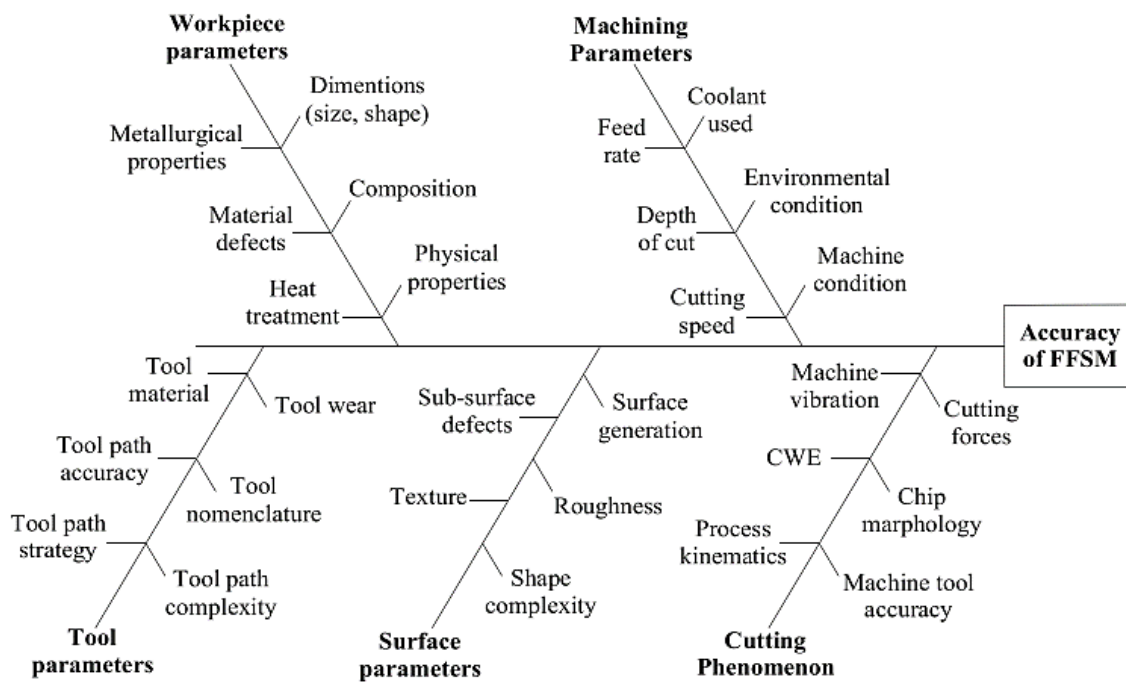


Figure II-12. Cause and effect diagram for free-form surface milling (Mali et al., 2021).

Among them are the tool contact changes, the tooltip effect, toolpath strategies, tool geometry, and other indirect problems like the multiple contact solutions in the 5-axis and machine response time highlights, detailed in the following subtopics. These definitions will support understanding the chip formation and the force oscillation that affects the signature left by the finishing by milling process.

#### II. 4. 4. Tool contact changes in complex surface milling

Due to the geometries of the tool and workpiece, the contact constantly changes when manufacturing free-form surfaces, even in 5-axis machining. It leads to changes in chip formation oscillating the cutting forces, resulting in several problems; surface damage and deviations are between them. Furthermore, the effective cutting radii changes, magnifying forces oscillation. Even for different shapes of ball-end tooltips, it happens in

some magnitude. Figure II-13 exemplifies the effective diameter changes with the contact.

As shown in Figure II-13, the variation on the cutting radius and then the cutting speed is one of the most critical problems in ball-end milling of free-form surfaces. In regions where the centre of the tool and nearby regions participate in the cut, the cutting speed tends to be null. This leads to the material being crushed instead of sheared. This characteristic is known as ploughing.

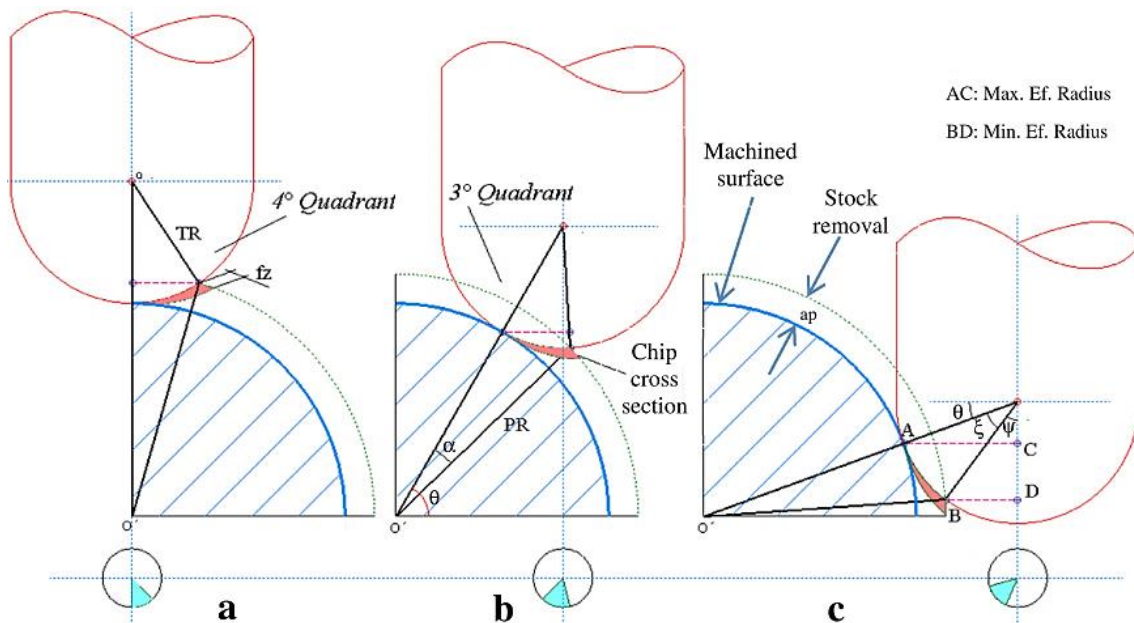


Figure II-13. Alterations of the tool contact and effective cutting radii in 3-axis ball-end milling of a half cylinder (de Souza et al., 2015).

The ploughing effect on metal-cutting was first addressed by Albrecht (1960). The author identified that besides the principal mechanism of chip formation, the shearing, a second one, ploughing, must be considered for proper force prediction. This mechanism depends on the sharpness of the metal cutting tool and the difference in rigidity of the chip and workpiece material. As the cutting edge's sharpness depends on its manufacturing process, tool material, coating, and wear, it can not be neglected. The pressure that the tool rounding edge applies on the material, until shear, provokes a chip bending (chip curling) at the same time that the surface is plastically deformed. This effect is more pronounced when milling small depths of cut, as in the finishing processes (Budak et al., 1996; Lee and Altintas, 1996).

The energy required for shearing and ploughing depends on the geometrical cutting parameters, kinematic cutting parameters, material properties, tool-workpiece geometry, system rigidity, friction, and lubrication. The energy distribution over time also affects the balance between shear and plastic deformation, resulting in direct dependence on the effective cutting radius and speed that modifies the dynamic of the cutting force



components. For this reason, when the tool centre acts in the cut, the forces increase, and vibrations may occur, damaging the surface.

Controlling the ploughing is important for reducing the components of cutting force, residual stress on the surface, and tool wear, which affect the time, cost, surface integrity, and tolerances of manufacture. It can be done using shaper tools and proper machining parameters, avoiding the centre contact (Coelho et al., 2010; de Lacalle et al., 2007; Oliveira and Diniz, 2009; Ventura and Hassui, 2013).

Tuysuz et al. (2013) propose an analytical model that considered the effect of ploughing of the material during machining; with the inclusion of the effect of the centre of the tool, there was a reduction in the prediction errors of the machining force in the tool axis in plunge machining, inclined, 3-axes and 5-axes. In the 5-axis, the error was reduced from 53% to 25%, which is still a significant error and an indicator that analytical models need improvements.

Besides, nowadays, it is common to define parameters according to the tool's maximum diameter, surface speed, and feed per tooth (or equivalent pair). However, in ball-end mills, the feed per tooth changes constantly with the local surface radius, even for 5-axis milling. To minimize the problems related to the ball-end tooltip, Käsemöller et al. (2020) proposed an algorithm (limited to 3-axis milling) to optimize the cutting condition by calculating the effective cutting radius for the ball-end tooltip and modifying the cutting speed and feed. These changes improved the surface quality and the manufacturing time by 21%. Likewise, Redonnet et al. (2013) developed an analytical model to calculate the effective cutting radius of toric tools. However, models for more complex tooltips, like double radii tooltips, are missing.

As a result of the numerous contact changes in free-form milling, another problem occurs – the NC machine processing saturation. The CNC machines work in a closed control loop with constant correction of positions during the toolpath movement. Besides, machines have kinematics limitations that limit movements, leading the user through programming or directly in the NC of the machine to choose between path error or feed rate error to run at the programmed parameters.

Also, the tight tolerance bands required to achieve accurate geometrical shapes using linear or spline interpolation in high-performance parts increase the number of control points that saturate the machine's control loop. It leads to more significant problems associated with speed reduction or stops, like oscillating cutting forces and surface damage (Coelho et al., 2010). Figure II-14 presents a schematic of a CNC machine control loop.

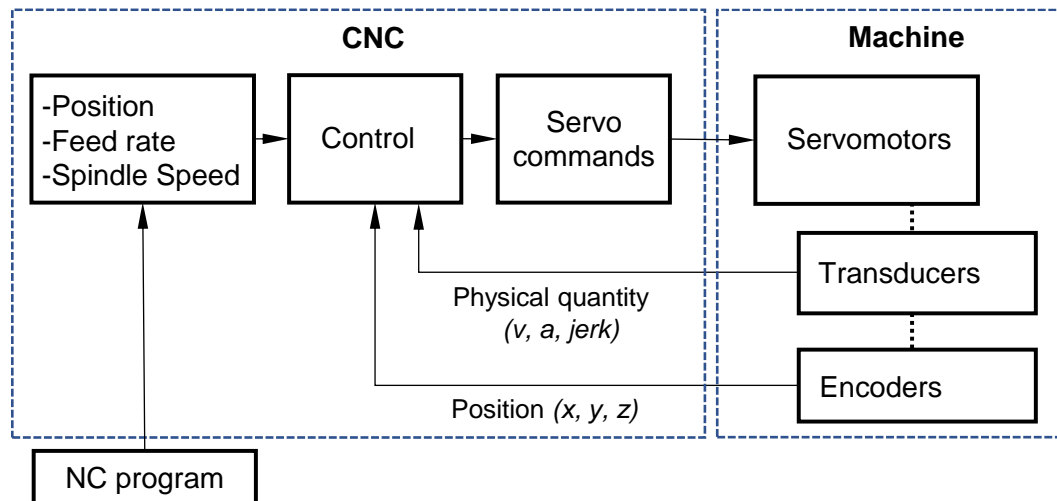


Figure II-14. Machine control loop, adapted from Coelho et al. (2010).

It is important to add that the data distribution (CL points) inside the tolerance band varies according to the software house because of its different mathematical models, resulting in different performances for each software (de Souza et al., 2019b). Thus, an evaluation of the process considers surface errors and machining time (Beño et al., 2016).

Coelho et al. (2010) studied the processing time of different NC machines. Evaluating the point distribution and machine response, they observed different times. The authors proposed a parameter to classify machines considering feed rate reduction and oscillation, denominated machine response time (MRT). They observed that as low as the MRT poor is the surface quality. In the same background, Souza et al. (de Souza et al., 2021) evaluated the MRT for 4-axis milling, including an angular axe. We identified that rotary axes present non-linear patterns, and a conditional MRT was proposed, reducing the prediction time error to less than 15%.

The contact changes can also affect the classification of the milling process with ball-end mills. The constant changes in the tool positioning modify the engagements with the workpiece, modifying the direction of the chip formation, making it critical, especially in finishing operations, where the cutting force components cause perturbations that affect the surface signature and tolerances.

Usually, the process is classified into upmilling, where the cutting tool rotates against the workpiece feed, and downmilling, where the tool moves in the same direction as the workpiece feed. Furthermore, these machining operations can be further differentiated based on the vertical movement of the tool, giving rise to three distinct classifications: ascendent, wherein the tool moves upwards relative to the workpiece; descending, where the tool moves downwards; and neutral, where both the tool and workpiece remain at the same level, ensuring a more uniform removal process.

Michalik et al. (2014) studied milling vibration and surface quality in thin-walled parts. The upward machining presented higher shear forces, roughness, and uneven distribution compared to the downward machining. Yao et al. (2018) evaluated the milling process with ball-end tooltips of different curved surfaces (concave and convex). The authors observed that the tool orientation influences the surface roughness, surface morphology and residual stress. Also, the authors identify that the roughness in upward is higher than in downward. Scandiffio et al. (2016) evaluated the effect of cutting direction on surface roughness, cutting forces, and tool life in a hard-to-cut material (AISI D6), and contradicting other studies of the literature, reported that descendant cutting presented lower vibration, cutting forces, and better surface roughness, probably due to centre actuation, exemplifying the complexity of free-form milling.

Basso et al. (2022), investigating the ball-end milling in different tool inclinations, identify that even programming the toolpath in some condition, i.e., down milling ascendent, depending on the engagement, a small or great part of the chip formation can occur out of the specified. For this reason, we proposed a classification of the milling process according to the main mechanism that generates the surface instead of the thickness variation, classifying it into *Tip-On* and *Tip-Out*. This classification propitiates a better classification of the process focused on the final surface quality.

#### **II. 4. 5. Multi-axis milling and tool orientation**

In multiaxis milling of free-form surfaces, several data are required, from the user inputs (tool geometrical data, toolpath strategy, and cutting parameters) to the computed by the CAM software cutter location (CL) and the tool orientation (Lasemi et al., 2010).

The tool orientation is one of the most important factors in the multiaxis milling of free-form surfaces. It can be used to avoid gouging manufacturing geometries that would be difficult or impossible to produce with traditional 3-axis. It allows wide control of the engagement of the tool with the workpiece, maintaining a more constant material removal rate and reducing damages caused by force variations, thus improving the finished surface. Also, it propitiates a reduction in the number of setups, improving lead times and costs (de Lacalle et al., 2007; Habibi et al., 2019; Ma et al., 2015).

The two angles that can be adjusted in multi-axis machining to orientate the tool are the lead and the tilt angle.

**Lead Angle:** also known as the tool lead or lead orientation, refers to the angle at which the tool approaches the workpiece in relation to the toolpath direction. It is the angle

formed between the tool axis and the direction in which the tool is moving along the toolpath.

**Tilt Angle:** also known as the tool tilt or tool angle, is the angle at which the cutting tool is tilted relative to the cross direction of the feed direction in the workpiece surface. In the machine reference system, this angle can be classified into tilt around the A-axis, related to the X-axis of the machine, and the B-axis when tilted around the Y-axis.

Even with interface simplification of the actual CAM software, depending on the geometry provided, the user ends up being responsible for defining the best cutting parameters to reduce cutting forces and improve surface quality. However, it isn't easy to predict and visualize the best tool orientation and its effect on the process dynamics, even using simulation tools.

5-axis machining promotes high precision in free-form milling compared to the 3-axis due to higher degrees of freedom. However, due to extra degrees of freedom, multiple solutions of contact are possible, favouring gouging between points. It makes the planning and prediction of a 5-axis milling complex (Wang and Sun, 2014).

CAM software calculates the tool's final position for each point to unify solutions and solve problems of intra-machine and NC control exchange. This archive has the name of APT CL file or just APT (Automatically Programmed Tool). It is an ANSI standard generic output file with toolpath information that any text editor can read; it has been possible for expert users to evaluate and, if necessary, manually modify the toolpath solution. This led the post-processor and the machine NC to decide the best and most suitable toolpath based on the number of blocks read. The parameters adjusted on the machine usually are the smoothness of corners, speed, and accuracy (Luo et al., 2015).

#### ***II. 4. 6. Toolpath strategies for finishing free-form surfaces***

Besides the cutting parameters and other geometrical parameters such as tool geometry and workpiece surface, the toolpath strategy plays an important role in manufacturing complex parts (Lasemi et al., 2010). Choosing the milling strategy is an optimization problem based on constraints, geometrical features of the tool, and the form of the surface to be machined (Quinsat et al., 2008), and there are several methods that can be used to generate the toolpath.

Besides the input parameters, such as the depth of cuts, two key elements guide the toolpath calculation: the machining boundaries and the generation of the guiding curves on the surface. The CAM software uses projection-based methods intersecting the guiding curves (or hybrid strategies) to define the toolpath over the milling surfaces inside

the defined boundaries. The more common techniques used to split the trajectories over the surface are iso-parametric, iso-planar, iso-offset, iso-scallop, spiral methods, and trochoidal.

**Iso-parametric:** toolpath uses a constant parameter of the surface, such as the u or v-parameter, to ensure that the tool moves along specific lines or curves of the surface. This technique has low-efficiency calculation because it involves computing the intersection between a plane and the surface, making it highly versatile and the most used for several shapes of surfaces.

**Iso-planar:** toolpath generation focuses on maintaining a constant toolpath plane during machining. This technique is particularly useful for machining flat surfaces.

**Iso-offset:** creates the toolpath on a plane offset at a specific distance of the workpiece surface, which can cause deviation on the scallop height, making this technique more efficient when the surface does not present large variations. So, it is commonly used for semi-finishing or finishing operations that require lower tolerances.

**Iso-scallop:** approach aims for a constant scallop height (usually stepover) along the tool path generation. By controlling the spacing between successive toolpath passes, a good surface finishing can be achieved, and multiple passes at the same regions can be avoided. However, this method tends to present more entrances and exits on some free-form surfaces, marking the surface and damaging some regions of the part.

**Trochoidal toolpath:** is characterized by a series of smooth arcs or circular patterns with trochoidal movement that uses a higher depth of cut and presents a high material removal rate, being widely used in HSM. Due to the constant change in tool movement, the components of the cutting forces constantly change, making it more suitable for rough, semi-finishing, or pocket operations.

**Spiral toolpath:** consists of moving in a continuous spiral pattern inward or outward from the centre of the workpiece. In cylindrical parts, a 3D spiral toolpath can be used to move in the direction of the extrusion or guidelines of the swept profile, promoting a smooth removal of the material, reducing tool wear, and improving machining efficiency.

Some sources of form errors can be controlled in the machining process by selecting an adequate feed direction, thus controlling machining force components that cause tool deflection (de Lacalle et al., 2007). Also, the toolpath strategy is an indirect parameter that guides the tool-workpiece contact variation problem, affecting the effective tool radius and the instantaneous cutting speed, thus affecting the final geometry. (Beño et al., 2016; Brooks et al., 2016; Ma et al., 2018). That way, the programming of the toolpath

can be used to improve the finished surface. However, the lack of predictive tools makes evaluating the process highly dependent on the user expertise and CAM software used.

Souza et al. (2015) investigated the effect of the toolpath on the cutting forces. The alteration of contact and effective tool diameter are the main factors responsible for the alteration of the component of cutting force that causes tool deflection, with direct consequences on geometrical deviation and surface signature. In another investigation, Souza et al. (2014b) evaluate the influence of the tool path trajectory on the manufacturing costs of dies and moulds. Analysing different strategies available in commercial CAM software for machining free-form geometries, there is a significant influence on manufacturing time and surface quality. Figure II-15 presents the comparison of 5 different strategies used in the manufacture of free-form surfaces, comparing the manufacturing time, surface roughness, and post-processing time required for polishing.

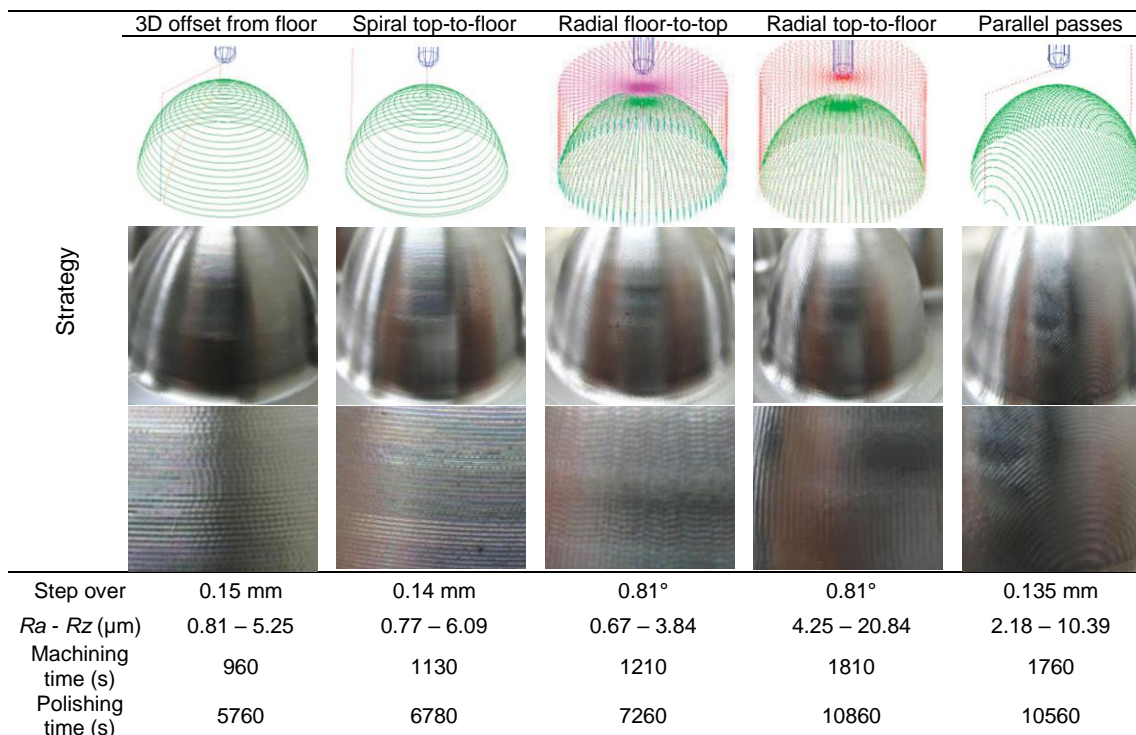


Figure II-15. Toolpath strategy influences the surface, machining, and polishing time. Adapted from Souza et al. (2014b).

Furthermore, different CL points are calculated depending on the mathematical implementation in the CAM software. It means that the milled surface can differ even if the user selects the same input parameters on different software. The effect of the MRT (feed rate oscillation) and the CL data distribution computed by the CAM software makes some better for milling concave areas and others for convex (de Souza et al., 2019b).

Still, some CAM software also presents specific modules to aid the manufacture of complex parts. Siemens NX presents a special module for machining IBRs, considering the blade, splitters hubs, blinds, and shroud, with optimized and gouging-free tool trajectory. Another high-end CAM software, Hypermill™ from Open Mind, presents strategies specially developed to manufacture parts with complex shapes using 5-axis like the aerospace sector and turbomachinery (Yin et al., 2019).

During the finishing of free-form surfaces by ball-end milling, minimizing magnitude and oscillations in the cutting force components is necessary to achieve tolerances and good surface integrity. Thus, 3D spiral strategies can be recommended for blade and BLISKs finishing by milling due to smooth tool changes, reducing entrances and exits, and avoiding undesirable surface marks. Besides, because the spiral milling is symmetric, it is easier to compensate for deformations of thin-walled parts. (Cao et al., 2015). However, this strategy requires multi-axis milling and more expensive CAM software to control positions and improve engagements, computing CL points free of interference and avoiding gouges. Besides, the dynamometers used for force acquisition for multitasking centres are more expensive and subject to more complex connectivity problems, being, in many cases, a research limitation.

#### ***II. 4. 7. Tools for finishing complex surfaces***

The costs and surface quality have significant importance on the finishing operation (Lasemi et al., 2010), with tool selection significantly influencing both efficiency and quality. For example, an end mill is 10 to 20 times more efficient than a conventional ball-end mill, presenting a much higher contact area and removal rate. However, tool orientation with the surfaces can not be adjusted continually and accurately, even using 5-axis milling (Cauí et al., 2003).

The most used tool to finish free-form surfaces is the conventional ball-end tooltip with a single radius. This tool is highly versatile; the tool tilt and its single contact point allow the machining of several complex and constrained surfaces with easy programming using most CAM software. However, the low material removal rate, crisp height marks, and the speed at the tool centre and nearby regions (which provoke ploughing and damage the surface) make its usage complex and inefficient.

In this context, a new kind of tooltip with characteristics of more rigidity, like conical tools or bigger effective tool radius, like the barrel ones, was developed. Modifying the tool body can improve tool rigidity, improving the precision of the finishing process, especially in low-stiffness parts like blades.

Due to the geometrical construction, conical tools present a higher rigidity than conventional ball-end tooltips, which has several advantages in the manufacture of BLISKs and some kinds of blades. This tool can mill several types of complex geometrical shapes using the tool's flank and the tooltip for blends. However, the transactions between the flank and the tooltip damage the surface and must be avoided. In this kind of tool, the flank of the tool must be used to obtain a higher material removal rate and effective cutting speed. However, it reduces tool tilt positions and transactions, limiting the manufacture of several free-form surfaces (Rajain et al., 2022).

In this direction, new tooltips with a better balance between tool engagement and material removal rate were developed. This new family of tools, namely barrel shape or circle-segment end mills, presents a bigger radius in the same tool handle, improving machine efficiency and surface quality (Suzuki et al., 2021). Besides, together with 5-axis milling, it reduces the number of fixations, improving complex geometrical shape finishing (Boschetto et al., 2018). Barrel tools can be used for both flank and floor milling. However, a better surface finish is obtained using the bigger tool radius, so the tool selection must be carefully made according to the finishing geometry. The barrel tools, nomenclature, and main characteristics are presented in Figure II-16.

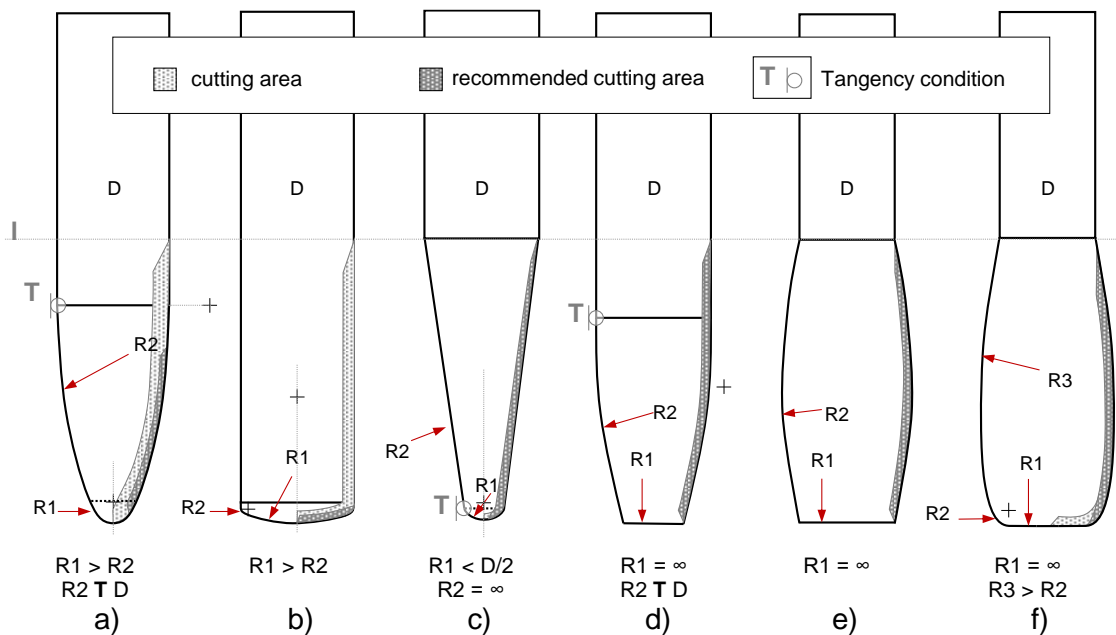


Figure II-16. Types of barrel tools and nomenclatures: a) barrel oval shape; b) lens shape; c) conical; d) drum taper; e) barrel; f) half-barrel.

The use of a bigger tool radius improves the machining time by reducing the depth of cut to produce the same crisp height as depicted in Figure II-17 or the surface roughness using similar parameters of manufacture. It also favours the shearing by reducing the ploughing effect with the tool height, allowing it to improve the surface quality and tool life. Due to productivity and finishing qualities, these tools gained space on the 5-axis



flank milling of aviation components like blades and BLISKs (Meng et al., 2014). On the other hand, the use of these tools presents intricate shapes, increasing costs associated with software acquisition, CAM programmers, and tool acquisition.

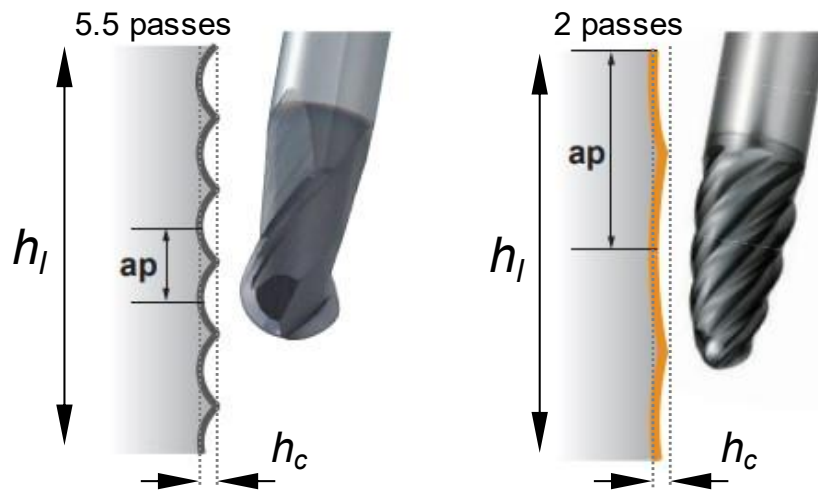


Figure II-17. Surface finishing comparison with a ball-end tooltip and an oval barrel-shaped mill to obtain similar crisp height, adapted from Mitsubishi (2023).

The calculus of free-form surface toolpath is unviable manually, especially for intricate shapes like the double radii tooltips. Wang et al. (2009) first investigated the relationship between the general barrel cutter with the CAD surface, calculating the error distribution according to the CC point for tool positioning. Barrel tool configurations and contact limitations for the optimal selection of the tool were also investigated by Meng et al. (2014). The authors proposed to avoid gauging by adjusting the centre of the generatrix of the barrel with the part.

Still today, many CAM software present limitations in generating and computing the engagement of double radii barrel tools, leading advanced CAM to decide the tracking points and simulate the trajectory, often not achieving the optimal toolpath strategy. Rajain et al. (Rajain et al., 2022) proposed a toolpath-planning algorithm with optimized trajectories to flank milling free-form with conical or custom-shaped tools applied to barrel tools. YaoAn et al. (2014) calculated a swept envelope of an iso-scallop toolpath to define the optimal barrel tool orientation in 5-axis free-form milling. However, due to the complexity of contact and the variety of barrel tool shapes, more models to compute trajectories and implementation on commercial CAM software are required.

Furthermore, unlike the conical tools, in some double radii barrel tools, it is geometrically possible to make a smoother transaction between both radii of the tool, having wide tool orientation and more accessibility to machines with more complex shapes. Yet, programming the milling process considering both radii is complicated and unavailable in commercial CAM software, missing simulation tools and routines to investigate the effects of this transaction zone.

### II. 4. 8. Milling tools materials

Besides the geometrical aspect of the tools, their material composition guides the economics of processes by material removal. The evaluation of tool material cost typically extends to various factors, including initial acquisition expenses, tool longevity, maintenance costs, and the overall impact on production efficiency and quality. Hence, the decision-making process should aim for performance and long-term benefits. Among the requirements of tool materials are strength, toughness, thermal conduction, chemical reactivity, corrosion resistance, improved hardness, thermal stability, thermal shock resistance, and wear resistance (Hosseini and Kishawy, 2014; Pervaiz et al., 2014; Smith, 2008).

It is well known that the properties of the material affect the manufacturing process and are directly correlated to errors of form and surface signatures. Depending on the material to be machined, different tool materials can be used. Figure II-18 compares the hardness of typical tool materials and the Yield strength of some alloys related to turbofan components both in function of the temperature.

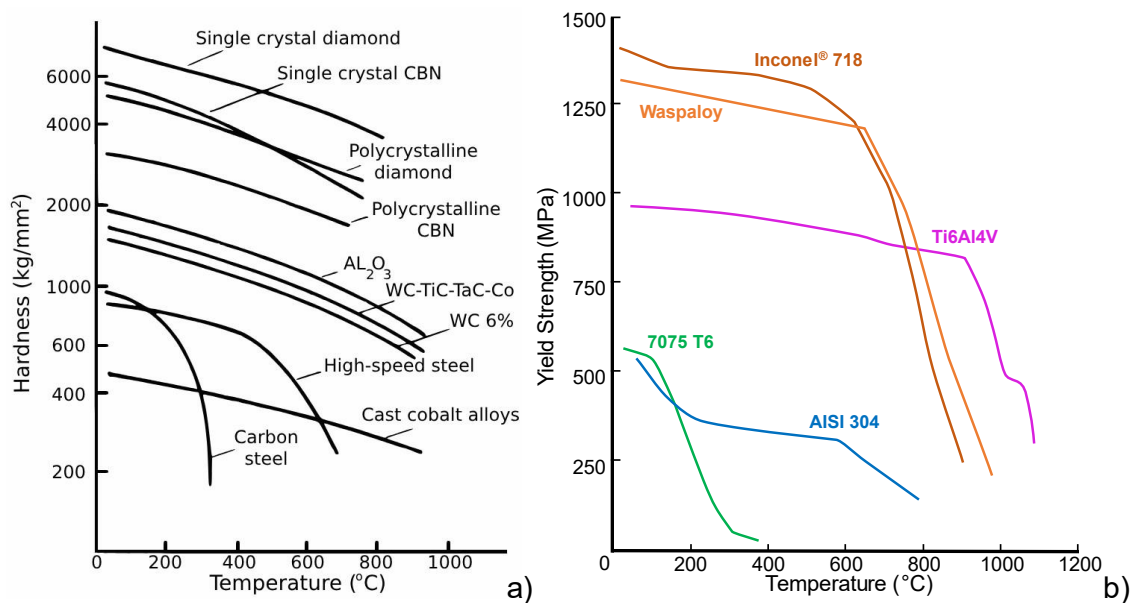


Figure II-18. Properties versus temperature: a) hardness of tool materials, adapted from Almond (1981); b) Yield strength of aeronautical alloys.

As can be seen in Figure II-18b, the internal energy necessary to Yield superalloys Inconel® 718 and Waspaloy is much higher than the titanium alloy Ti6Al4V under 800°C, which is direct related to its shearing properties. So, for the same tool material, the manufacturing parameter must be lower.

Coating tools can increase productivity and lifespan by reducing friction and increasing superficial hardness, giving more wear resistance. CVD and PVD are the main processes used. Nowadays, multilayer coatings are applied, and their composition as

the manufacturing know-how is saved by manufacturers (Chuan et al., 2012). Among the most common coatings are Titanium Nitride (TiN), Titanium Carbonitride (TiCN), Titanium Aluminium Nitride (TiAlN), Aluminium Titanium Nitride (AlTiN), Chromium Nitride (CrN), Zirconium Nitride (ZrN) with different properties of hardness, adhesion, thermal stability, and oxidation resistance (Grigoriev et al., 2023; Rodríguez et al., 2002). Moreover, certain coatings, such as Diamond-Like Carbon (DLC), have particular applications due to specific properties (self-lubricating plus thermal fragility) being suitable for dry machining (Liu et al., 2021).

Currently, the most common tool materials to machine hard-to-cut materials like Inconel® 718 are cemented carbides, ceramic, and cubic boron nitride (CBN). Carbide tools are usually applied to machining heat-resistant alloys with cutting speeds ranging from 10 to 30 m/min. However, with the use of a wear-resistant coating, it can increase by around 50 m/min more.

Other options are ceramic tools like aluminium oxide ( $Al_2O_3$ ) and silicon nitride ( $Si_3N_4$ ), which present very good thermal and chemical stability and higher hardness, allowing higher cutting speed than carbide tools, ranging from 120 to 240 m/min, making it suitable for high-speed and high-temperature machining applications (Coelho et al., 2004; Ezugwu et al., 1999). However, ceramic tools present low thermal conductivity, chemical compatibility with alloying elements, and thermal cracking with most cooling solutions, increasing workpiece temperature and damaging surface integrity. Besides, it has a fragile comportment that reduces its lifespan and, together with its higher costs, may not be worth their use in machining a wide range of materials.

Another high-end material applied to machining hard-to-cut alloys is the cubic boron nitride (CBN). Its higher hardness, extraordinary abrasion resistance, and thermal conductivity render it valuable in challenging cutting scenarios. However, the high costs involved and the high reaction with the materials often do not compensate for its usage.

#### ***II. 4. 9. Tool wear***

Understanding wear mechanisms is essential for selecting machining tools and obtaining a good surface finish. The selection of tool geometry, core material, coatings, and the use of lubricants can extend tool life and enhance machining quality. The main consequences of the tool wear are increased temperatures, cutting forces, power consumption, and poor surface finish. Besides, it leads to tool breakage and often causes deviations on the cutting edge that, if not adequately compensated, lead to unacceptable form deviations.

Among the techniques to correct deviations caused by tool wear, a presetter can be used together with toolpath compensation. However, constant measurements are required, interrupting the process and decreasing productivity. It can be especially critical if external measurement equipment is used or the NC control doesn't present correction cycles, requiring programming alterations. In situ monitoring minimizes form errors, avoiding productive losses and non-quality.

Furthermore, tool wear is strongly influenced by changes in the cutting conditions (cutting speed, feed rate, depth of cut), geometries, and other aspects that affect the process thermally or dynamically. Usually, to reduce the tool wear and extend tool life, the cutting parameters are optimized to reduce the cutting force (M'Saoubi et al., 2015). Besides, dynamic variations, material imperfections, and the wear mechanism affect the wear of the tool, which usually presents a non-linear pattern with a probability of breakage increasing with the increase of the cutting forces.

Figure II-19 depicts the main types of tool wear: flank wear ( $V_b$ ), chipping, adhesion and built-up edge (BUE), crater, edge rounding, notch, and plastic deformation of the tool edge. Figure II-20 presents the main mechanisms of wear in metal cutting and their relation to the cutting temperature.

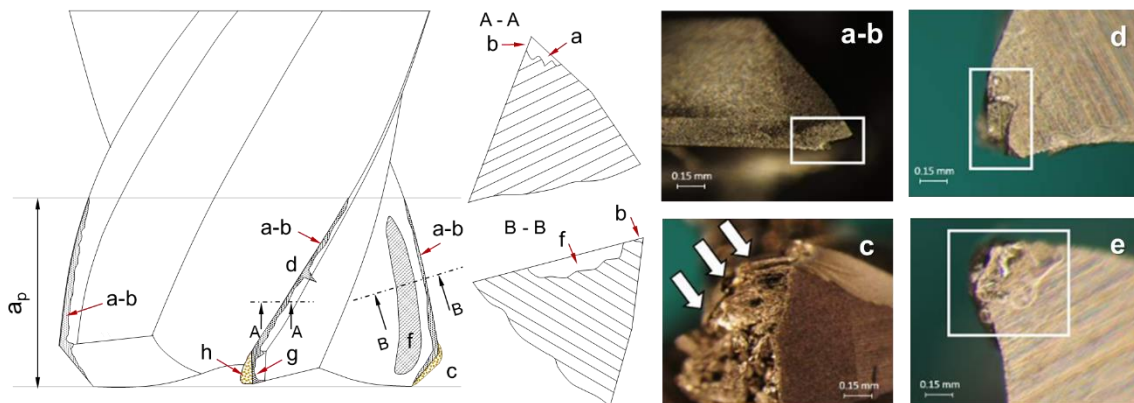


Figure II-19. Types of tool wear: a) flank wear; b) chipping; c) adhesion; d) notch; e) plastic deformation; f) crater; g) rounding edge; h) built-up edge. Adapted from ISO 6888-2 (1989) and Khatri and Jahan (2018).

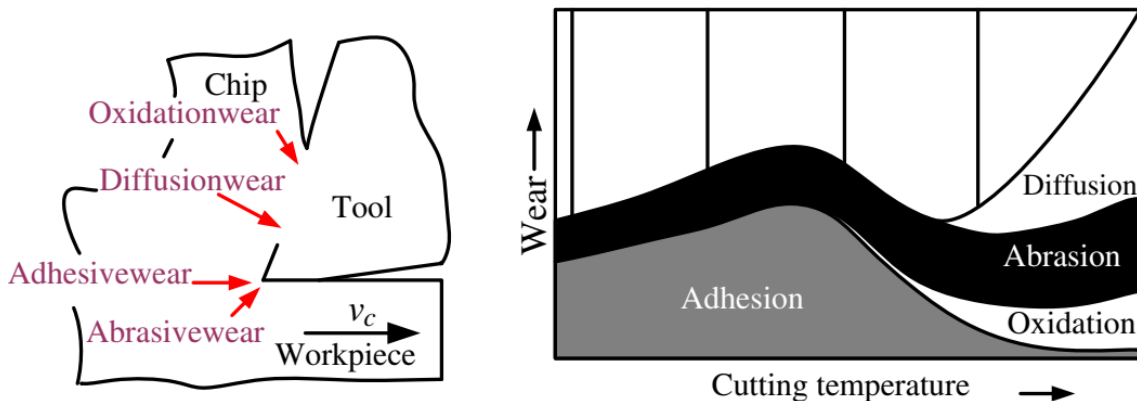


Figure II-20. Wear mechanism in metal cutting tools (Li, 2012).

**Diffusion:** involves the movement of atoms or elements between materials that increases with the temperature. This diffusion of hard elements from the tool into the workpiece weakens the tool, reducing its properties and wear resistance.

**Adhesion:** This refers to the tendency of materials to adhere to the tool's edge due to high temperatures and pressures involved, increasing friction, which can lead to premature wear and damage surface integrity.

**Abrasion:** occurs when there is mechanical wear due to the repeated contact between the tool and the workpiece and the friction wearing down the tool's cutting edge.

**Oxidation:** the high temperature and the exposure of the tool's surface to an atmosphere rich in oxygen and nitrogen propitiate the formation of oxides on the tool's surface, reducing tool life and impacting cutting performance.

Besides, other three effects related to high pressure/stresses and temperatures involved in the machining process can be cited:

**Thermal wear:** refers to changes in the tool microstructure due to high temperatures, which can cause deformation or hardness loss.

**Plastic deformation:** occurs when the tool undergoes permanent deformation due to extreme pressures and temperatures that change its shape.

**Fracture:** occurs when the cutting tool breaks due to excessive stresses or not favourable machining conditions, resulting in the tool's failure.

#### ***II. 4. 10. Lubri-coolant systems***

Even dry machining has been environmentally friendly and worker-friendly (easy and cheap to maintain). The high temperatures associated with the machining process favour the direct use of cooling solutions, Figure II-21a. In machining, around 98% of the energy is converted into heat energy, severely increasing the temperatures in the cutting zone, provoking distortion in both workpiece and tool geometry and rapid tool wear, denigrating the surface integrity (Mahesh et al., 2021; Mia et al., 2022).

Furthermore, the constant pursuit for high removal rates in machining hard-to-cut materials, such as nickel-based alloys, requires elevated cutting speeds, increasing the heat generated and chip flow, making cutting fluids necessary. In this context, the lubri-coolant solutions increase tool lubrication and chip flow, reduce the heat generated and cutting zone temperatures, minimize tool wear, and improve tool life and economic performance. On the same front, efforts have been directed at more sustainable solutions than the usual flood cooling, emerging near-dry and cryogenic alternative solutions (Kopac, 2009). Figure II-21b presents the five main lubri-coolant techniques used in machining, and Table II-3 compares the different lubri-cooling solutions.

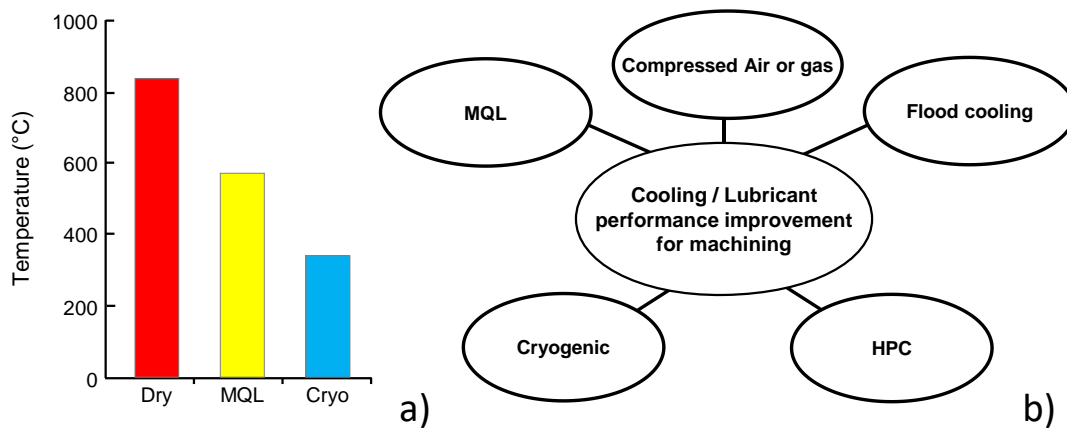


Figure II-21. a) Temperature machining Inconel® 718 with different cooling conditions, adapted from Kaynak (2014); b) Cooling techniques to reduce machining heat generation and improve chip flow.

**Compressed air:** direct a compressed air stream onto the cutting area to remove the heat by convection. This technique has a good chip flow and low installation and maintenance costs. With lower heat extraction than the other techniques, it is a good solution for fragile tools like ceramic that crack with excessive cooling.

**Flood Cooling:** is effective for a wide range of materials and machining processes, it removes the heat flooding the cutting area with a continuous flow of water-based coolant, lubricating the tool and improving chip flow. Even favouring corrosion, contamination by fungus and bacteria, and high maintenance costs, its high efficiency makes flood cooling the most used technique in machining.

**High-Pressure Cooling Condition (HPC):** is an advanced machining technique that utilizes a high-pressure jet of coolant directed at the cutting area, typically with pressures ranging from 5.5 to 35 MPa. The high pressure provides high efficiency dissipating heat, excellent chip flow, and breakage, preventing BUE. It also reduces friction and cutting forces, enhancing tool life and improving finishing (Sharma et al., 2009).

**Cryogenic cooling:** is an advanced cooling method that uses extremely cold gases or liquids, such as liquid nitrogen (LN<sub>2</sub>) or carbon dioxide (CO<sub>2</sub>), to cool the cutting zone. This method provides exceptional heat dissipation, allowing for increased cutting speeds and extended tool life. It is usually applied at high pressure, which helps the chip flow. It is environmentally friendly and effectively reduces thermal stress (tool and workpiece), improving surface finish in hard-to-cut materials (Jawahir et al., 2016; Pereira et al., 2022).

**Minimum Quantity Lubrication (MQL):** is considered an eco-friendly lubrication technique with enhanced chip flow that minimizes lubri-coolant usage. It spreads a minimal amount of lubricant, often in the form of a fine mist or aerosol, directly to the cutting area. The lubricant dispersion reduces friction, heat generation, and heat

dissipation, extending tool life. This technique can be combined with cryogenic (CryoMQL), improving cooling performance but increasing maintenance and installation costs (Pereira et al., 2016).

Table II-3. Effect of different cooling lubrication strategies on machining performance, adapted from Jawahir et al. (2016).

	Effects of lubricant-coolant strategy	Flood	Dry	MQL	Cryogenic	HPC
Primary	Cooling	Good	Poor	Marginal	Excellent	Excellent
	Lubrication	Excellent	Poor	Excellent	Marginal	Excellent
	Chip flow	Good	Good	Marginal	Good	Excellent
Secondary	Product quality (Surface integrity)	Good	Poor	Marginal	Excellent	Good
	Sustainability and concerns	Water pollution, microbial and high costs	Poor surface and thermal damages	Harmful oil vapour	Initial cost	Initial cost

#### II. 4. 11. Signatures of free-form milled surfaces

Surface integrity guides the quality of the milling processes. The major errors that affect the surface quality are geometrical error, residual stress, and roughness (Benardos and Vosniakos, 2003). It is also important to include undesirable surface damages – that are not properly a geometrical error.

Several key factors previously presented affect the surface integrity and functional performance of milled parts: material properties, cutting parameters, tool orientation, surface curvature, feed rate oscillation, tool wear, cooling, and lubricating system are some of them (Guo et al., 2009; Mhamdi et al., 2012; Ulutan and Ozel, 2011). Figure II-22 presents the effect of six tool orientations on the marks left on the milled surface, where the author denotes the tool lead angle by  $\theta$  and the tilt angle by  $\beta$ .

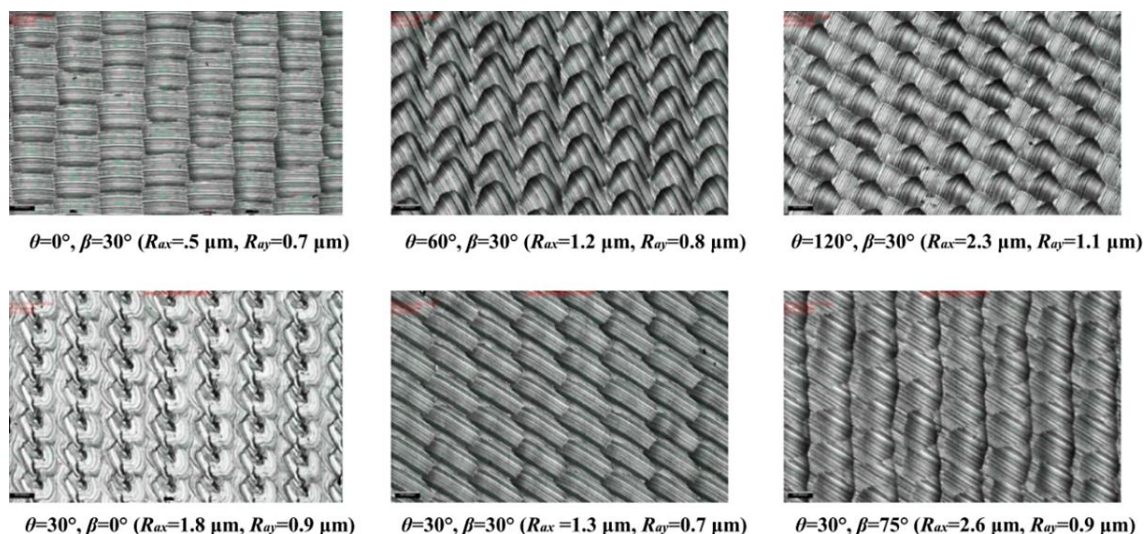


Figure II-22. Signature of milled surface with different tool inclinations (Yao et al., 2018).

Benardos and Vosniakos (2003) classify the surface quality according to deviations in the surface continuity. The authors divided these errors into six groups of sources. The

first is form deviation, and the second is waviness. These two come from machine tool errors, bad setups, fixation, and material anisotropy. The third and fourth refer to periodic grooves, cracks, and dilapidations directly related to the geometry and wear of the cutting edges, chip formation, and process kinematics. The fifth and sixth refers to workpiece material structure, which is connected to physical-chemical mechanisms.

Figure II-23 presents a schematic of the zones affected by the machining process. As can be seen, the machining process is affected thermally and mechanically. Also, it is possible to split the machined zone into two main regions, the first characterized by surface deviations and damages and the second one affected thermo-plastically, with microstructural changes and grain refinement.

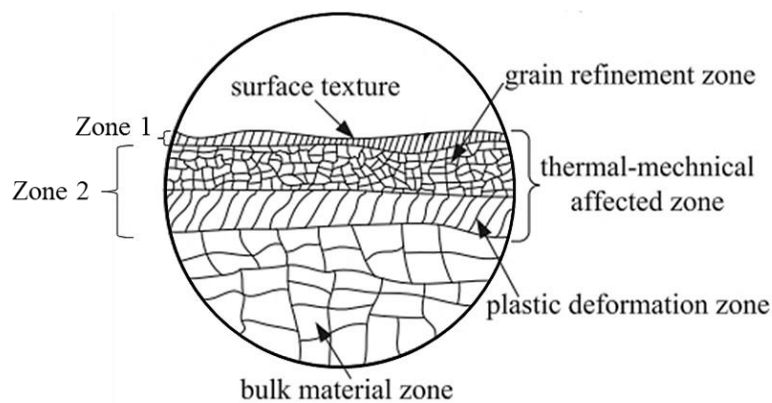


Figure II-23. Zones affected by machining, adapted from Liang and Liu (2017).

Some factors, such as residual stresses, affect safety means; others, like form error and surface roughness, affect the surface shape and component performance.

**Residual stresses:** X-ray diffraction and incremental hole drilling with strain gauges are the most common methods to measure residual stresses. The destructive characteristic and limitation to measure residual stresses in the different phases of the matrix make non-destructive X-ray diffraction the most used (Bobzin et al., 2020; Guo et al., 2009). The residual stresses can lead to premature material failure, so understanding and controlling them is essential to avoid problems related to safety means, especially in the case of aeronautic components, where hard-to-cut materials such as titanium and nickel-based alloys are highly susceptible to residual stresses due to material stability and magnitude of forces involved in the process (Ulutan and Ozel, 2011).

Depending on the tool engagement, tool-workpiece friction, and cutting parameters such as the effective cutting speed, different temperatures are produced, producing different residual stresses. Tensile residual stresses are usually associated with high-temperature processes, while compressive tensions are characteristic of lower temperatures with higher mechanical working and plastic deformations (Aspinwall et al., 2007).



One way to minimize residual stresses is with the feed-per-tooth (Axinte and Dewes, 2002; Caruso et al., 2010). The tool wear is also related to the magnitude of the residual stresses. Using sharp edges and highly effective cutting speed reduces the ploughing problem, reducing the magnitude of residual stresses, especially compressive ones. The smaller the tooltip, the bigger the plastic deformation of the surface. This effect is still present with the use of lubricant solutions (Arunachalam et al., 2004). However, compressive residual stresses improve fatigue life, creep life, and resistance to stress corrosion cracking.

In this direction, the use of barrel tools that present a bigger radius than a ball-end tooltip with the same handle tends to produce less residual stress, which needs special attention regarding undesirable property reduction for some applications.

**Form error:** In addition to the above aspects, form error is another critical consideration in surface integrity. The deviation of the ideal surface usually causes functionality and efficiency losses, an important phenomenon to address. However, several factors affect the milling process that oscillates the components of the cutting force and its magnitude.

Some of the factors related to the form error are associated with the process kinematic: MRT and kinematics (section II. 4. 4), tool orientation (section II. 4. 5), toolpath planning (section II. 4. 6), and rigidity of the system machine-tool-part (section II. 5. 3). Additionally, non-cutting actions like ploughing, minimum chip thickness, and thermal distortions which occur during machining operations, can introduce errors and negatively impact surface integrity.

**Roughness:** Considering the intermittent characteristics and tooltip geometrical shape, the surface topography can be characterized by feed rate ( $f_z$ ), transverse step, and tool radius. However, due to defects intrinsic to the process, such as plastic deformations, tool wear, vibrational, and machine dynamics, several other marks are present on the surface with variable patterns, leading to evaluations based on points cloud and statistical measurements (Grandguillaume et al., 2015).

Roughness evaluation is a crucial aspect of surface quality that can significantly affect part functionality, appearance, and performance (Mali et al., 2021). It is split between linear measurements on the surface, 2D roughness, and 3D roughness. Linear roughness measurement is the most common method used for investigation. It allows easy and non-destructive surface measurement for a wide range of parts. Liu et al. (2016), investigating the effect of tool wear, identify the emergence of random surface scratches that increase the surface roughness, as depicted in Figure II-24.

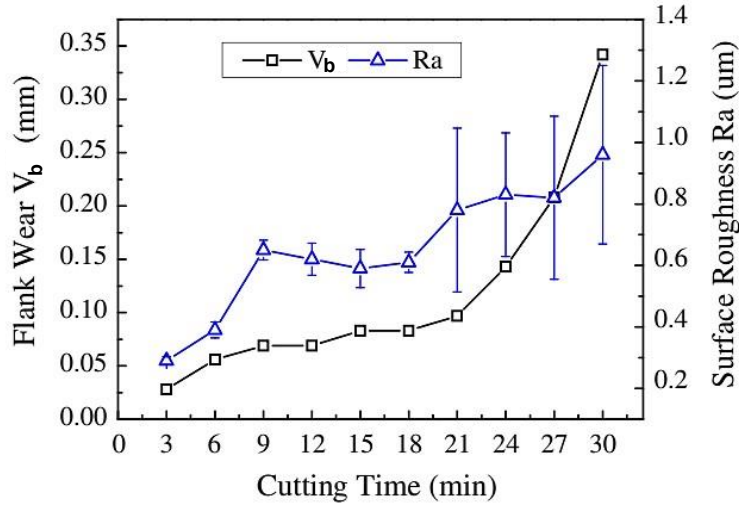


Figure II-24. Tool flank wear and surface roughness progression during face milling of 17-4PH stainless steel (Liu et al., 2016).

However, despite possible correlations of the roughness with some process parameters, the linear roughness inspection cannot adequately quantify the quality of the finished free-form surfaces (de Souza et al., 2015). Besides, the roughness method can be extrapolated to measure surface areas with optical measurement equipment (Quinsat et al., 2008). The main advantages to working with a 3D profile instead of 2D are better surface visualization, a large number of statistical evaluations, and easy detection of errors. The confocal microscope is commonly used for this kind of evaluation; its working principle and characteristics are discussed in subsection II. 6. 1.

Among the 3D roughness parameters, the arithmetic mean deviation ( $S_a$ , Eq. 6) and height deviation ( $S_z$ , Eq. 7) parameters are the most used to evaluate milled surfaces, measuring the primary amplitude parameter of the height of the defects in the surface plane, and the amplitude of the surface defects, respectively.

$$S_a = \left( \frac{1}{l_x \cdot l_y} \right) \iint S |\eta(x, y)| dx dy \quad \text{Eq. 6}$$

$$S_z = (|\max(\eta(x, y))| + |\min(\eta(x, y))|) \quad \text{Eq. 7}$$

Still, the 3D surface profile obtained by confocal microscopy can be used to get insights into the manufacturing process through 2D roughness measurements. Lineal roughness facilitates the evaluation of specific surface characteristics related to its manufacturing process, like the direction of manufacture. Among the linear roughness parameters, the most common are  $R_a$ ,  $R_z$ , and  $R_t$  (Mitutoyo, 2010).

**The arithmetical mean roughness ( $R_a$ )** is the arithmetical mean of the absolute values of the profile deviations from the mean value of the roughness profile, quantified by the upper and lower areas from the mean line.

**Mean roughness depth ( $R_z$ )** is the mean value of peaks and depths of each section of the sampling length equally split into five regions.

**The total height of the roughness profile (Rt)** is the difference between the height peak and deepest valley within all the evaluation lengths.

**Surface damages:** Surface damage affects all aspects of the surface integrity. Detecting and addressing them is crucial to ensure the reliability and safety of the final product. They can be classified into more coarse ones, including side flow, built-up edges (BUE) and adhered material particles, chip debris (db), long grooves (lg), smeared material, and fine-scale damages that include micro-cracking, cracks of carbides, surface tearing, small cavities formation, plastic flow, and grains deformation (Ulutan and Ozel, 2011; Zhou et al., 2012). Guo et al. (2009) evaluate the main defects that happen when machining titanium and nickel-based superalloys. The authors cited material adhesion (BUE), smeared material, molten chips on the surface, and tearing as the main defects. Other defects that can be present in the milling process of HRSA are feed marks, dimples, slip zones, laps, and scratches. Figure II-25 presents SEM images of the most common defects in HRSA machining.

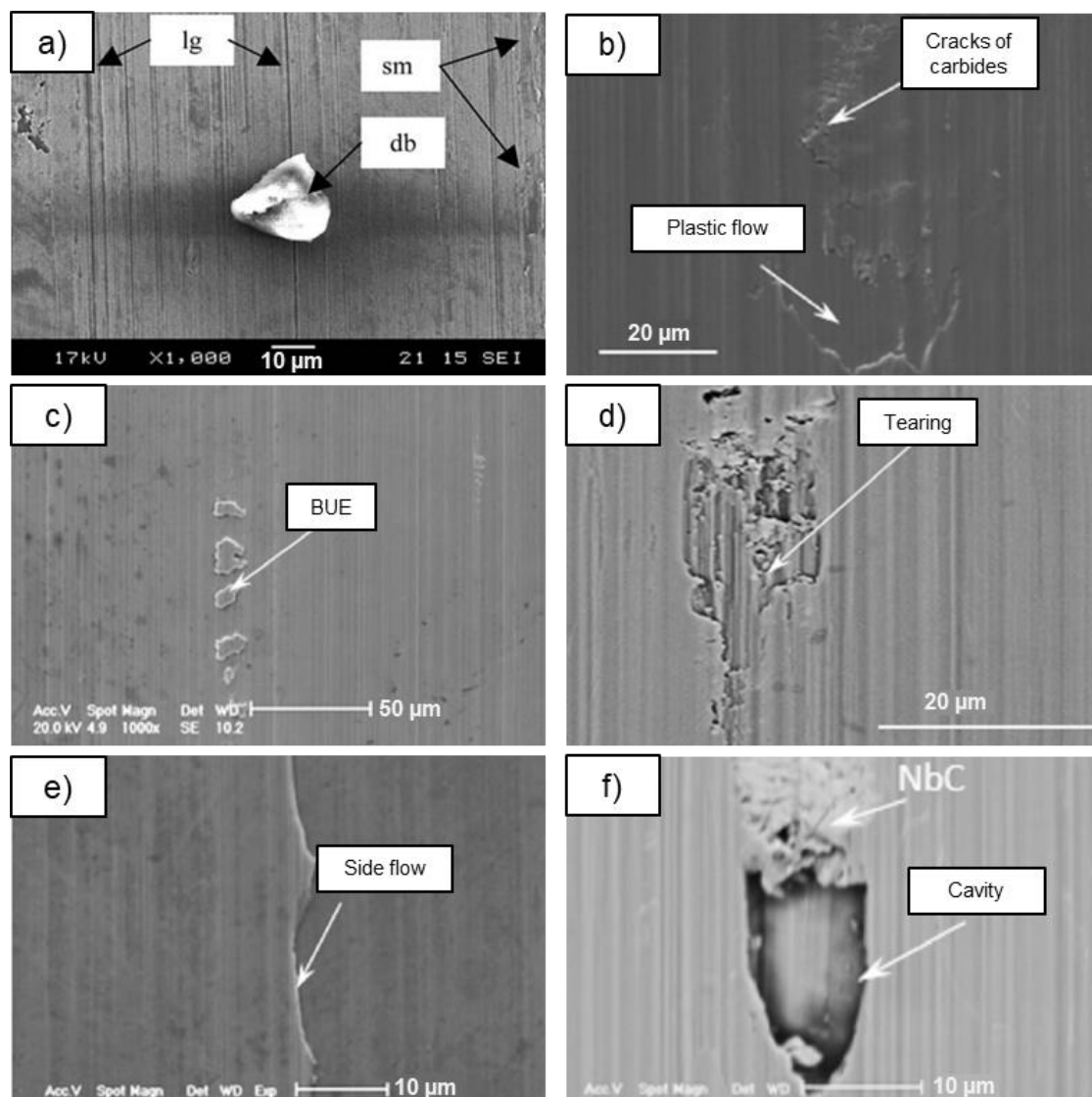


Figure II-25. Most common surface damages when milling HRSA. Adapted from Zhou et al. (2012) and Arunachalam et al. (2004).

## ***II. 4. 12. New manufacturing processes***

In recent years, the emergence of new materials and the design of parts powered the development of new manufacturing processes. Intricate geometrical shapes, topological optimization, internal structures with functional performance, and microstructures lead to the development and optimization of metallic AM processes, aiming to obtain mechanical properties similar to parts manufactured by conventional manufacturing processes by material removal.

Among the most important advantages of the AM process are the wide range of materials, complex geometrical designs, high efficiency, reduced material waste, and the manufacture of products close to the part's final shape (Jiménez et al., 2021). Besides, in the context of Industry 4.0, and with AM machines spread worldwide, it supports the mass customization and production of parts near the final user (Dilberoglu et al., 2017). However, it increases concerns about intellectual property and cybersecurity. These characteristics make it attractive for diverse areas, from medical and aeronautical to aerospace, to repair parts or build them from zero.

### ***II. 4. 12. 1. Powder Bed Fusion Laser Beam***

Between the AM processes, powder bed fusion laser beam (PBF-LB) highlights due to the capacity of production parts with more than 99% density, obtaining mechanical properties close to the material as forged or cold-rolled (Ahn, 2011). It is used to manufacture metallic components from medium to small sizes with wide control of the process through the manufacturing strategies and processing parameters. Besides, it allows design optimization by directional properties (Pérez-Ruiz et al., 2021, 2022) or manipulating mechanical properties and porosity levels (Narasimharaju et al., 2022).

In the Powder Bed Fusion Laser Beam (PBF-LB) process, a thin layer of powder is pre-deposited onto the manufacturing platform, where a concentrated energy source selectively melts the powder in those regions, the platform moves down, and a new layer of powder is deposited by a wiper system, repeating the manufacturing process layer by layer until building up the part according to CAD design. The manufacturing planning of each layer is done using a dedicated CAM software that slices the CAD models, allowing the setting of the manufacturing parameters and the strategy for each layer. Figure II-26 presents a schematic of PBF-LB processes.

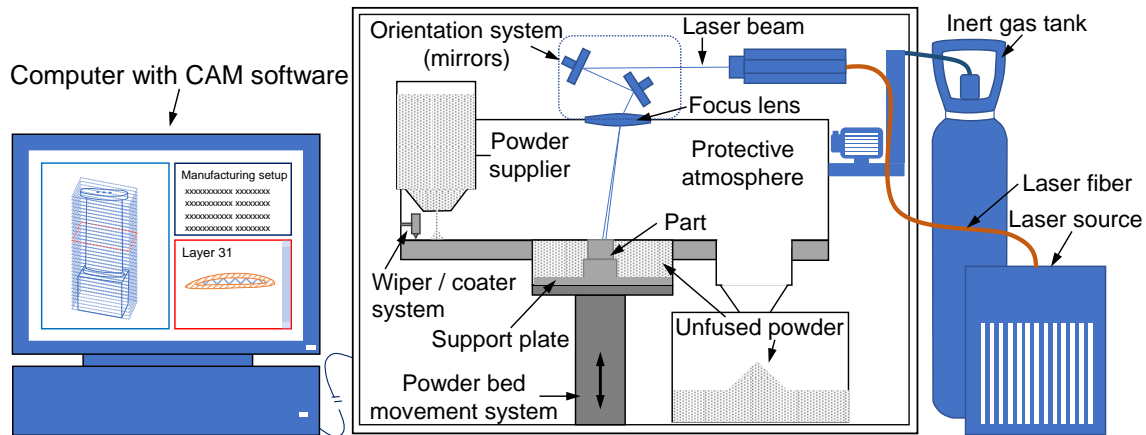


Figure II-26. PBF-LB process schematics.

In the PBF-LB process, the powder size and distribution are important parameters affecting particle packing and posterior parts properties. In this process, the particle ranges usually go from 15 to 53  $\mu\text{m}$  following a Gaussian distribution. Fine particles ( $<10 \mu\text{m}$ ) must be avoided due to lower flowability that promotes cohesion and agglomeration besides high tendency in oxidation. The use of coarse particles ( $>75 \mu\text{m}$ ) makes it difficult to proper powder packing and is also limited by the layer thickness that in the PBF-LB process ranges from 30 to 120  $\mu\text{m}$  (Hyer and Petrie, 2022; Xue et al., 2023).

The porosity of the process can be adjusted with the manufacturing parameters and strategies. In most engineering parts, like the aeronautical components, the mechanical property is improved with a lower porosity level. That way, it is common to investigate parameters of processes that minimize porosity. Furthermore, as the mechanical properties are fundamental to the safety of aeronautical components, understanding the distribution of defects and their relation to the manufacturing process is necessary for the wide application of this new manufacturing process on the field.

In AM, the microstructures obtained are directly related to the energy and times. The processing parameters directly affect the part's anisotropy and mechanical properties and are directly related to manufacturing strategy, including beam overlap, laser scanning path in a layer, and the inter-layer scanning orientation. The combination of PBF-LB manufacturing parameters can result in the same energy density and different mechanical properties. The use of high-energy lasers (over 1000 W) was investigated to improve the productivity of the PBF-LB process. However, the increase in productivity also magnifies the gradient of temperature, anisotropy, and the number of defects. Nowadays, better mechanical properties are achieved in the range of 100 to 400 W (Kamath et al., 2014).

Liu et al. (2011) reported that the microstructure and mechanical properties of parts manufactured by PBF-LB are significantly affected by processing parameters such as scanning speed, power size and distribution, build orientation, laser power, and width. The processing parameters can be parametrized in terms of the volumetric density of energy  $E$  (J/mm<sup>3</sup>), presented in Eq. 8. Where  $P$  is the laser power (W),  $v$  is the scanning speed (mm/s),  $t$  is the layer thickness (mm), and  $h$  is the hatch spacing (mm).

$$E = \frac{P}{v h t} \quad \text{Eq. 8}$$

Scanning speed ( $v$ ) is a critical parameter that affects the volumetric density of energy and the productivity of the process, with an operational window for each material used. Choi et al. (Choi et al., 2017) observed that the mechanical properties tend to improve by reducing the scanning speed. However, excessively slow speeds can cause melting pool evaporation and gas entrapment, generating porosity and decreasing the mechanical properties. At the same time, high scanning speed promotes the formation of pores by a phenomenon known as melt pool separation (Chouhan et al., 2021). Furamoto et al. (2015), investigating pores structures at different scanning speeds, show a reduction in mechanical properties (tensile test and hardness) with the density of energy used.

Nowadays, beam shaping is also investigated to optimize the manufacturing process. It allows a wide control of the melting pool formation, thus, on the microstructural properties of the printed part. Besides, modifying the radiation profile can improve the hatch distance, increasing productivity. The use of a wider melt pool propitiates shorter heating time, favouring the production of equiaxial-columnar microstructure, larger grains, and higher density (Bi et al., 2023).

The fast-directional cooling of the PBF-LB process promotes columnar grain formation, causing anisotropy and affecting the mechanical properties (Pérez-Ruiz et al., 2021). Thus, considering the process limitations, selecting the direction and the laser scanning strategy for part manufacture is important. Souza et al. (de Souza et al., 2019a) show that the yield strength and hardness are improved by manufacturing the parts horizontally. However, it can cause higher deviations due to the higher thermal gradient involved between manufacturing layers.

Also, the deformations during the manufacturing process of additive components due to the high potential heat involved and variation of the part shapes and bulky characteristics can cause severe deviations that compromise the dimensional accuracy and tolerances. According to Boivie et al. (2012), accuracy, surface quality, and production speed are the causes that make AM processes less price-competitive than conventional processes.

Furthermore, the surface produced by all AM processes has a granular aspect with quite a high surface roughness. Using optimized manufacturing parameters allows for obtaining roughness close to 15  $\mu\text{m}$  using PBF-LB and 35  $\mu\text{m}$  in a process like EBM (Pratheesh Kumar et al., 2021). However, in some regions of complex geometrical, due to lack of support or geometrical features, overpassing 100  $\mu\text{m}$  roughness is possible. That way is common in the design of PBF-LB parts with additional stock for later finishing operations by conventional manufacturing process by material removal.

The machining process still plays an important role in finishing printed components for most applications, especially where the component has functional requirements that affect the part's performance (Boschetto et al., 2018). Also, machining processes are still necessary to remove supports and their marks or adjust deviations. On PBF-LB parts, the costs related to post-finishing operations can reach about 27% of the total, as reported by Baumers et al. (2017).

#### **II. 4. 12. 2. Lattice structures**

One of the advantages of the AM process is the ability to produce microstructures. The lattice structure is the name given to the volumetric cell repeated several times to produce a geometrical feature. The design of these structures and the repetition pattern allow the production of parts with a high strength-to-weight ratio, gaining engineering attention. Besides, depending on microstructural orientation, directional properties can benefit the design of high-performance components.

Among the particular characteristics of lattice structures are energy absorption, especially mechanical ones, the improvement of heat dissipation with embedded cooling channels, and biomedical implant compatibility. The use of microstructures also gave PBF-LB a higher freedom in designing. Due to the possibility of design with a small distance between beams, these structures can be self-supported, allowing the production of internal structures with different proposes like fluid flow or weight relief. There are many types of lattice structures: body-centred-cubic (BCC), face-centred-cubic (FCC), gyroidal, diamond, etc. Among them, the BCC has been widely used due to its good mechanical performance – relatively high strength-to-density and stiffness-to-density ratios (Linling et al., 2022).

Because of the complex geometry and the complicated plastic deformation behaviour, the simulation of the lattice structure is difficult. The use of a high number of cells and complex shape intersections exponentially increase the mathematical and computational complexity, challenging the designing or programming of the PBF-LB process. Thus, numerous studies still focus on the simulation of lattice structures with a macro size and

a low number of repetitions, not evaluating its use embedded into mechanical parts with big sizes or complex shapes for weight relief or mechanical damping. The evaluations are usually done by FEA or simple compression assays, with SEM and tomographic analysis (Scalzo et al., 2021).

Gangireddy et al. (2019) evaluated the performance of cell sizes of 1 mm with diameters from 0.1 mm to 0.5 mm in impact using a high-speed camera. The increase of the truss radius allowed an increase in the energy absorbed during the test. However, the highest specific strength and largest specific energy absorption capacity were observed on the lower truss diameters, a fact attributed by the authors to the enhanced and prolonged elastic deformation. This characteristic can be beneficial to application in thin-walled structures and parts with a high aspect ratio.

Rosa et al. (2018), Sortino et al. (2019), and Scalzo et al. (2021) evaluated the lattices structured response to excitation in different frequencies and showed a higher damping capacity than bulk materials. The authors attributed it to the internal friction in the beam joint structures. It is amplified by the dislocations glide, microscopic cracks, and other defects on beam surfaces such as partially molten particles and spatters. Figure II-27 presents a schematic of the damping mechanisms on lattice structures.

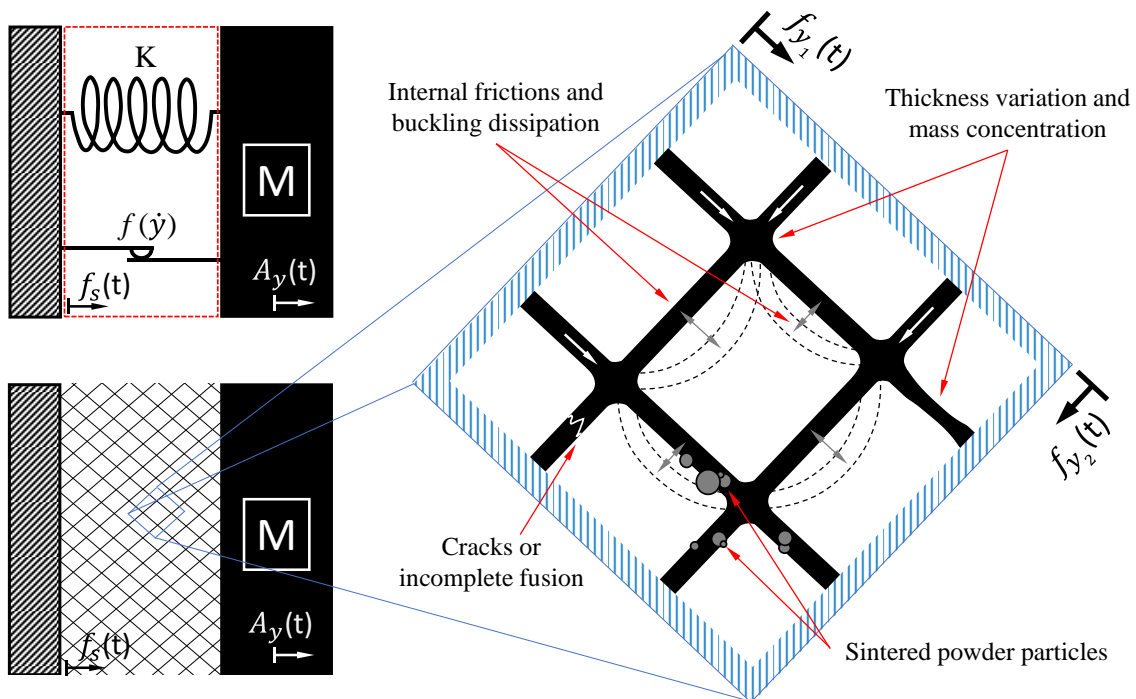


Figure II-27. Schematic of the damping mechanisms on lattice structures.

According to Aguiar et al. (2013), it is necessary to work outside of the natural frequency to obtain good surface finishing and tool life. Thus, the use of lattice structures to change the natural frequencies of the part can be beneficial to the finishing process of complex geometrical shapes. Nevertheless, the understatement of the effect of this kind of



structure on the intermittent manufacturing process by material removal like milling is not well known, and it is an important factor to be addressed, aiming at surface integrity.

#### ***II. 4. 12. 3. Manufacturing of hybrid parts***

Depending on the variables involved, hybrid parts can be classified into hybrid by manufacturing processes and hybrid by using different materials. In both cases, the potential of AM techniques to make the part's design more attractive (economically or functionally) emerges. Furthermore, hybrid manufacturing propitiates lighting aeronautical components by combining metals and advanced composites.

In the hybrid manufacturing of parts using an AM process, a portion of the part is first manufactured by a conventional machining process. After that, the other portion is fabricated by additive manufacturing, welding both portions in-process, as happens with the part and the platform in supportless manufacturing by PBF-LB. With the hybrid manufacturing process, a reduction in the volume of the additive manufacturing process and a post-finishing operation are expected.

Using both processes result in a melting interface zone between the machined part (the PBF-LB substrate) and the first layers of the deposited material by the PBF-LB. This melting interface depends on the material and is not well understood so far. Also, the powder material used in the PBF-LB process sometimes is not available in ordinary blocks. The fusion region and part's mechanical properties need to be addressed by uniting different materials. Besides, in an ordinary PBF-LB process, the part is removed from the substrate after manufacturing, so alignments between the substrate and part are not important. But for a hybrid process, this alignment affects the part precision and performance, so the PBF-LB portion must meet precisely with the machined substrate.

At the same time, the fast cooling rate of the PBF-LB process and the selection of parameters allow for obtaining unique microstructures that can increase the welding compatibility of dissimilar materials like Inconel<sup>®</sup> 718 over Stainless steel 316H (Chen et al., 2020). It has been possible to produce complex parts with intricate shapes or internal microstructures over substrates distinct from the printed. It has also been possible to manipulate properties, reducing weight or manufacturing intelligent and functional parts with improved directional properties or in regions subject to high loads (Marin et al., 2023).

In hybrid manufacturing of parts using AM processes, the rupture of the part tends to occur in the region with the highest pores concentration. Godec et al. (2021) manufactured a hybrid part using Inconel<sup>®</sup> 718 with different AM processes (PBF-LB and

L-DED). The part broken on the L-DED portion, probably the higher number of defects on this portion, caused a failure by crack propagation. That way, defect control and understanding the failure mechanisms are important parameters to measure hybrid component's resistance, increasing its application in the aeronautical field. However, the understanding of a critical level of defects or porosity to the failure of the part manufactured by PBF-LB has not been addressed so far.

## ***II. 5. Modelling of the milling process***

Modelling of the milling process plays a significant role in modern manufacturing, being essential for achieving higher precision, efficiency, and cost in the manufacture of complex geometrical shapes. It helps to train users by showing principles and complexities, avoiding process planning by trial-and-error.

With the use of computational techniques to predict the machining process, it is possible to quickly predict the tool deflection, geometric deviations, and thermal distortions; other indirect vantages stand on strategies selection that minimizes tool wear, surface damage, and energy consumption. However, most methods require several boundary conditions and very complex calculations to predict the milling free-form surfaces.

As in any modelling process, inputs are required to mathematical model the phenomenon. The input of milling free-form surface modelling can be split between the parameters related to the cutting, the geometry, and the tool positioning. As can be seen in Figure II-28, all these elements are inputted through the CAD / CAM software. Figure II-28 presents a schematic of the main steps involved in free-form milling modelling and the interaction between them.

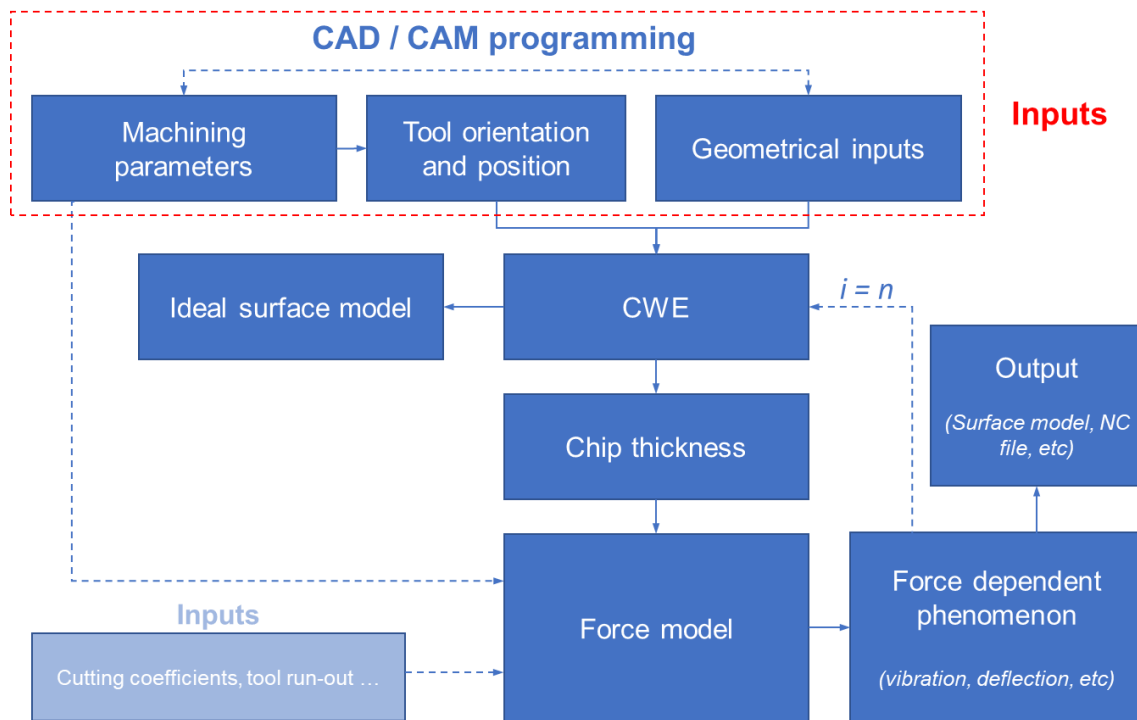


Figure II-28. Flowchart for modelling free-form milling, inputs, and relations.

In the sequence, other main features dependent on the parameter inputs are discussed: the geometrical model, the cutting force, the surface prediction, and other phenomena that can be calculated to support free-form milling process prediction and optimization.

### II. 5. 1. Geometrical modelling

The geometrical model of both tool and part is necessary to model any phenomenon related to the milling process. It will determine the resulting contact between them, pressure area, chip formation, and components of the force, affecting the process and the topography of the machined surface.

It is well known that in free-form milling of sculptured surfaces, the previous operations can leave different amounts of material, known as stock. During the machining planning of geometrically complex workpieces, intermediary geometries can be created to avoid collisions, known as in-process workpieces (IPW) (Ning and Zhu, 2019). This tool is widely present in up-to-date CAM software and makes a more real and visual representation of the engagement of the tool with an in-process workpiece. However, this part can not be considered to predict cutting forces and the final geometry of the machined workpiece efficiently, which is one of the limitations of the actual CAM software. Furthermore, it leads to subjective analysis, and at the same time, it is computationally heavy in the context of exporting and modelling with other software.

The interaction between the tool and the workpiece during the machining operation is defined by the term cutting workpiece engagement CWE. Predicting CWE boundaries or

domains is one of the key factors in predicting the cutting forces for five-axis milling (Guo et al., 2018b; Lazoglu, 2003). Another term related to the CWE to be introduced is the in-cut edge (ICE) element, commonly used to analyse the ball-end milling process.

Determining the tool-workpiece contact is the most complex stage of obtaining forces in milling with ball-end tools, especially analytically. Thus, in many studies, simplifications are done to compute the chip formation. One of the most used is considering the chip undeformable, measuring its radial chip thickness. To model the CWE and solve derived phenomena, different techniques considering the undeformed chip thickness can be used. The most common are solid, analytical, discrete, and semi-discrete.

Among the methods, solid modelling is one of the most used for surface and chip evaluation due to its accuracy. In this method, CAD software performing Boolean operations determines the CWE that generates the surface and chips. During the computation of several surfaces, a lot of mathematical data is generated, increasing the computational cost and limiting the application for free-form milling (Lazoglu, 2003).

Analytical methods utilize mathematical expressions to describe the CWE boundaries, avoiding Boolean operation or meshing procedures. Thus, they are more efficient and easier to implement once mathematically described. All of the instantaneous CWE boundaries can be obtained analytically in the form of quadratic and quartic polynomial equations (Ghorbani and Movahhedy, 2019a).

Unfortunately, due to the continuous change of the surface curvatures along the tool paths, the analytical methods remain a challenge in the ball-end milling of free-form surfaces. Until now, CAD/CAM software has limited or made the data collection of free-form surfaces difficult, limiting the modelling to well-known and monotonic surfaces or with an associated error using semi-discrete models (Wei et al., 2019).

Discrete and semi-discrete methods are the most used and reported in the literature. In a discrete model, the balance between precision and efficiency is given by the user. Increasing the discretization leads to higher accuracy but lower efficiency. Z-map is one of the most used discrete methods. They determine the CWE by projecting the tool and the surface onto a discrete plane in a given direction, typically in the Z direction (Mou et al., 2020). Wei et al. (2011, 2013) significantly increased the efficiency of the Z-map method by introducing matrices comparison using logical operators.

That way, some researchers use tool orientation and toolpath data to simplify the surface, discretizing it into a series of infinitesimal planes. This procedure allowed the computation of CWE discretely or semi-analytically in 5-axis milling. Lamikiz et al. (2004),

considering the surface tangent plane, computed the CWE boundaries along complex tool paths. Similarly, Wei et al. (2018) used an analytical ICE method on discrete oblique planes of free-form surfaces to predict forces in a sinusoidal 5-axis ball-end milling process (error lower than 1%).

Sai et al. (2018) developed a new approach for computing the CWE for free-form surfaces based on entrance and exit angles of the tool edge and geometrical features, considering the instantaneous and previous positions and approximations with planes, spheres, and cylinders. Sun et al. (2009) presented an approach to estimate CWE based on the relative motion of the tool in a flat plane and ruled surface milling. Zhang et al. (2017) proposed an analytical model considering tool orientation and cutter runout to determine the CWE boundaries when ball-end milling cylindrical and spherical surfaces.

Some researchers have also employed CAM software to obtain the machining conditions and surface data necessary for the analytical modelling of the CWE (Tunc, 2016; Tunc and Budak, 2009). Lazoglu et al. (2011), using the output CL from the NC data file, calculated the CWE through Boolean operations using the sequential CL tool positions and their projection on the plane of the tool. Still, there are limitations to extracting the CWE when milling a free-form surface in 5-axis milling. Furthermore, developing models for free-form milling considering more complex tools like barrel shapes cares for the development.

## ***II. 5. 2. Force estimation***

In the milling process, different depths of study can be modelled. Force modelling is the most studied because it directly affects other machining phenomena and the final surface. In the simulations of the free-form milling process, one of the most important parameters is the fast and accurate determination of the instantaneous chip loads along the tool path (Ozturk and Lazoglu, 2006).

Understanding the behaviour of machining force components during the manufacturing process of complex surfaces is of fundamental importance for process optimization and non-quality identification. It is dependent on several factors, such as geometries, material properties, cutting parameters, and tool edge positions (according to the ICE element) in time. It highlights the need for robust geometric models to properly predict the force and other force-dependent problems (Kurt and Bagci, 2011).

Mechanistic or semi-mechanistic models are often used to predict the cutting force in ball-end milling. Mechanistic models are easier to implement than analytical models but require the calculus of empirical coefficients. It recurs to geometrical modelling with the

discretization of cutting-edge elements and empirical results to adjust the cutting force coefficients for a specific material, tool, and cutting conditions (Engin and Altintas, 2001).

The force model is the equation in which one component of the machining force is correlated with the geometric parameters of the cutting and calibrated model parameters. Model calibration involves parameters that require experimental data and depend on the characteristics of the workpiece material and the tool. Also, this force model usually simplifies the cutting-edge element, where oblique or orthogonal cuts are usually considered. The posterior integration of all infinitesimal solutions can predict more complex edge geometry and cutting conditions, like ball-end tooltips for free-form milling. However, this procedure creates a unique database of coefficients, which limits its application, requiring tests to calculate them for each set of tool-material and cutting conditions (Lamikiz et al., 2005).

Figure II-29 presents a flowchart for modelling the cutting force considering the discretization of the ICE elements. To do so, the geometrical modelling of the tool and the surface must first be defined according to the reference system, usually at the tooltip centre. Then, with a series of experiments, it is possible to compute the cutting coefficients for a specific parameter window. After that, these coefficients can be extrapolated to compute infinitesimal forces under the model scope. Then, with the integration of the force of all cutting elements, it is possible to predict the cutting force of the milling process.

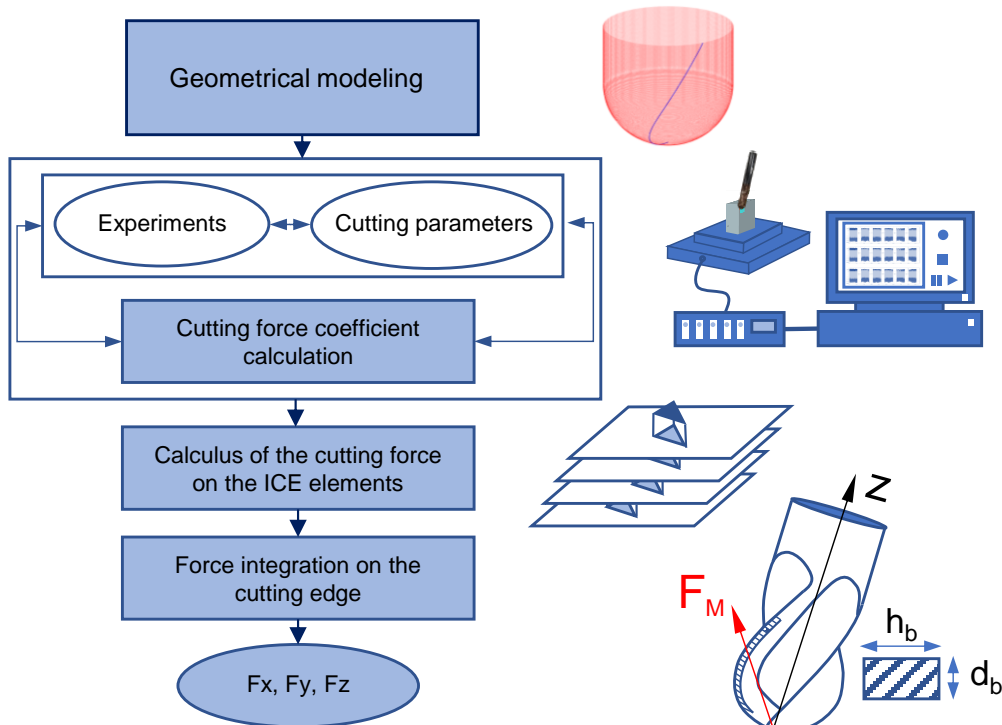


Figure II-29. Mechanistic model of force, adapted from Ochoa (2015).

Kienzle was the first researcher to develop a method for calculating the cutting force ( $F_c$ ) of the machining process 9. It specifies a cutting force coefficient,  $k_c$ , representing the energy required to remove a unit volume from the workpiece. The force calculation (Eq. 9) is given by the product of the specific cutting force with the theoretical cross-section area of the chip (Eq. 10).

$$F_c \cong k_c A \quad \text{Eq. 9}$$

$$A = d_b h_b \quad \text{Eq. 10}$$

As presented in Eq. 9 and Eq. 10, the force establishes a geometric relationship between the specific cutting force and the machining thickness  $h$ , which can be used to calculate the linear cutting force coefficient  $k_c$ .

In the force model developed by Altintas (1996), specific for the ball-end milling case, the chip thickness  $h$  is defined based on the position of the infinitesimal tool edge element in space (Eq. 11).

$$h(\psi, \theta, \kappa) = f_z \sin(\psi) \sin(\kappa) \quad \text{Eq. 11}$$

So, the local components at the tool edge can be defined based on the forces on the tool, taking into consideration the tangential,  $F_t(\phi)$ , the radial  $F_r(\phi)$ , and the axial cutting force  $F_a(\phi)$ . Thus, the cutting force can be modelled as a proportion of the instantaneous undeformed chip area. The system that defines the tool forces components tangential, radial, and axial is described in Eq. 12.

$$\begin{cases} dF_t(\theta, z) = K_{t,e} dS + K_{t,c} h_b(\theta, \psi, \kappa) db \\ dF_r(\theta, z) = K_{r,e} dS + K_{r,c} h_b(\theta, \psi, \kappa) db \\ dF_a(\theta, z) = K_{a,e} dS + K_{a,c} h_b(\theta, \psi, \kappa) db \end{cases} \quad \text{Eq. 12}$$

Where  $db$  is the chip width for a given height  $z$ ,  $dS$  is the differential length of the curved cutting edge of the tool,  $c$  is the index for the edge, and  $e$  is the shear component, including the contributions of the par searing-ploughing on the force model. Lastly, the cutting force on the x-y cartesian plane can be written in the function of the infinitesimal components of the tool force (tangential, radial, and axial), Eq. 13.

$$\begin{bmatrix} dF_x \\ dF_y \\ dF_z \end{bmatrix} = \begin{bmatrix} -\sin(\kappa) \sin(\psi) & -\cos(\psi) & -\cos(\kappa) \sin(\psi) \\ -\sin(\kappa) \cos(\psi) & \sin(\psi) & -\cos(\kappa) \cos(\psi) \\ \cos(\kappa) & 0 & -\sin(\kappa) \end{bmatrix} \begin{bmatrix} dF_r \\ dF_t \\ dF_a \end{bmatrix} \quad \text{Eq. 13}$$

The cutting force models for end mills have been better developed because of the simple cutting geometry. In end milling, the action of an ICE is the same regardless of its axial position in the cutter, while in ball-end milling, it changes along the cutting edge. Thus,

integrating the solution of the infinitesimal elements according to angular position and tool height is required, increasing the complexity and the computational cost. Furthermore, because of the tool helix angle and tooltip geometry, the cutting force is significantly affected by the chips produced in previous cuttings (Kim et al., 2000).

For more than three decades, several authors have been investigating the cutting force on ball-end milling. Yang and Park (1991) were the first to calculate the cutting force for a ball-end milling tool. The authors used the orthogonal cutting model on infinitesimal edge elements of the ball-end tooltip and obtained an error inferior to 30% machining a flat plane.

Later, Feng and Menq (1994b; 1994a) defined the undeformed chip thickness contact to predict (mechanistically) the cutting force for inclined planes, the first studies considering run-out effects on ball-end milling. The cutter run-out and the surface curvature are two main factors that clearly affect the milling forces. Besides, the axial runout, related to tool axis tilting, increases with the tool diameter, affecting cutting forces and surface quality (Ghorbani and Movahhedy, 2019b).

Chiang, Tsai, and Lee (1995) improve mechanistic models by introducing the concept of specific cutting pressure in the axial and radial direction, first considering concordant and discordant milling on a flat surface. Tai and Fuh (1995a; b) used the orthogonal cutting model, with analytical discretion of the CWE by spheres and flat plane, to calculate the cutting force considering the rake angle along the ball-end tool edge.

Lee and Altintas (1996) proposed a semi-mechanistic model to measure force coefficients integrating the force (orthogonal cutting) on each ICE element to obtain the specific coefficients and the cartesian components of cutting force, the first study that evaluates the par shear-ploughing.

El-Mounayru et al. (1997), using a mechanistic approach, CWE calculation by Boolean operations, and data input from the CL file, calculated with high accuracy cutting force components in ball-end milling; however, with high computational costs. Abrari and Elbestawi (1997) proposed an efficient algorithm to predict the cutting force in ball-end limited to channel milling on flat planes. Lazoglu and Liang (Lazoglu and Liang, 1997), still considering milling with full contact of the ball-end tool (channel), calculated the dynamic forces using Fourier transformation of the forces in terms of tool geometry.

Abrari, Elbestawi, and Spence (1998) projected the cutting areas on orthogonal planes to obtain the cutting force coefficient. Altintas and Lee (1998), still considering the orthogonal cutting model and full contact (channel), used the cutting forces to predict the



process's dynamic stability and milling topography. Imani, Sadeghi, and Elbestawi (1998) used solid modelling to determine the chip area to calculate the cutting force for inclined surfaces. Kim, Cho, and Chu (2000), using the z-map method and a non-deformed chip, calculate the cutting force considering channel, ramp, and contour milling conditions.

Lazoglu and Liang (2000) and Lazoglu (2003) used solid modelling for CWE and an analytical approach to determine the instantaneous chip load and cutting forces for specific positions of a curved surface based on the tool position of the NC file (CL). Li et al. (2001) proposed a dynamic force model for channel milling and orthogonal cutting. The authors introduced the concept of transient cutting, determining the start and end of the cut by a  $\beta_e$  parameter.

Zhu, Kapoor, and Devor (2001) proposed a mechanistic multi-axis ball-end milling for free-form surfaces using z-map to determine the CWE, with a limitation in the z component. Ikua et al. (2001, 2002), modelling the cutting force in concave, convex, and flat or inclined, in concordant and discordant cutting conditions, identified that greater surface errors happen in the curved regions due to CWE calculation.

Lamikiz et al. (2004, 2005), using a semi-mechanistic model to calculate the cutting force coefficients on slot milling of inclined planes considering ball-end tool lag angle, obtained a prediction error of the cutting force below 15%; the authors used linear coefficient for shearing and constants for ploughing. Ozturk and Lazoglu (2006); Ozturk, Lazoglu, and Erdim (2006) modelled channel and ramp milling conditions for free-form surfaces. The author calculated the CWE analytical using the chip geometry and the CL data, assuming the errors that come with it.

Lacalle et al. (2007) studied the effect of the cutting force on the FFSM and applied a mechanistic model to calculate the force on the tool axis. A selection of a CAM strategy (toolpath and tilt angles) that produces minimum tool forces improved the finishing of free-form surfaces and reduced surface deviations. Ozturk and Budak (2007) calculated the contact for 5-axis ball-end milling and cutting forces, investigating the effects of tool tilt angles (lead and tilt) on deflection with a mean error of 18%.

Zeroudi et al. (2012) calculated the milling force in 3-axis ball-end milling directly on the CAM software based on a post-processed NC file. The authors evaluate two cutting methods, the Johnson and Cook constitutive law and the classical cutting coefficient, to evaluate tool run-out and ploughing effects on the cutting force level; 5-axis milling CAM implementation is still a challenge.

Dikshit, Puri, and Maity (2017) propose a model for calculating the force coefficients using the mean force considering variations in the rotation speed during HSM. Considering chip deformation, Sonawane and Joshi (2018) calculated the cutting force with ball-end milling of inclined surfaces. Guo et al. (2018a) discretized the CWE of 5-axis milling into inclined surfaces. A discrete calculation of the cutting force coefficients for each position and orientation of the tool on the surface propagated estimation errors below 20%. However, over 200 experiments were conducted.

Ghorbani and Movahherdy (2019b) extracted the surface curvature from CAM software to predict the CWE analytically and calculate the cutting forces of free-form geometries in 3-axis milling. Lin et al. (2019) predict cutting force in a 5-axis ball-end milling inclined surface using a mechanistic model with an average error of 15%. Wang et al. (2020) proposed a method to predict the cutting force for 5-axis ball-end milling by using dextral modelling for the in-process workpiece and CWE identification, demanding high computational efforts on the Boolean operations.

Mou et al. (2020) proposed a prediction model of cutting force for ball-end milling of sculptured surfaces, considering arbitrary tool position and feed direction. The CWE was defined by the surface of the cutter revolution and toolpath data swept. The accuracy of the model was close to 15%. Qin et al. (2023) developed an analytical and semi-discrete model considering the trochoidal trajectories and tool runout with an error lower than 0.5%. The authors also state that the tool orientation controlled by the lead and tilt angles significantly affects the machining process, so it is important to know exactly the tool and part position for each set of CC and CL.

The systematic review of CWE and cutting force modelling using a ball-end mill revealed an increase in the power of the models over the years, improving accuracy and the capacity to predict free-form surfaces using 3-axis and 5-axis machines. However, it was identified that none of the proposed models could efficiently predict the cutting force for generic free-form surfaces using the CAD model or the data from the post-processed NC file (usually recurring to monotonic surface models or inclined planes), been one of the limitations to predicting cutting force directly on CAM software.

### ***II. 5. 3. Deflection***

Deflection is another important subtopic in FFSM because it affects the final geometrical shape. The deflection comes from different sources, mostly affected by cutting forces, and the geometrical features of the tool and the workpiece been directly related to the CWE. The sequence details the phenomenon related to and studies made in the field.

It is well known that there is a strong correlation between the forces involved and the form error. The tendency to maximize cutting parameters to increase productivity increases the components of the cutting force and deflections, resulting in errors in the machined surface. Depending on the rigidity of the components involved, it can cause more or less deviations. According to Desai and Rao (2012), for a given tool-piece set, there is a limit of increment in the parameters. Several studies in the literature address the problems related to rigidity and stiffness, but there is no consensus on the parameters that optimize machining due to several parameters involved and complex relations of the parameters, especially in thin-walled parts.

One of the main sources of machining errors is related to the tool stiffness. The tool's stiffness significantly influences the surface's quality obtained in the milling process, especially in hard-to-cut materials. In this process, the tool tends to be the most susceptible to deflection due to its small rigidity and high cantilever required to avoid gouges, requiring more attention (Soori et al., 2014).

The tool stiffness is defined by the tool's slenderness ratio ( $L/D$ ) quantified by the length of the tool in relation to its diameter. González et al. (2016) varied the slenderness ratio and proposed a parameter ( $L^3/D^4$ ) to describe dimensional errors caused by the tool. For Lacalle et al. (2007), the toolholder presents a similar, or even bigger, influence on the stiffness during machining in relation to the tool balance. Rigidity problems in the toolholder and part fixation have a large proportion of the final error requiring attention.

Cao et al. (2012) compared an FEA simulation with a bi-dimensional cantilever model considering the tool and the toolholder deflection. The results of the tridimensional simulation of the free-form ball-end milling presented higher precision.

Besides the problems of the rigidity of the tool, the part milled can also lead to significant problems. The materials used, the geometry of the part, and the machining strategy influence the rigidity and impact the machining rigidity. For example, in moulds and dies machining, the tolerance is quite narrow, in the range of 0.05 - 0.1 mm for stamping and less than 0.04 mm for injection moulding (de Lacalle et al., 2007).

In the manufacture of aeronautic components, the use of nickel/chromium-based alloys and titanium alloys due to superior properties propitiate higher cutting forces, leading to bigger deformation and undesirable alteration of machined surfaces (Diez et al., 2015; Ulutan and Ozel, 2011). As well, in the aeronautic parts, a high buy-to-fly ratio is required. Machining those components from monoblocks removes a high quantity of material, which could reach 90 to 95% (Del Sol et al., 2019). It significantly modifies part rigidity

during the process, causing deformation that modifies chip thickness and forces, provoking more geometrical deviations.

Habibi et al. (2011), considering cutting force results, calculated and compensated the tool deflection in the slot milling process. The authors compared the tool deflection model with one considering the part deflection and observed an error reduction of over 50%. Thus, part deflection must be considered when the forces involved are significant.

One way to increase the rigidity of the part is by choosing a manufacturing strategy that propitiates smooth force transactions. Another one is modifying the geometry for the gradual remotion of the material and smooth reduction of the local stiffness of the part. Figure II-30 presents three different stock strategies for finishing the operation of components with low rigidity, like blades and thin-walled parts. It can be observed that incremental stock causes modification in the part stiffness and in the part rigidity, and the higher forces are directed to regions with a lower slender ratio.

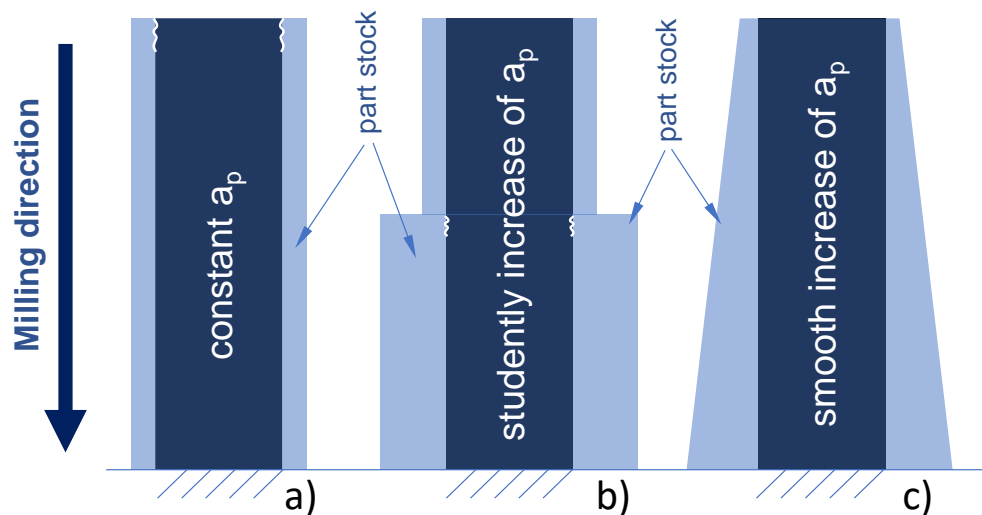


Figure II-30. Different approaches of part stocks to control part deflection: a) constant  $a_p$ ; b)  $a_p$  with a sudden increase; c)  $a_p$  with smother increase.

Sometimes, the recommended depth of cut is also not achieved, and the tool can not remove material by shearing. Depending on the system's rigidity, it completely or partially deforms the surface, provoking undesirable marks or deviations. In all these cases, the dynamic properties of the part can be acquired through experimental modal analysis (EMA) and finite element analysis (FEA) using part IPW (Yan et al., 2022).

One way to ensure the geometrical integrity of the product, especially for thin-walled parts, is compensating the tool path until the tolerances are accomplished (Ratchev et al., 2005; Soori et al., 2014). This procedure is usually done by mirroring the tool position in the opposite direction of the deformation. Law Geddarn (2003) modelled the tool deflection as a cantilever beam with linear deformation and proposed correcting the trajectory by interactively mirroring the original toolpath. Using the mirroring method to

adjust the tool position, Altintas et al. (2018) reduced deviations from 70  $\mu\text{m}$  to 10  $\mu\text{m}$  in 3-axis milling of a flexible blade.

Ma et al. (Ma et al., 2015) used the mirroring method to calculate new positions and tool orientations to compensate deflections in 5-axis ball-end milling of an arbitrary free-form surface. The results demonstrated a substantial improvement in surface accuracy, with an enhancement of about 42% compared to the original NC file.

Habibi et al. (2019) also developed modules to modify the tool orientation to compensate deformations in the 5-axis ball-end mill. The model was divided into two modules; the first, computationally light, could reduce the error by about 70% by only calculating and modifying the tool orientation. The second, computationally heavy, uses the mirror method to modify the position of the ball-end mill interactively to reduce geometrical deviations. However, the same magnitude of error was achieved.

In another study, Yang and Choi (Yang and Choi, 1998) developed a method to compensate tool deflections in end milling; the model can be used to estimate the surface error. Kim et al. (2003) modelled the tool as a cantilever and used the force results to estimate tool deflection and compensate for shape deviation when milling with a ball-end tool. Soori et al. (2014) developed a model to compensate form errors caused by the tool deflections in 3-axes milling. The proposed model increases the accuracy of 89% of the machined surface by considering forces and the dimensional requirements of the part.

Lacalle et al. (2004) milled inclined planes with ball-end mills to address tool deflection and part deviation problems. The study reveals that the assumption of a linear cantilever is not ideal, and the helix angle must be considered. The authors also evaluated cutting directions; downward concordant cutting presented a lower deviation. Ratchev et al. (2004) simulated the deflection of thin-walled parts using finite elements and cutting force data. The authors also developed a methodology easily integrated into NC program simulators such as VeriCut<sup>®</sup> to modify the toolpath and minimize surface errors, considering multilevel optimization.

Dittrich and Uhlich (2020) developed an IA model to adjust the tool position and reduce surface deviations in 5-axis ball-end milling. The training procedure and the multivariable regression allowed deflection error reduction by over 70% in the two workpieces evaluated. Gok, Gologlu, and Demirci (2013) conducted an experimental investigation of deflection for inclined, concave, and convex surfaces and observed lower deformations on convex surfaces. Duan et al. (2015) investigated the impact of lead and tilt angles on cutter deflection and form error produced in five-axis milling. Statistical analysis showed

that the surface deviation was most influenced by the geometry. Also, the effect of the tool's cantilever outweighed the effect of the effective diameter by tool tilting.

Some research used sensors to monitor tool deflection, others static deflection models, and others the cutting force to iteratively (or not) map the tool deflection and adjusted machining parameters and tool position. However, these models usually use a cantilever beam that underestimates the tool's torsion and rigidity of the tool's helix, which can modify the real direction of the components of the cutting forces. It can be done by applying the superposition principle to the infinitesimal elements of the tool, as depicted in Figure II-31. The ICE elements radius in the function of the tool height is given by Eq. 14, the flexion by Eq. 15, and the torsion by Eq. 16.

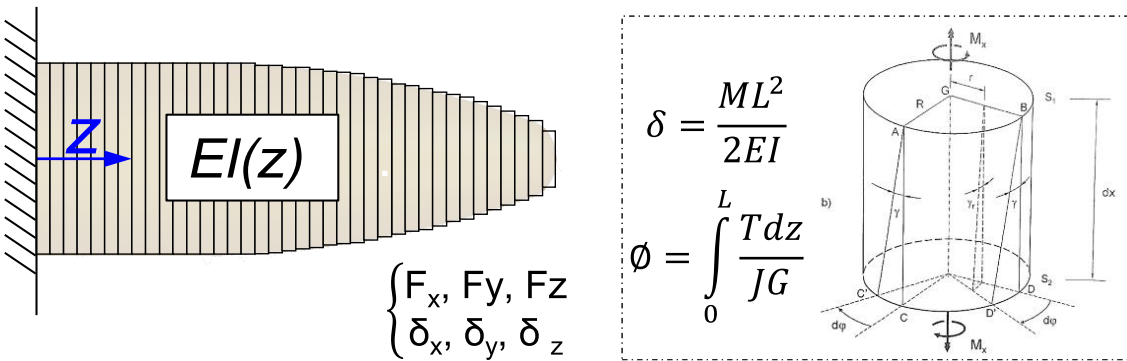


Figure II-31. Tool ICE element under flexion and torsion.

$$R(z) = \int_0^{z_1} r(z)dz + \int_{z_1}^{z_2} r(z)dz + \int_{z_2}^L R_0 dz \quad \text{Eq. 14}$$

$$\delta = \left( \int_0^L \frac{F(x)}{E A(x)} dx \right) i + \left( \int_0^L \frac{F(y)}{E A(y)} dy \right) \quad \text{Eq. 15}$$

$$\phi = \left( \int_0^L \frac{F_x dx}{JG} \right) i + \left( \int_0^L \frac{F_y dy}{JG} \right) j \quad \text{Eq. 16}$$

However, it is still necessary to correct the rigidity of the sulcus of the tool helix. In this direction, the compliance study made by Kops and Vo (1990) to properly characterize milling tools in terms of momentum of inertia and rigidity milling tools proposed a coefficient to relate the real diameter with an equivalent diameter. The authors found that the diameter equivalent is about 80% of the cutter, independent of whether it has 2 or 4 flutes. Budak and Altintas (1995) found a coefficient value of about 0.75. In both studies, end-mills were carried out, and a real value that characterizes other kinds of ball-end tooltips for free-form surface milling needs to be investigated, mainly because this kind of tool has more cross-section variations with the tool helix.

### II. 5. 4. Modelling of the machined surface and the cutting energy

Surface modelling is one of the most important tools for predicting the final part, especially in 5-axis milling of free-form surfaces. Besides, an accurate prediction of surface patterns, together with proper process planning, are required to manufacture high-performance components with functional requirements (Denkena et al., 2011; Peng et al., 2018).

The intermittent cutting conditions and the several variations in contact during free-form milling make the surface prediction challenging. The surface signature of milled surfaces was discussed in section II. 4. 11, the intermittent marks and their influence on part durability and performance elevated the investigation of the milling process for both academic and industrial fields, highlighting the inspection methods and modelling techniques. The modelling of the surface signature can be split between: idealized surface modelling (II. 5.4.1); models considering the trochoidal movement of the ICE and machine kinematics (II. 5.4.2); and energetic studies of the machined surface (II. 5.4.3).

#### II. 5. 4. 1. Idealized surface

In the idealized surface modelling, only the geometrical features are considered together with instantaneous tool positions. Considering the tool geometry or the complete revolution of the tool edge, the surface geometry can be estimated using Boolean operations, discrete methods, or analytical methods. However, several aspects related to the finishing of free-form surfaces are neglected. Figure II-32 presents a theoretical surface produced by a ball-end tooltip with  $f_z$  of 0.1 mm/tooth and  $a_e$  of 0.1 mm.

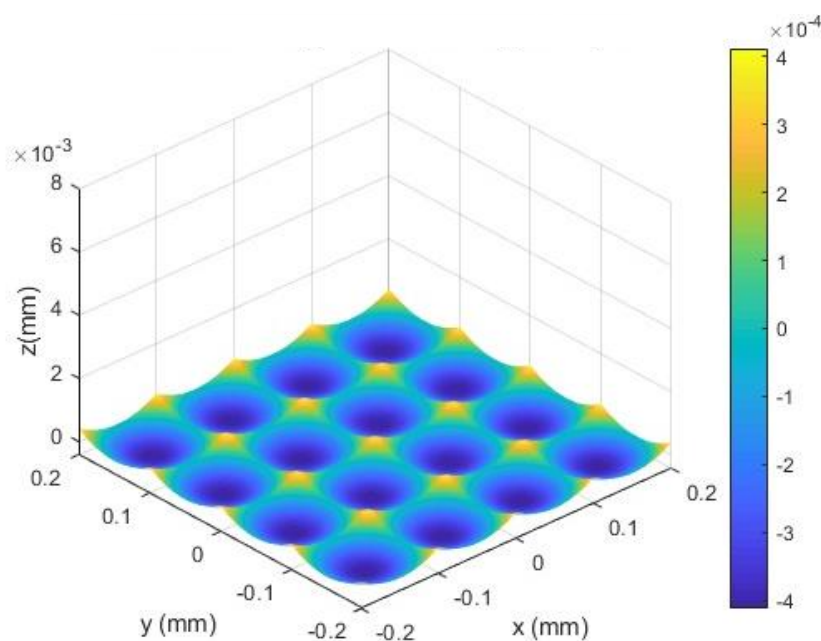


Figure II-32. Theoretical roughness using ball-end tooltip.

CAD software and implemented routines can be used to predict the surface. However, obtaining the positions of CL and tool orientation for a given feed per tooth and properly representing the machining process of free-form surfaces is challenging. Besides, this approach has a high computational time and is very limited even when using up-to-date high-end computers, being mostly used for modelling validation or specific analysis (Liang and Yao, 2011). So, most of the efforts are focused on surface prediction using discrete and semi-analytical approaches.

Wang et al. (2021c) predicted the surface of the ball-end milling process using a discrete model of the cutting-edge and sweeping surface by Newton's method using Z-vectors of the workpiece. The proposed approach presents robustness issues with small tilt angles and surface inputs that limit its usage to monotonous surfaces and inclined planes because it requires solid modelling data of the surface that leads to high computational time. Lavernhe et al. (2014) pointed out that there are two types of models to predict the surface; the most common models only use geometrical data of tool and surface to predict the surface but cannot predict defects in the surface integrity. Thus, considering the trochoidal movement of the ICE elements is required to improve surface estimation.

#### II. 5. 4. 2. Models considering the trochoidal movement and machine kinematics

In the direction of properly characterizing and simulating the surface of ball-end tooltips, several types of research stand out. One of the first researchers was Rao et al. (1997), who simulated the crisp height formation to evaluate the surface topography in 5-axis milling with different tooltips. Toh et al. (2005) explored how cutting parameters impact surface roughness, tool wear, and cutting forces and how the tool-surface engagement phenomena are correlated to the final machined surface.

Arizmendi et al. (2008) were among the researchers to introduce the trochoidal trajectory of ball-end mills considering tool helix angle and run-out. The authors used the equations of cutting-edge trajectories and envelope equations of the material to predict the tool swept. Figure II-33 presents the tool trajectory, the surface, and the simulated surface.

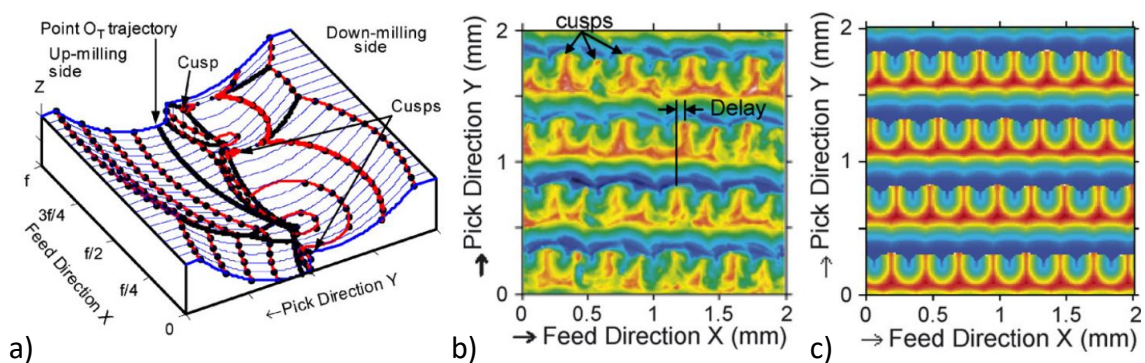


Figure II-33. Simulation of surface machined by ball-end milling: a) ICE trajectory; b) measured surface; c) predicted surface. Adapted from Arizmendi et al. (2008).



Quinsat et al. (2011), considering the importance of predicting the topography and machining strategy selection on 5-axis milling of free-form surfaces, proposed a model discretizing with infinitesimal planes free-form surface to predict the 3D topographies considering tilt and lead angles. Zhang et al. (2013) proposed a model to predict the surface topography in 3-axis ball-end milling, considering tool wear and the effect of the trochoidal edge movement. A high precision was obtained predicting the crisp height on a half-cylinder using the raster strategy. However, the model still does not predict cusp marks over the feed direction.

Lavernhe et al. (2014) proposed simulating surface defects by considering the tool movement's kinematic and real cutting-edge measurements. Although the method can more accurately represent the surface topography than the model using an ideal edge, it overestimated roughness values compared to measurements and is limited to evaluating only one contact condition. Layegh and Lazoglu (2017) proposed the first analytical model to predict the topography and roughness of the machined surface in 5-axis ball-end milling, considering the trochoidal movement of the tool edge and its run-out. However, the proposed model considered the trajectory as straight lines with variable distance (obtained with consecutive CL points) and independent of tool rotation, which led to a 20% error for the case evaluated.

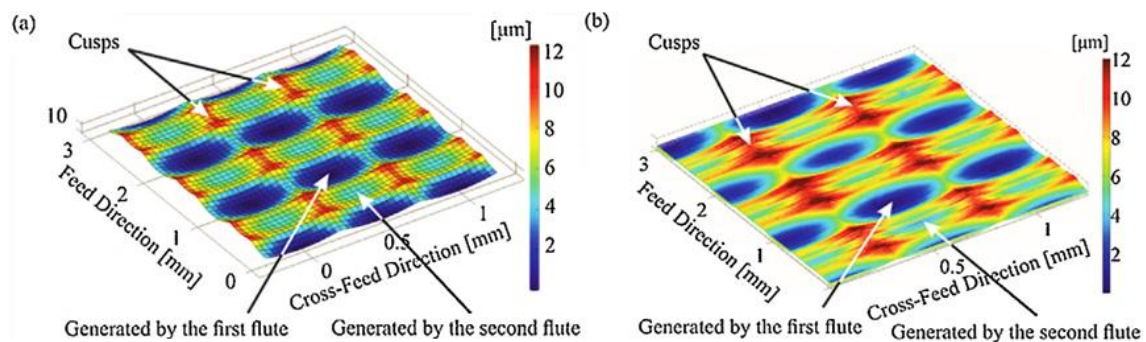


Figure II-34. 5-axis ball-end milling surface topography: a) Simulated; b) measured (Layegh K and Lazoglu, 2017).

Xu et al. (2018a) developed an approach to modelling the topography by sweeping the tooltip edge (considering the trochoidal movement) over the toolpath. Shujuan et al. (2019) proposed an improved Z-MAP algorithm to simulate the topography in ball-end milling, considering the trochoidal toolpath of the ICE with a Newton iteration method. The method was validated with the surface roughness profile and used to evaluate the influence of the tilt and lead parameters on the process. The authors also noted that in the feed direction, the surface profile fluctuation is relatively larger due to the sliding and plastic flow of the metal cutting.

Zhou and Chen (2021) proposed a semi-analytical model to predict the ball-end milling in the 4-axis and used the model to evaluate the surface response against different tilt

angles and cutting speeds. The tool run-out, tool deformation, tool wear, and vibrations were not considered, and there were still certain errors between the measured and simulated profiles. Urbikain et al. (2021) modelled the surface roughness of a barrel-shaped tooltip considering run-out and the helix angle, with a scope limited to the flank cutting of a flat plane with a single radius.

Besides the tool deflection mentioned in the last section and its inclusion on the surface prediction through discrete or semi-discrete modelling of the movement of ICE elements, vibrational problems can severely change the surface topography. The recurrent problems with vibration in free-form surface milling often lead to a balancing of the quality of the machined surface with productivity (Coelho et al., 2010; Dong et al., 2014).

The vibrational dynamic of the process caused by oscillation of the cutting force due to contact changes in free-form milling is critical and can severely damage the surface, as depicted in Figure II-35b. It has been the focus of investigation and modelling by several researchers. Yang et al. (2016) developed a model to predict vibration when machining thin-walled components. According to the authors, it is necessary to consider the dynamics of the product and the response to the material removal, tool position, and length when machining these components.

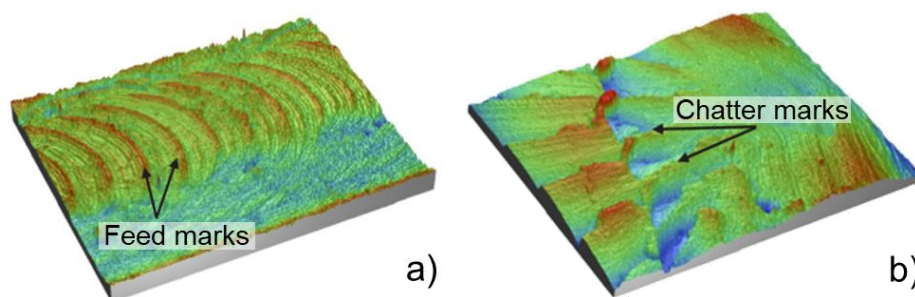


Figure II-35. Surface topography after ball-end milling: a) feed marks; b) chatter marks. Adapted from Wojciechowski et al. (2018).

Stability lobe diagrams can be used to reduce vibration in milling operations, especially for critical components such as thin-walled parts. Using a stability lobes diagram, Qu et al. (2016) found that the feed rate had a minor influence. Thus, increasing the material removal rate makes it possible to increase the feed per tooth. However, the surface quality for the thin-walled part dropped as feed per tooth increased due to the higher cutting force involved, which intensified vibrations.

Wang et al. (2019) simulated the topography in ball-end milling of thin-walled parts considering vibrational response. The vibration of the system is the main factor that impacts the topography of thin-walled components and happens in some regions independent of the tool inclination. The variations of vibration amplitude significantly influence the texture interval, crisp height, and roughness.

Vibrations also provide important information about the milling process. When the dominance of the material removal is ploughing, vibrations occur, and the unstable cutting condition damages the surface, making the prediction difficult (Balázs et al., 2020). Batista et al. (Batista et al., 2017) investigated the effect of the tooltip centre in the 3-axis ball-end milling and observed several marks on the machined surface, identifying regions with material crush and ploughing. Evaluating the specific pressure and the effective tool diameter in-cut observed a region with exponential growth that can be used to determine crushing or ploughing regions, as depicted in Figure II-36.

Peng et al. (2018) simulated the surface topography of micro-milling with ball-end tooltips, where the size effect directly influences the ploughing. The model accurately predicts the conditions evaluated by considering the inclination of the cutter, run-out, cutting force, and plastic deformation of the material. However, it is still unable to predict free-form milling. Wojciechowski et al. (2018) used a multiple regression analysis using the least square method to obtain regression coefficients to predict, in-process, the surface roughness at a 95% confidence level. The exponential function employed relays the surface roughness through the dynamic of the cutting force and the cutting parameters (spindle speed, feed rate, tool diameter, and depth of cut).

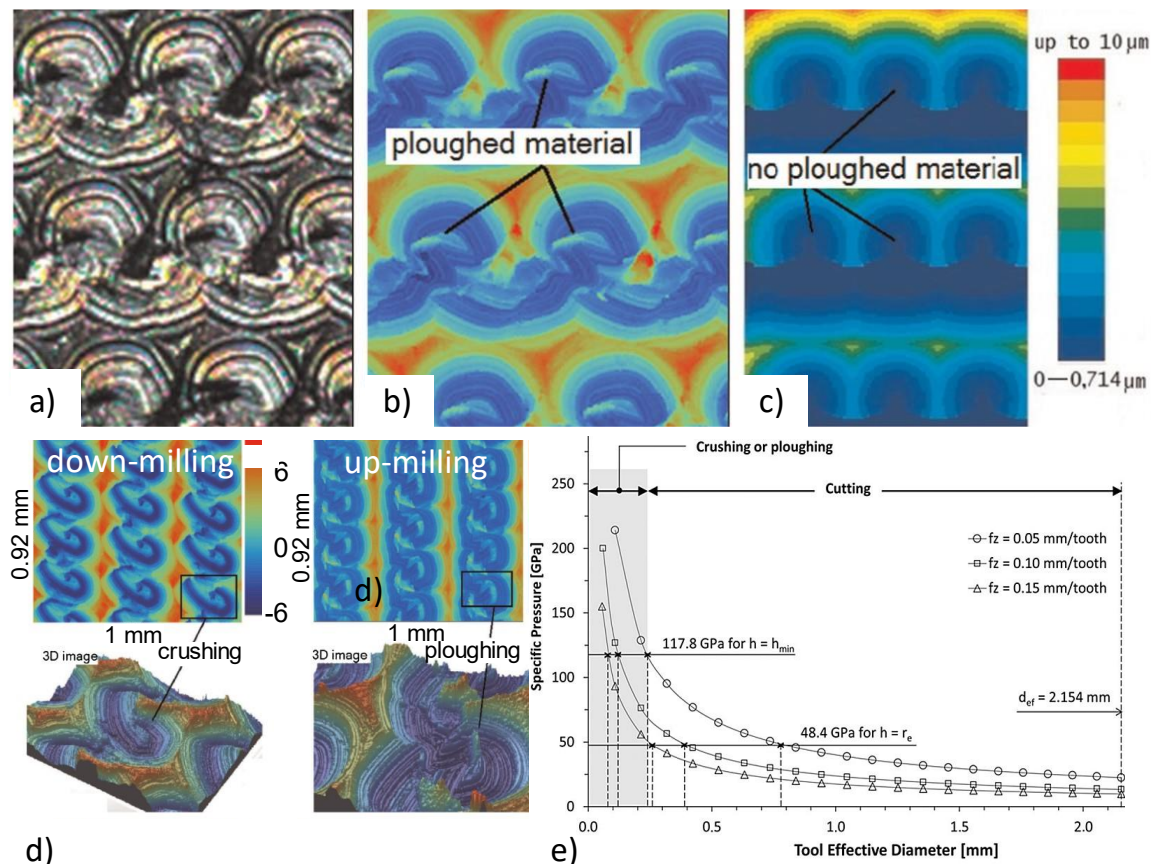


Figure II-36. a) Milled surface. B) optical profilometry analysis, c) simulated surface, d) down-milling and up-milling confocal images, and e) Specific pressure versus effective diameter. Adapted from Batista et al. (Batista et al., 2017).

According to Denkena et al. (2015, 2011), the literature provides various models for predicting surface topography. The most accurate models incorporate the actual machine kinematics and the intersection of the tool with the workpiece. However, this type of simulation overlooks other factors, such as vibrations and tool imperfections. The authors modelled the topography by combining kinematic surface simulation with empirical data regression. In this process, a quadratic regression is performed to predict the standard deviation, skewness, and kurtosis, obtaining a stochastic surface that represents the difference between the real and simulated surfaces. Applying the stochastic surface to another untested cutting condition allows the simulation of the topography closer to the real one. Despite the strong correlation, this procedure requires surface sampling for each combination of material and cutting conditions to obtain the regressions. Also, the simulations considering the centre of the tooltip were not possible due to the significant variation in the surface roughness. Figure II-37 presents the stochastic procedure proposed by Denkena et al. (2015).

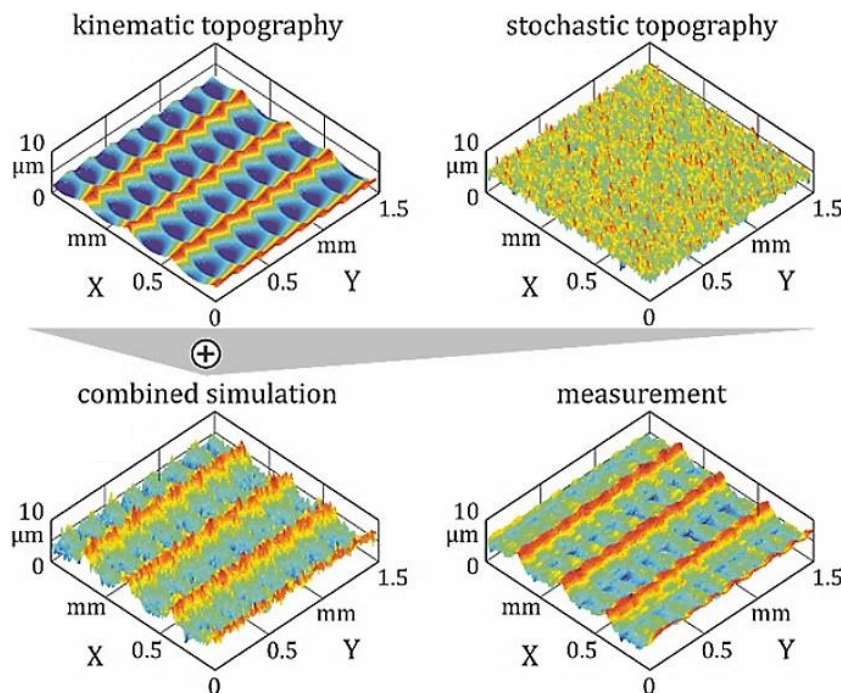


Figure II-37. The stochastic approach to simulate the surface of the ball-end milling process proposed by Denkena et al. (2015).

However, the regressions and stochastic methods require the evaluation of many conditions, making them invariable to more complex parts or free-form milling modelling.

#### II. 5. 4. 3. Energetic study of the surface

The energy involved in surface generation is another topic of important understanding related to surface integrity. Cutting energy has been used as an indicator to assess surface integrity and establish thresholds for energy levels that can cause surface damage. The energy involved during machining is related to its main macro

phenomenons, shearing, plastic deformation (ploughing), and friction, being dependent on the material (friction and thermomechanical properties) and cutting parameters. The cutting energy ( $E_c$ ) is defined by Eq. 17.

$$E_c = E_s + E_f + E_p \quad \text{Eq. 17}$$

Where  $E_s$  is the shear energy,  $E_f$  is the friction energy and  $E_p$  is the ploughing energy.

The usual relation of the cutting energy in the machining process follows the sequence of shearing, friction, and the contribution, usually lower, of the ploughing (Budak et al., 2016; Shaw, 2005). However, when the centre of ball-end mills acts in the cut, the material is crushed, and ploughing energy increases, becoming dominant (Batista et al., 2017). Moreover, the friction energy can increase, magnifying the total energy of the system. So, determining the energy components can be a good approach to evaluating surface damages independently of cutting parameters and material (Xu et al., 2019).

Specific cutting energy is a representative quantity required to suppress the workpiece material resistance during chip removal, as the higher the specific cutting energy, the higher the heat transfer rates and residual stress on the part material (Salmon, 1992; Shaw, 1996). Besides, it is also possible to address the accumulated energies during the process. It represents all the nucleation and growth of micro voids generated during the trans granular surface cracks and cavities formations (Dieter, 1988).

Xu et al. (2020, 2019) studied surface integrity based on materials and cutting energy using a pendulum-based method. The authors evaluated several rapid cutting conditions transitions, as happens in free-form milling with ball-end tooltips, with the objective of quickly characterizing different material behaviours. The cutting parameters were varied, and the system energy was measured to relate to the surface damages. This same procedure can be extrapolated to improve surface damage prediction when the centre of the ball-end tooltip acts in the cut.

Fontaine et al. (2006) used an analytical oblique cutting approach to obtain the thermomechanical behaviour of the workpiece material and the tool-chip interface friction characteristics, considering run-out and ploughing. However, more data, such as surface discretization and toolpath, are needed to adapt the approach to free-form milling. Also, in the literature, few works related to the plastic deformation field and its pattern in the milled surface.

## **II. 6. Inspection of components**

Among the tests for inspecting components are destructive and non-destructive testing (NDT). NDT is preferable for highly value-added parts and the continuous evaluation of critical components. Among the most common NDT techniques are ultrasound (suitable for big-sized parts), magnetic particles, liquid penetrants, and X-ray computer tomography. The last one is often limited to smaller-sized parts or regions of evaluation.

Among the destructive inspection processes are metallographic assays by optical imaging, tensile tests, hardness, impact tests, and fatigue life. Between them, optical imaging microscopy highlights. It is one of the most versatile techniques used in several fields of knowledge. In the analysis of the machining process, if the samples are well prepared, it is possible to obtain high-resolution images of the sample to identify phases, microstructures, defects, plastic deformation, and other features.

SEM, which stands for Scanning Electron Microscope, is another destructive technique used in several fields of knowledge to produce high-resolution imaging of materials at the micro-nano scale. SEM works by focusing an electron beam over the sample's surface and measuring the interactions between the electrons and the sample, usually with two kinds of detectors, a backscattered electron detector and a secondary electron detector, generating detailed images and indirect material compositional information. It is a powerful tool for research, quality control, and material characterization in semiconductor materials, which is suitable for the evaluation of machined surfaces.

Two other processes commonly applied to inspect microstructures and machined surfaces are detailed in the sequence: confocal imaging and computed tomography.

### **II. 6. 1. Confocal microscopy**

Confocal imaging is an advanced technique that uses optical and electronic techniques to obtain high-resolution, three-dimensional, and sharp images of specimens that would be blurred in a conventional microscope. However, this process requires a long measurement time, large data collection, and the use of expensive equipment (Benardos and Vosniakos, 2003).

The working principle of confocal microscopy (depicted in Figure II-38b) incorporates the idea of point-by-point illumination and rejection of out-of-focus light, first introduced by Marvin Minsky in 1955 (Minsky, 1988), and optical sectioning techniques. By scanning the specimen at different depths, a series of 2D images is produced. These images are used to reconstruct a 3D model, usually by alpha blending technique. This technique

computes an alpha value representing the pixel transparency weight for each pixel position of the 2D images. Its value is used to 3D reconstruct the image with the optimal value for each pixel position (Carter, 2013).

Confocal microscopes typically use laser light sources, providing a very narrow and intense light beam at specific wavelengths. By the use of a sheet with a pinhole, the out-of-focus lights emitted or scattered lights are blocked. New approaches try to filter the images digitally or replace the passive pinhole with a compound detector, increasing the resolution (initially limited by the pinhole dimension) and reducing measurement time and equipment costs. Nevertheless, the principle of slicing and reconstructing in a 3D model 3D is maintained. Figure II-38 presents the confocal microscope equipment and its working principle.

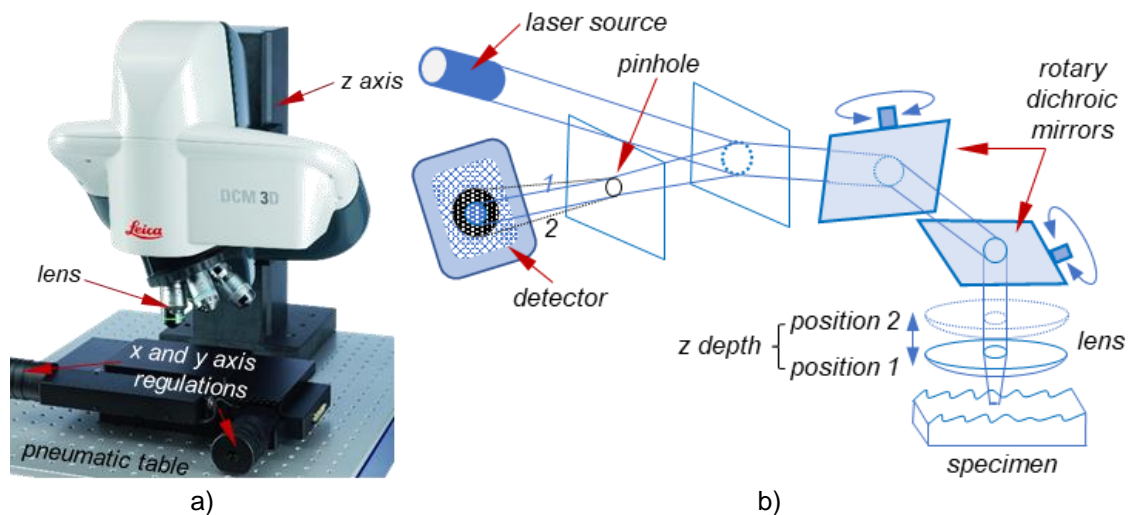


Figure II-38. Confocal optical microscope; a) Leica DCM 3D; b) working principle.

## II. 6. 2. Computed tomography

Computed tomography (CT) or tomography analysis is a powerful, non-destructive inspection tool with micrometre precision that has gained space in the industry in the last decades, powered by the development of more stable X-ray sources and drive detectors (Ortega et al., 2017). This technique has several applications by highlighting the inspection of cross-sections of objects.

It works by using X-rays to obtain multiple views of the object from different angles and then using computer algorithms to reconstruct these views into detailed 2D and 3D images. The inspection range depends on X-ray (power and position), detector sensitivity, material, and noise reduction techniques (active filtering, digital filters, and data processing). Figure II-39 exemplifies the computer tomography components and the principle of work.

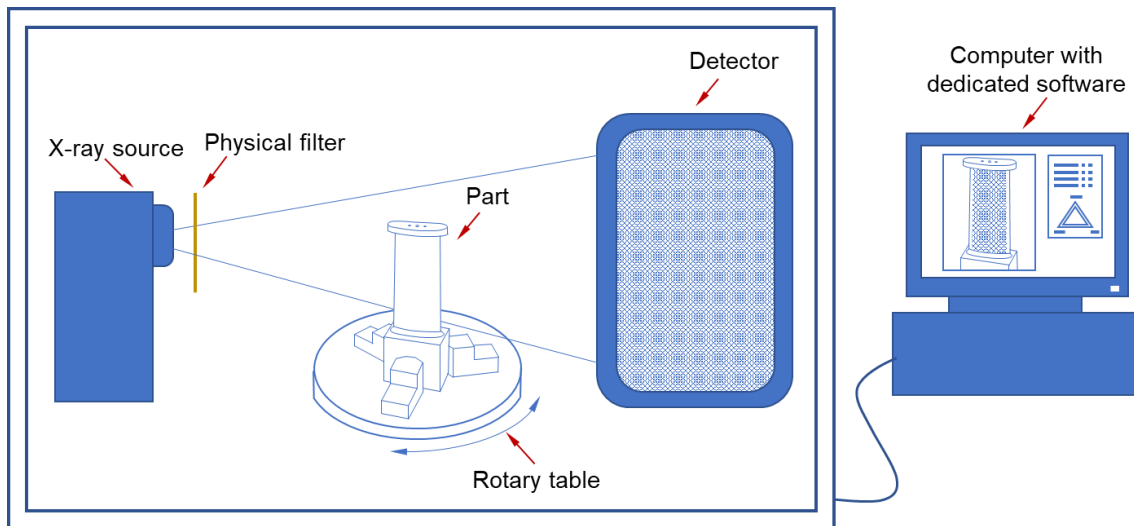


Figure II-39. Operation principle of computerized tomography.

In mechanical parts, the permeability of some metals reduces the CT inspection range drastically. For example, Inconel® 718 has crystallographic structures (FCC) and compositions that make difficult X-ray particle passage, severely reducing the inspection range to a few millimetres, been a challenge to the inspection of bulky solids with high-resolution (Ziółkowski et al., 2021).

Depending on the parameters used very small voxel size can be measured. Due to the processing technique, at least three voxels are necessary to detect the border of vacancies such as pores and cracks (Ketcham, 2005). Ziółkowski et al. (2021) obtained a voxel size of around 14.8 to 7.4  $\mu\text{m}$  using a GE Phoenix V tome X Series tomograph with Cu filter of 2.5 mm and 270 kV; almost the minimum focal spot size of the equipment (Hiller et al., 2012). However, the concerns and radiation control lead to the industrial use of a lower source potential, decreasing its resolution. Wang and Xu (2021) evaluated tomography resolution using Inconel® 718 powder particles ranging from 10 to 30  $\mu\text{m}$ . Using 180KV, a volumetric error lower than 0.3% was obtained.



---

## **Chapter III. Investigation of finishing processes for complex shapes**

---



## Chapter III. Investigation of finishing processes for complex shapes

*This chapter presents works directly or indirectly related to the manufacture of complex shapes, emphasizing the problems related to free-form milling, low-rigidity parts, and big-sized components. It highlights the importance of tools and machines in understanding the finishing process, aiming for posterior modelling.*

### III. 1. Introduction

The studies are presented according to their general purpose and application. They are related to machine kinematics (III. 2), cutting contact on finishing milling with ball-end tooltip (III. 3), and milling complex shapes (III. 4). All subtopics are related to the finishing of complex parts by milling and indirectly addressing the contact of the tool with the surface and the quality of the process. Thus, incrementally highlighting the importance of the topic and propitiating knowledge for the understanding of more complex cases of manufacturing free-form surfaces with reduced stiffness.

### III. 2. Machining kinematics – movements and tool orientation

#### ***III. 2. 1. Machine response time with 4-axis***

The present study is based on the paper published in the Procedia CIRP entitled “New mechanistic model to predict machining time for milling free-form geometries using 4-axis milling”.

Predicting the required time to machine a component is very important for production planning. However, commercial CAM software cannot estimate the time precisely when milling free-form surfaces. Coelho et al. (2010) showed that the real-time milling of a free-form surface can take 1244% more than forecasted by the CAM software. This is because the CAM does not consider individual machine limitations. Thus, marks on the feed direction appear, damaging the surface integrity.

The linear interpolation of small straight-line segments (G01 NC code - DIN 66025) is the most used method to describe a tool path to mill free-form surfaces. This simple technique is an easy way to connect the CAD/CAM to the machine controller (CNC -

computer numerically controlled). The CAM software calculates the cutter contact points (CC) and then the cutter location points (CL), converting them into NC codes under a specific tolerance. As lower this tolerance, lower the chordal error between the tool path and the desired geometry. On the other hand, it generates a huge amount of data, and in most cases, the CNC-machine cannot compute or manage it in a short time to keep the programmed feed rate. So, the CNC reduces the feed rate according to its capacity and/or the speed to close the control loop within the time of executing each NC block. It is limited by the servo response, feedback devices, CNC characteristics, and its implementation on the machine tool.

In such milling processes, the feed rate oscillation occurs even in high-end machines. The real machining time depends on the CNC, machine architecture and dynamic, and NC implementation, besides the CL points calculated by the CAM software used. Figure III-1 shows the feed rate oscillation when milling a free surface and how the CAM software (5 different commercial CAM software) influences such feed oscillation (de Souza et al., 2019b).

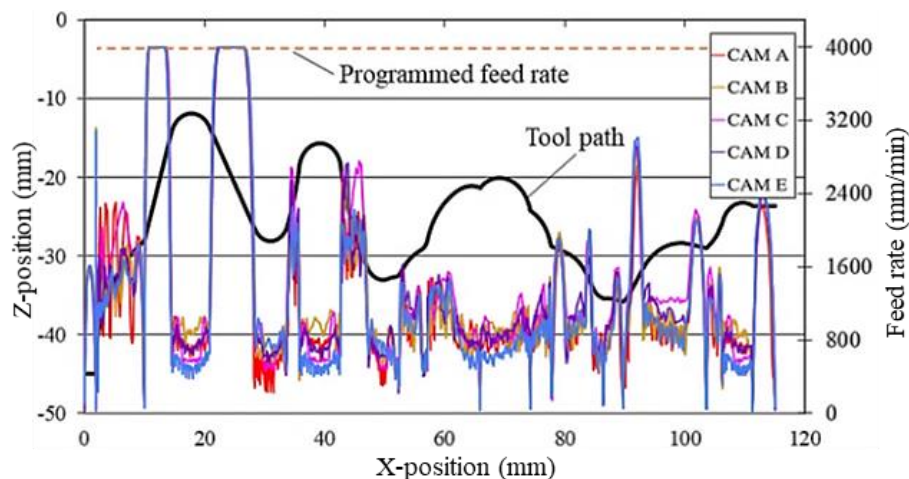


Figure III-1. Feed rate oscillation with different CAM, adapted from de Souza et al. (2019b).

The current commercial CAD/CAM software estimates the milling time by dividing the toolpath length by the feed rate value set by the user ( $time = displacement/velocity$ ), excluding processing limitation and feed rate oscillation related to the moving tolerances of the machine/CNC, like the acceleration profile, positional accuracy and the capacity to move at high speed. That is the main reason for the time estimated by the CAM being very inaccurate in free-form milling (Siller et al., 2006; Yan et al., 1999).

Some analytical proposals to predict the milling time of free-form geometries have been presented by Dugas et al. (2003) and Heo et al. (2006). These approaches need to get specific data from the CNC machine, like CNC cycle time, control loop sample time, and acceleration. However, these data are not easy to obtain; the information about its implementation is scarce, and there are many machine tool builders and CNC

commands. Therefore, the current work proposes a mechanistic model to predict the time to mill free-form geometries of 4-axis machines by identifying the machine processing capacity for moving in linear and angular trajectories. The developed methodology can be applied to any 4-axis machine independent of the NC command, tolerance settings, and the CAM used for programming.

### III. 2. 1. 1. Experimental procedure

The experimental procedure of the proposed work is divided into three tasks: *i)* Using the results of some simple experimental tests (linear and non-linear assays), develop a method to describe the real feed rate considering linear and angular movements. *ii)* Develop an algorithm to predict the feed rate using the NC file according to a specific CNC machine. *iii)* Experimental validation of the method in real applications.

#### *i) Identifying the real feed rate for linear and angular movements*

A series of simple tests on the CNC machine was done to obtain the real feed rate for both linear movements –  $v_{fl}$  (X, Y, Z directions) and angular movements –  $v_{fa}$  (A, B or C rotation axes).

The NC codes were programmed to move the machine in a straight line with the path discretized by small linear segments to calculate the linear feed rate ( $v_{fl}$ ) (which can be used to represent free from milling). Four NC programs were run to identify the machine's behaviour during linear movements, each containing different linear segment lengths ( $L_i$ ) to complete a linear trajectory of 200 mm, as presented in Table III-1. In this case, the programmed feed rate was 6,000 mm/min. In general, the set feed rate must be high enough for the machine not to reach the programmed value with the defined segment lengths.

Table III-1. Linear segment length used to evaluate the machine (de Souza et al., 2021).

Feed rate	Linear increment ( $L_i$ ) (mm)			
6,000 mm/min	0.1	0.2	0.4	0.8

Running these NC programs, the real feed rate ( $v_{fl}$ ) was registered. After the evaluation, the real feed rate ( $v_{fl}$ ) was plotted against the respective linear segment length for each case, and a linear regression equation was obtained, characterizing the machine.

Analogically to linear, the real angular feed rate ( $v_{fa}$ ) was evaluated, testing NC codes of an angular path of  $360^\circ$  described by small angular increments ( $A_i$ ). During the first tests, it was observed that for angular cases, the behaviour of the machine is more complicated to describe by equations. Therefore, to obtain more accurate  $v_{fa}$ , ten NC programs were run using different and constant angular increments, as described in Table III-2.

Table III-2. Angular increments used to evaluate the machine response (de Souza et al., 2021).

Feed rate	Angular increment ( $A_i$ ) ( $^\circ$ )				
	6,000 mm/min	0.05	0.1	0.15	0.2
	0.3	0.35	0.4	0.45	0.5

Then, the proposed algorithm uses both variables  $v_{fl}$  and  $v_{fa}$  and computed regression equations to compute the real milling time.

*ii) Proposed method to estimate the milling time*

The proposed algorithm reads each line of the NC code and identifies the linear and the angular displacement for each incremental movement (between two blocks of the NC file). After that, the algorithm uses the  $v_f$  (angular and linear) achievable for a specific CNC machine using the method presented in Item (i). Then, considering the maximum feed achievable for the specific machine (equation regressions for linear and angular movements) and the maximum angular feed rate ( $v_{famax}$ ), computes the corresponding time for each displacement.

The algorithm identifies the biggest time (between linear and angular) to accomplish the movement and assumes it as the time that the machine will take to accomplish the specific displacement (since the biggest time is equal or higher to theoretical time, which corresponds to the programmed feed rate). This procedure is accomplished for all lines of the NC file, and the total machining time is computed at the end. Figure III-3 presents the developed algorithm.

*iii) Experimental validation of the method*

The proposed method was evaluated in a 4-axis milling machine ROMI-D600 controlled by a GE-Fanuc 0i-MC CNC. The CAM trajectories were programmed on Siemens® NX software, and three different geometries were evaluated, as depicted in Figure III-2. The tool paths were calculated under a tolerance band of 0.1 mm and 0.01 mm. Thereby, six NC codes were evaluated. The programmed feed rate was 3,500 mm/min for all geometries, and a 6 mm diameter ball-end cutting was used with a stepover of 1 mm.

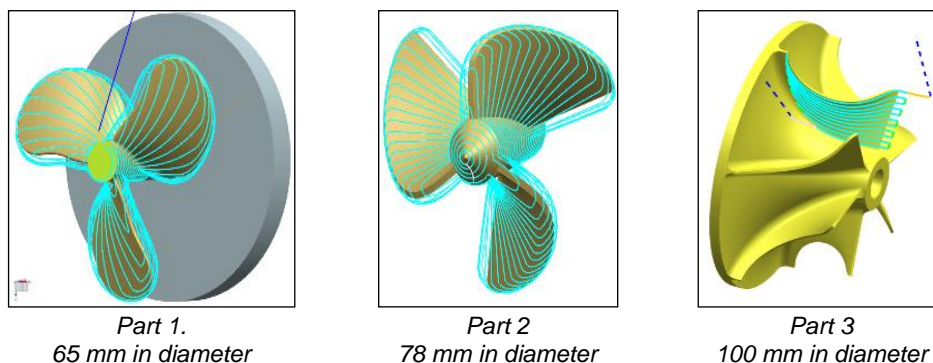


Figure III-2. Part geometries and 4-axis CAM trajectories used for the evaluation of the proposed method (de Souza et al., 2021).

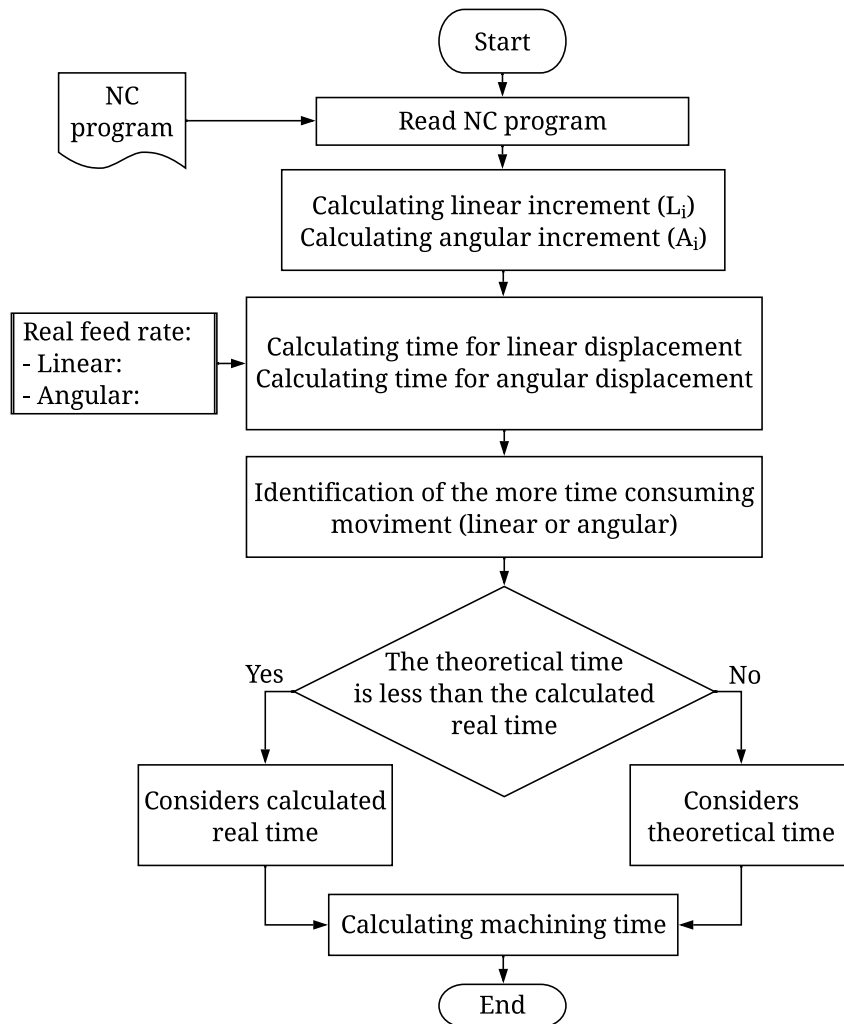


Figure III-3. Schematic diagram of the MRT method, adapted from de Souza et al. (2021).

### III. 2. 1. 2. Results and discussion

First, the behaviour of the real feed rate is presented. After that, the results of a practical application to validate the method are presented. The Linear Feed Rate ( $v_{fl}$ ). Figure III-4 shows the maximum linear feed rate according to the linear segment length ( $L_i$ ).

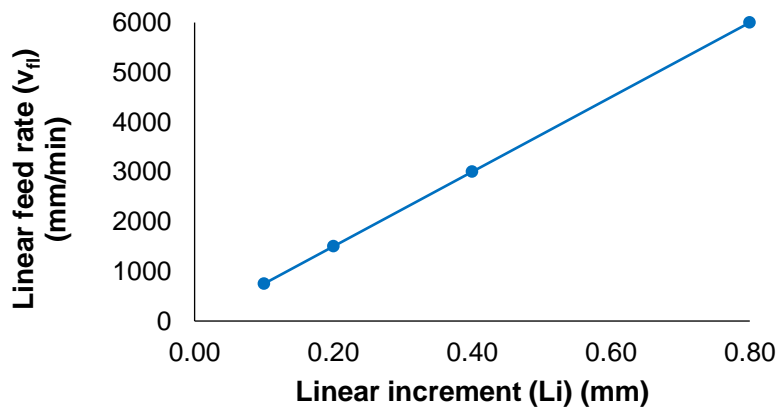


Figure III-4. Maximum linear feed rate with incremental linear movement (de Souza et al., 2021).

Since the linear movements have a linear behaviour (Figure III-5), a simple linear regression can express the machine performance for such a trajectory (Eq. 18).

$$v_{fL} \left( \frac{mm}{min} \right) = 7500 \cdot L_i \quad \text{Eq. 18}$$

The linear coefficient of Eq. 18 represents the Machine Response Time Linear (MRT<sub>L</sub>). This parameter characterizes the real capacity of the CNC machine of movement at high feed rates in free-form geometries (Coelho et al., 2010).

Angular trajectories were run using small angular increments to identify the behaviour of The Angular Feed Rate ( $v_{fa}$ ). Figure III-5 shows the maximum angular feed rate according to the size of the angular increment ( $A_i$ ).

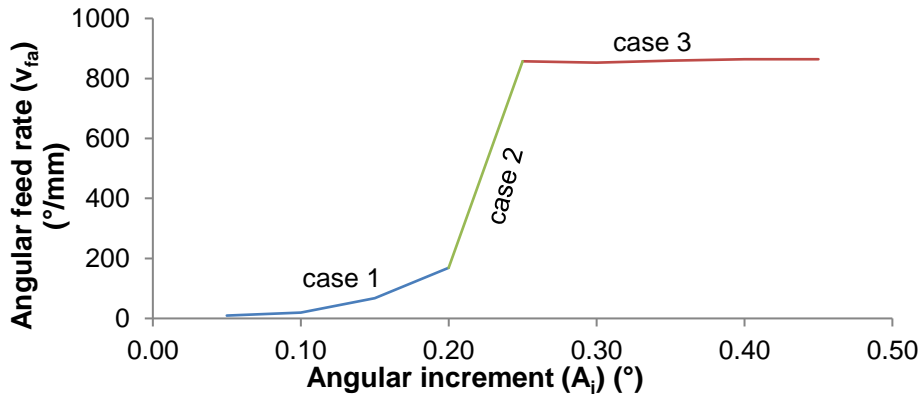


Figure III-5. Maximum feed rate with incremental angular movement (de Souza et al., 2021).

Because it is not possible to represent the machine's capacity with just a single value (like for linear movement MRT<sub>A</sub>), the CNC machine needs to be characterized by Eq. 19 and Eq. 20. From case 3, the machine has reached its limit of angular feed rate, and this is a constant  $v_{famax}$ .

$$v_{fA1} \left( \frac{^\circ}{min} \right) = 35378 \cdot A_i^3 - 4273 \cdot A_i^2 + 285 \cdot A_i \quad \text{Eq. 19}$$

$$v_{fA2} \left( \frac{^\circ}{min} \right) = 13768 \cdot A_i - 2584 \quad \text{Eq. 20}$$

The data of the feed rate obtained by the CNC machine has been used for the validation of the method. Figure 6 presents the time estimated by the commercial CAM, the real milling time, and the time estimated by the proposed method, according to the tolerance used to generate the NC codes and part geometry evaluated.

It can be noted that the error of the time estimated by CAM is very high, ranging from 716% up to 1456%. This happens because the commercial CAM considers neither the tolerance value used to calculate the tool path nor the machine processing capacity.

Using the proposed method and considering the machine and the tolerance band used resulted in a machining time estimation very close to the real one. The error ranges from 0.4% up to 15%, depending on the case evaluated. This small divergence might happen because the machine's acceleration and deceleration are not considered. Besides, the behaviour of the angular feed rate is not linear. Thus, increasing the number of angular



increments on the initial procedure can propitiate a more accurate angular  $MRT_A$  and a more accurate estimation of the time for 4-axis milling.

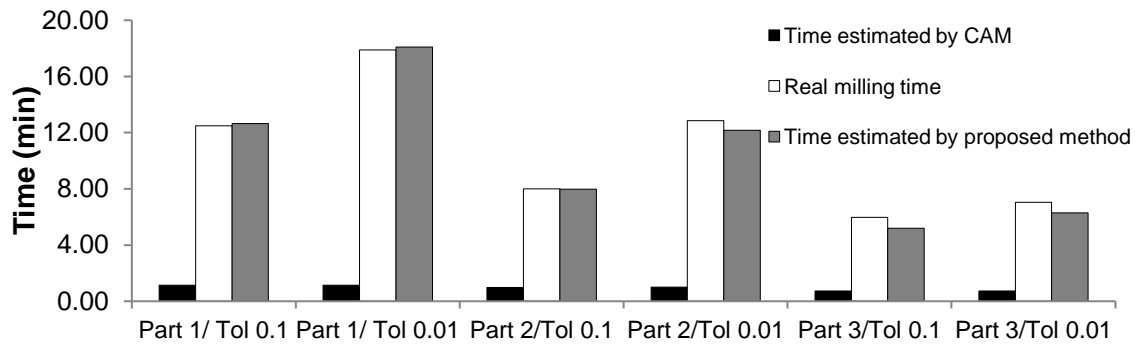


Figure III-6. Estimated machining time by the CAM software, by the proposed method, and the real milling time (de Souza et al., 2021).

### III. 2. 1. 3. Conclusions

The experimental procedure showed that the commercial CAM software considers neither the tolerance for tool path calculation nor the machine CNC processing capacity to estimate the milling time when milling free-form geometries. The machining time estimated by the commercial CAM was 716% up to 1,456% lower than the real 4-axis milling investigated in this work. The proposed method presented errors from 0.4% up to 15% of the real milling time. It is 100 to 1,000 times more precise than commercial CAM software and can be used successfully by industries.

For future works, the evaluation of the surface damages produced on the milling process with the limitation of both MRT (linear and angular) should be addressed, relating the instantaneous displacements with the machine kinematics.

### III. 2. 2. Dynamic calculation of the effective cutting radius and implementation in CAD/CAM software

In the finishing process of free-form surfaces with ball-end tooltips, the contact tool-workpiece constantly changes, altering the effective cutting radius and the effective cutting speed of the tool together with the chip area, chip thickness, and the components of the cutting force (Souza et al., 2014a). Nowadays, CAM software are not capable of considering such conditions. Consequently, potential optimizations to enhance the productivity of this process are not taken into account.

As a consequence of the contact change, two regions with distinct phenomenon dominance occur, as depicted in Figure III-7. When the central region of the tooltip participates in cutting, the effective radius ( $R_{ef}$ ) tends to be null as the tangential speed.

In this case, the predominant cutting mechanism is ploughing rather than shearing, resulting in higher cutting forces that can degrade both the tool and workpiece surfaces.

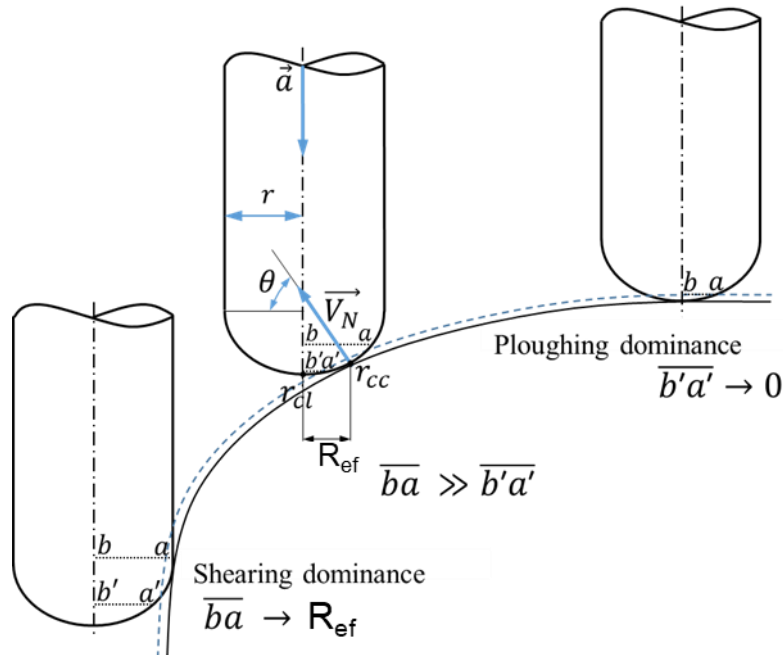


Figure III-7. Changes in the tool-workpiece contact at different instants during free-form milling.

Where  $\vec{a}$  e  $\vec{V}_N$  are the tool vector and the normal vector of the surface in a given instant of the toolpath and  $\theta$  is the angle relative between them,  $r$  the ball-end tool radius,  $R_{ef}$  the effective cutting radius, and  $\overline{b'a'}$  and  $\overline{ba}$  represents the start and end of the contact between the tool and the surface.

Current commercial CAM software offers various trajectory options for machining complex surfaces. However, the choice of the most suitable trajectory is left to the user's selection. Although these systems have reached a high level of development, basic problems/limitations in trajectory calculation can still be observed (Souza et al., 2014b). Therefore, more advanced tools to assist users in optimizing the machining toolpath still require development.

Thus, this work presents a computational tool specifically developed for calculating the effective cutting radius for a ball-end mill while machining free-form surfaces in the 3-axis. The tool was implemented in the CAD/CAM software Siemens® NX through its programming interface to assist the CAM operator in visualizing and performing optimized programming of milling complex surfaces and contributing to developing and implementing new routines for intelligent machining programming of complex shapes.

### III. 2. 2. 1. Experimental procedure

A computational tool has been developed with the aim of assisting the CAM programmer in free-form surface manufacturing by identifying the effective cutting radius based on

the ball-end tooltip radius and the specific positions over the calculated toolpath. After that, the tool was implemented on a commercial CAD/CAM system with an open user interface through the software API as an extension module (*plug-in*).

The methodology proposed to obtain the tool's effective radius utilizes the point of contact of the ball-end tooltip for a given position of the surface, known as Cutter Contact (CC), calculated by the CAM module, as well as the surface's normal vector at this point. The effective cutting radius is defined as the perpendicular distance between the CC point and the tool's axis, as depicted in Figure III-7.

Considering the reference system at the tooltip, it is possible to obtain the CC point from the Cutter Location (CL) point, which is computed by the software. The CAM software computes the CL and the tool position over the surface and delivers it to the user through the post-processed NC file, making it easy to obtain. The normal vector of the surface for a given CL position is given by Eq. 21.

$$\hat{n} = \frac{(0,0,0),(n_x,n_y,n_z)}{|(0,0,0),(n_x,n_y,n_z)|} \quad \text{Eq. 21}$$

Where  $n_x$ ,  $n_y$  and  $n_z$  are the normal components of x, y, and z, respectively. Thus, the effective cutting radius can be written in function of  $\hat{n}$  and the tool radius using Eq. 22.

$$r_{ef} = r(\hat{n}) = r \sqrt{n_x^2 + n_y^2 + n_z^2} \quad \text{Eq. 22}$$

Where the CC and CL points are correlated to the tool vector ( $\vec{a}$ ), and surface normal vector ( $\hat{n}$ ) through Eq. 23 (Käsemodel et al., 2020).

$$r_{ef} = r_{CC} - r_{CL} \quad \text{Eq. 23}$$

$$r_{CL} = r_{CC} + r(\hat{n} + \vec{a}) \quad \text{Eq. 24}$$

Then, using Siemens® NX software, a model was implemented through the open programming interface (NX Open). The CAD module was employed to model the surfaces and extract their normal vectors, and the CAM module was used to obtain the toolpath data (CL). A language compatible with the software, namely C#, was utilized for programming.

With the tool diameter input, Eq. 22 was applied to calculate the effective radius at each position and provide the data to the user. The methodology implemented for calculating the effective cutting radius is presented in Figure III-8.

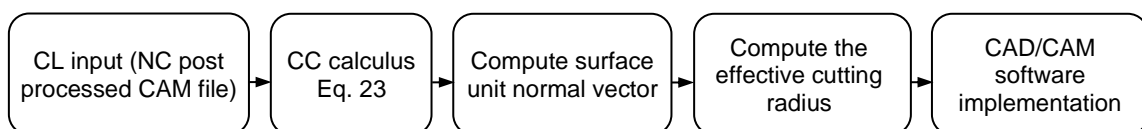


Figure III-8. Methodology for calculating the effective cutting radius using software.

For methodology validation, a free-form geometry was defined. The toolpath calculation was done considering a ball-end tooltip with a 10 mm diameter. The normal vector of the surface was obtained based on a trajectory perpendicular to the surface profile (considering 3-axis milling). Then, the normal vector and the effective radius were calculated using the proposed model implemented in the Siemens® NX software.

The validation was done using the values computed by the implemented routine against the theoretical value measured using the CAD. Hence, the toolpath was first simulated, obtaining the tool position for a given inspection position. Then, the real distance between the tool centreline and the CC position was measured using the CAD inspection module. This procedure was conducted for the first ten positions of the computed toolpath trajectory.

### III. 2. 2. 2. Results and discussions

The results of this study are presented as follows: *i)* Identification of the surface normal vector along the machining trajectory; *ii)* Calculation of the effective tool radius as a function of the machining position, implementation, and validation of the obtained values; *iii)* Implementation of the tool in commercial CAM software.

#### *i) Identification of the surface normal vector*

The steps for obtaining the vector on the surface along the CAM trajectory are shown in Figure III-9. The first that can be seen is that the data distribution varies with the surface curvature. Figure III-9a depicts the CAM programming trajectory together with the CL / CC points calculated by the CAM software (which is the same for 3-axis milling) and the support points calculated by the proposed mathematical approach. Figure III-9b presents the vectors obtained overlaid over the computed toolpath.

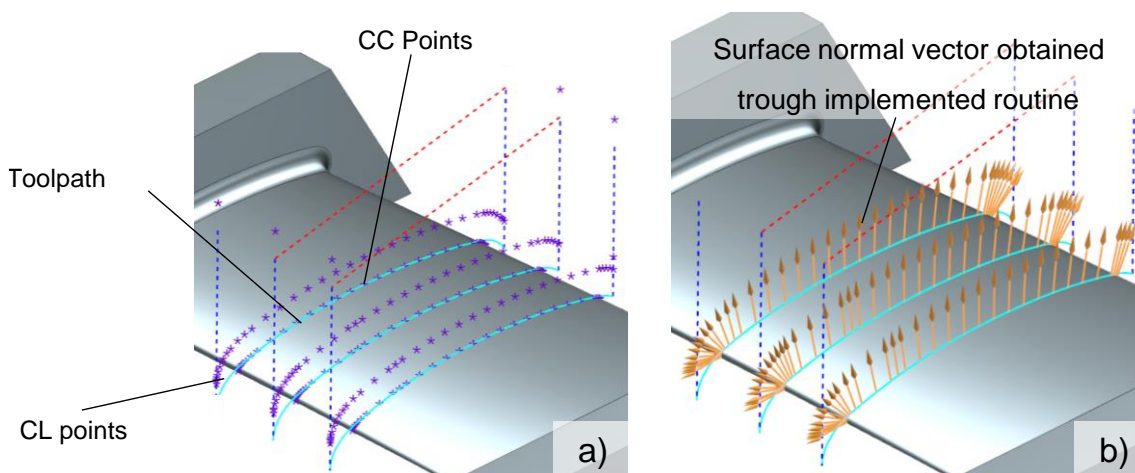


Figure III-9. Stages of the calculation of surface normal vectors: a) CC, CL, and support points calculated by the routine; b) normal vectors obtained through the routine.

The discretization of points is a factor that can be adjusted according to the required precision. It is important to highlight that Figure III-9 presents a limited number of vectors and lateral passes for better visualization. Also, the scope of the study did not evaluate or propose a new discretization for such passes. After obtaining the vectors on the surface, the next step is the calculation of the effective radius.

*ii) Calculation of effective cutting radius, implementation, and validation*

Based on the normal vectors obtained in stage (i), the effective cutting radius was calculated using Eq. 24. During the routine, the calculated values were included in the post-processed lines of the NC file processed by the CAM, with comments for ease of analysis of the user and verification, as shown in Figure III-10.

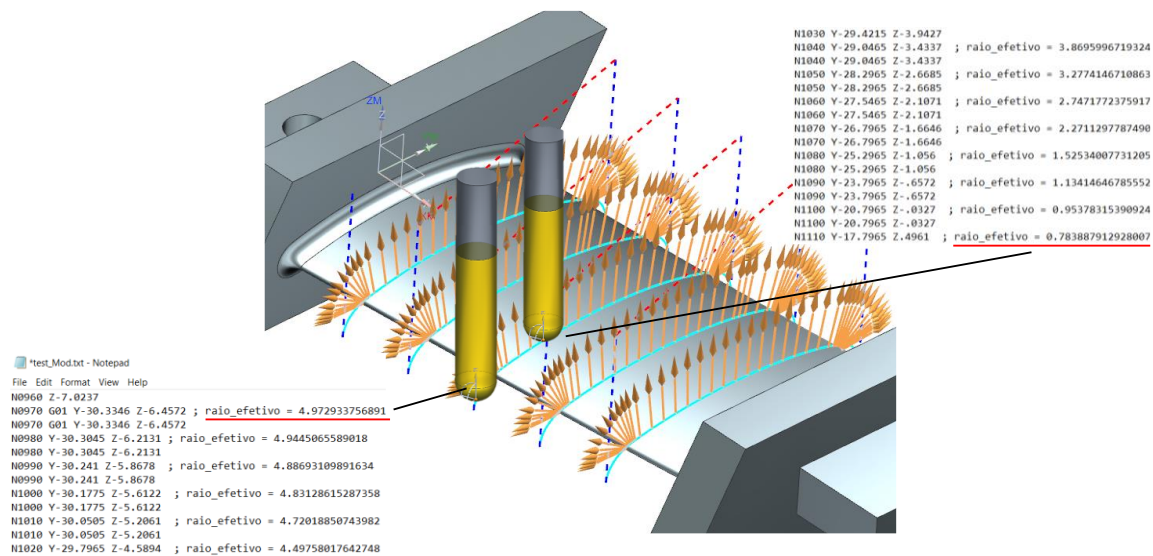


Figure III-10. Tool position over the trajectory and the NC programs modified, including the instantaneous effective cutting radius.

By plotting the values of the effective cutting radius, it can observe the magnitude of the tool-workpiece contact variation, indicating that for the same radial tool speed, there is a significant variation in the tangential tool cutting speed during manufacturing ( $v_{ef} = \omega r$ ). For the validation of the implemented routine, data from both the CAM and the geometry were used.

A cross-section passing through the centre of the tool is shown in Figure III-11 to display the selected measurement features. The tool's centreline and a point on the surface were utilized. Selecting the shortest distance between these entities provides the theoretical value obtained with CAD/CAM software, allowing for a comparison with the value calculated by the developed routine.

The comparison of the first ten effective radius values measured using the CAD software with those calculated by the routine is shown in Table III-3. It can be observed that there

is a good correlation between the theoretical and calculated effective radius values. The percentual error was lower than 0.4%. Also, it can be observed that there is a trend of increased calculation accuracy as the effective radius decreases. This is important for two reasons: *i)* most of the time, due to the tool-workpiece contact, the effective radius is closer to zero values, and *ii)* as the radius decreases, the variation between the programmed cutting speed by the CAM operator and the reference speed for the ball-end tooltip radius becomes more significant.

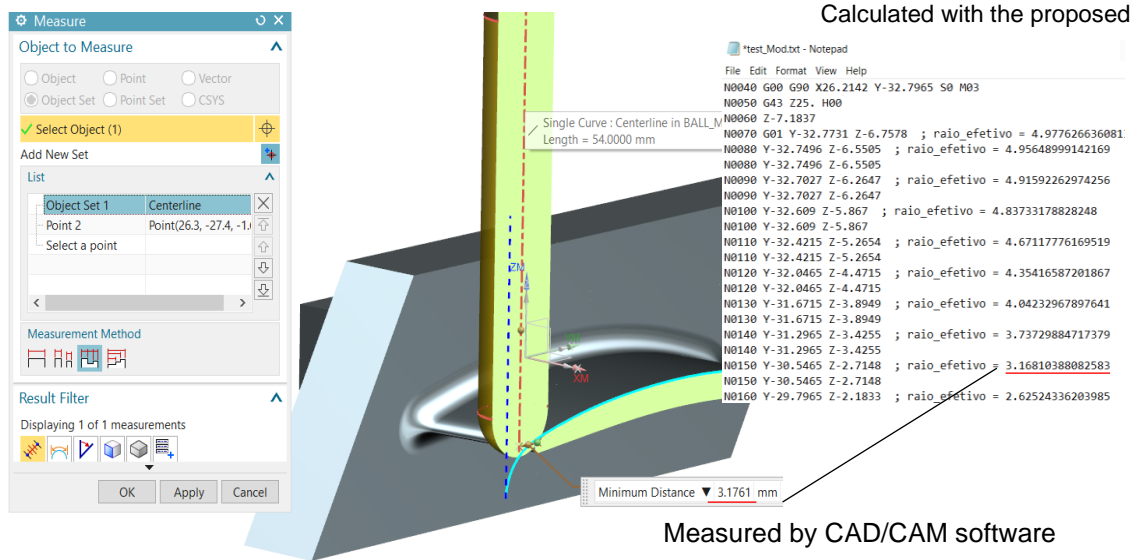


Figure III-11. Comparison of the effective cutting radius calculated by the proposed routine with the measured by the CAD/CAM software.

Table III-3. Values of the effective cutting radius calculated and theoretical.

Z (reference position)	R <sub>ef</sub> CAD	R <sub>ef</sub> calculated	Error %
6.76	4.99	4.97	0.31
6.55	4.97	4.95	0.33
6.26	4.93	4.92	0.29
5.87	4.85	4.84	0.28
5.26	4.68	4.67	0.29
4.47	4.37	4.35	0.35
3.89	4.05	4.04	0.31
3.42	3.74	3.74	0.11
2.71	3.18	3.17	0.25
2.18	2.63	2.63	0.09

*iii) Implementation of the tool in commercial CAM software*

The programmed C# code was implemented in the NX software using the User Interface Developer tool (Block UI Styler). A menu was created incorporating the code programmed and the input variables to interact with the user, as depicted in Figure III-12.

As depicted in Figure III-12, the menu input data are the text file in format (.txt), the CAM operation used for its generation, and the surfaces used during programming. However,

in future implementations, the automatic selection of the features inside the software is expected, shortcutting and avoiding the error possibilities by the final user.

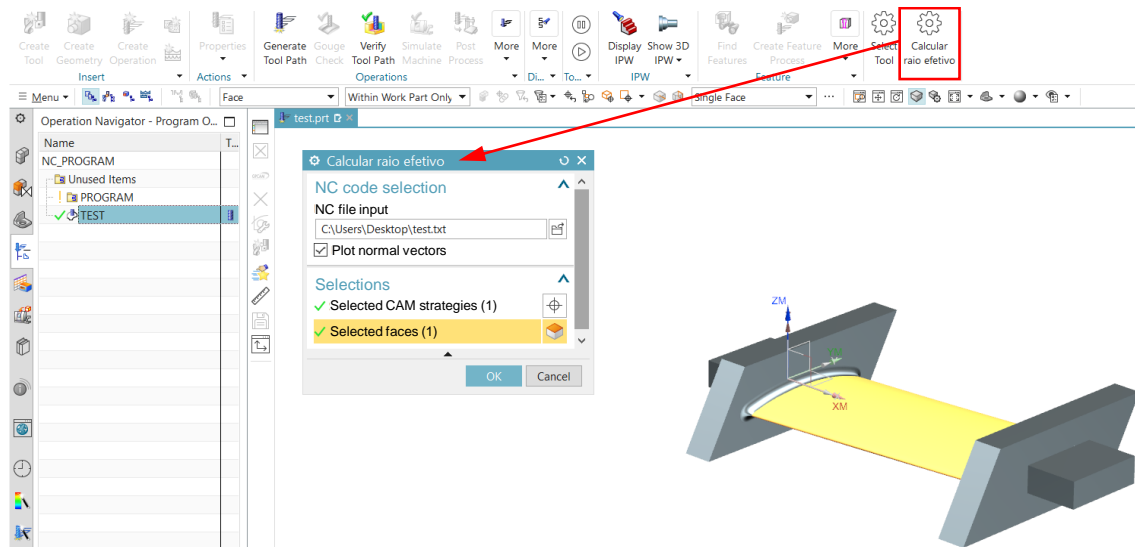


Figure III-12. Customized menu for user interaction.

### III. 2. 2. 3. Conclusions

The proposed development to compute the effective cutting radius is an initial step for programming using CAM software. The tool developed tool will assist in future work and implementations that require effective cutting radius data, which, along with the study of tool-workpiece contact, will estimate cutting force components, tool wear, tool deflection, and machined surface topography. The main conclusions of this work are presented hereafter.

- Even though software often has closed information to protect its algorithms, it is possible to implement routines with geometry and CAM-calculated trajectory data in commercial software with an open programming interface, which is an important step in the direction of the development of SMART CAM software.
- The developed programming routine allowed the extraction of normal vector data from the surface and machining trajectories to calculate the effective contact radius and optimize CAM programming in 3-axis milling of free-form surfaces.
- The validation of the values obtained by the tool developed for calculating the effective cutting radius during the milling of complex shapes demonstrated high accuracy. Therefore, this tool can be successfully used to support the development of extension modules to optimize CNC programming for milling free-form surfaces.
- Analysing the variations of effective radii of the modified NC code, it was observed that the effective radius varies between the nominal value (tool radius) and zero. However, it remains closer to zero than the nominal value most of the time.

- With the mathematical method implemented in the C# language, the developed algorithm exhibited a shorter computational time calculation. This was confirmed by memory control, a feature of this programming language that enhances the robustness and performance of the extension module developed.

### ***III. 2. 3. Remarks of the Sub-section***

The two studies presented highlight the necessity of obtaining NC data distribution and a relation between the cutter contact and cutter location and the normal vectors for the orientation of the tool for programming free-form milling with ball-end tooltips. In this context, and as reviewed in the literature, this kind of procedure is missing for 5-axis milling, which has been one of the limiting factors for modelling implementation in software. Besides, the machine kinematics and its relation with the NC code are not well documented, and the development of computational tools can allow easy visualization and user interaction for a better understanding of the process or results. In this context, a proposed routine to obtain these data, considering a 5-axis milling condition, is presented in Chapter IV.

## **III. 3. Study of the contact on the finishing**

### ***III. 3. 1. Influences of the workpiece material and the tool-surface engagement on surface finishing in ball-end milling***

The present study is based on the paper published in the Journal of Manufacturing Processes entitled “Influences of the workpiece material and the tool-surface engagement (TSE) on surface finishing when ball-end milling”. It delves into examining tool-surface engagement (TSE) and how it impacts the milling process of free-form geometries with ball-end tooltips. Therefore, three distinct materials were addressed: electrolytic copper, AISI H13 annealed, and hardened state. The materials were machined under three TSE conditions to assess the influence of the material properties on the finishing process when using ball-end tooltips.

Nowadays, most of the ball-end milling models used for predicting the process only consider geometrical and kinematic aspects without taking into account the specific material of the tool or workpiece, which significantly affects the milling process (Zhang et al., 2022). Commercial CAM software cannot provide realistic topographical simulations based on TSE and the material being machined. Understanding these effects can be a basis for robust modelling and prediction of surface roughness when ball-end milling, as Denkena et al. (2021) suggested.



In this context, this study contributes to the knowledge of milling free-form surfaces with different materials, considering the tooltip effect on the cutting zone. The kinematics of the cutting edge related to the TSE, machining force, surface topography, real roughness ( $S_z$ ), and the machining accumulated cutting energy were assessed to understand the final surface milled with ball-end tooltips. This study provides support tools for understanding free-form surface milling with ball-end tooltips, contributing to new modelling tools.

### ***III. 3. 1. 1. Experimental procedure***

Machining experiments were carried out to explore the impact of the milling process on the surface produced by ball-end tooltips. These experiments assessed several factors, including tool-surface engagement (TSE), surface topography, roughness, and the accumulated and specific energy of the process.

An experimental workpiece was designed to represent the TSE alterations that happen in free-form milling. In the design process, three flat surfaces with  $0^\circ$ ,  $5^\circ$ , and  $85^\circ$  inclinations in 3-axis milling of flat surfaces is the lead angle and allows the evaluation of different effective cutting speeds, as depicted in Figure III-13a. The workpiece was machined in down-milling and up-milling modes to address all cases of free-form surface milling with ball-end tooltips.

The workpieces were machined using three different materials: electrolytic copper, annealed, and hardened AISI H13 steels. Electrolytic copper has a face-centred cubic crystalline structure and presents high thermal conduction and plasticity. Annealed and hardened AISI H13 steels present body-centred cubic and body-centred tetragonal crystalline structures, respectively. Both result in good mechanical properties with high rigidity, hardness, and thermal stability.

The experiments were carried out in a 3-axis machining centre using a ball-end mill with a 6 mm diameter,  $30^\circ$  helix angle, two flutes, solid carbide with (Al, Ti, Cr)N multilayer coating manufactured by Mitsubishi (code MP2SBR0300). Previously, the ball-end mills were inspected by a confocal 3D microscope Olympus<sup>®</sup> OLS4100. The tools had a  $2.7 \mu\text{m} \pm 0.6 \mu\text{m}$  cutting edge radius and  $58.6 \mu\text{m} \pm 10.7 \mu\text{m}$  width of chisel edge, as depicted in Figure III-13b.

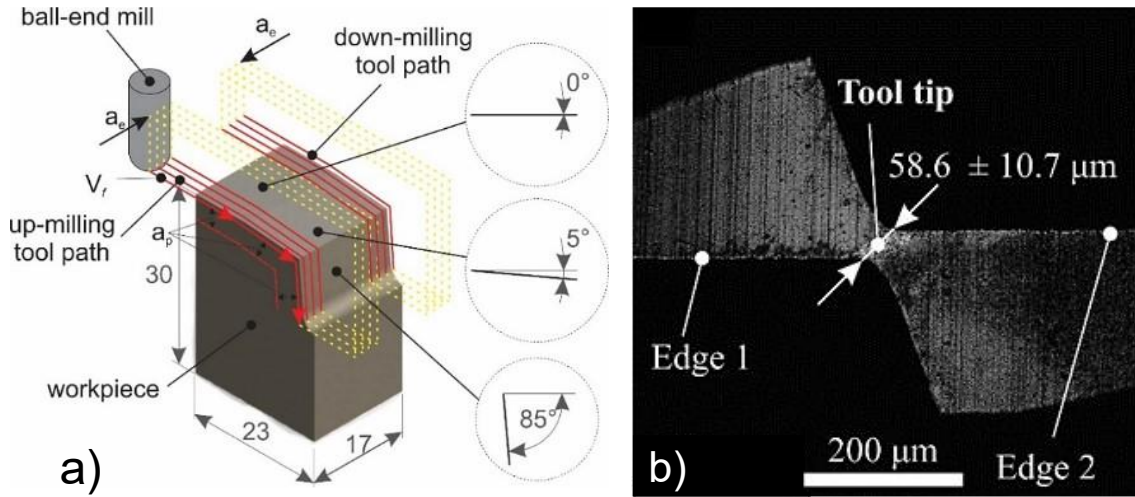


Figure III-13. Workpiece geometry and tool path; b) tooltip, adapted from Basso et al.(2022).

The cutting parameters used in the study were 0.1 mm/tooth feed per tooth, 180 m/min nominal cutting speed, 0.1 mm radial depth of cut, and 0.5 mm axial depth of cut. These conditions were selected under the cutting conditions ranges recommended by the tool manufacturer. Table III-4 presents the control factors and their levels and the real effective cutting speed for each angular face of the workpiece.

Table III-4. Experiment control factors and levels (Basso et al., 2022).

Control factor	Levels
Lead angle and effective $V_c$	0° (0-90 m/min), 5° (0-85 m/min), 85° (150-180 m/min)
Material	Electrolytic copper, annealed AISI H13 steel, hardened AISI H13 steel
Milling mode	Up-milling, down-milling

The assessment of machined surfaces was done using a Veeco<sup>®</sup> WYKO NT1100 optical profiler, aided by Vision 4.20 software for data analysis. The maximum height surface roughness ( $S_z$ ) was chosen to evaluate the surface quality due to its sensitivity in identifying potential damage compared to other roughness parameters. A mean value was computed for each experimental condition based on three measurements taken at different locations. The analysis of variance (ANOVA) for  $S_z$  was conducted using Minitab<sup>®</sup> software under a 95% confidence interval.

### III. 3. 1. 2. Modelling of the process

The ball-end milling process was modelled using the improved z-map proposed by Wei et al. (2013). The method was used to compute all positions of the CL file, manually generated, maintaining a uniform distancing distribution (constant  $f_z$  between CL). The uncut thickness chip is calculated using Eq. 25, proposed by Lee and Altintas (1996).

$$h(\theta, \kappa) = f_z \sin(\theta) \sin(\kappa) \quad \text{Eq. 25}$$

$$\kappa = \sin^{-1} \left( \frac{R_{ef}}{R_N} \right) \quad \text{Eq. 26}$$

Where  $\theta$  is the tool rotation angle,  $R_{ef}$  is the effective tool radius,  $R_N$  is the nominal tool radius, and  $\kappa$  is the radial immersion given by Eq. 26. The maximum uncut chip thickness ( $h_{max}$ ) was determined as a function of the tool rotation angle using Matlab® software.

The accumulated energy and instantaneous specific energy were assessed through the cutting forces to establish a correlation with surface damages. The components of the cutting force were measured using a Kistler® 9257BA dynamometer, Kistler® 5233A charge amplifier, and National Instruments NI USB-6216TM data acquisition hardware at an acquisition frequency of 100 kHz. Labview® software version 13 was used to obtain the force signals and Matlab® software was used for post-processing calculation. The specific energy ( $u$ ), total energy ( $U$ ), and accumulated energy ( $U_a$ ) were calculated using Eq. 27, Eq. 28, and Eq. 29, respectively.

$$u(\theta) = \frac{F(\theta)}{A(\theta)} \quad \text{Eq. 27}$$

$$U(\theta) = u(\theta)V_{chip}(\theta) \quad \text{Eq. 28}$$

$$U_a(\theta) = U(\theta) + U_a(\theta - d\theta) \quad \text{Eq. 29}$$

Where  $F$  is the resultant force ( $F_x$ ,  $F_y$ , and  $F_z$  measured by dynamometry),  $A$  is the instantaneous chip cross-area given by Eq. 30, and  $V_{chip}$  is the instantaneous chip volume given by Eq. 31.

$$A(\theta) = \int h(\theta, \kappa)b(\theta, \kappa)d\kappa \quad \text{Eq. 30}$$

$$V_{chip}(\theta) = \int h(\theta, \kappa)b(\theta, \kappa)S(\theta, \kappa)d\kappa \quad \text{Eq. 31}$$

$$h(\theta, \kappa) = \frac{R_N[1 - \cos(d\kappa)]}{\sin(\kappa)} \quad \text{Eq. 32}$$

$$S(\theta, \kappa) = \sqrt{R_N + \sin^4(\kappa)\tan^2(\alpha)}d\kappa \quad \text{Eq. 33}$$

Where  $b$  is the instantaneous chip width (Eq. 41),  $S$  is the length of an infinitesimal curved cutting-edge segment (Eq. 42), and  $\alpha$  is the nominal helix angle. Figure III-14 shows the schematic of instantaneous specific energy and accumulated energy calculation.

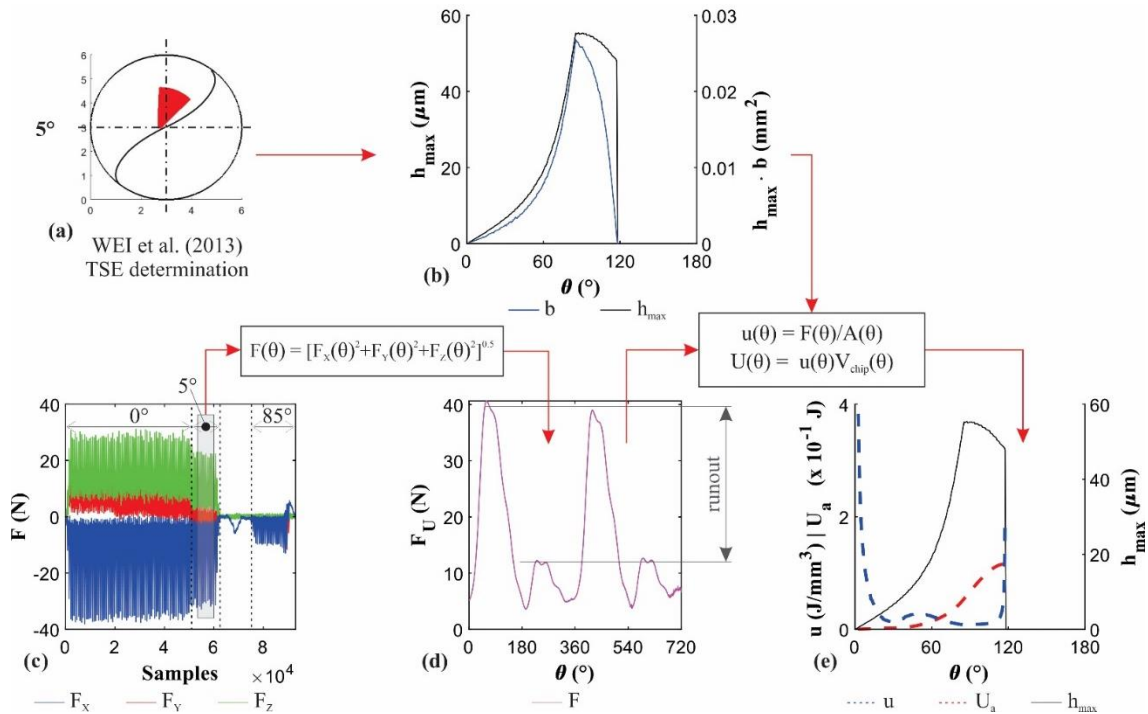


Figure III-14. Instantaneous specific and accumulated energy calculation. (a) TSE; (b) uncut chip geometry; (c) components of the cutting force; (d) resultant cutting force; (e) instantaneous specific energy, accumulated energy, and maximum chip thickness. (Basso et al., 2022).

### III. 3. 1. 3. Results and discussion

The results of the current study are presented in main items: i) analysis of the tool-surface engagement (TSE), ii) roughness and topography of the machined surfaces, and iii) cut mechanism when the tooltip generates the final surface.

#### i) Analysis of the tool-surface engagement (TSE)

Figure III-15a presents the TSE and the uncut chip thickness according to the conditions evaluated ( $0^\circ$ ,  $5^\circ$ , and  $85^\circ$ ). It can be observed that the tooltip of the ball-end tool is involved in the material removal process at lead angles of  $0^\circ$  and  $5^\circ$ . However, the contact with the final machined surface only occurs at  $0^\circ$  (Figure III-15b), affecting the material removal mechanisms and, consequently, the roughness, as debated in Item ii). There is no interaction between the tool tip and the workpiece when milling at  $85^\circ$ , and the effective cutting speed remains close to the nominal value (Figure III-15d).

It is noticeable that the  $\kappa$  (or effective radius) experiences minimal variation for  $0^\circ$  and  $5^\circ$  of inclination, but  $\theta$  is large ( $\sim 0^\circ/50^\circ$  to  $180^\circ$ ). While for  $85^\circ$  inclination is large, and the  $\theta$  variation is minor ( $\sim 180^\circ$  to  $230^\circ$ ). These specific conditions and selected parameters resulted in a consistent maximum chip thickness of  $60 \mu\text{m}$  across all cutting conditions.

When assessing chip formation and the rotation angle ( $\theta$ ), a  $0^\circ$  inclination results in a smooth tool entry and a gradual exit from the workpiece. However, for a  $5^\circ$  inclination,

the exit varies according to the milling mode. Specifically, there is an abrupt entry in up-milling, and in down-milling, there is a gradual exit.

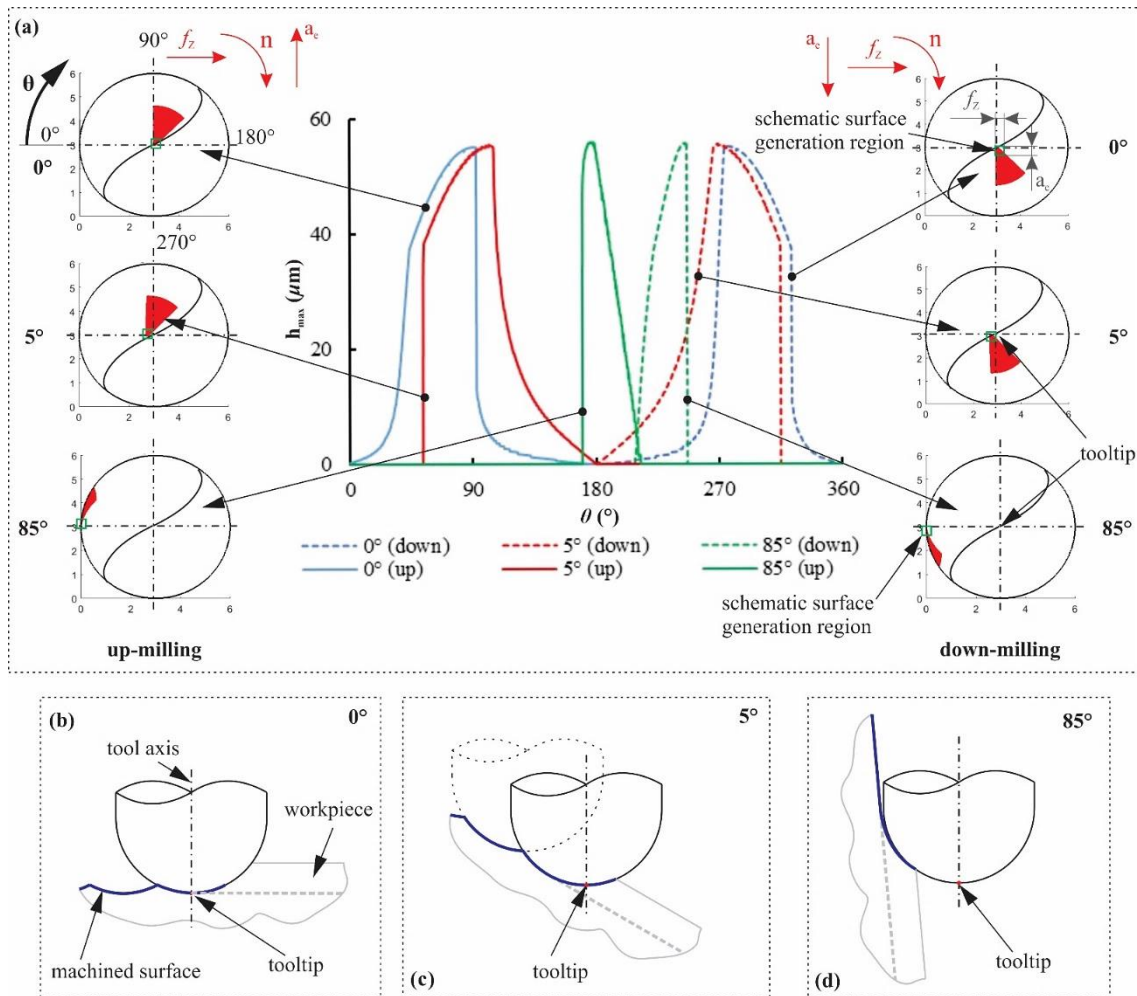


Figure III-15. Maximum uncut chip thickness vs. rotation angle and TSE (Basso et al., 2022).

Figure III-15 shows that the maximum uncut chip thickness ( $h_{max}$ ) used to classify standard milling processes (chip thickness increasing in up-milling and decreasing in down-milling) can not properly classify ball-end milling. The quadrant changes alter the compartment of chip formation. Hence, we recommend defining the milling in relation to surface generation rather than chip thickness variation. In up-milling, the machined surface is created at the end of the cutting, while in down-milling, the final surface is generated at the beginning. These definitions must be taken to evaluate the surface damages of the ball-end milling process, as discussed in sub-section (iii).

### ii) Roughness and topography of the machined surfaces

This section presents and briefly discusses the ANOVA and the surface topography. We delve into examining several hypotheses concerning the cutting mechanisms that might occur in the cases investigated. The ANOVA results considering the TSE conditions and materials investigated are presented in Table III-5 and Figure III-16.

Table III-5. Analysis of Variance (ANOVA) for  $S_z$  (Basso et al., 2022).

Source	Degrees of freedom	Contribution	Sum of squares	Mean of squares	F-value	P-value
<b>Electrolytic copper</b> ( $R^2_{ajs} = 0.843$ )						
Milling mode	1	8.5%	22.74	22.74	5.94	0.051
Lead angle	2	81.4%	218.13	109.06	28.49	0.001
Milling mode x lead angle	2	1.6%	4.29	2.15	0.56	0.598
Error	6	8.6%	22.97	3.83		
Total	11	100.0%				
<b>Annealed AISI H13 steel</b> ( $R^2_{ajs} = 0.831$ )						
Milling mode	1	2.4%	1.76	1.76	1.56	0.259
Lead angle	2	75.7%	55.73	27.86	24.68	0.001
Milling mode x lead angle	2	12.7%	9.38	4.69	4.15	0.074
Error	6	9.2%	6.77	1.13		
Total	11	100.0%				
<b>Hardened AISI H13 steel</b> ( $R^2_{ajs} = 0.951$ )						
Milling mode	1	4.1%	0.50	0.50	9.03	0.024
Lead angle	2	20.0%	2.44	1.22	22.21	0.002
Milling mode x lead angle	2	73.3%	8.96	4.48	81.58	0.000
Error	6	2.7%	0.33	0.05		
Total	11	100.0%				

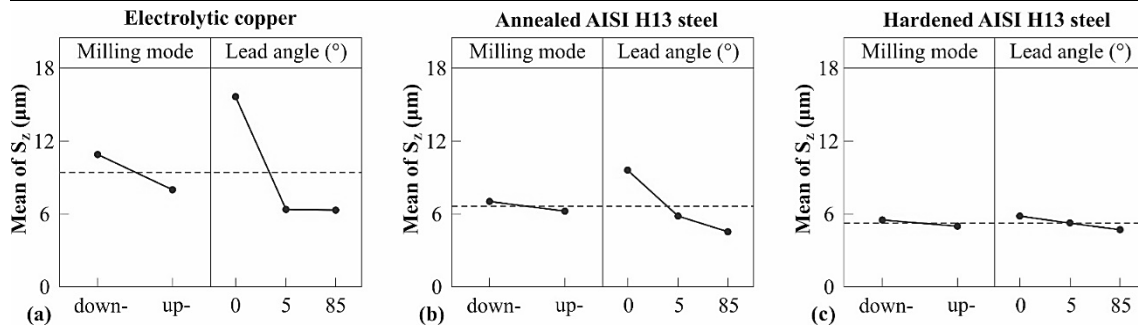


Figure III-16. Main effects for  $S_z$  roughness when milling: (a) electrolytic copper; (b) annealed; (c) hardened AISI H13 steels (Basso et al., 2022).

The ANOVA shows that the inclination (lead angle) is a significant control factor for the maximum height area roughness ( $S_z$ ). Also, different levels of influence were identified according to the workpiece material, with a reduction of the influence of the lead angle on the material's ductility.

Taking into account the theoretical  $S_z$  value of 0.83  $\mu\text{m}$  for the milling parameter used of 6 mm diameter, lateral pass of 0.1 mm, and feed-per-tooth 0.1 mm (Quinsat et al., 2008), the contribution of the lead angle for  $S_z$  on the copper was about 81%, 76% for the annealed H13 steel, and 20% for the hardened H13 steel.

Figure III-17 presents a first analysis of the surface topography. It can be observed that the machined surfaces depend strongly on the elastoplastic behaviour of the material. Electrolytic copper (more ductile) presented the highest  $S_z$  values, while the hardened AISI H13 steel produced the best surface finishing with 5° and 85° inclination angles.

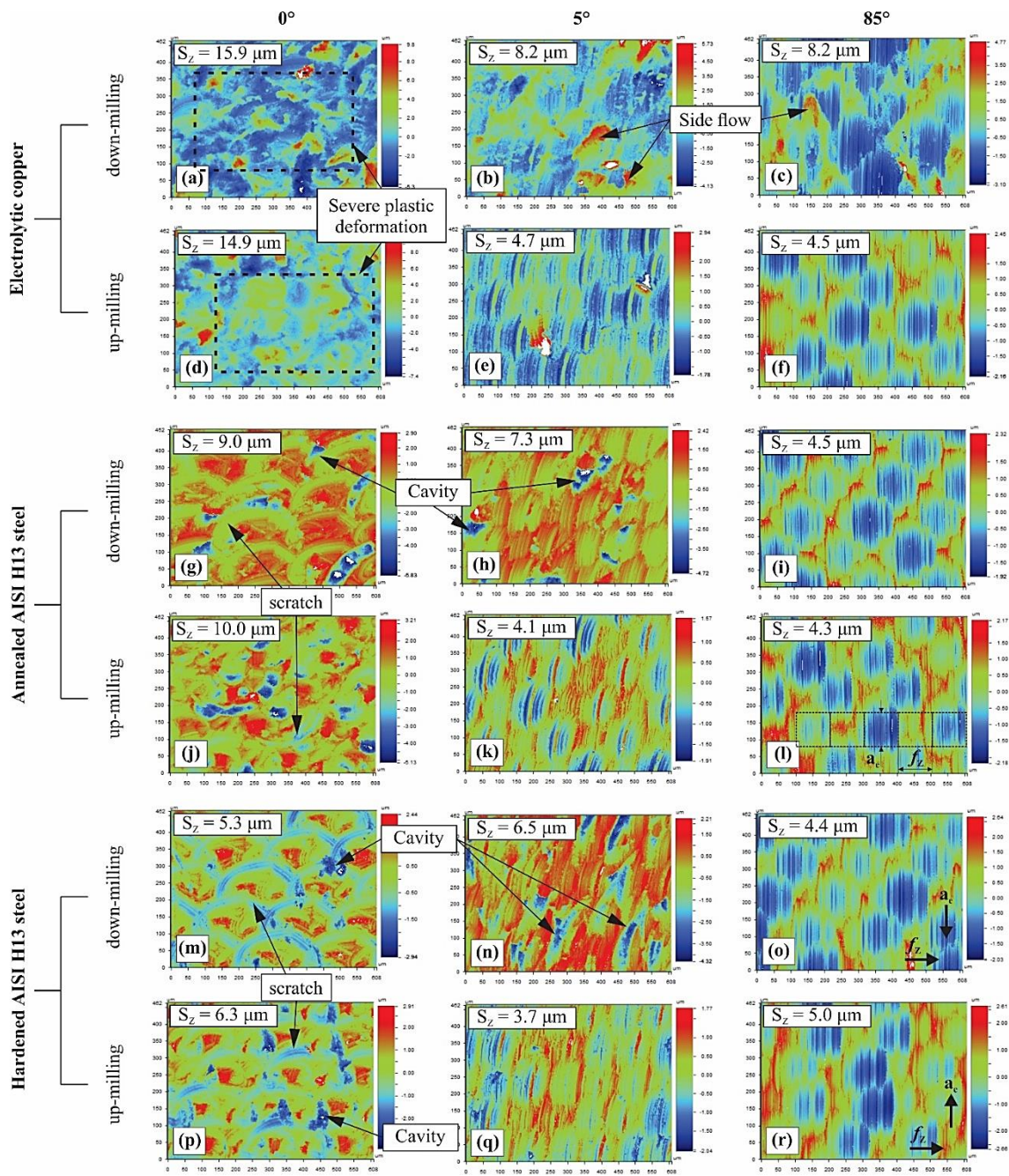


Figure III-17. Confocal images and averaged  $S_z$  values according to workpiece material, milling mode, and lead angle (Basso et al., 2022).

The identification of the influence of the material and its correlation with the roughness allowed us to identify two cutting conditions. First, in  $0^\circ$  lead angle, the highest  $S_z$  values are obtained, mainly because the tooltip generates the final surface. Second, on  $5$  and  $85^\circ$  lead angles, independent of the participation of the tooltip centre and the effective cutting speed, when the tooltip does not generate the final surface, the  $S_z$  values decrease. This cutting mechanism is discussed in-depth in sub-section (iii).

The theoretical  $S_z$  value ( $0.83 \mu\text{m}$ ) was compared to the average value of  $S_z$  (Figure III-17) to identify factors that contribute to the surface roughness. First, it was observed that the real  $S_z$  was approximately 12 times higher with  $0^\circ$ , seven times higher for  $5^\circ$ ,

and 6 times higher for 85° inclination. The divergences between the real  $S_z$  and theoretical are explained by the vibration observed in the machining process and on the inspected surface texture (Figure III-17) and by tool run-out identified on machining force (Figure III-14d) and surface texture (Figure III-17l).

The difference between the best and the worst real  $S_z$  values was from 3.7  $\mu\text{m}$  to 15.9  $\mu\text{m}$ . The ANOVA results showed that the influence of the material and TSE are approximately four times more significant than the tool's run-out to the surface roughness  $S_z$ . This indirectly means that the contact between the material and the tool significantly influences the roughness of free-form milling.

Figure III-17 presents some damages observed on the milled surface, responsible for the increase in the  $S_z$ . Damages were observed in all cases with 0° inclination and with 5°, only in down milling. The damages were characterized according to the literature to understand the phenomena better. The damages identified in Figure III-18 are:

**Severe plastic deformation:** damage characterized by a non-uniform surface texture and a high  $S_z$  value. It is induced by elevated machining force and temperatures. In the case of free-form milling, when the tooltip and vicinities are in contact with the machined surface, the effective tool diameter is small, reducing the effective cutting speed and increasing the machining force by the dominance of the ploughing mechanism.

**Side flow:** characterized as a small burr at the planar machined surface, as depicted in Figure III-18b. It can be formed when the edge extrudes the material to flow to the side of the tool edge (Xu et al., 2017).

**Scratch:** characterized by the marks caused by the centre of the tooltip with a non-linear pattern (Figure III-17 for both H13 steel). Supposedly, the tooltip trajectory should be a straight line. However, because of the tool's run-out and deflection, it has semi-elliptical shapes and is more expressive in hardened materials due to higher cutting forces. The effect is not present when severe plastic deformation is present.

**Cavities:** characterized by the remotion of a portion of material further than the tool edge. This damage was not evident in the copper material, likely due to high ductility.

External damage to the surface can be easily removed from the surface with post-processing by polishing. In contrast, internal damages such as cavities and scratches are more critical. They are more difficult or impossible to remove and thus must be avoided.



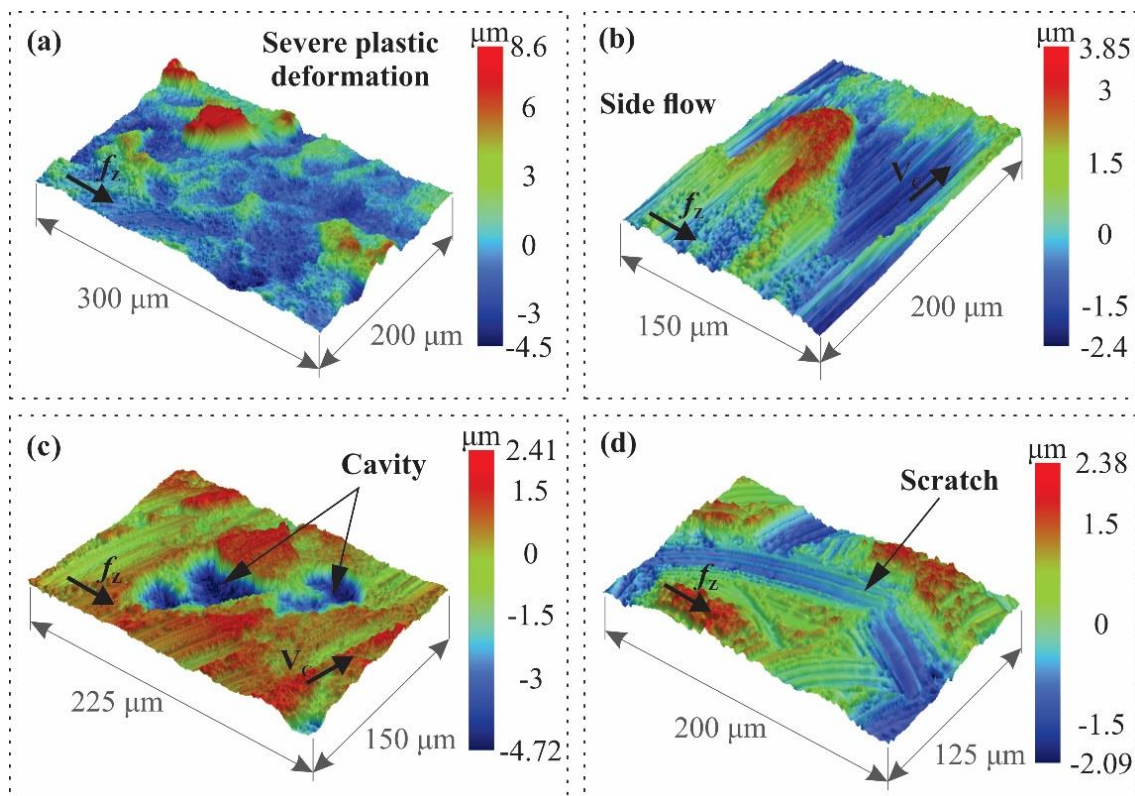


Figure III-18. Damages identified on the machined surfaces: a) severe plastic deformation; b) side flow; c) cavity; d) scratch lead angle at down-milling (Basso et al., 2022).

### iii) Cut mechanism when the tooltip generates the final surface

Summarizing the results obtained with the surface evaluation (ii), it is remarkable that:

- Tooltip participates in the cutting process at a  $5^\circ$  lead angle but does not generate the final surface.
- Considering the measured  $S_z$  values, the material can influence the roughness up to three times and the TSE up to 3.3 times.
- The milling mode (up-milling and down-milling) strongly influenced the roughness produced under TSE of  $5^\circ$  inclination, whereas it has no significant influence with  $0^\circ$  and  $85^\circ$  inclination angles.
- Cavities and stronger scratch marks are present in down-milling.

Considering these statements, it can be assumed that two different cutting mechanisms occurred when milling free-form geometries: **1. Tip-On:** when the tooltip generates the final surface ( $0^\circ$  lead angle). **2. Tip-Out:** when the tooltip does not contact the final surface, even when it is involved in the cut process ( $5^\circ$  and  $85^\circ$  lead angle).

#### 1. Tip-On

Ball-end mills usually do not present a sharp edge at the tooltip but a chisel edge (like a drill bit), as shown in Figure III-13b. In drill bits, the chisel induces an elastoplastic

deformation field that extrudes the workpiece material into the direction of the edges with a higher cutting speed. Likewise, this phenomenon happens in ball-end tools, while the tool moves and rotates, the tooltip compresses the workpiece material, inducing an elastoplastic deformation field that affects the surface. The volume of this deformation field arises with the material ductility, as depicted in Figure III-19.

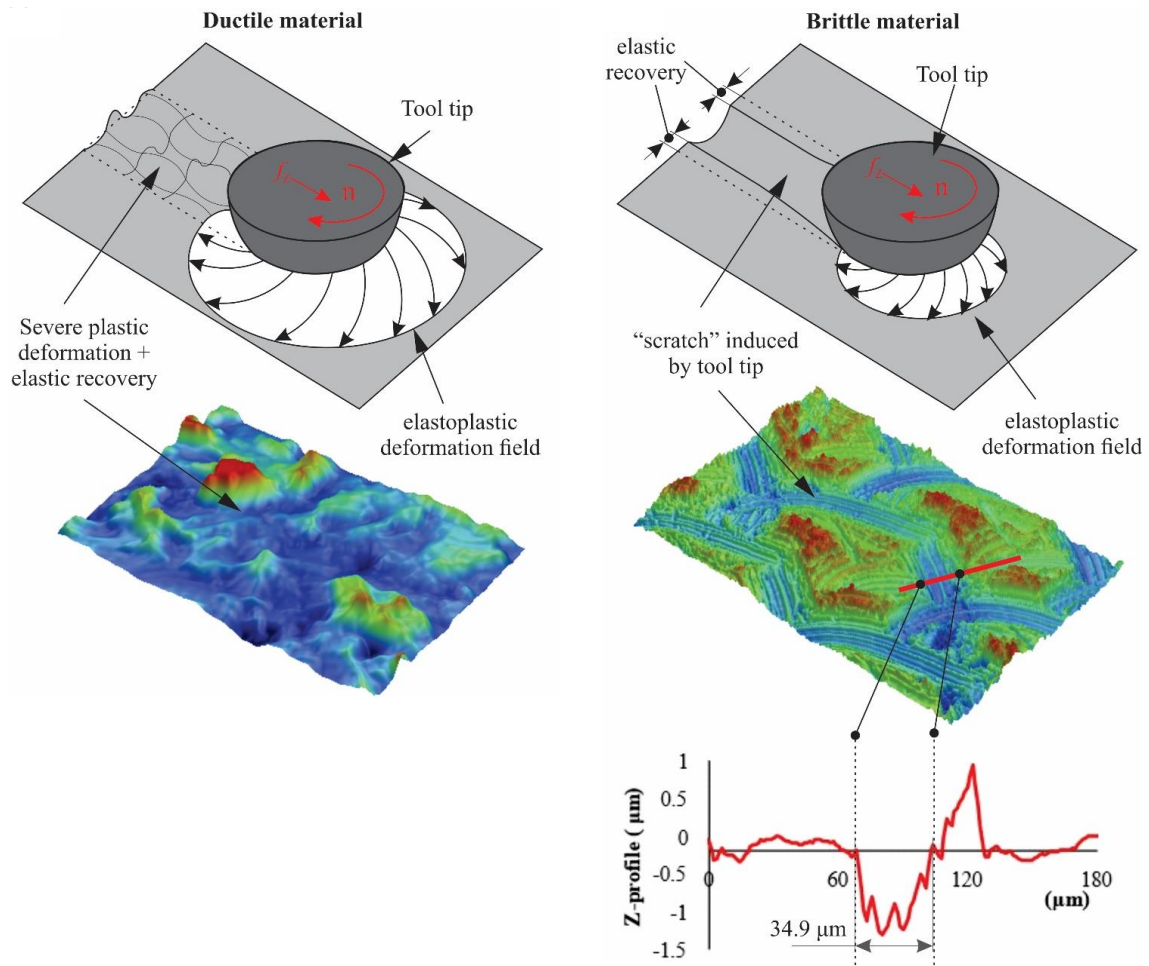


Figure III-19. Tool tip effect on the surface of brittle and ductile materials (Basso et al., 2022).

Harder materials like AISI H13 steel (in a hardened state) have reduced ductility and can not endure large plastic deformations, so the chips generated in the milling process pass through brittle fractures. At the same time, the tooltip scratches the surface due to the very low cutting speed at the tooltip centre and vaccines, as shown in Figure III-19. The scratch width of  $34.9 \mu\text{m}$  is close to the tooltip width (about  $58 \mu\text{m}$ ). The scratch width observed in Figure III-19 is lower than the tooltip width, probably because of the material elastic recovery after the tool's displacement and the ceasing of pressure due to the end of contact. Also, it can be observed that the mark left by the tool centre is not linear as a consequence of the tool deflections induced by the oscillation of the cutting force.

In materials with higher ductility, such as electrolytic copper, the elastoplastic deformation zone beneath the machined surface extends, producing stretched chips and

a plastic-deformed surface. In the region machined with the tooltip centre, no chips are formed, and the tool's flank face promotes severe plastic deformation and temperature increase that lead to thermal softening and material flow, making the tooltip action quite similar to the stir welding process. As a result, the machined surface presents poor quality in terms of surface integrity, as can be seen in Figure III-17a, Figure III-17d, Figure III-18a, and Figure III-19. The average  $S_z$  and the material's hardness were plotted for  $0^\circ$  to evaluate the effect of the tooltip centre according to material (Figure III-20a).

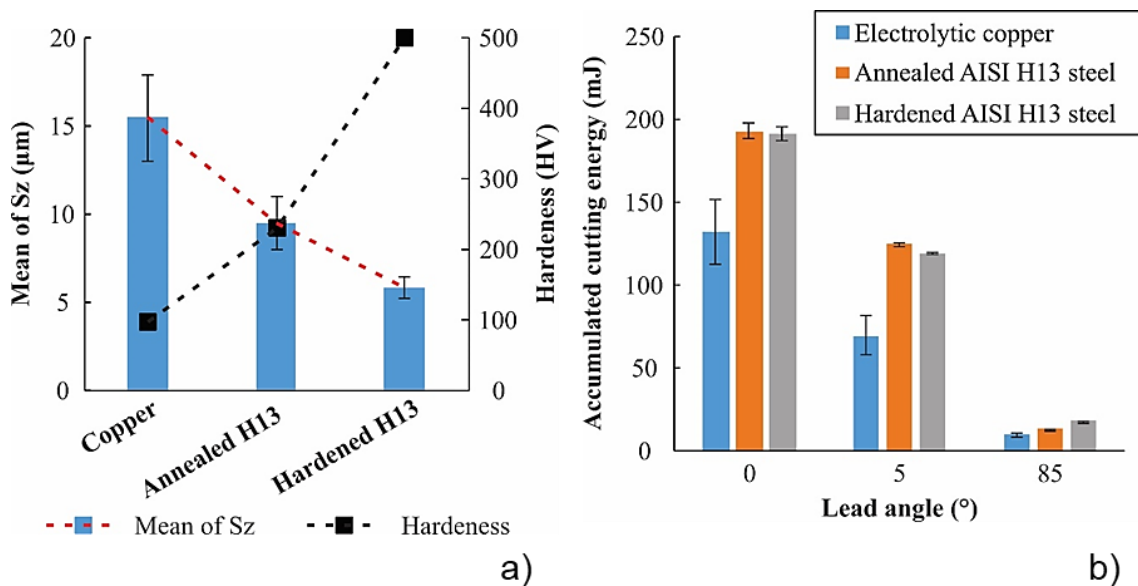


Figure III-20. a) Influence of the ploughing according to the material's hardness (HV) and mean  $S_z$  values ;b) Accumulated cutting energy for down-milling mode versus workpiece materials and tool lead angle. Adapted from Basso et al. (2022).

Figure III-20a shows the ploughing effect according to the material's hardness. It can be observed that the material hardness is inversely related to surface roughness, and the high plasticity of the workpiece favours the ploughing.

## 2. Tip-Out

Observing that for the lead angle of  $85^\circ$ , the surface texture presented the characteristic intermittent marks of the ball-end milling process, highlighting only the tool run-out, which might be responsible for increasing the  $S_z$  value (Figure III-17l).

It can be highlighted that at a lead angle of  $5^\circ$ , the tooltip participates in the cutting process but not in the final surface generation. In this case, the milling mode (up-milling and down-milling) influenced the roughness. Contrary to the literature, the  $S_z$  values for down-milling were nearly twice as high as the up-milling cases, and the surface texture presented cavity damages (Figure III-17). This behaviour occurred for all materials evaluated.

The cutting kinematics were examined for both milling modes to comprehend this phenomenon. First, was analysed the down-milling mode (Figure III-21a) to verify the final surface generated at the end of the tool edge action. Then, the up-milling mode is investigated, evaluating the surface generated by the start of edge action (Figure III-21b).

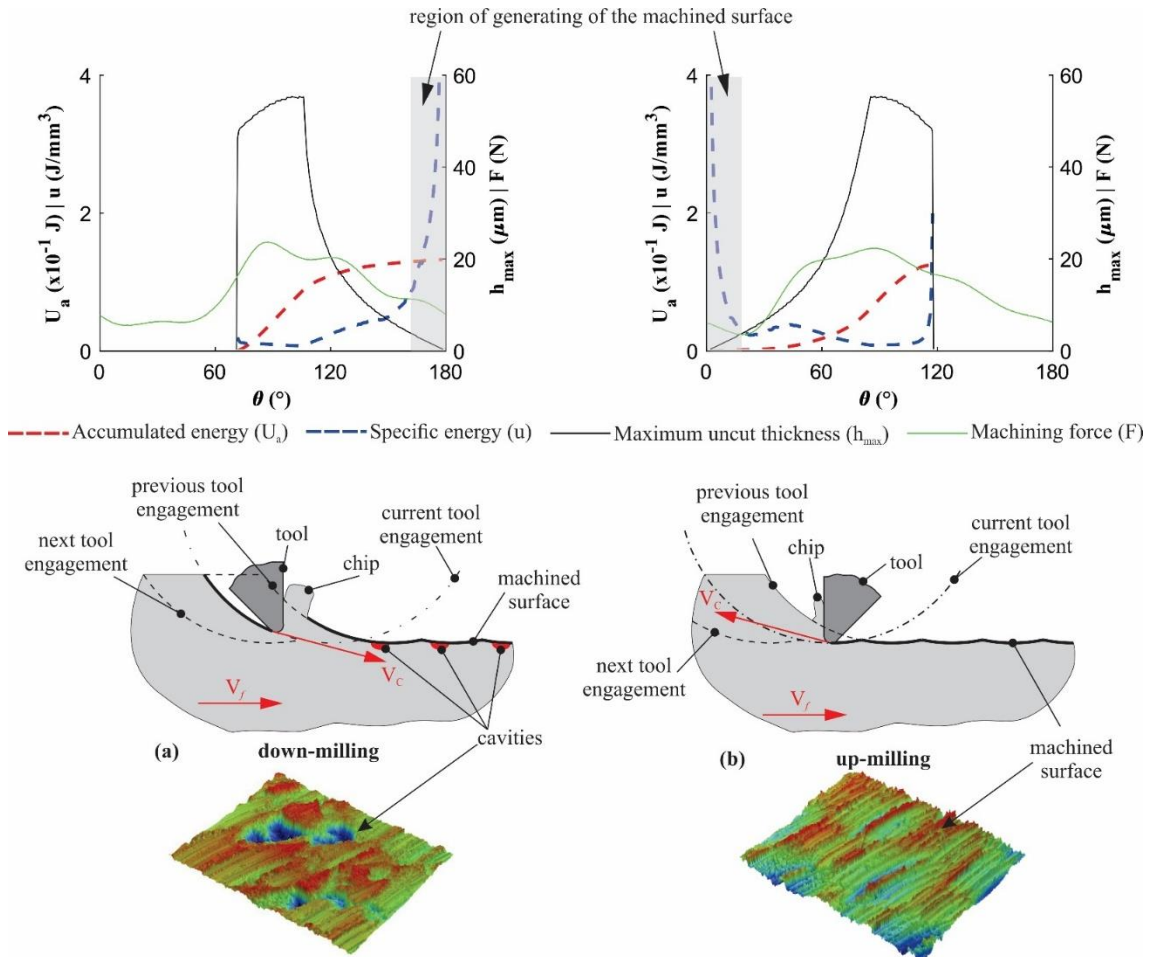


Figure III-21. Accumulated cutting energy, specific cutting energy, machining force, and maximum uncut thickness versus rotation angle, and scheme for surface generation in (a) down-milling and (b) up-milling. Results for annealed AISI H13 steel milled at  $5^\circ$  lead angle (Basso et al., 2022).

The analysis of cutting energy was carried out to enhance the comprehension of the phenomena associated with machining kinematics in both up-milling and down-milling modes.

Figure III-20b presents the results of the calculated accumulated energy at the end of the tool edge action. The highest accumulated energy for down-milling at lead angles  $0^\circ$  and  $5^\circ$  was observed, where the increase can be associated with the surface cavities. The damages of these cavities increased the  $S_z$  about two times if compared with the up-milling for the respective materials. With the exception of a  $0^\circ$  lead angle, these types of damages are not observed in up-milling. This is because the final machined surface is formed at the end of the cutting when the accumulated energy is minimal. In the case

of the lead angle of  $85^\circ$ , the increased effective cutting speed reduces the accumulated energy, likely due to lower machining forces and a lack of significant damages, approximating the roughness to theoretical values (Figure III-17).

In summary, it was observed that the *Tip-Out* does not interfere significantly with the  $S_z$  (lead angle  $85^\circ$ ) if the accumulated energy is low mechanism and that the surface damage on the final machined surface (especially in down-milling) increases with the cutting energy.

### III. 3. 1. 4. Conclusions

This study addressed the influences of the tool-surface contact and the properties of the machined materials on the surface topography during free-form milling. The main conclusions are outlined as follows:

- The cutting tool edge movement analysis highlighted that the classification of free-form milling modes in terms of surface generation instead of chip thickness variation is more accurate. Classify in up-milling when the machined surface is generated at the beginning of the cutting action and down-milling when it is produced at the end.
- In ball-end milling, the engagement between the tool and surface can occur in three cases. The first is when the tooltip centre produces the final surface. The second is when the tooltip takes part in the material removal but not with the final surface. And thirdly, when the tooltip centre is out of the cutting. Therefore, this research identifies two distinct mechanisms for cutting, named *Tip-On* and *Tip-Out* of the final surface, which allows for identifying the surface quality after milling.
- The surface machined with the tooltip centre presented several damages due to the ploughing mechanism dominance (*Tip-On*), with a roughness 18 times higher than the theoretical  $S_{z,theoretical}$  value. Otherwise, the average  $S_z$  was lower with the *Tip-Out* mechanism, but still, it was seven times higher than the theoretical value due to the tool run-out identified. Nevertheless, the tool contact is about four times more significant than the tool run-out on the surface roughness in ball-end milling of free-form surfaces.
- The kinematics analyses show that high accumulated energy occurs in down-milling mode at the end of the tool action, and it produces cavities that are hard to remove in post-processing operations and can lead to higher form errors. Therefore, up-milling must be preferred to produce better surface finishing.

### **III. 3. 2. Ball-end tooltip deflection according to CWE**

As presented in Chapter II, the stiffness of the components involved in the milling process plays an important role in the final quality of the surface, especially regarding form deviations with ball-end tooltips. The sources of deviation come from several features of the process. So, to improve the understanding, it is common to investigate, separately, the influence of specific features like the cutting forces and the rigidity of the components involved, like the set tool-holder, the clamp system, or the part stiffness.

In this study, the form error produced by a non-conventional ball-end tooltip with double radii was investigated to improve the understanding of the finishing process by this kind of circle-segment end mill. Thus, the finishing operation of a rigid block of Inconel® 718 (forged and precipitated) was conducted under different cutting conditions and CWE produced by different tool inclinations, evaluating the form deviation and simulating what happens to the tool in stable free-form milling.

#### **III. 3. 2. 1. Experimental procedure**

A non-conventional ball-end tooltip typically used in the finishing process of complex thin-walled parts such as blades and BLISKs was selected to study the surface deviation produced by the tool. The tool evaluated is an oval barrel tool with a recommendation for side milling (Figure II-16a). This condition favours the tool's deflection due to the slender ratio and cutting force directions. The tool used has a handle of 10 mm diameter, four flutes, a constant helix angle of 30°, a minor tool radius of 2 mm, and a major tool radius of 85 mm, as depicted in Figure III-22a. Figure III-22b presents the top view of the tooltip, depicting the cutting-edge changes with the effective cutting radius and the constant helix angle. The tool material is a micrograin solid carbide with 10% Co coated with multilayer TiSiN (3800 HV 0.05).

The tools were mounted in a high-torque toolholder with a 40 mm cantilever, presetted on a Zoller® SmartCheck 600. To minimize the effect of the part and holding system and mitigate the effect of the CWE on the set tool-holder rigidity, a rigid block of forged and precipitated Inconel® 718 ( $49.7 \pm 1.2$  HRC) was selected as a specimen. The block was semifinished (squared and planned) to minimize possible deviations using a 20 mm end mill in a downward zig strategy, leaving final dimensions of 150 x 87 x 45 mm. For the finishing experiments, 72 flat regions (45 x 7 mm) were machined in sets of 12 using both sides of the block (one clamping fixture for CWE), evaluating all cutting parameters selected for each tool inclination. Figure III-22d presents the experimental schematic of the workpiece and CAM programming.

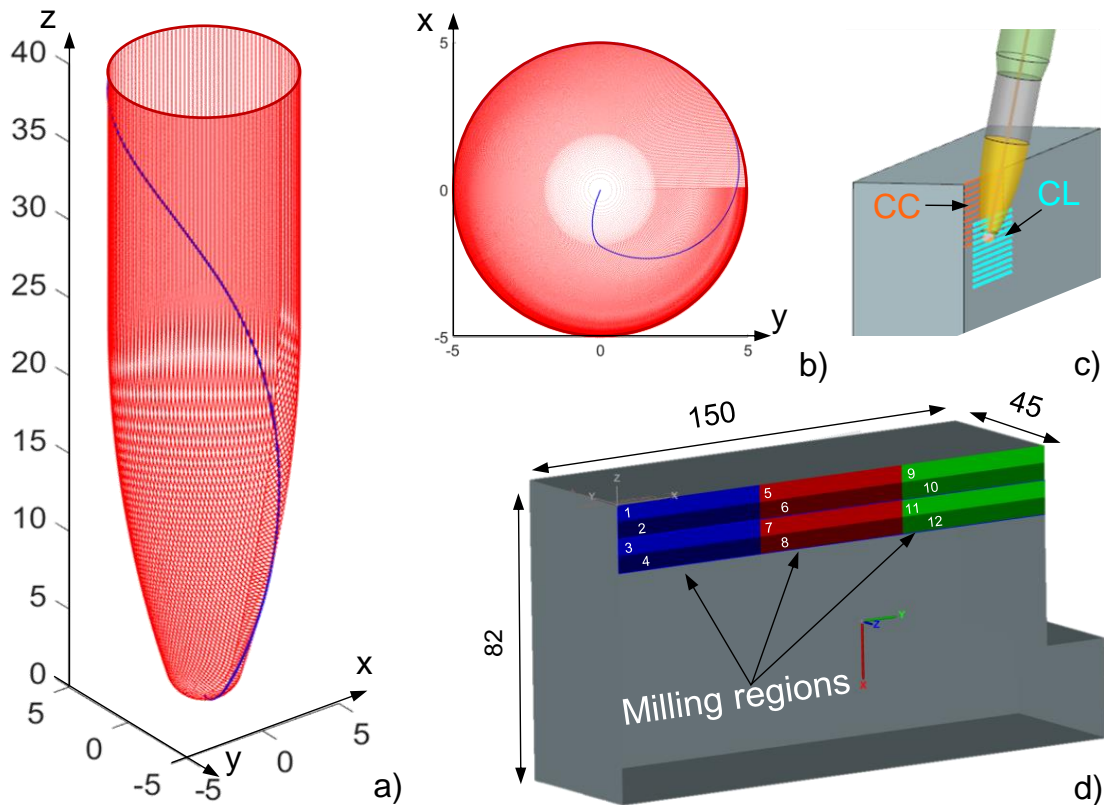


Figure III-22. Tool and workpiece schematics: a) oval barrel tool; b) tool top view; c) CAM programming schematic; d) workpiece dimensions and milling regions.

The different radii of the tool, together with the major radius centre out of the tool spinning axis, allowed a higher modification of the CWE engagement and effective cutting speed with the tool tilting, at the same time that the flat milling condition and constant tilting allowed the evaluation of the cutting force that causes form error mainly by the tool deflection.

Three levels of tool tilt (5, 10, and 15 tilt angles) were selected according to the CWE previously evaluated, taking into account the minimum and maximum effective radius and respective cutting speeds of the major tooltip radius (85 mm). The higher tilt angle was selected according to the minimum effective cutting speed with the bigger tool radius and the minimum tilting to maximize the cutting speed, which was close to the nominal value (related to the tool handle speed). The third tilt was the middle value of inclination that did not represent the average cutting speed of the extreme tilting angles selected, thus avoiding a linear analysis.

The experiments were conducted in a 5-axis multitasking centre Ibarria THR16. The toolpath was programmed using Open Mind hyperMILL<sup>®</sup> CAM software, guaranteeing the referencing system with verification of the toolpath on the virtual environment. The force data was obtained using an OROS NV Gate acquisition software together with an OROS OR35 signal analyser, a Kistler<sup>®</sup> 9255B dynamometer ( $\sim 7.9$  pC/N for  $F_x$  and  $F_y$ , and  $\sim 3.9$  pC/N for  $F_z$ ) and a Kistler<sup>®</sup> 5017B amplifier under 16384 sampling rate. The

force signals were treated individually using Matlab® 2021 software, calculating the resultant force and discarding each region's first and last path, thus evaluating the central tool paths where a more stable cutting condition is present, improving the process analysis and the statistical rigour.

The workpiece referencing was done using the machine presetter Renishaw PMP-600R with a ruby probe with a nominal diameter of 6 mm (A5000-3709), which was also used for in situ measurement of the part before and after the finishing process. As reported by (Duan et al., 2015), methods that measure the tool deflection in the finishing of free-form shapes are difficult because sometimes the CL points are under the surface, making it impossible to measure. Thus, measuring the surfaces before and after the milling process tends to minimise the measurement uncertainty by nullifying errors inherent to the machine and clamping conditions' variations.

For the finishing operation, cutting speeds from 20 to 40 m/min and  $f_z$  ranging from 0.02 to 0.04 mm/tooth were selected, as recommended by the toolmakers. Also, HPC was used within 80 bar of pressure, as depicted in Figure III-23b. The milling parameters evaluated were: 3 levels of tilting angle, 3 levels of cutting speed, four levels of feed-per-tooth, 2 levels of lateral depth of cut ( $a_e$ ), and a constant depth of cut ( $a_p$ ), all experiments under down milling condition. The experimental parameters and their levels are presented in Table III-6.

Table III-6. Experimental parameters and their levels.

Tilt (°)	$V_c$ (m/min)	$f_z$ (mm/z)	$a_e$ (mm)	$a_p$ (mm)
5	20	0.020	0.1	1
10	30	0.026		
15	40	0.003	0.2	
		0.040		

Besides the deviation measured, the central region of each region with dimensions of 5 × 5 mm was accessed using a confocal microscope Leica® DCM3D (as depicted in Figure III-23a), with data treatment through Leica® Map 6.2 software. These were the same regions used to measure in-process deviations, making it possible to identify and correlate more complex problems, if present, during the milling process.

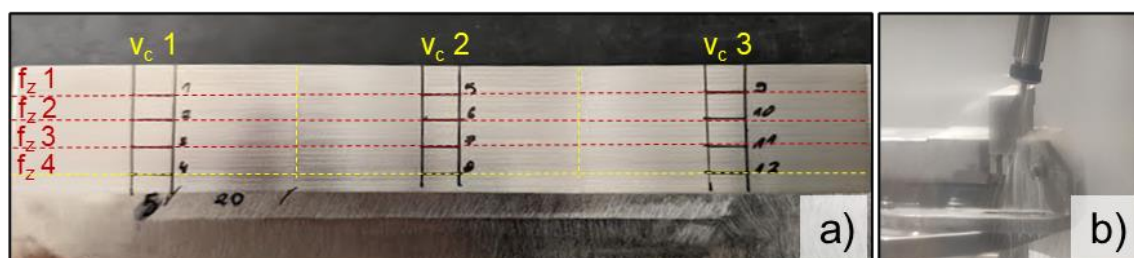


Figure III-23. Milled regions according to cutting parameters schematic and inspection regions.



For statistical analysis of the results and the influence of the tool tilt angle with the force and roughness obtained, Minitab® 21 software was used, performing a full factorial analysis of the cutting parameter factors (Table III-6). After that, the tool deflection was simulated using Siemens NX (Nastran) software, considering a 40 mm cantilever and the measured cutting forces. Two tool designs were simulated; the first is the usual solid dome of the tool, and the second one considers the real cutting edges of the tooltip obtained by reverse engineering. Finally, a regression model is presented to quantify and compensate for the deviation caused by the tool deflection on the surface deviation according to the tilt angle used.

### III. 3. 2. 2. Results and discussion

Hereafter are presented the results obtained. First, the contact involved under the 3 tilting conditions and 2 lateral depths of cut (Figure III-24a) is introduced, followed by the measurement of the deviations (Figure III-25). After that, the measured components of the cutting force and the resultant cutting force are presented (Figure III-26). Lastly, the roughness  $R_a$ ,  $R_z$ ,  $S_a$ , and  $S_z$  of the surfaces, measured in the feed direction, is presented (Figure III-27).

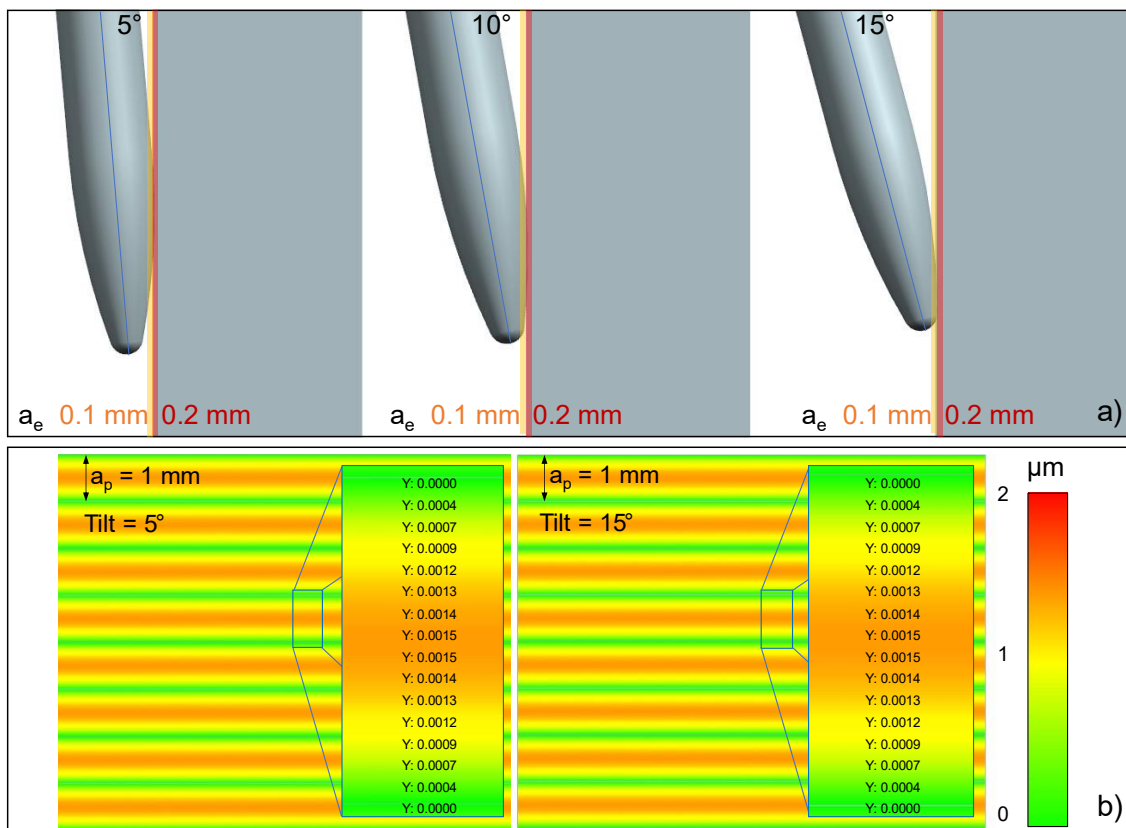


Figure III-24. a) CWE according to the tool tilting, b) simulated crisp height.

As depicted in Figure III-24b, the final surface aspect, ruled by the crisp heights on the cross-feed direction, did not change with the tilt angle. It happens because the same tool

radius and depth of cut ( $a_p$ ) generate the final surfaces. However, during the milling process, intermediary steps can remove more or less material and change the stock between passes, as in the case of the  $15^\circ$  tilt angle, where the minor radius acts in the cut but does not form the final surface, as exemplified in Figure III-24a where the same pattern and roughness is observed, an indication that only the major radius act in the cut for the small lateral depth of cut selected  $a_e$ . This can assist in justifying roughness and deviation patterns together with the effective cutting radius and measured forces.

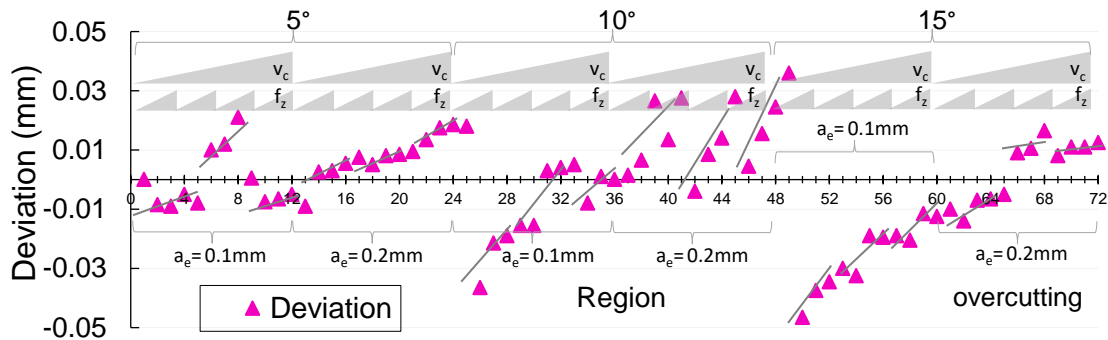


Figure III-25. Surface deviation according to cutting parameters and tool tilting.

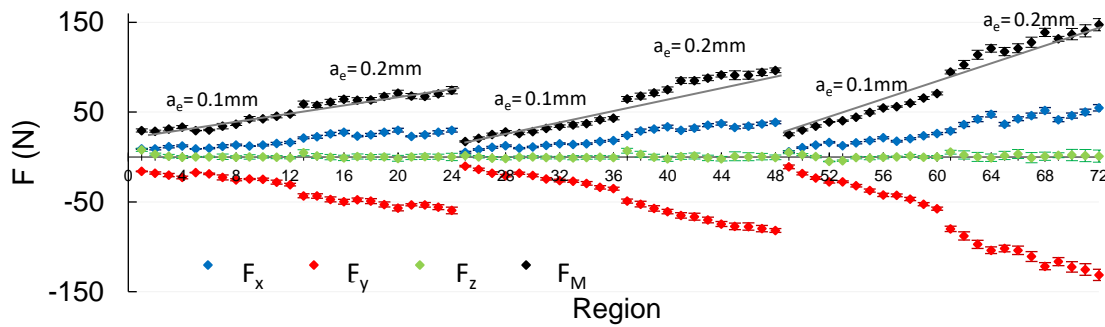


Figure III-26. Resultant cutting forces and components according to cutting parameters and tool tilting.

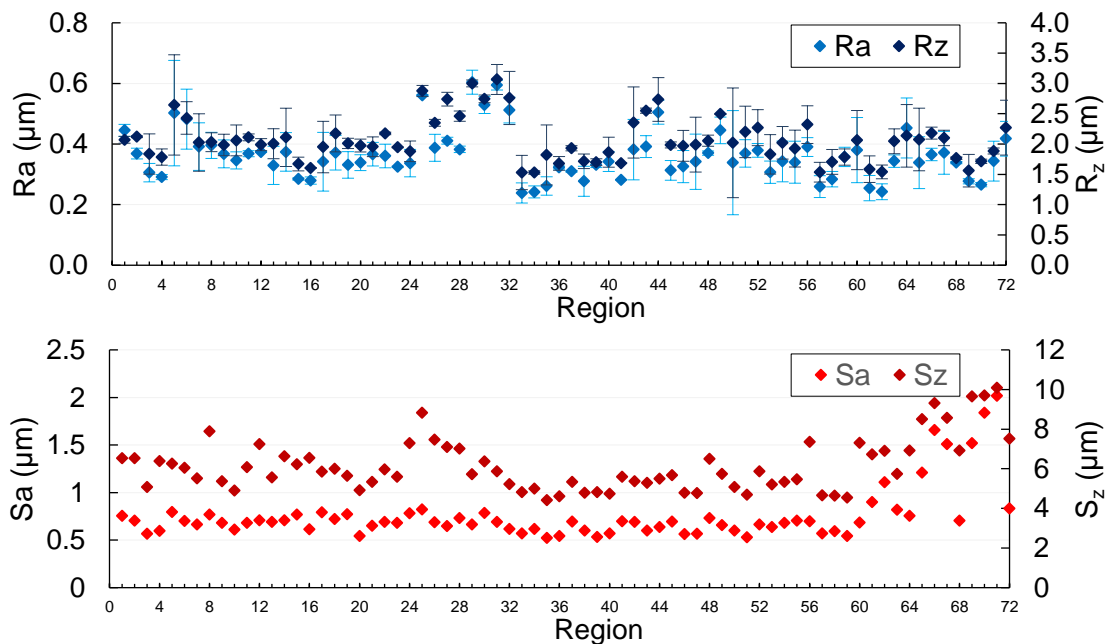


Figure III-27. Roughness Ra, Rz, Sa, and Sz of each region.

The first thing that can be seen when analysing the milling process results is that the deviation pattern changes with the milling condition. It seems to be more influenced by the lateral depth of the cut and tilting angle. Also, a clear pattern of slight deviation increase can be seen for almost all samples with the feed per tooth increase, with a clear presence of blocks. Likewise, the slope pattern of deviation for each tilt angle seems to have a relation with the cutting force, being higher for 15° than 10° and 5°.

The cutting force results show that the dominant component is the  $F_y$ , followed by the  $F_x$ , with a minor influence of  $F_z$ , a characteristic similar to peripheral milling with end mills. This characteristic justifies the classification of oval barrel tools as circle-segment end-mills by some toolmakers. It also can be seen that the cutting force increases with the cutting speed, feed per tooth, and mostly by the lateral depth of cut for all tilting conditions. On the other hand, the measured roughness results did not present clear patterns. Thus, a statistical analysis (full factorial analysis) of all three results was conducted to identify the factors, cross-relations, and their significance.

Table III-7 presents the results of a full factorial analysis of the resulting cutting force, assuming the influence of the cutting force components and the roughness Ra and Rz as covariants.

Table III-7. Analysis of Variance of the Resulting Cutting Force.

Source	Degrees of freedom	Contribution	Sum of squares	Mean of squares	F-Value	P-Value
<b>Model</b>	36	99.97%	82090.3	2280.28	3391.11	0.000
<b>Covariates</b>	5	99.52%	133.9	26.78	39.82	0.000
<b><math>F_x</math></b>	<b>1</b>	<b>96.06%</b>	<b>7.2</b>	<b>7.21</b>	<b>10.73</b>	<b>0.002</b>
<b><math>F_y</math></b>	<b>1</b>	<b>3.40%</b>	<b>45.3</b>	<b>45.25</b>	<b>67.30</b>	<b>0.000</b>
$F_z$	1	0.04%	0.1	0.07	0.10	0.757
Ra	1	0.00%	0.7	0.69	1.02	0.320
Rz	1	0.01%	0.1	0.15	0.22	0.641
<b>Factors</b>	8	0.23%	128.5	16.06	23.88	0.000
<b>Tilt</b>	<b>2</b>	<b>0.11%</b>	<b>56.5</b>	<b>28.26</b>	<b>42.03</b>	<b>0.000</b>
$V_c$	2	0.02%	1.7	0.83	1.24	0.303
$f_z$	3	0.09%	14.0	4.68	6.95	0.001
$a_e$	1	0.00%	2.5	2.54	3.78	0.060
<b>2-Way Interactions</b>	23	0.22%	184.5	8.02	11.93	0.000
<b>Tilt*<math>V_c</math></b>	<b>4</b>	<b>0.10%</b>	<b>34.2</b>	<b>8.54</b>	<b>12.70</b>	<b>0.000</b>
Tilt* $f_z$	6	0.02%	4.6	0.76	1.14	0.362
<b>Tilt*<math>a_e</math></b>	<b>2</b>	<b>0.07%</b>	<b>44.8</b>	<b>22.38</b>	<b>33.28</b>	<b>0.000</b>
$V_c$ * $f_z$	6	0.01%	5.2	0.86	1.28	0.291
<b><math>V_c</math>*<math>a_e</math></b>	<b>2</b>	<b>0.02%</b>	<b>12.5</b>	<b>6.27</b>	<b>9.32</b>	<b>0.001</b>
$f_z$ * $a_e$	3	0.00%	2.6	0.87	1.29	0.292
<b>Error</b>	35	0.03%	23.5	0.67		
<b>Total</b>	71	100.00%				

As expected, the full factorial analysis confirmed that the component force normal to the plane ( $F_y$ ) is more significant on the resultant cutting force followed by the feed direction component ( $F_x$ ), and no significant influence by the  $F_z$  component can be assumed for

both linear roughness results. Among the cutting parameters evaluated, the tilt was the one with the most influence, followed by the interaction of the lateral depth of cut ( $a_e$ ) with cutting speed. It can be correlated to the chip thickness formation that produces more resistance on the cutting, increasing forces and deviations. Feed-per-tooth and lateral depth of cut also present significant influence individually, different from cutting speed, which only presented influence associated with other cutting parameters.

Table III-8 presents the results of the full factorial analysis of the cutting parameters on the surface deviation.

Table III-8. Analysis of Variance of the Surface Deviation.

Source	Degrees of freedom	Contribution	Sum of squares	Mean of squares	F-Value	P-Value
<b>Model</b>	31	91.59%	0.018599	0.000600	14.06	0.000
<b>Factors</b>	8	76.06%	0.015446	0.001931	45.24	0.000
<b>Tilt</b>	<b>2</b>	<b>15.38%</b>	<b>0.003122</b>	<b>0.001561</b>	<b>36.58</b>	<b>0.000</b>
<b><math>V_c</math></b>	<b>2</b>	<b>12.50%</b>	<b>0.002539</b>	<b>0.001269</b>	<b>29.74</b>	<b>0.000</b>
<b><math>f_z</math></b>	<b>3</b>	<b>5.93%</b>	<b>0.001204</b>	<b>0.000401</b>	<b>9.41</b>	<b>0.000</b>
<b><math>a_e</math></b>	<b>1</b>	<b>42.26%</b>	<b>0.008581</b>	<b>0.008581</b>	<b>201.04</b>	<b>0.000</b>
<b>2-Way Interactions</b>	23	15.53%	0.003153	0.000137	3.21	0.001
<b>Tilt*<math>V_c</math></b>	<b>4</b>	<b>2.83%</b>	<b>0.000574</b>	<b>0.000144</b>	<b>3.36</b>	<b>0.018</b>
<b>Tilt*<math>f_z</math></b>	<b>6</b>	<b>3.73%</b>	<b>0.000757</b>	<b>0.000126</b>	<b>2.96</b>	<b>0.018</b>
<b>Tilt*<math>a_e</math></b>	<b>2</b>	<b>5.45%</b>	<b>0.001106</b>	<b>0.000553</b>	<b>12.96</b>	<b>0.000</b>
<b><math>V_c</math>*<math>f_z</math></b>	6	0.36%	0.000074	0.000012	0.29	0.940
<b><math>V_c</math>*<math>a_e</math></b>	<b>2</b>	<b>2.76%</b>	<b>0.000561</b>	<b>0.00028</b>	<b>6.57</b>	<b>0.003</b>
<b><math>f_z</math>*<math>a_e</math></b>	3	0.40%	0.000081	0.000027	0.64	0.596
<b>Error</b>	40	8.41%	0.001707	0.000043		
<b>Total</b>	71	100.00%				

The analysis of the influence on the surface deviation highlights that all the factors evaluated are significant, with second-level interaction significance for all cases with the exception of the combination of cutting speed with feed-per-tooth and the feed-per-tooth with depth-of-cut. Supposedly, each parameter variation modifies the deviation pattern, and it can be associated with the combination of factors and their main effects. The tilt increase tends to reduce the deviation while the other parameters increase, as can be seen in the main effects chart for the surface deviation (Figure III-28).

The analysis of the variance of the cutting parameters on the linear roughness results ( $R_a$  and  $R_z$ ) did not allow the identification of any significant influence with the cutting factors, highlighting the importance of studies related to the ICE element and surface modelling for better understanding.

Figure III-28 presents the Pareto results summarizing the three statistical analyses conducted together with the main effects plots for the resulting cutting force analysis and the surface deviation, where an inverse relation of the factor effects on each response can be noted. It is justified by the inverse relation between the resulting cutting force and the deflection of the tool that causes surface deviation.

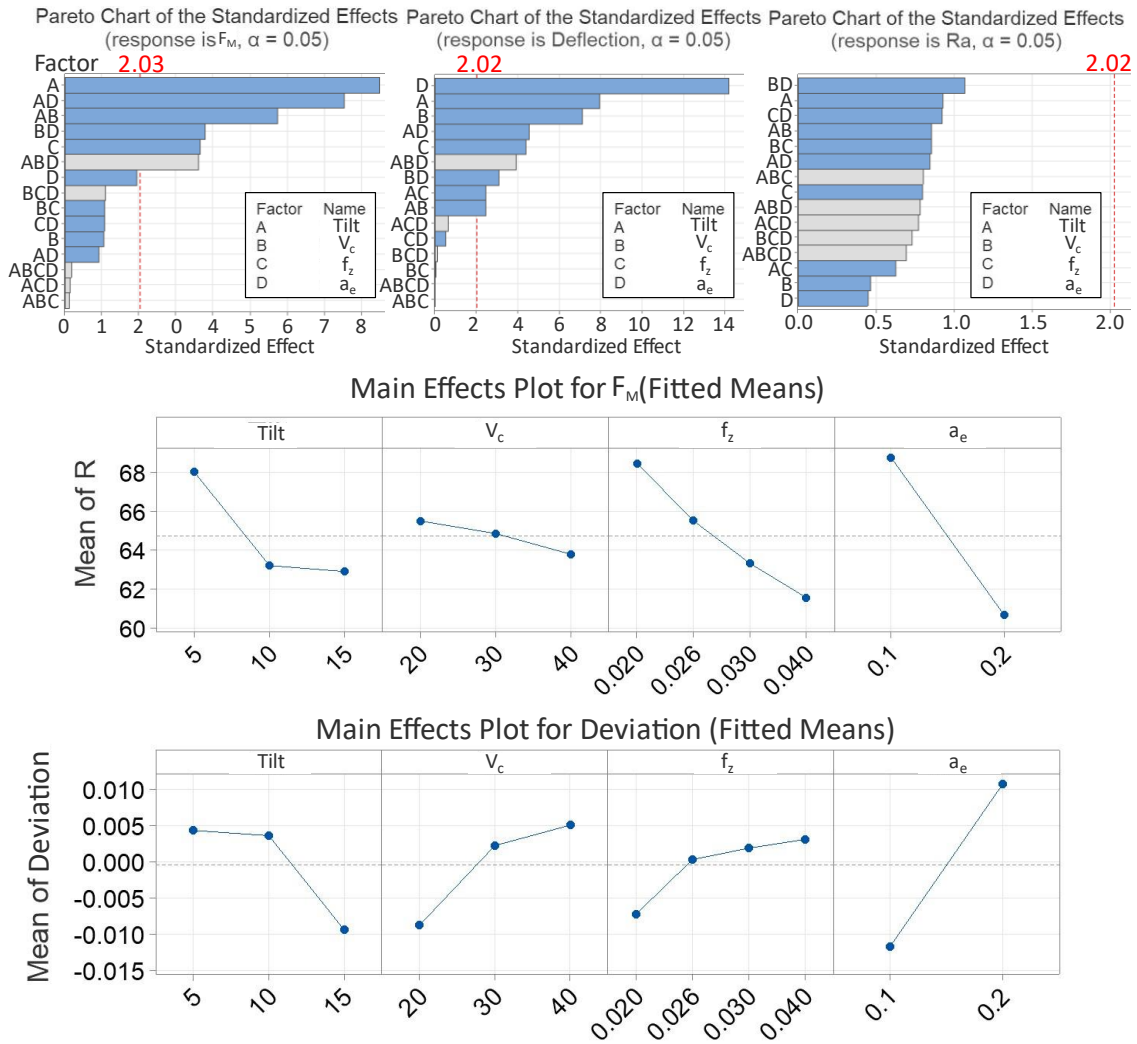


Figure III-28. Pareto chart response for resultant cutting force, surface deviation, and roughness, and main effect plots of resultant cutting force and surface deviation.

Surprisingly, the covariance analysis of the linear roughness results on the feed direction ( $R_a$  and  $R_z$ ) against the surface roughness ( $S_a$  and  $S_z$ ) showed no significance. Also, marks between different passes on all measured topography images could be identified, but with different depths, ranging from 4.6 to 10.1  $\mu\text{m}$ . It also can be observed that the distance between crisp or valleys is spaced by a depth of cut, as depicted in Figure III-29.

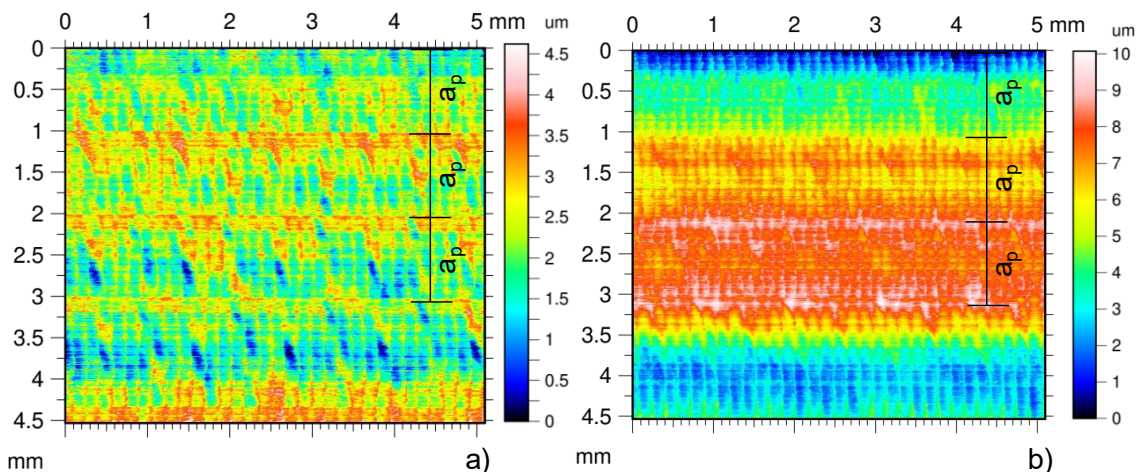


Figure III-29. Topography of lower and higher surface roughness: a) Region 36; b) Region 71.

Thus, a variance analysis was conducted to investigate if there is a relation between the surface roughness and the surface deviation and to identify the factors with significance. The summarized results are depicted in Table III-9.

Table III-9. Analysis of Variance of the Surface Roughness (Ra).

Source	Degrees of freedom	Contribution	Sum of squares	Mean of squares	F-Value	P-Value
Model	32	82.08%	4.90425	0.153258	5.58	0.000
Covariates	1	3.69%	0.00768	0.007684	0.28	0.600
Deviation	1	3.69%	0.00768	0.007684	0.28	0.600
Factors	8	37.36%	2.11854	0.264817	9.64	0.000
<b>Tilt</b>	<b>2</b>	<b>31.21%</b>	<b>0.52302</b>	<b>0.261512</b>	<b>9.52</b>	<b>0.000</b>
$V_c$	2	0.04%	0.02807	0.014033	0.51	0.604
$f_z$	3	5.98%	0.17866	0.059553	2.17	0.107
$a_e$	1	0.13%	0.06973	0.06973	2.54	0.119
2-Way Interactions	23	41.03%	2.45154	0.106589	3.88	0.000
<b>Tilt*<math>V_c</math></b>	<b>4</b>	<b>3.50%</b>	<b>0.24530</b>	<b>0.061325</b>	<b>2.23</b>	<b>0.083</b>
Tilt* $f_z$	6	5.35%	0.30432	0.050720	1.85	0.115
<b>Tilt*<math>a_e</math></b>	<b>2</b>	<b>22.61%</b>	<b>1.21717</b>	<b>0.608584</b>	<b>22.16</b>	<b>0.000</b>
$V_c$ * $f_z$	6	1.39%	0.07619	0.012698	0.46	0.832
$V_c$ * $a_e$	2	4.17%	0.25858	0.129291	4.71	0.015
$f_z$ * $a_e$	3	4.01%	0.23953	0.079844	2.91	0.047
Error	39	17.92%	1.07095	0.02746		
Total	71	100.00%				

The analysis of the variance showed no covariance between the surface roughness and the surface deviation, expressing process stability for the parameter window selection. The tilt angle was the unique individual factor that influenced the surface roughness. It happens probably because of the different engagement with the surface under a constant depth of cut ( $a_p$ ), which results in 3 different levels of marks. Still, it is important to highlight that these texture variations were inferior to 10  $\mu\text{m}$ , suitable for aeronautical application according to Klocke et al. (2015), and controlling the surface deviation can produce complete complex surfaces under tight specification bands.

After the statistical analysis concluded, the tool deflection was investigated through a CAE simulation. Nevertheless, some considerations were taken into account, simplifying and reducing the number of experiments, which led to qualitative results. Therefore, the milled block was considered rigid and undeformable without contributing to the surface deviation. As the force results and factorial analysis depicted no influence of the  $f_z$  on the measured deviation, it was disregarded. Lastly, as the toolholder is much more rigid than the tool, a cantilever condition of 40 mm in length was considered in the simulation.

Figure III-30 compares the deformation of the oval barrel tooltip considering two designs and the most critical cutting condition (region 72 - a tilt angle of 15 degrees and higher cutting forces measured). In design 1 the tool is modelled as a solid of revolution in cantilever. Design 2 considers the real geometry of the tooltip obtained by reverse engineering, considering the cusps and reliefs that reduce the tool rigidity.

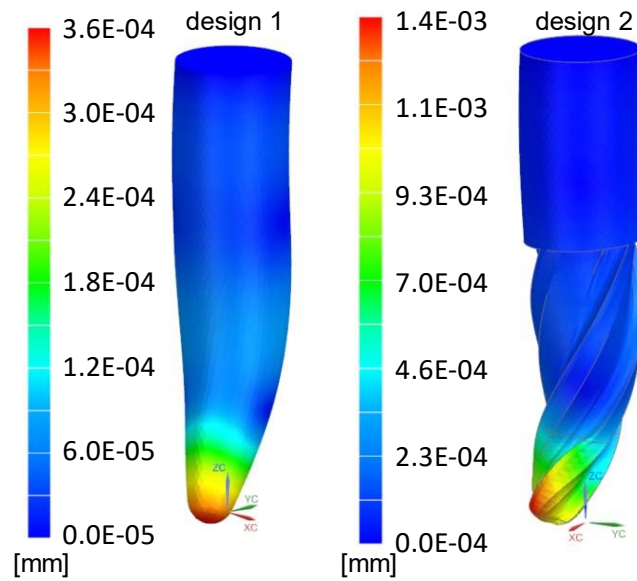


Figure III-30. Simulation of the oval barrel tool deflection considering geometry and measured cutting forces.

The tool deflection simulation showed that if the real geometry of the tooltip is not considered, an error of about 64% is obtained. The magnitude of the error also indicates that corrective parameters recommended for deflection modelling of ball-end tooltips or end-mill proposed by Kops and Vo (1990) and Budak and Altintas (1995), respectively 0.8 and 0.75, can not be used for this tool's geometry, probably because of the severe section variations along the tool body.

Figure III-31 and Table III-10 present simulation results considering the real tool geometry and the most significant cutting parameters on the surface deviation, the tool tilting, and the lateral depth of the cut ( $a_e$ ). For each pair of parameters, three regions were chosen and blocked according to the resultant cutting force, selecting the higher, lower, and one intermediary condition, addressing the tendency of the tilt angle and  $a_e$ .

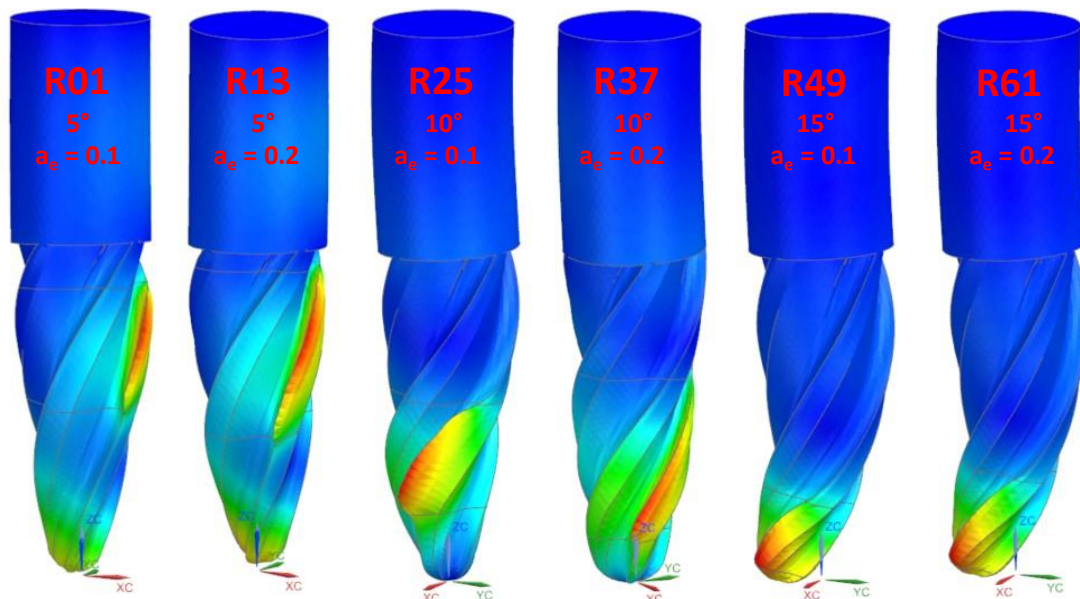


Figure III-31. Deflection pattern according to tool contact by tilting and lateral depth of cut.

Table III-10. Maximum deflection and resultant cutting force of the simulated regions.

Region	Resultant force (N)	Maximum deflection ( $\mu\text{m}$ )	Region	Resultant force (N)	Maximum deflection ( $\mu\text{m}$ )
01	29.5	0.052	37	64.7	0.163
04	33.4	0.074	40	75.2	0.209
12	47.9	0.098	48	96.6	0.269
13	59.0	0.105	49	25.3	0.147
15	61.3	0.116	52	39.1	0.375
24	74.5	0.145	60	70.8	0.750
25	17.4	0.040	61	94.7	0.839
28	28.0	0.087	64	121.0	1.117
36	43.2	0.140	72	147.4	1.397

Analysing the simulation results and comparing the tool deflection against the surface deviation (Figure III-25), a clear correlation of increases is observed with the lateral depth of cut ( $a_e$ ), the second more significative cutting parameter on the surface deviation. It becomes clearer by analysing Figure III-32a, where the deflection results by groups are graphed against the resultant cutting force.

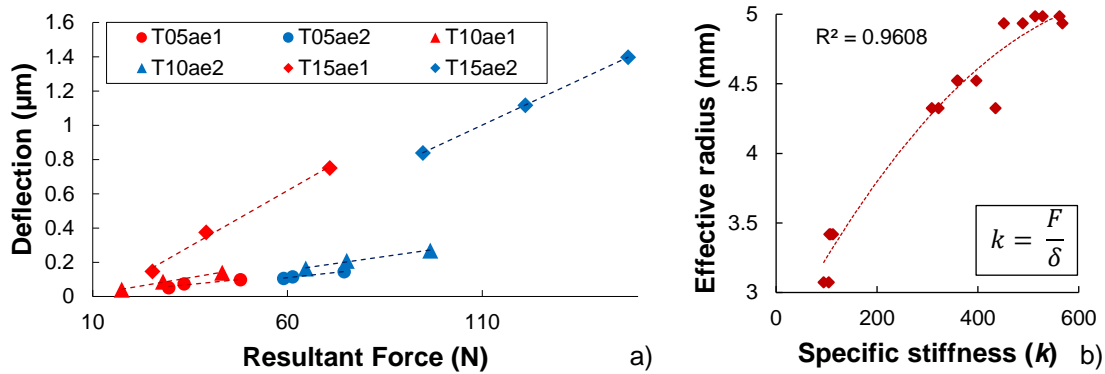


Figure III-32. a) Simulated tool deflection versus measured resultant cutting force blocked by tool tilt and  $a_e$ , b) effective cutting radius versus specific stiffness.

Considering the tilt angle, the simulation of the tool deflection presented a direct correlation with the resultant force. However, the magnitude of the results was lower by one magnitude in relation to the measured deflection. Also, it can be seen that the average surface deviation was higher at  $10^\circ$  degrees followed by  $5^\circ$  and  $15^\circ$ , increasing the variance heterogeneity with the tilt angle as observed in Figure III-25. This is a strong indicator of the presence of more complex problems, like the tool run-out. Assumption supported by the presetting of the set (tool + toolholder) where a static run-out of about  $5 \times 10^{-5}$  m was measured; as the cantilever increases, the run-out tends to increase, magnifying the diameter of revolution and overcutting the surface, while the tool deflection act as a reactive force and goes through the tool body ( $F_y$  component), provoking an undercutting response, and performing a competition phenomenon.

This means that the supposition of the dominance of the tool rigidity by the element with lower rigidity is not sufficient for modelling the final surface deviation, requiring a more complex modelling of the process.



Figure III-32a also shows different deviation patterns combining the tool tilt and the lateral depth of the cut, which is justified by its direct relation to the contact of the tool with the surface that alters the magnitude and directions of the cutting force. By recurring to an indirect comparison, it can be observed that the slope reduces about 66.5% from 15° to 10° and only 32.8% from 10° to 5°, indicating a non-linear rigidity for this tool geometry.

Figure III-32b shows the specific stiffness against its effective cutting radius. By comparing the specific stiffness against a geometrical parameter of the tool that defines the variation of the tool cross-section, it is possible to identify a second-order relation, indicating that the adjustment of the deflection by a linear coefficient is not possible for this kind of tool, requiring complex adjustment for modelling or simulations according to the CWE.

### ***III. 3. 2. 3. Conclusions and Future Works***

Hereafter, the main conclusions of the presented study are presented:

- The geometrical modelling of the contact showed that 5°, 10°, and 15° of tilt angle and the two levels of lateral depth of cut ( $a_e$ ) produce the same theoretical roughness with a crisp height of 1.5  $\mu\text{m}$ . The measured topographies showed very similar results even with 15°, where the minor tool radius participated in the cut,  $S_a$  ranging from 0.5 to 2.0  $\mu\text{m}$ , and  $S_z$  ranging from 4.4 to 10.1  $\mu\text{m}$ , highlighting a very good finishing even varying the cutting speed and feed per tooth.
- As expected, the deviation changes with the cutting conditions, as do the measured forces. The statistical analysis of the results showed that the tilt and feed per tooth are significant parameters to the cutting force, all other factors are significant for surface deviation, and only the tilt angle is significant on the surface roughness. The tilt angle was the only factor with significance for all the results, being the most important in the finishing process with oval barrel tools.
- Among the tilting angles, the lower one (5°) presented better-finishing results in both surface deviation and simulated tool deflection, also presenting the lower cutting forces, which can extend the tool's life.
- The cutting force results show that in the finishing process with oval barrel tools and other circle-segment end mills, the dominant component is normal to the part, followed by the component of force on the feed direction and minor influence of forces on the tool axis, been only the tangential and radial cutting force significant to the resultant cutting force and contributing on tool deflection and surface deviation.
- The simulation of the tool deflection using the measured cutting force depicted that the deflection of the tool was most influenced by the tool tilt and the lateral depth of

the cut, the most significant cutting parameters to the surface deviation. Comparing the simulated results against the surface deviation made it possible to identify a strong influence of the tool run-out. It magnifies the tool diameter in revolution, overcutting the surface while increasing the tool tilting, which produces deflections that propitiate undercutting, being necessary to ponder them according to the cutting conditions.

- The simulation also propitiates the analysis of the specific stiffness of the tool against its effective diameter. It was demonstrated that constant coefficients can not be used to compute the deformation because the tool shape propitiates a non-linear deflection with the tool engagement.

For future works, a simple programming routine is proposed to modify the NC file point-to-point and mirror the simulated tool detection, interactively reducing the surface deviation. However, this still required the development of an instantaneous chip thickness model for predicting forces and the non-linear deviation of the tool. The proposed methodology is depicted in Figure III-33.

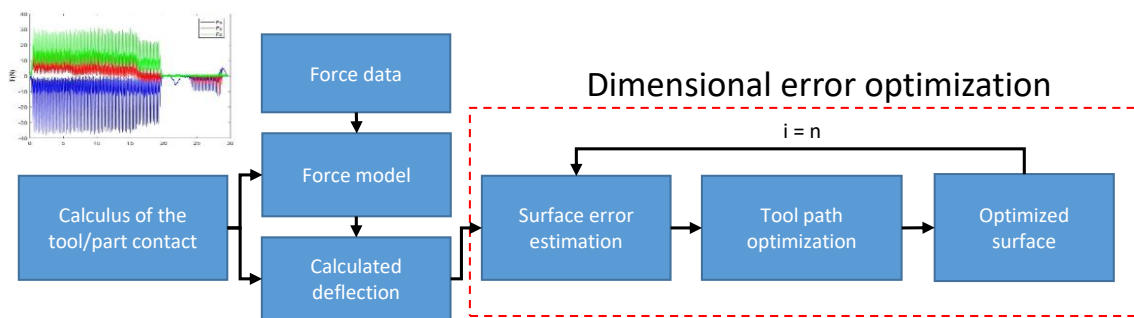


Figure III-33. Procedure for error correction using the force and CWE geometrical data.

### III. 3. 3. Remarks of the Sub-section

The sub-section presented two studies of the surface milled with ball-end tooltips, identifying the mechanism that damages the surface is multi-thematic and includes several factors, from the contact of the tooltip with the surface materials to the deviation caused by the component of the cutting forces and in-cut energy.

Minimizing the surface deviations and milling damages is still challenging. It cares for the development even in sufficient rigid parts, even though the geometrical characteristics of the milled surface aggravate this problem. When milling free-form surfaces, more complex problems related to tool engagement are expected, and when thin-walled parts are manufactured, problems of cutting stability are present. Thus, the development of tools for discretising the toolpath and better understanding the milling process with conventional ball-end tool tips and circle segment end mills is required.

## III. 4. Milling complex shapes

### III. 4. 1. Manufacture of big-size thin-walled component

Part of the study in this subsection contemplates the results of the work entitled “*Polygonal errors in thin-walled medium-size casings due to lap-flanges and isogrid milling*” presented at the 16<sup>th</sup> International Conference on High-Speed Machining.

#### III. 4. 1. 1. Experimental procedure

A big-scale thin-walled part was designed and manufactured using the facility of the Advanced Manufacturing Centre for Aeronautics (CFAA) from the University of Basque Country (UPV/EHU). The part is an aeronautic case manufactured from a bulky forged martensitic stainless steel block (AISI XM-12) due to higher mechanical properties, resulting in a high buy-to-fly ratio with several manufacturing hours.

From a technological point of view, the big size and the required weight reduction resulted in several challenges in designing, manufacturing planning, and execution. Weight reduction is one of the most important aspects in the development of the aeronautical sector, together with the costs and safety of the components. Hence, design optimization, manufacturing, and selection of materials govern the latest aeronautic industry developments.

One of the major problems in reducing the thickness is the increase of deviations and form errors due to the high cutting forces involved in manufacturing these parts in hard-to-cut materials. Surface roughness, vibrational problems, and deviation are just some of the problems magnified using hard-to-cut materials. New shapes and geometrical features are being developed to optimize the weight of the components. Another problem is the high demand for cutting tools and manufacturing time that increases the costs of manufacturing.

Considering this scenario, a medium-sized casing was designed using the software Siemens® NX. During the design steps, it was attempted to include features that were difficult to manufacture and ones to evaluate advanced manufacturing processes used in this kind of component. The component's wall thickness was specified at 8 mm, but depending on the region and stiffener features, it reaches 13 mm, a diameter of 900 mm, and 400 mm height. The final version of the design is presented in Figure III-34.

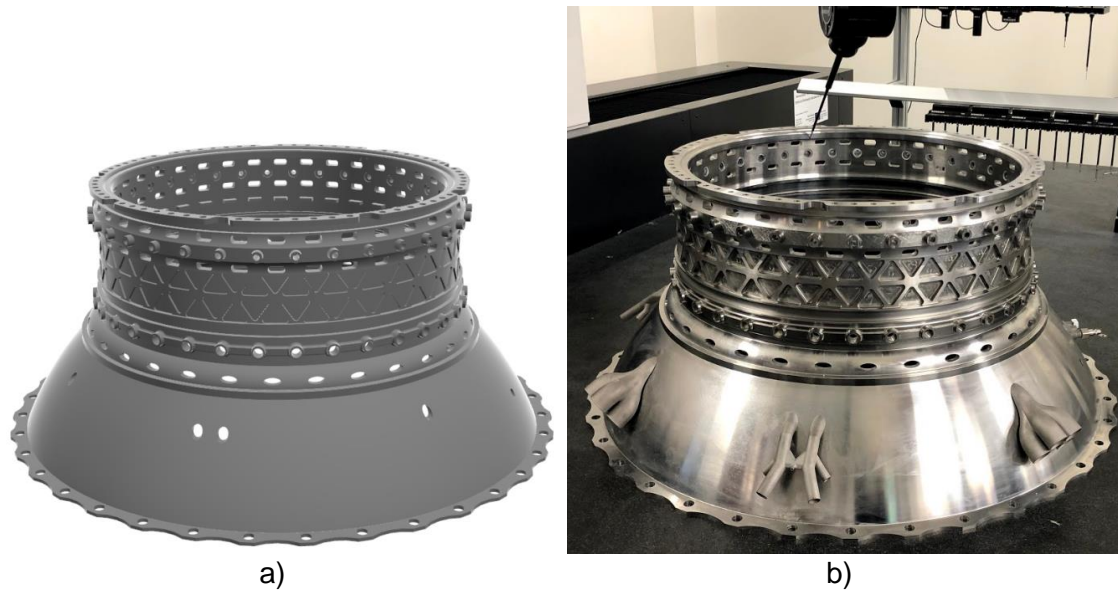


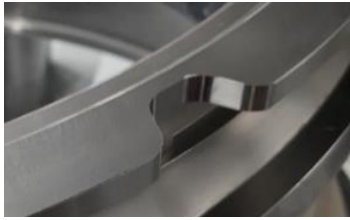
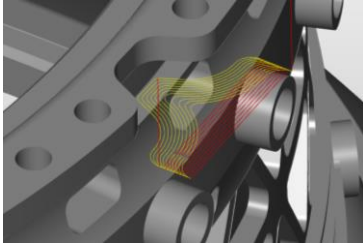
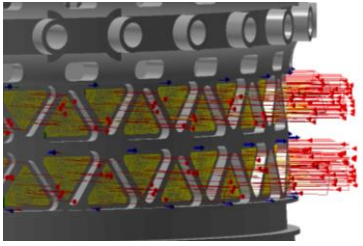




Figure III-34. AISI XM-12 aeronautical casing: a) CAD design; b) manufactured.

From the point of view of the manufacturing process, turning was used in the first roughing. The cylindrical shape of the forged block and the final part propitiate a high and continuous material removal rate with this process. It was proven high-feed turning, prime-turning, and ordinary turning, such as grooving on a GMTK VR-2.4 machine, processes with high material removal rate and associated forces.

After that, the milling process was conducted on a multitasking centre Ibarria THR16, and the operations were programmed with OPEN MIND hyperMILL™. The number of manufacturing clamping positions was minimized to 3 to reduce positioning errors. Table III-11 presents the programming toolpath of some critical regions and compares the CAM machining time with the time consumed obtained by the machine monitoring system.

Finally, the bosses manufactured by additive manufacturing were welded in the thin-walled case, as depicted in Figure III-34b, and it proceeded to component inspections.

Table III-11. Estimated versus real milling time of Casing critical regions.

Region	Toolpath	Virtual Time	Real-Time
<p><i>Upper flange</i></p> 		00:38:56	1:05:51 (+69.13%)
<p><i>Honeycombs</i></p> 		18:09:22	23:40:42 (+30.41%)
<p><i>Elliptical holes</i></p> 		05:05:02	05:55:05 (+16.41%)
<p><i>Upper ring</i></p> 		09:14:28	11:43:52 (+26.95%)
<p><i>Lower ring</i></p> 		08:31:47	09:46:16 (+14.55%)
<p><i>Flat holes</i></p> 		10:13:35	11:29:43 (+12.41%)
<p><i>Waves</i></p> 		01:16:54	03:02:09 (+136.9%)

III. 4. 1. 2. Manufacturing remarks

The first result directly observed is the discrepancy between the time estimated by the CAM and the consumed during the process. Among the causes are tool breakages, unreal feed rate, and unprogrammed stops for verification, among others. So, in manufacturing this kind of component, a machining time of over 43% can be expected. But depending on machine kinematics, it can be higher or lower (Chapter III. 2).

Another topic observed during the manufacture of slots and holes by milling is that there is a severe variation in engagement. The corners are critical in pocket milling, especially for hard-to-cut materials applied in the aeronautical sector, where more material is removed, and tool-part engagement could reach up to 50%, significantly increasing the forces (Han and Tang, 2015). Supposedly, the increase in the cutting forces justifies the accelerated tool wear and breakage observed during the manufacture of the elliptical holes and the isogrid honeycombs. In the elliptical holes, the stepover was modified, and the tool diameter was reduced (from 6 to 4 mm) to minimize the CWE, which increased the manufacturing time and the number of tools used.

For the specific case of the honeycombs, the initial strategy was changed to accomplish the objectives. However, it leads to an increase in the machining time and surface marks. Figure III-35 presents the change in the 3D offset strategy from 6 to 9 mm and the change to the trochoidal toolpath used in roughing and finishing, resulting in a time increase of about 68% and characteristic surface marks. The surface signature left on the finished pocket can be seen in Table III-11.

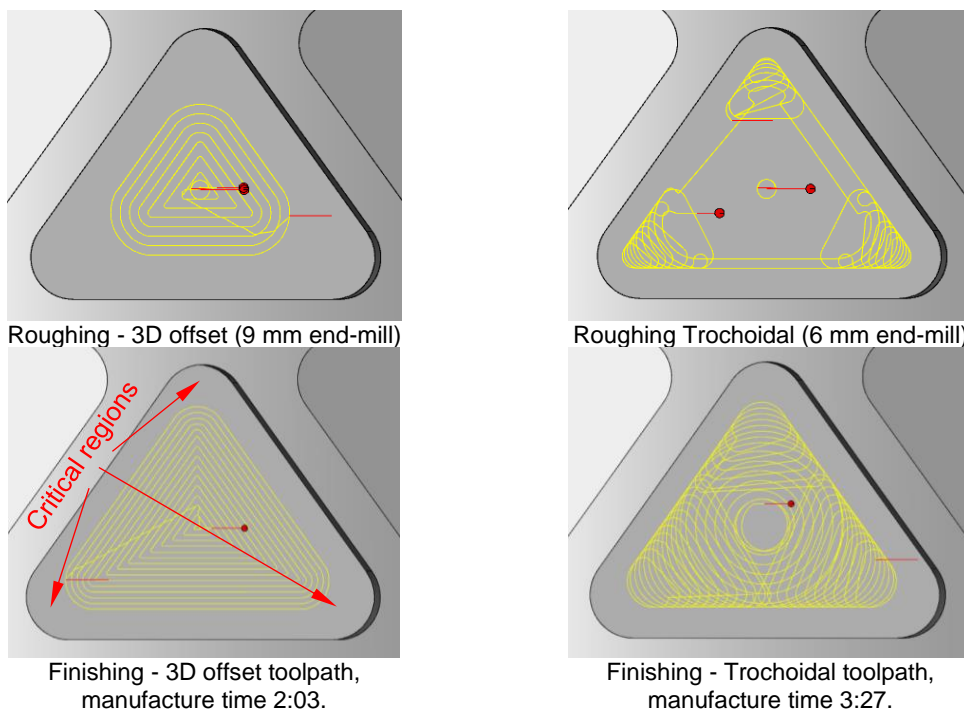


Figure III-35. Toolpath strategy for slot milling of honeycomb triangles.

In this case, with a 3D offset toolpath, it was possible to manufacture only two pockets with a single tool. While using a trochoidal manufacturing strategy, 142 pockets were made with only two tools. However, the manufacturing time increased by about 70% for each pocket, corroborating with the literature (Li et al., 2019; Pleta and Mears, 2016).

Figure III-35 also depicts an example of roughing using tools with diameters of 9 mm and 6 mm. In the presented case, it was possible to manufacture the corners using a trochoidal toolpath without using smaller tools, optimizing times related to tool set-ups.

#### III. 4. 1. 3. Methodology for part inspection

One of the critical dimensions of the part is its cylindricity, which can be affected by the internal tensions of the bulky raw material (previously forged) and the high amount of material removed. Knowing that the raw material used was previously forged, it presents compressive stresses that can cause roundness deviations with the machining process by material removal. The milled contour of the upper flange is critical, and its coupling requisites lead to a careful evaluation of the part. Another functional application of the flange is weight reduction, which gradually reduces part rigidity and releases internal tension, provoking the roundness of the machined part.

To evaluate the roundness of the part, a CMM model Crysta Apex S-162012 was used for inspection. An RSP2 module with a probe with a carbon fibre stem and silicon nitride sphere of 2 mm in diameter was used for all measurements.

The casing was measured in 20 sections parallel to Datum A to obtain the overall roundness, as depicted in Figure III-36. A continuous scanning probing strategy with internal and external measurements was done to maximize the number of evaluation points. Just section S7 was defined by 36 points because continuous measuring was impossible due to the presence of oblong holes. Table III-12 presents the distance of each measured section to Datum A.

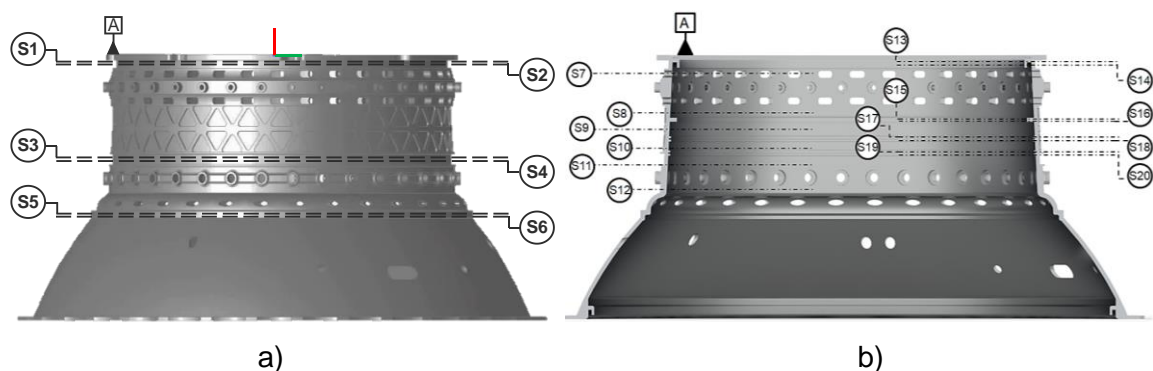


Figure III-36. Measured sections of the casing: a) external sections; b) internal sections.

Table III-12. Distance in mm from Datum A to each section.

S1	S2	S3	S4	S5	S6	S7	S8	S9	S10
4 mm	13 mm	17 mm	155 mm	160 mm	138 mm	242 mm	29 mm	85 mm	112 mm

S11	S12	S13	S14	S15	S16	S17	S18	S19	S20
164 mm	204 mm	10 mm	16 mm	97 mm	99 mm	125 mm	130 mm	146 mm	151 mm

### III. 4. 1. 4. Roundness and dimensional results

Figure III-37 presents the measurement results of sections 1, 2, and 3 and the clamping system used. It can be noted that there is a geometrical effect of the 9 flanges milled on the roundness of the casing. Also, for all the inspected sections, the maximum form deviations are found in the same angular position of the flange's waves.

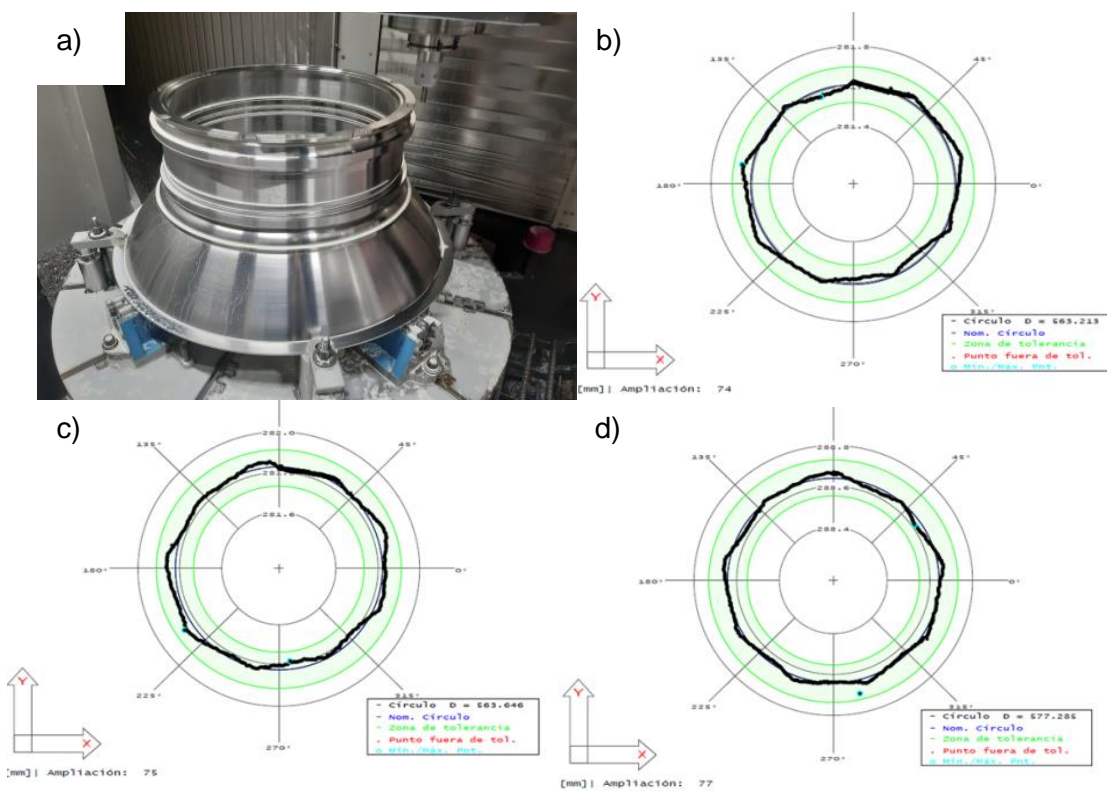


Figure III-37. a) Upper flange milling; b) Roundness graph of section S1 (0.087  $\mu\text{m}$ ); c) Roundness graph of section S2 (0.083  $\mu\text{m}$ ); d) Roundness graph of section S3.

The effect of the milled flange on the form error could be detected more than 150 mm away, indicating that including roundness and harmonic analysis in casing manufacturing is necessary to minimize and detect form errors caused by the geometry itself.

Regarding the effect of the turning process on the casing geometry form errors, due to its lack of rigidity, 2<sup>nd</sup> harmonic appears in section S1 with an amplitude of 25.802  $\mu\text{m}$ , which reveals an oval shape. The same harmonic appears in sections S13 and S14 with an amplitude of 30.584  $\mu\text{m}$  and 29.612  $\mu\text{m}$ , respectively. The influence of the fixturing system, formed by 4 clamps separated by 90° from each other (Figure III-37c), can be detected with the clear appearance of the 4<sup>th</sup> harmonic on almost all sections. The



geometrical effect of the flange milled can be seen on the 9<sup>th</sup> harmonic on the first 4 sections. Its magnitude reveals a stronger effect than the clamp system used. The honeycomb structure (with 32 triangles) had a low impact, with the 32<sup>nd</sup> harmonic presenting less than 2  $\mu\text{m}$  in all sections evaluated. Figure III-38 illustrates the harmonic analysis of sections 1, 2, 3, 4, 13, 14, 15, and 16.

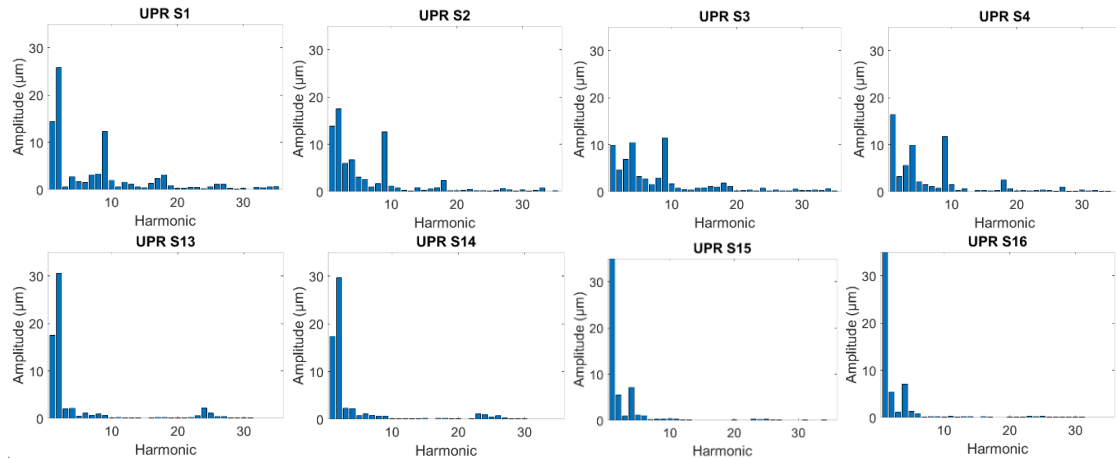


Figure III-38. Harmonic response of sections 1, 2, 3, 4, 13, 14, 15 and 16.

Table III-13 shows the points collected in each section of both nominal and measured diameters.

Table III-13. Measurement data from sections S1 to S20.

Section	S1	S2	S3	S4	S5	S6	S7	S8	S9	S10
Points	885	887	909	909	1023	1023	36	1741	1746	1757
Nom $\varnothing$ (mm)	563.252	563.633	576.776	577.252	650.000	650.000	552.762	558.095	560.667	563.143
Actual $\varnothing$ (mm)	563.213	563.646	576.795	577.285	649.913	649.908	552.773	558.124	560.830	563.252
Section	S11	S12	S13	S14	S15	S16	S17	S18	S19	S20
Points	1764	1776	1653	1653	1653	1653	1734	1734	1742	1742
Nom $\varnothing$ (mm)	565.619	569.429	530.000	530.000	538.000	538.000	556.014	556.014	558.537	558.537
Actual $\varnothing$ (mm)	565.663	569.471	530.102	530.100	537.654	537.661	556.114	556.101	558.611	558.601

Regarding dimensional deviations, the maximum error was found in section S19, with a relative dimensional error lower than 0.02%, an acceptable value for aeronautical parts (Klocke et al., 2015).

### III. 4. 1. 5. Conclusions

This study investigated the manufacture of a thin-walled mid-size casing using forged bulk AISI XM-12 in big-size multitasking machines. As follows are presented the main conclusions regarding the manufacture:

- The limitation on the machine kinematics and the unplanned setup changes due to tool wear and tool changes resulted in about 43% more manufacturing time than planned by the CAM software.
- The continuous measurement of the casing cross sections allowed the identification of harmonics with a greater effect on form deviations related to the part design and milling process of big-sized parts. The harmonic response related to the flanges milled

(9<sup>th</sup> harmonic) presented a higher effect on the form deviation than the fixation system (4<sup>th</sup> harmonic), which had a higher effect than the honeycombs (32<sup>th</sup> harmonic). The combination of compressive residual stresses of the forged bulk, high material removal, and rigidity part rigidity was probably responsible for spreading the form error deviation to further than 150 mm after the flange milling.

- The Honeycomb design and manufacture had the lowest influence on the form deviation and can be used successfully to reduce part weight. However, the triangular structure caused high tool engagement, requiring a change in the manufacturing strategies where the trochoidal finishing showed a good performance but a bad finishing aspect, which could be unacceptable depending on the component or region.
- It is worth noting that the flanges manufacturing strategies using flank milling allowed a high removal rate. However, this may have caused deviations in the roundness of the part, which was inferior to 0.02% (section S19), an amount under control for the aeronautical specifications.

### ***III. 4. 2. Blade manufacture in multitasking centre***

Machining of aeroengine components such as blades and BLISKs is still a challenge for aeronautical industry due to the complexity of their shapes and the strict requirements for their functioning. Multitasking operations are preferred in order to generate such complex parts. Besides, blades are difficult to manufacture parts due to their shape and stiffness. These parts have free-form surfaces only finished by ball-end tooltips. However, during the milling, the CWE oscillates, modifying the components of the cutting force, affecting tool wear and chip formation, damaging the surface, and producing parts that are out of tolerance, reducing performance. Thus, a slender blade part was designed, and the surface produced under different conditions by continuous 4-axis milling on a multitasking turn-mill centre was investigated.

The present study addresses preliminary aspects related to the geometry and guides into cutting parameters selection by manufacturing an aluminium alloy blade with a conventional ball-end tooltip, giving the first insights into the process and guiding posterior manufacturing cases with harder materials and more complex tooltips for the designing geometry.

#### ***III. 4. 2. 1. Experimental procedure***

To investigate the finishing process of thin-walled components containing free-form surfaces, a blade part was modelled using Siemens NX 12 software. The maximum thickness of the part was defined as 7 mm, and the total cantilever was 100 mm, resulting

in a slenderness index ( $L/h$ ) of about 14.3. The central region of the blade was split into 8 regions with 10 mm length, leaving 5 mm for blending with the side walls at extreme regions. Figure III-39 presents the blade schematic together with a rolling ball analysis showing the thickness of the part along the length.

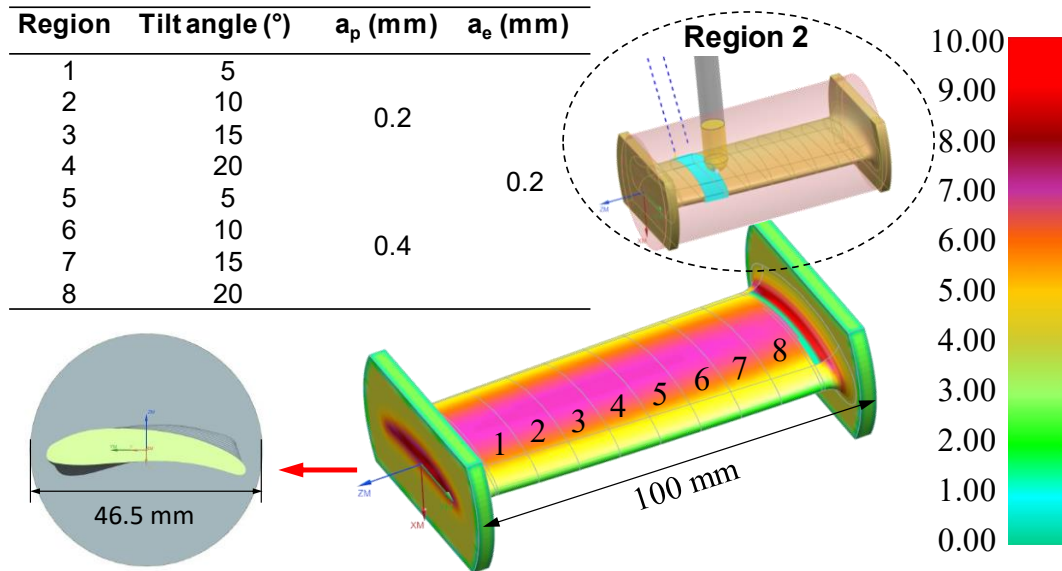


Figure III-39. Aluminium blade thickness analysis and milled regions.

The machining operations were realized on a CMZ TC25BTY multitasking machining centre with Fanuc controller 31i and a custom post-processor developed in Matlab<sup>®</sup> for the live toolholder used, which rotates in 90 the tool. The initial blank, made from 7075 aluminium alloy, has a cylindrical shape with dimensions close to 47 mm in diameter and 150 mm long. The blank was tied on a 3-clamp chunk and machine using tailstock in all operations in one batch to avoid re-referencing issues. First, the roughing was conducted, reducing the external diameter to 46.5 mm by turning them with a 38 mm top-end mill (R200-038Q22-12M) and a 10 mm toroidal tool with a 2 mm rounding radius was used to leave the part close to the final shape, saving 1 mm of stock. Then, it was semi-finished with a ball-end mill with a 5 mm radius in a spiral toolpath strategy with 0.4 mm of the axial depth of cut ( $a_e$ ), leaving half of the blade with 0.2 mm stock and the other half with 0.4 mm.

The finishing operation was conducted using an ordinary ball-end mill mounted within a 40 mm cantilever on a live toolholder TL20/10400/01 with a maximum rotation speed of 4000 RPM. The tool has a nominal diameter of 5 mm manufactured in solid carbide with 10% Co, has four flutes, and has a 30° helix angle. As depicted in Figure III-39, 4 levels of lead angles (5°, 10°, 15° and 25) and 2 levels of depth of cut (0.2 and 0.4 mm) were proven, with constant lateral depth of cut of 0.2 mm, cutting speed and feed per tooth. The tolerance band used during the CAM programming was 0.01 mm, a recurrent value for the finishing process of this kind of component by ball-end milling.

As a limitation of the ordinarily mill-turn centre and live toolholder of 4000 RPM, the recommended cutting speed by the tool manufacturer was not accomplished, been used the higher value possible of 125 mm/min with constant feed per tooth of 0.055 mm/tooth. The strategy used was a 3D spiral in the downward condition that propitiates a smooth tool path and less variation in the engagements, reducing the possible damages in the surface, which are usually hard to remove in post-processing operations and cause performance lows in such components.

As a preliminary investigation, only optical inspection and machining times were used to inspect the quality of the process and the machined blade. Visual inspection and optical imaging were used to inspect the surface quality of the milled surface, followed by confocal microscopy through Leica® DCM3D, with the software Leica® Map 6.2 used to obtain surface topography and measure roughness.

### **III. 4. 2. 2. Results and discussions**

Figure III-40 presents the results of the roughing, semi-finishing and finishing operations.

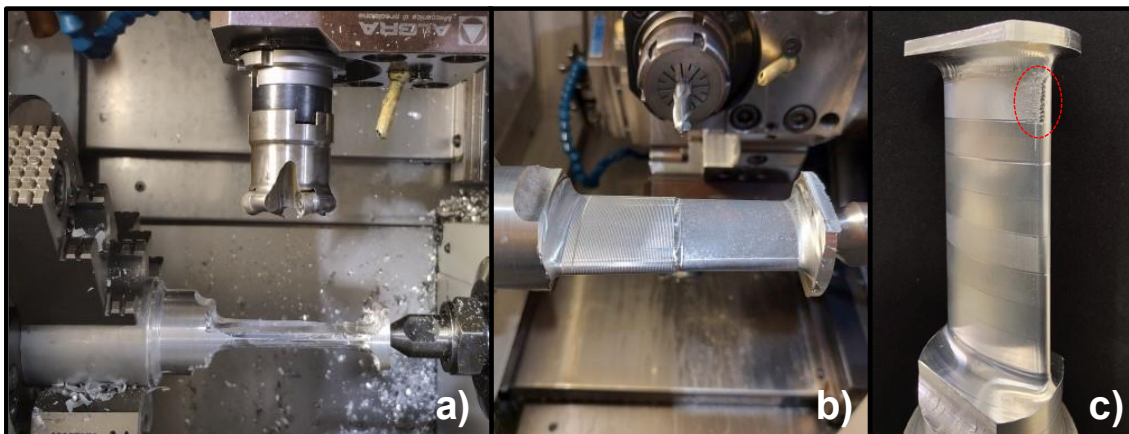


Figure III-40. Milled part after operations: a) roughing, b) semi-finishing; c) finishing.

The first that can be seen is that even when using an aeronautical class aluminium that propitiates a higher removal rate and good surface finishing, several marks were present on the finished blade due to intermittent stops during the milling process due to saturation of the NC processing loop. The oscillation in the feed rate could be noted visually during the milling time and quantified by comparing the estimated milling time by the CAM software with the recorded milling time (Table III-14). It is important to highlight that most critical oscillations in the feed rate reduction always occurred after the transaction between the concave to the convex surface and vice-versa, with different magnifications according to the lead angle used. It happened at great magnitude, even when using a reduced cutting speed for this material, which also magnified plastic deformations. Figure III-41 depicts the milling marks with the side transaction observed during the milling process, and Figure III-42 shows the profile of such regions.

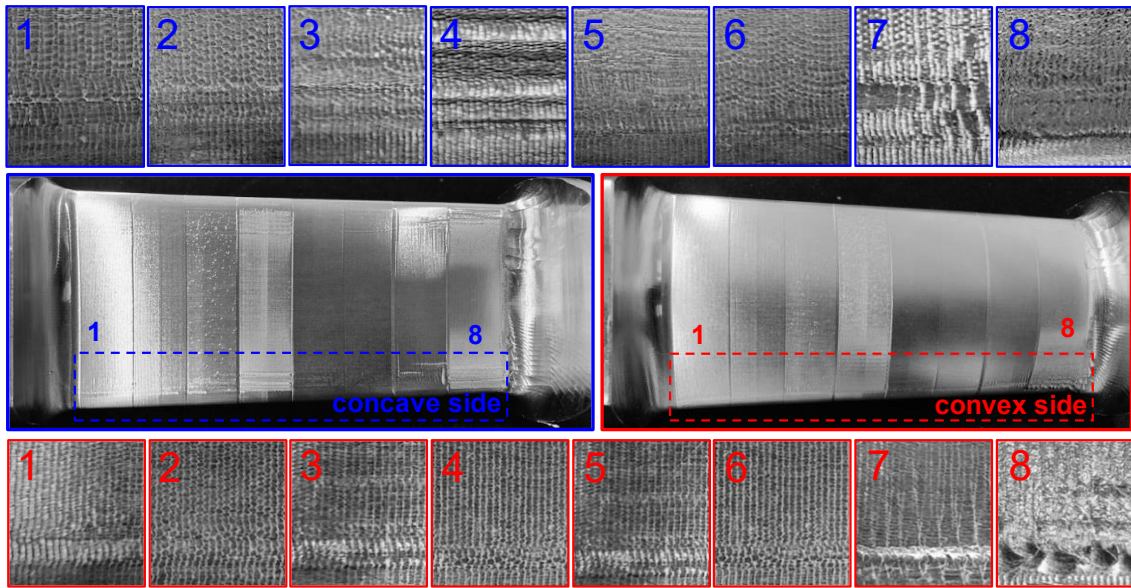


Figure III-41. Magnification of the milled marks due to control loop saturation.

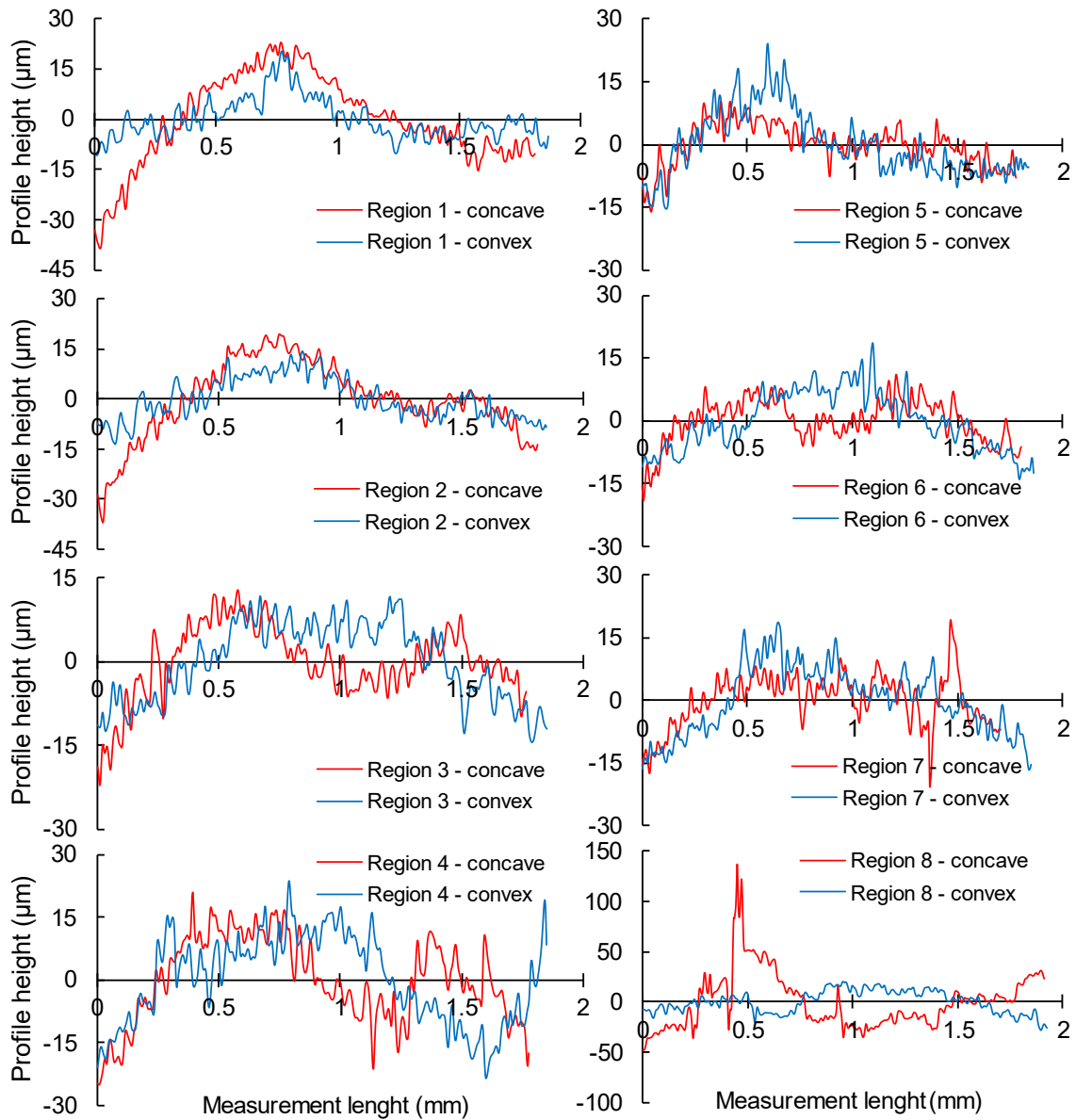


Figure III-42. Measured profile height at each region after face transaction.

Table III-14. Comparison of the number of NC lines versus the predicted and real milling time for each milled region.

Region	NC lines	Estimated time (s)	Real-time (s)	% Error	Toolpath inversion schematic
1	10467	292	918	68.2	
2	15501	301	1335	77.5	
3	20849	312	1457	78.6	
4	27943	323	1691	80.9	
5	10863	311	966	67.8	
6	16093	318	1374	76.9	
7	20722	328	1484	77.9	
8	28432	339	1733	80.4	

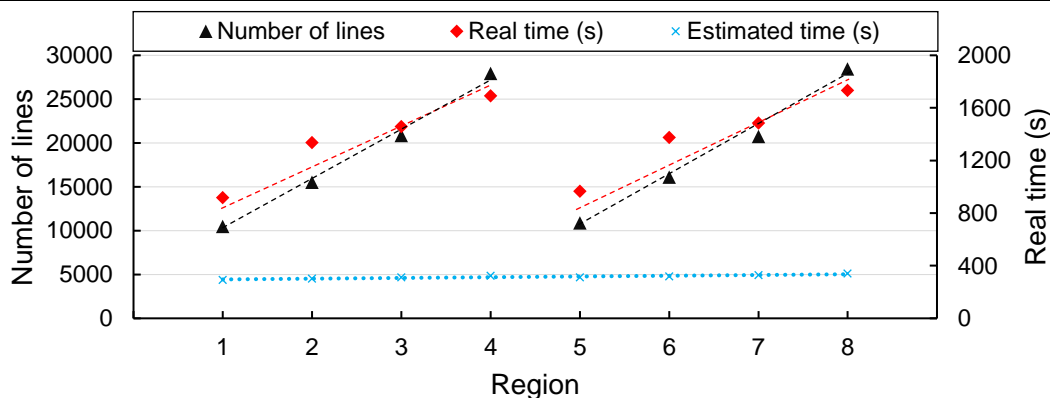


Table III-14 depicts that by increasing the lead angle, there is an increase in the number of computed NC lines, and it directly affects the real milling time. This can be related to the change in the contact of the tool dome with the surface moving the CL over the tooltip, which makes the trajectory of the centre of the tooltip CC bigger, as depicted.

Analysing together the results depicted in Figure III-41, Figure III-42 and Table III-14, it can be seen that the increase in the lead angle increases the surface damage. Severe plastic damages were observed on the convex side of region 8 (as depicted in Figure III-41). Also, the measured profile (Figure III-42) showed a magnification of about 4 times the depth of the profile compared to other cases, indicating depth marks that can be harder to remove. Region 4, which was also manufactured using a 25° lead angle, presented some vibrational marks after the tool moved from the convex to the concave face, as seen in Figure III-41. Region 7 also depicted some damages, indicating attention to the manufacture of this geometry with a 15° lead angle on similar machines.

It can also be seen, as expected, that the increase in the number of computed lines by the CAM software did not produce an increase in the time prediction by the CAM software. This is because the geometry remains constant, preserving the distance travelled by the tool, and the CAM software takes into account the theoretical cutting speed input to calculate the time. However, the real milling time increases from 68 to

81% according to the tilt angle. Also, it can be correlated that the greater the error, the greater the magnitude of the damages observed.

The best results occurred with the 5° and 10° lead angles, where the deviation marks were minor and tolerable at 15°. By using the methodology proposed in study 1 (III. 2) to compute the MRT for the different post-processed NC files, it ranged from 0.035 m·s for 25° lead angle to 0.064 m·s to 5°.

Figure III-43 presents the results of the roughness analysis on the central region of each face on the concave and convex sides.

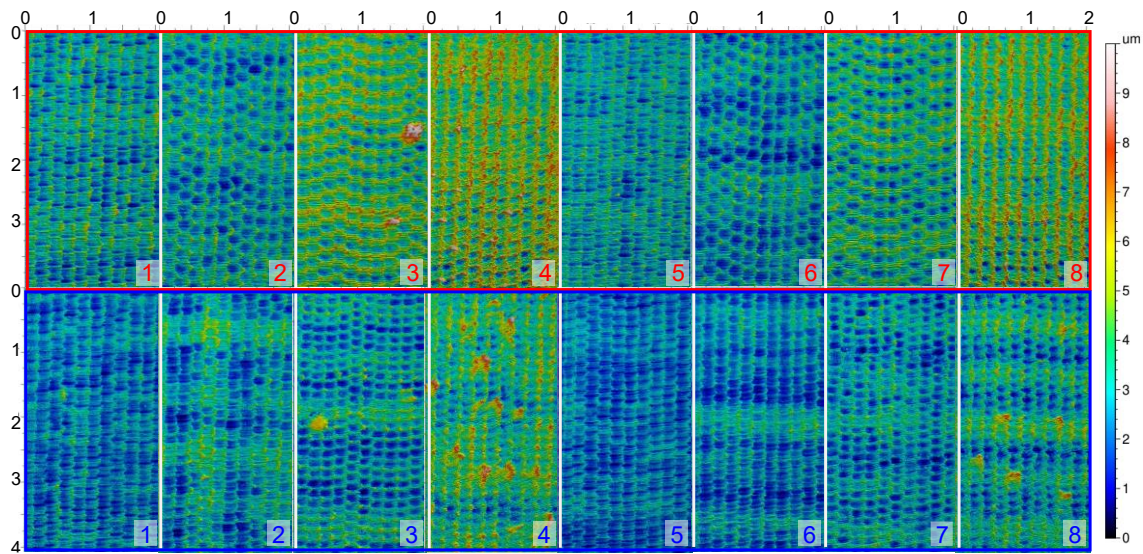


Figure III-43. Surface texture at the centre of concave and convex regions.

Figure III-44 summarises the results of the measured roughness Ra and Rz on each region depicted in Figure III-43.

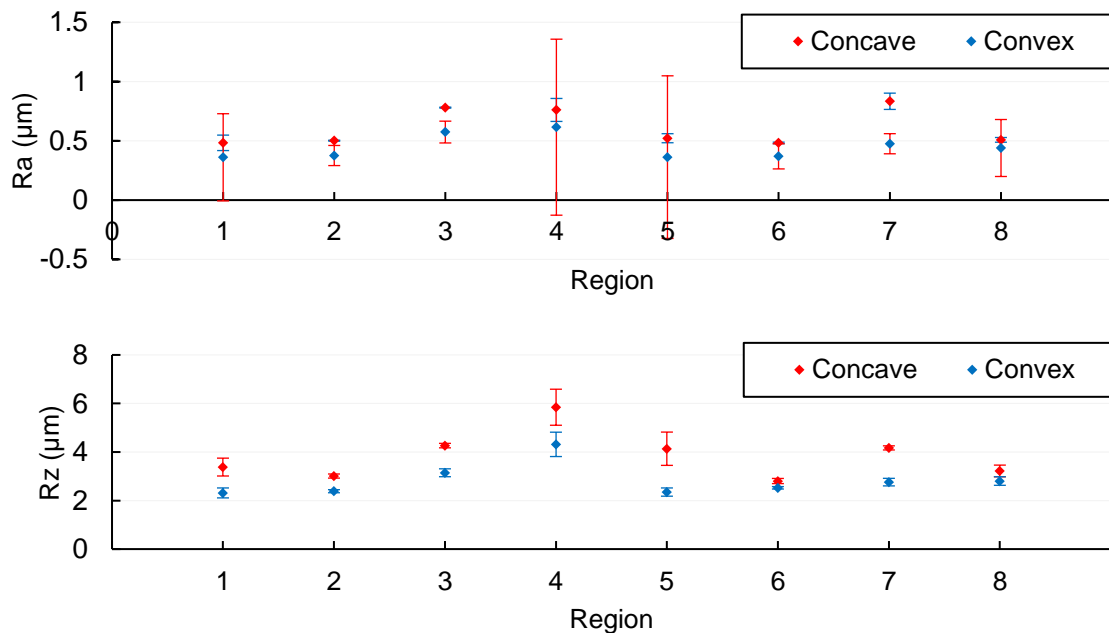


Figure III-44. Measured roughness Ra and Rz at the centre of concave and convex regions.

As depicted in Figure III-43, the topography obtained by changing the lead angle did not significantly change, but it was possible to identify some attached and smashed damages in regions 3, and with more intensity in regions 4 and 8, but still not significant to compromise the surface quality, being in all cases under 10  $\mu\text{m}$  high.

Figure III-44 presents the quantification of the roughness Ra and Rz of each region, confirming no significant changes in the roughness with the lead angle under stable cutting conditions. A higher roughness was observed in region 4 manufactured under 25 lead angle and with a lower depth of cut (0.2 mm), probably because of the surface's damage (Figure III-43).

The results concluded that the lead angle only causes substantial influence with severe changes on the toolpath. However, it was identified that the concave side tends to produce a slightly higher roughness than the concave side, probably due to higher CWE conditions.

### **III. 4. 2. 3. Conclusions and Future Works**

The designed blade used to investigate the manufacturing process of thin-walled parts with free-form surfaces by ball-end tooltips was strongly influenced by the lead angle and machine response on the continuous 4-axis milling process. The main conclusions obtained with the milling process using a turn-mill centre and aeronautical aluminium alloy as a workpiece are:

- The increase of the lead angle increased the number of lines of the NC program, increasing the milling time and the oscillations in the feed rate. The analysis of the predicted versus real milling time showed that the machine response decreases with the lead angle, achieving errors of about 80% when 25° is used.
- The oscillation in the feed rate during the milling due to saturation of the machine control loop tends to occur in the transition between concave-convex surfaces, producing milling marks, deviations or even severe plastic damages as obtained with the lead angle of 25 degrees, where the measured in the profile obtained of region 8 had an amplitude 4 times higher than with other tilting conditions.
- The designed blade showed optimal milling results in the range of 5° to 10° of lead angle, and no significant changes were observed in modifying the depth of cut from 0.2 mm to 0.4 mm.
- Increasing the lead angle to 25° also resulted in some smashed and attached material damaging the surface, which was identified by the roughness analysis and produced an undesirable visual aspect.



- The topography analysis showed good surface finishing under stable cutting conditions and similar quality for all tilting conditions and depth of cut evaluated, with marks under 10  $\mu\text{m}$  amplitude, the abrupt changes in direction being the most critical concern to the surface signature.

The reported results of the preliminary investigation with the designing geometry emphasized critical areas for future works: optimizing lead angle and removing limitations caused by machine kinematics. Using multitasking centres with limited factors such as spindle speed, machine kinematics, and NC control resulted in critical parts resulting in irreversible damages, removing the spotlight of damages on the surface caused by the process itself. Thus, it is recommended to use machines with improved performance and response times to address the challenges of free-form milling with ball-end tooltips effectively.

### ***III. 4. 3. Remarks of the Sub-section***

In this subsection, two studies related to the manufacture of complex parts were presented. The first one investigated the complexity of manufacturing a big-size and thin-walled component. These geometrical characteristics led to a high material removal that resulted in unwanted deviations and tool breakages for optimum manufacturing performance, which led to toolpath modifications and optimizations. The results show that deviations in big-sized parts mostly come from the geometrical features and the clamping setup. It should be focused on optimizing the manufacturing chain of such components.

The second study evaluates the manufacture of a slender blade in aluminium alloy on an entry-level multitasking CNC machine. Besides the preliminary results regarding the cutting parameters and engagements of the ball-end tooltip with the designed geometry, the milling results showed that feed oscillation could compromise the quality of the finished part, producing parts with bad finishing aspects in specific regions of the component, leading to deviations out of tolerance even when tight tolerance bands and continuous milling toolpath, such as 3D spiral, are used.



---

## **Chapter IV. Ball-end milling - surface prediction**

---



## Chapter IV. Ball-end milling - surface prediction

*This chapter proposes a method to obtain and use data directly from commercial CAD/CAM software with an open architecture with a modelling proposal. Furthermore, the 5-axis milling process is modelled, considering ball-end tooltips with up to two radii for surface prediction, and it is validated on a free-form surface.*

### IV. 1. Introduction

Several parameters affect the surface texture in the ball-end milling process of free-formed surfaces, making its prediction challenging. Therefore, it is common to consider the surface as an idealized geometrical model for analysis. However, current commercial CAM software cannot properly predict the idealized surface. The CAM software uses simplified assumptions such as infinite spindle speed and Boolean operations to predict the milled texture, considering locally the engagement of the dome of the tool with sequential points computed by the CAM software. By neglecting the relative movement of the tool and the cutting edge nor considering an even data distribution in the feed direction, its estimation presents errors according to the distribution of the calculated CC points, as depicted in Figure IV-1.

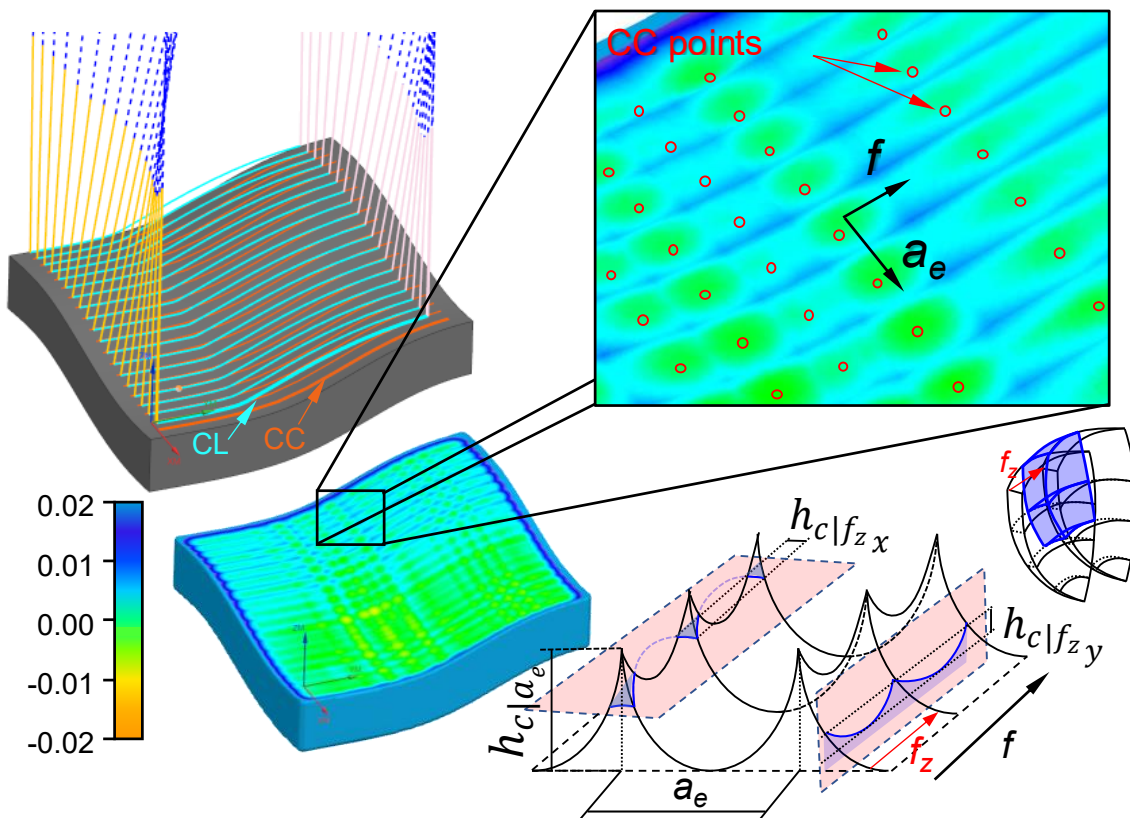


Figure IV-1. CAM surface prediction.

It can be observed in Figure IV-1 that the concave or convex region shows a higher number of marks, coinciding with regions with a higher number of cutter contacts due to the local surface curvature and tolerance band used during CAM calculation. Considering that the feed-per-tooth used during calculation is constant, this generates errors influencing models based on the NC data, deserving proper attention. Also, to obtain a robust milled model to predict the texture of free-form surfaces, including material properties, the effective cutting speed of the tooltip, feed rate oscillation, tool run-out, cutting parameters, as well as cutting geometries and CWE geometrical model, is necessary.

Nowadays, there are some models to predict topographies and other aspects of the machining process that include forces and their derived problems. However, there are many limitations when complex surfaces are involved due to several data inputs required and boundary conditions. Additionally, studies with this kind of surface usually use tools with ball-end tooltips that result in more complex geometric problems, requiring the processing of a significant amount of data previously, such as the mathematical model of the surface that is usually protected by the CAD/CAM software. So, it is common to find limited or idealized studies focused on specific geometries, contact conditions, or cutting parameters.

Considering this issue, a routine was developed to extract both trajectory and geometric data directly from the CAD/CAM software and adapt it for modelling. Then, a methodology is applied to predict the topography aspects of the free-form milling; In the same way that a set of infinitesimal straight-line segments can represent splines, a free-form surface can be discretized into infinitesimal planes to predict the milling process, as better the discretization lower is the error associated. This approach can also be extended to predict more complex problems dependent on the force, considering both CL (Cutter Location) and CC (Contact Condition) data.

For better understanding, the proposed development was organized into six topics. First is presented an overview of the proposed methodology (IV. 2), then the routine for data collection developed in the software Siemens NX is presented (IV. 3.), followed by the geometrical modelling of tooltips (IV. 4), toolpath data treatment (IV. 5), and surface prediction procedure (IV. 6). Finally, is presented two study cases for evaluate the proposed methodology, first evaluating the surface finishing with a conventional ball-end tooltip (IV. 8). Then, a second one comparing the surface finishing with different ball-end tooltips (IV. 9). In both study cases the materials and methods for evaluating the implemented routine followed by the results and discussions, are presented.

## IV. 2. Overview of the proposed methodology

A programming routine was developed to obtain a set of data necessary for modelling the surface. The first step of the proposed methodology is obtaining any complex surface's cutting contact (CC), cutting location (CL), and respective normal vectors by an implemented routine on the CAD/CAM software. A standard language C#, was used in the programming routine because it is compatible with the open interface (NX Open) of the software used – Siemens NX. It is worth noting that the same methodology can be adapted to other software programs that have an open programming interface.

Then, a geometrical model was developed based on the routine outputs to predict the topography of 5-axis milling using ball-ended tooltips. In this second step, the geometries of the tool were mathematically modelled with a scope limited to ball-end tooltips with up to two radii and a constant helix angle. In this step, two approaches were considered. The first considers the dome after a complete rotation of the tool (instantaneous position), and the second one considers the instantaneous cutting edge (pondered movement), which allows to include, i.e., the tool run-out. After that, both data were used to calculate the surface, measuring topography, scallop height, and theoretical roughness. Figure IV-2 presents the flowchart of the proposed methodology.

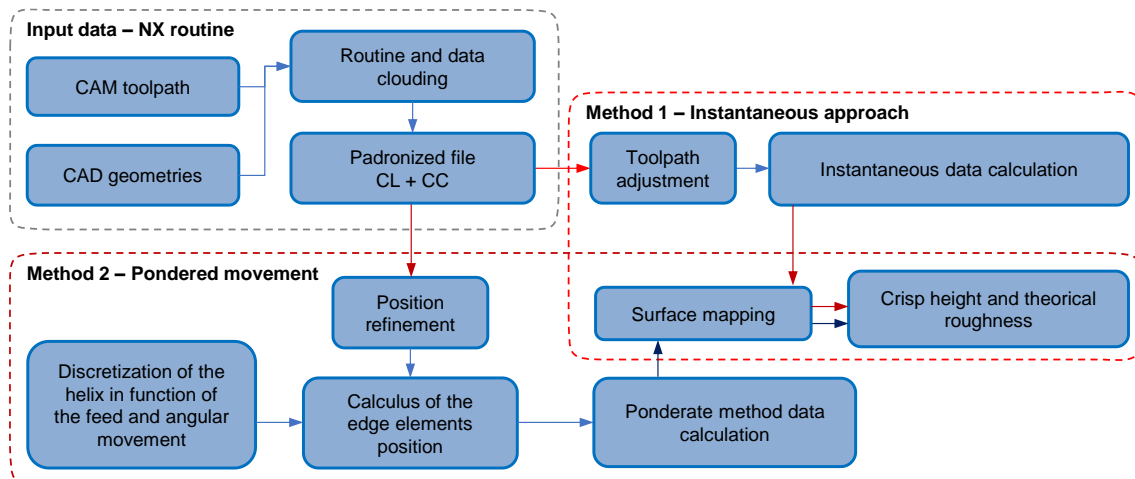


Figure IV-2. Flowchart of the proposed methodology for surface prediction.

## IV. 3. Routine for data collection

For the surface mapping, a routine was developed using an API (application programming interface) on the high-end CAD/CAM software Siemens NX 1953 to obtain a list of the cutting location (CL), cutting contact (CC), and respective vectors. A series of procedures and requirements must be followed in accordance with the developed routine to obtain these data. The first requirement is to import or model the geometry in the software, followed by the usual CAM programming. Thus, both geometry and

trajectory will be available for computation and posterior machining. As a second requirement, it obtains the post-processed NC program file in the standard format (Cutter Location Source File - CLSF), providing normalized data to the routine.

Then, with the path and directory of the exported CLSF file or the data extracted directly on the software by the routine, a series of filters and sorts are done while is computed line-by-line the output data missing – the surface normal vectors for a given contact point (CC). Highlight that most CAD/CAM software has closed architecture, so obtaining data relative to the surface in a specific position is not trivial. At the end of the calculation, all the non-cutting moves lines are filtered, and the other lines are presented in a standardized file e with 12 columns. The first three columns represent the x, y, and z coordinates related to the CL points, columns 4, 5, and 6 present vectors  $\hat{i}$ ,  $\hat{j}$  and  $\hat{k}$  (related to the tool orientation), columns 7, 8, and 9 represent the x, y, and z coordinates of the respective CC points, and the last three columns represent the  $\hat{q}$ ,  $\hat{r}$ , and  $\hat{s}$ , vector normal to the surface on a given CC point, as exemplified in Figure IV-3.

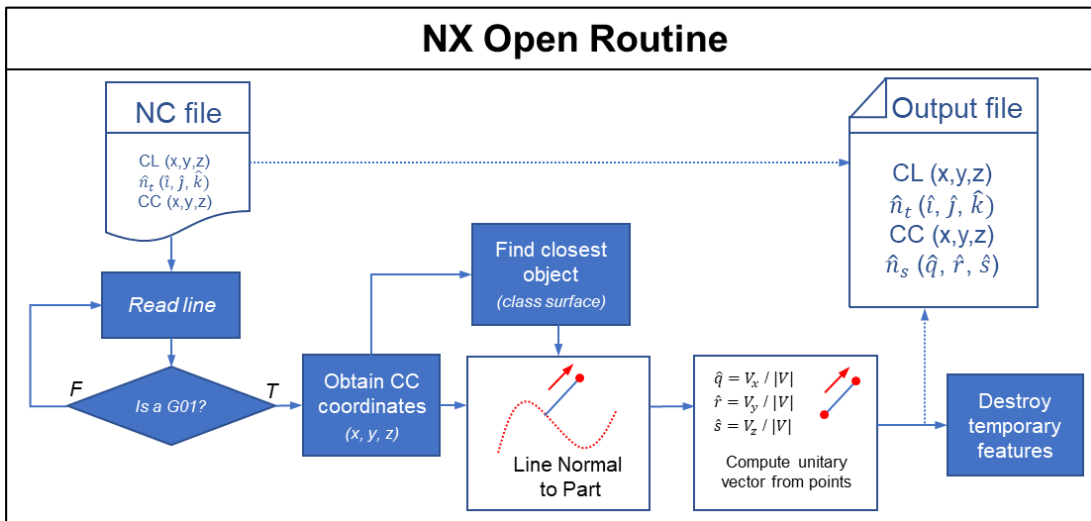
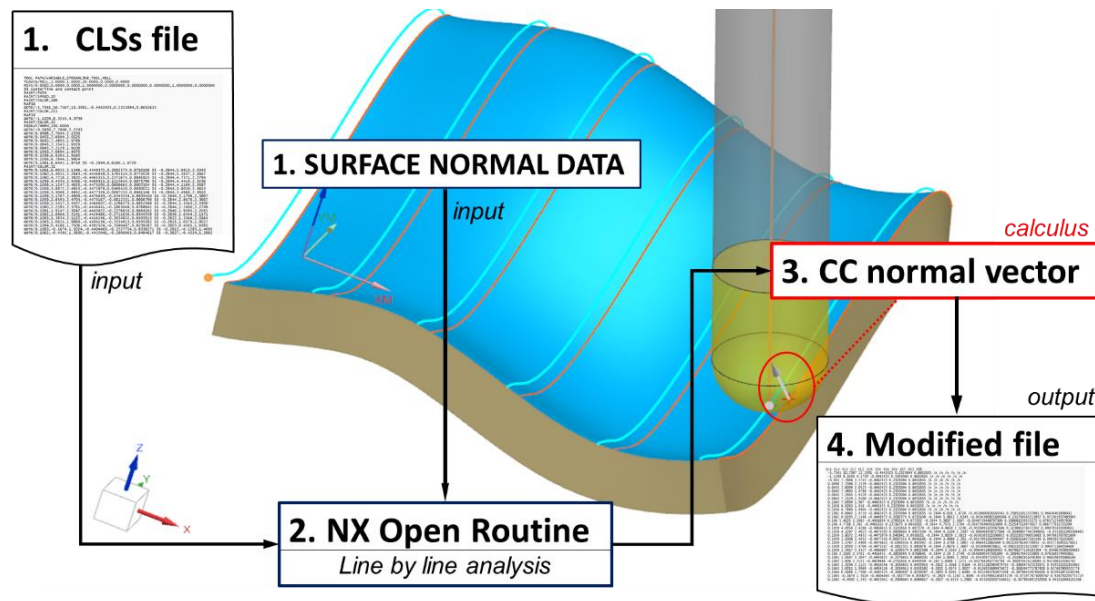


Figure IV-3. NX Open routine flowchart and NX Open programming routine.



It is also important to highlight that this routine was developed thinking in future implementations of force and force-dependent models, so even for surface prediction, the CC and the surface vector are not necessary; they are required during the chip thickness calculation, thus being computed and recorded in the file.

## IV. 4. Geometrical modelling of the tooltip

Before modelling the tool, was defined the reference system to describe its position and orientation in the space. It was defined using the right-hand rule at the centre of the tooltip, with a clockwise rotation on the tool axis, as depicted in Figure IV-4. Then, a mathematical model considering the different geometrical shapes of the finishing tools was developed to describe the tool dome. The first approach considers a single radius tooltip (IV.4.1), and the second expands to a double radius tooltips (IV.4.2). For both cases, is calculated the local radius according to the tool's height, and then the axial and radial immersion angles are calculated to describe the edge position inside the dome of the tool. Finally, the effect of the tool run-out in ball-end tooltips (IV.4.3) can be included as a function of the tool's height –  $r(z)$ . Figure IV-4 presents the tool's schematic for both types of tooltips.

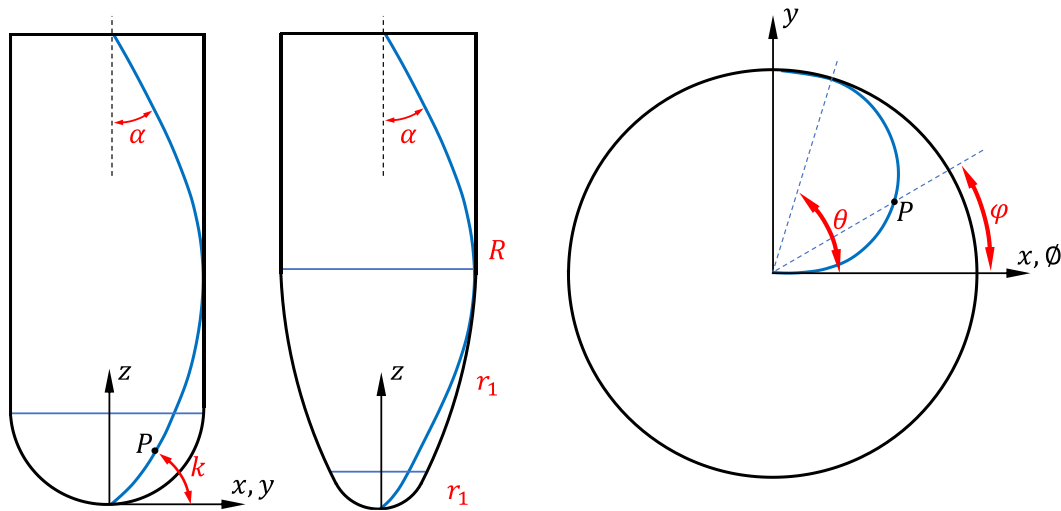


Figure IV-4. Tool schematics for single and double-radius tooltips.

### IV. 4. 1. Single radius tooltip

Considering the given reference system at the end of the tooltip, Eq. 34 gives the coordinates of the dome of a ball-end tooltip;

$$\begin{cases} x_i = R \sin(k_i) \cos \theta_i \\ y_i = R \sin(k_i) \sin \theta_i \\ z_i = R - R \cos(k_i) \end{cases} \quad \text{Eq. 34}$$

where  $k_i$  is the axial immersion,  $\theta_i$  is the angular position, and R is the radius of the tool shaft.

To model a single cutting edge, infinitesimal elements  $i$  must be defined as a function of the height. Considering that the angular position increases as the height increases, a helix can be defined at the tool dome. Defining an angular reference  $\varnothing$  measured from the X-axis and the angular increment with height as  $\varphi_i$ , it gives the angular position  $\theta_i$  (Eq. 35).

$$\theta_i = \varnothing - \varphi_i \quad \text{Eq. 35}$$

Where the angular increment with height  $\varphi_i$  is defined by the tangent at a given point with a plane perpendicular to the tool axis (Eq. 36).

$$\tan \alpha = \frac{\Delta\varphi}{\Delta Z} \therefore \tan \alpha_i = \frac{R\varphi_i}{z_i} \quad \text{Eq. 36}$$

Considering that the ball-end tooltip has a constant helix angle, the infinitesimal edge increment with height can be expressed by Eq. 37.

$$\varphi_i = (1 - \cos k_i) \tan \alpha \quad \text{Eq. 37}$$

Combining equations Eq. 34 to Eq. 37 is possible to define the edges of a ball-end tooltip with a constant helix angle.

#### IV. 4. 2. Double radius tooltips

To model double radius tooltips, first, it was defined a function  $z_i$  that represents the growth of the radius with the high increment at the xz plane (symmetric to the yz plane). Due to the discontinuity of the domes, with one translated from the centre, a piecewise function is used to define the tooltip. Equations Eq. 38 and Eq. 39 define the centre of each dome at xz plane.

$$C_1 = (C_{1x}, C_{1z}) \quad \text{Eq. 38}$$

$$C_2 = (C_{2x}, C_{2z}) \quad \text{Eq. 39}$$

Assuming that the tooltip is symmetric results in  $C_{1x} = 0$  and  $C_{1z} = r_1$ . With continuity of position and tangency (G2) between the shank and the tooltip, and considering the centre  $C_2$  in a plane that contains the tool axis, results in  $C_{2x} = R - r_2$  and  $C_{2z} = c_{zz}$ .

The domain of the tooltip varies from (0,0) to  $(c_{x|y}, c_z)$  for the dome that contains the reference system, and the second dome is defined from  $(c_{x|y}, c_z)$  to  $(c_{xx|yy}, c_{zz})$ , where:

$$c_{x|y} = \frac{Rr_1 - r_1r_2}{r_1 - r_2} \quad \text{Eq. 40}$$

$$c_z = r_1 - \sqrt{r_1^2 - c_x^2} \quad \text{Eq. 41}$$

$$c_{xx|yy} = R \quad \text{Eq. 42}$$

$$c_{zz} = c_z + \sqrt{r_2^2 - (c_x + r_2 - R)^2} \quad \text{Eq. 43}$$

Thus, it is possible to define a piecewise function for the local radius of the tool at a given high  $z_i$ , Eq. 44.

$$r_{(z_i)} = \begin{cases} \sqrt{r_1^2 - (r_1 - z_i)^2} & \text{for } c_z < z_i \\ C_{2x} + \sqrt{r_2^2 + 2c_{zz} - c_{zz}^2 - z_i^2} & \text{for } c_z > z_i > c_{zz} \\ R & \text{for } z_i > c_{zz} \end{cases} \quad \text{Eq. 44}$$

The definition of the helix of the tool is similar to the single dome tool, depending on the axial immersion angle  $k_i$  (given by Eq. 45) and the angular increment with height  $\varphi_i$  (given by Eq. 46), both dependent on the piecewise function  $r_{(z_i)}$ .

$$\begin{cases} 0 < k_{lim1} < \cos^{-1}\left(\frac{c_x}{r_1}\right), & \text{for } [c_x|y, c_z] \\ \cos^{-1}\left(\frac{c_{2x} + c_x}{r_2}\right) < k_{lim2} < \cos^{-1}\left(\frac{c_{2x} + c_{xx}}{r_2}\right), & \text{for } [c_{xx}|yy, c_{zz}] \end{cases} \quad \text{Eq. 45}$$

$$\varphi_i = \frac{z_i \tan \alpha}{r_{(z_i)}} \quad \text{Eq. 46}$$

The combination of equations Eq. 44, Eq. 45, and Eq. 46 defines any helix angle of any ball-end tooltip with a double radii that presents G2 continuity with the tool's shank.

#### IV. 4. 3. Run-out in ball-end tooltips

Run-out  $\rho$  involves both manufacturing errors and clamping miss alignment of the tool-holder system. It can be described as a function of the local radius with the height (Eq. 47), thus dependent on the micro edge element and reliant on angular position and axial immersion angles.

$$r_j(z) = r(z) + \rho(z) \quad \text{Eq. 47}$$

Where  $r_j(z)$  is the local radius of the micro edge element related to the  $j$  flute,  $r(z)$  is the local radius of the tool, and  $\rho(z)$ , the radial deviation of the respective micro edge element depends on the element's position in the space. Considering an ideal manufacturing process for the tools,  $\rho(z)$  can be approximated to a linear function with a reference system as an offset (in the xy plane) and tilt ( $\tau$ ) from the reference tool axis (Eq. 48).

$$\rho(z) = \rho_0(x, y) + f(z, \theta) \quad \text{Eq. 48}$$

Figure IV-5 instantaneously exemplifies the linear movement of an infinitesimal edge element  $i$  with the effect of the tool run-out on the top view. Additionally, other factors, such as tool wear and thermal expansion, can be modelled similarly as a function of the local radius but are not considered in this work.

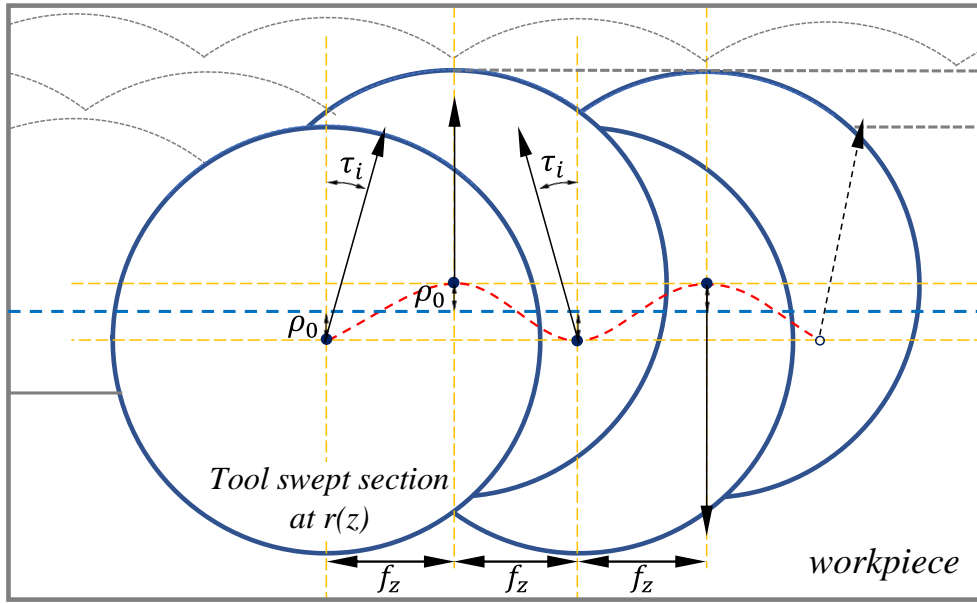


Figure IV-5. Centre deviation caused by run-out at a generic  $z_i$  plane of the tool.

Figure IV-5 shows that in the milling process with run-out, it is possible that only one tooth generates the final surface, so it is proposed a simple calculation to adjust the surface prediction based on the feed-per-tooth, tool run-out, and the number of teeth. The logic consists of comparing the bigger effective radius ( $r_1 = r_{max}$ ), subtracting the theoretical crisp wave ( $h_c$ ) and comparing it to the other teeth; if the value of the effective radius is smaller, it will not participate in the surface generation. Also, the index number of those teeth must be saved for plotting. The average distance of the surface feed-per-tooth mark is given by Eq. 49.

$$\bar{f}_z = f_z \left( \frac{z}{z_c} \right) \quad \text{Eq. 49}$$

Where  $z_c$  is the number of teeth participating in the surface generation, given by Eq. 50.

$$z_c = \sum_{i=1}^{z-1} 1 + i : \{i = 1 \text{ if } r_z > r_1 - h_c; \text{ else } i = 0\} \quad \text{Eq. 50}$$

## IV. 5. Toolpath data treatment

Using the tool geometry (section 2.3) and the toolpath generated by the CAD/CAM (section 2.2), with two procedures, it is possible to predict the surface with an error lower than the tolerance band used in the toolpath generation. The first is calculating the instantaneous positions pondering the known contact positions. The second one is computing the angular position and tilt of the cutting-edge element and pondering with the feed (pondered movement), allowing a better estimation.

### IV. 5. 1. Instantaneous position

Usually, the spindle speed is much higher in the milling process than in the feed. So, it is possible to consider that a complete rotation happens instantly, removing the material. However, in a discrete model, this assumption leads to an additional error associated with the difference between the segment's lengths from the feed per tooth ( $f_z$ ). Thus, a good correlation between these parameters is important for the model's accuracy. When the segment length is bigger than the  $f_z$ , more material is removed, while when  $f_z$  is bigger, the material is underestimated. Otherwise, is necessary to calculate intermediary points to discretize the movement.

Naturally, on complex surface milling, the distance between the NC points can change significantly depending on the surface's tolerance band and local curvature. So, it is necessary to interpolate the mapped surface data obtained by the routine according to the  $f_z$  used to increase accuracy. Figure IV-6 presents a schematic of the method applied to compute intermediary points using the CL and its respective tool orientation.

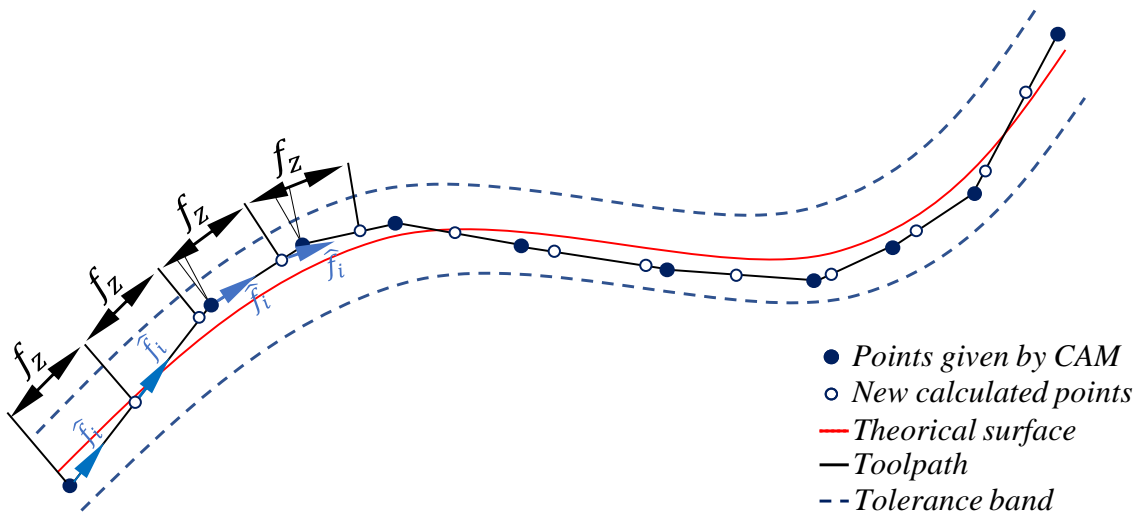


Figure IV-6. Schematics of toolpath adjustment for surface prediction using instantaneous positions.

In the process of discretizing intermediate positions, it also calculates its respective unitary vectors. It is known that the unitary vector of the tool position ( $\hat{n}_t$ ) obtained from the processed 5-axis CL file can be written in terms of  $\hat{i} \hat{j} \hat{k}$  positions given the orthogonal cartesian components relative to  $x$ ,  $y$ , and  $z$  (Eq. 51). At the same time, the data obtained by the programming routine gives the instantaneous tangent plane at the same surface position using its respective CC point and the unitary vector  $\hat{n}_s$  (Eq. 52).

To calculate the instantaneous direction ( $\hat{f}_i$ ), Eq. 53, the product of the unitary vectors relative to CC and CL is computed. And by the cross-product of the tool position with the local surface vector (Eq. 54) is obtained the instantaneous lateral pass  $\hat{g}_i$ .

$$\hat{n}_t = n_x \hat{i} + n_y \hat{j} + n_z \hat{k} \quad \text{Eq. 51}$$

$$\hat{n}_s = n_x \hat{q} + n_y \hat{r} + n_z \hat{s} \quad \text{Eq. 52}$$

$$\hat{f}_i = \frac{\hat{n}_s \times \hat{n}_t}{|\hat{n}_s \times \hat{n}_t|} \quad \text{Eq. 53}$$

$$\hat{g}_i = \hat{n}_s \times \hat{n}_t \quad \text{Eq. 54}$$

### IV. 5. 2. Adjustment of the angular position with the feed

If the spindle speed is not considerably higher than the feed or a better estimation is required, the angular position of the tool edge must be considered. Additionally, cutting-edge orientation is required to include the effect of the tool's helix and the run-out on the surface estimation. Thus, an additional procedure was developed to adjust and synchronize the angular position with the feed (axial movement of the tool). Equation Eq. 55 expresses the angular position in terms of the nominal feed per tooth, which allows the computation of the angular position for each CL (or intermediary point) according to the tool's displacement.

$$f_z = \frac{\Delta d T}{t_{i+1} - t_i} = \frac{\Delta d}{t_{i+1} - t_i} \frac{2\pi}{\omega} \quad \text{Eq. 55}$$

Where  $\Delta d$  is the distance between consecutive CL points, T is one rotation period,  $\omega$  the angular velocity, and  $t_{i+1}$  and  $t_i$  are the intermediate and the initial positions during one rotation, respectively. Considering that the tool has a constant angular speed ( $\omega$ ), it is possible to indirectly correlate the feed distance covered with the angular position ( $\theta$ ). Splitting the toolpath into constant intermediary points will also result in a constant  $\Delta\theta$ . With this consideration and knowing the total distance covered by the tool, it is possible to obtain the angular position of any micro edge elements on the toolpath. Figure IV-7 presents a 2D schematic of a  $\Delta\theta$  weighted interpolation between the CL points.

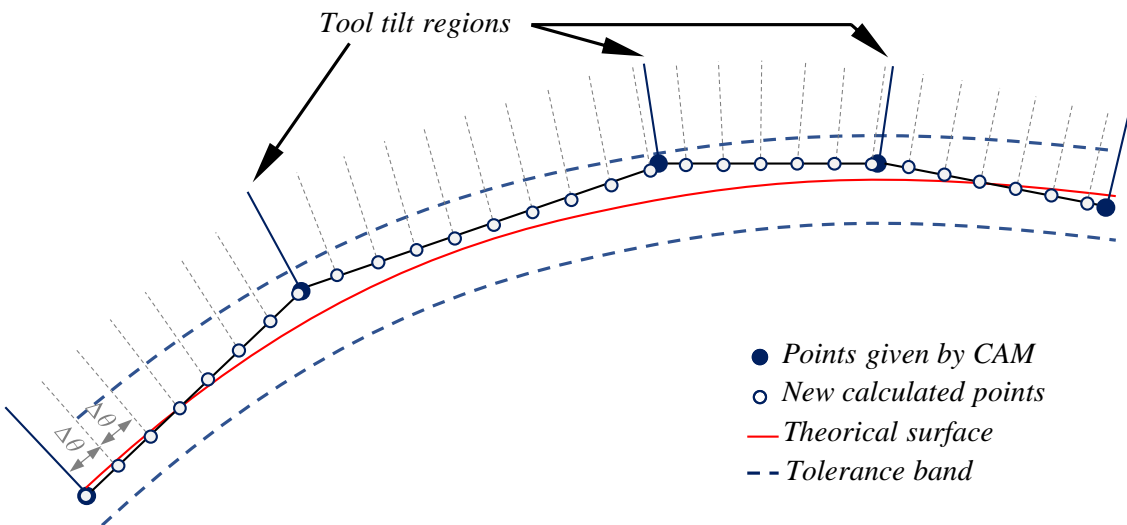


Figure IV-7. Schematics of toolpath discretization with a constant  $\Delta\theta$  and tilt ponderation.

However, when new data points are generated, it is necessary to compute the related tool's tilt. It is done by adjusting to the previously known unitary vectors. Furthermore, in both methods presented, instantaneous or pondered movement interpolation, the data created can be used for any surface. Still, it uses increases the computational time. In the specific case of angular interpolation ( $\Delta\theta$ ), the discretization process is more critical and must be optimized to obtain a good correlation between the precision and the computational time. The smaller the  $\Delta\theta$ , the better the precision, but the higher the computational time. Thus, the trochoidal toolpath of the micro-edge elements were graphed using spline with cubic regression.

## IV. 6. Surface prediction

First, the data were sorted according to the part's world coordinate system (WCS) for easy graphical visualization and evaluation of the surface. To do so, a mesh at the xy plane was created considering the maximum and minimum positions of the NC code, leaving the high in z to be computed considering (IV.6.1) the instantaneous positions and (IV.6.2) the pondered movement of the tool. The tools dome or infinitesimal edge element was translated and oriented according to (WCS) using the procedure described in Figure IV-8. Hereby, each geometrical feature was oriented according to the data obtained by the routine and optimized with the procedure presented in the previous section, obtaining the z height for each respective mesh position.

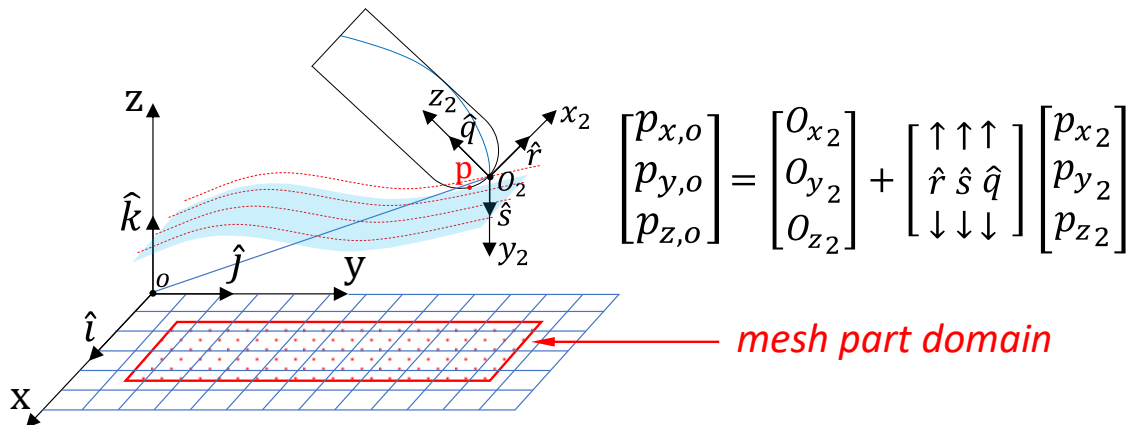


Figure IV-8. Geometrical rotation and translation procedure applied to tool dome and infinitesimal edge elements.

After that, two different methods were applied to validate the surface modelling. The first was a simple analytical model to predict the scallop height and theoretical roughness, considering the instantaneous positions of the tool dome. The second is using the data cloud of the surface mesh to compute the surface roughness and deviations.

**IV. 6. 1. Scallop height considering instantaneous positions of the tool**

In order to obtain a local estimation of the quality of the surface using instantaneous positions, a simple model to calculate the scallop height of a generic shape tooltip was developed. The scallop height can be directly associated with the roughness and indirectly to measure the quality of the milling process.

To estimate the theoretical roughness of the surface considering the instantaneous positions, the tool's geometry, the discretized toolpath, and cutting parameters  $a_e$  and  $a_p$  are required. In the case of 5-axis milling, the tilt and lead angle must be considered. In the specific case of 3-axis ball-end milling on a flat plane where only the ball-end tooltip acts in the cutting process, the scallop height only depends on tool radius and stepover, as presented in Eq. 56. The scallop height ( $h_c$ ) also can be used to calculate the roughness  $Rz$  (Eq. 57) when are repetitive patterns (Liu et al., 2005; Ozturk et al., 2009).

$$h_c = R \left( 1 - \sqrt{1 - \left(\frac{f_z}{2R}\right)^2} \right) \tag{Eq. 56}$$

$$Rz = \frac{\sum_{n=1}^5 Rz_n}{n} \tag{Eq. 57}$$

Where  $\tau_l$  is the tool inclination on the feed direction and  $\tau_t$  is the lead angle.

To include the run-out of the tool and calculate the scallop height for a generic tool shape considering the lead angle  $\tau_t$ , it is first necessary to know the engagement between 2 consecutive instantaneous positions. Considering the generatrix curve of the dome and the instantaneous positions, it is possible to include the tool run-out as a function of the  $r(z)$ , as described in Eq. 47. Figure IV-9 presents a schematic of a generic tool shape in two consecutive cutting steps.

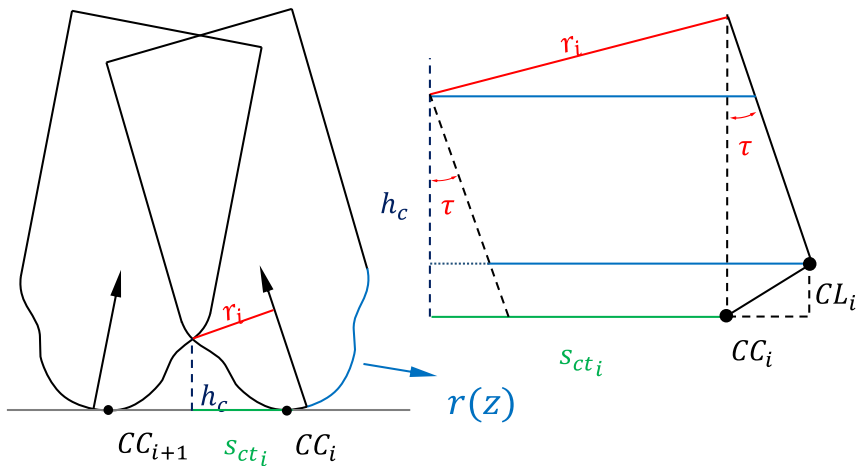


Figure IV-9. Scallop height of a generic tool shape considering two consecutive cutting steps.

As the scallop height of a generic tooltip is dependent on the distance to the crisp wave  $s_{ct}$  (Eq. 58) another function is necessary for its calculation. Knowing that the sum of the



distances of two consecutive points to the scallop height is equal to the distance of the cutting contact points (Eq. 59). By substituting equation Eq. 58 into Eq. 59 (for the two consecutive positions), the scallop height for 5-axis milling (Eq. 60) can be obtained.

$$s_{ct_i} = (h_c - |CL - CC|_z) \tan \tau + \frac{r_i}{\cos \tau} - |CC - CL|_x \quad \text{Eq. 58}$$

$$s_{ct_i} + s_{ct_{i+1}} = \overline{CC_i CC_{i+1}} \quad \text{Eq. 59}$$

$$h_c = \frac{|CL-CC|_{z_1} \tan \tau_1 + |CL-CC|_{z_2} \tan \tau_2 + |CC-CL|_{x_1} + |CC-CL|_{x_2} - \frac{r_{i_1}}{\cos \tau_1} - \frac{r_{i_2}}{\cos \tau_2}}{\tan \tau_1 + \tan \tau_2} \quad \text{Eq. 60}$$

Even the CAM software precisely predicts the scallop height on lateral passes, mostly because it is required for some of the toolpath calculations; the model can be expanded using the same methodology to predict the roughness in the cross-feed direction. However, some considerations must be addressed, like the angle tilt instead of the lead and a linear point distribution in the feed-cross direction. To improve process estimation it is necessary to consider the 3D texture marks of the surface. In the sequence, the development for predicting the surface texture is presented.

#### **IV. 6. 2. Surface prediction using the mesh data cloud**

The simulated surface can be obtained by translating the tool position and plotting the minimum z distance for each position of the equally distributed data cloud. Then, the data can be compared with confocal microscopy results.

Likewise, the toolpath of an infinitesimal cutting-edge element was plotted according to a specific height, obtaining the trochoidal movement of the ICE element, and it is possible to compute the trochoid intersections for the surface estimation. The smaller the  $\Delta\theta$  used for computation, the higher the precision of the trajectory of the element.

### **IV. 7. Developed routine and modelling outputs**

This section presents the results obtained simulating the use of the routine for data collection considering a generic free-form surface and 5-axis ball-end milling using a raster strategy. Then, the output data obtained is used to simulate the milling texture of ball-end milling considering the two proposed approaches, the instantaneous position, and the pondered movement of the ICE element.

#### **IV. 7. 1. Routine outputs**

Figure IV-10 presents an example of a 5-axis toolpath program and the results obtained using the developed methodology.

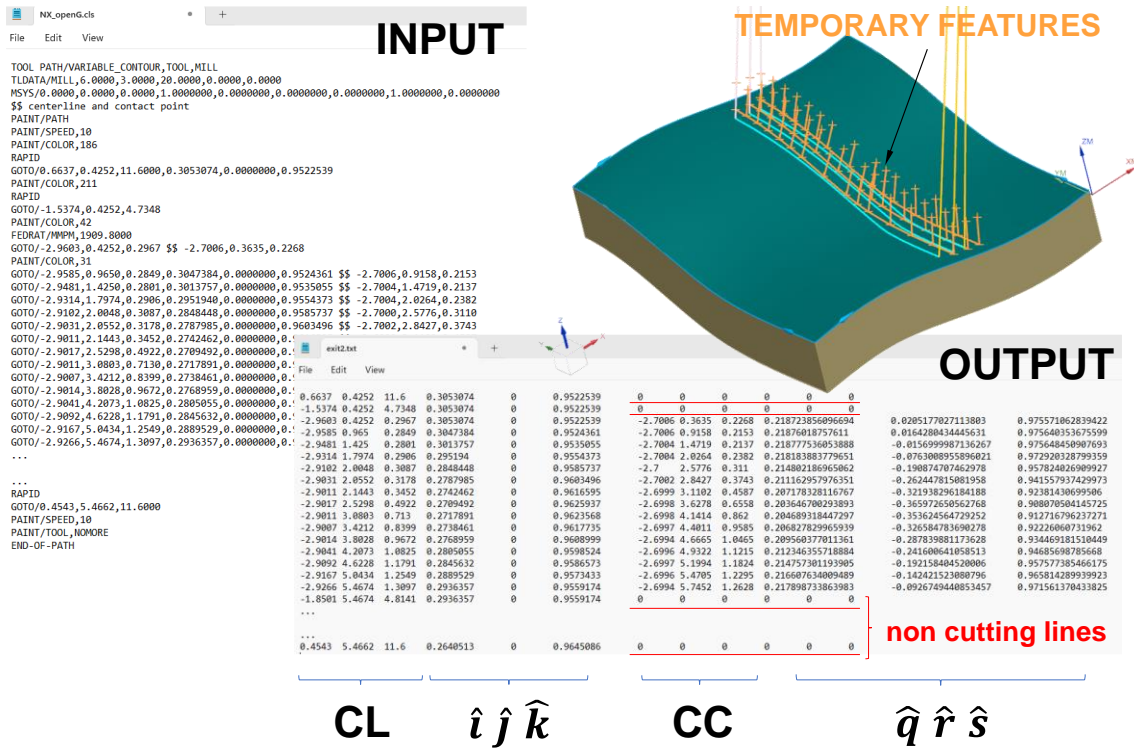


Figure IV-10. Programmed routine for 5-axis data acquisition outputs.

As can be seen, Figure IV-10 presents the temporary features (lines and points) used to support the computation of the normal vector at the CC location and the output data (CL, CC, and respective vectors of the tool and surface). The output file also shows that the non-cutting lines can be identified through the null values of CC and surface normal vector columns. However, depending on the software used for posterior analysis, it can change to NA or N/A.

During the development of the routine, it was observed that the graphical representation of features and part rotations consumes a lot of computational resources, making the routine slow. Thus, in a depuration step, camera rotations and the graphical plotting of the temporary features were suppressed.

### IV. 7. 2. Data treatment and model outputs

Figure IV-11 presents an example of the results obtained using the geometrical model developed together with the routine data output. Figure IV-11a presents the geometrical model of the ball-end tooltip considering the dome and the infinitesimal cutting-edge element according to the tool's height  $r(z)$ . Figure IV-11b presents a 5-axis toolpath trajectory and the topography simulated by the software Siemens® NX. Then, two approaches for data treatment and milling process evaluation are presented. The first is by computing intermediary data according to a specific feed-per-tooth aiming the topography prediction using the instantaneous position procedure (Figure IV-11c). The

second procedure, depicted in Figure IV-11d, discretizes the lineal toolpath into constant  $\Delta\theta$  and uses this data to compute the toroidal toolpath of the ICE (pondered movement). Even though the instantaneous position method is simpler, the pondered movement procedure allows a more precise prediction of surface texture, especially in the lateral feed direction. Additionally, the detailed movement of each ICE allows including the tool run-out, enhancing the prediction of surface roughness and topography.

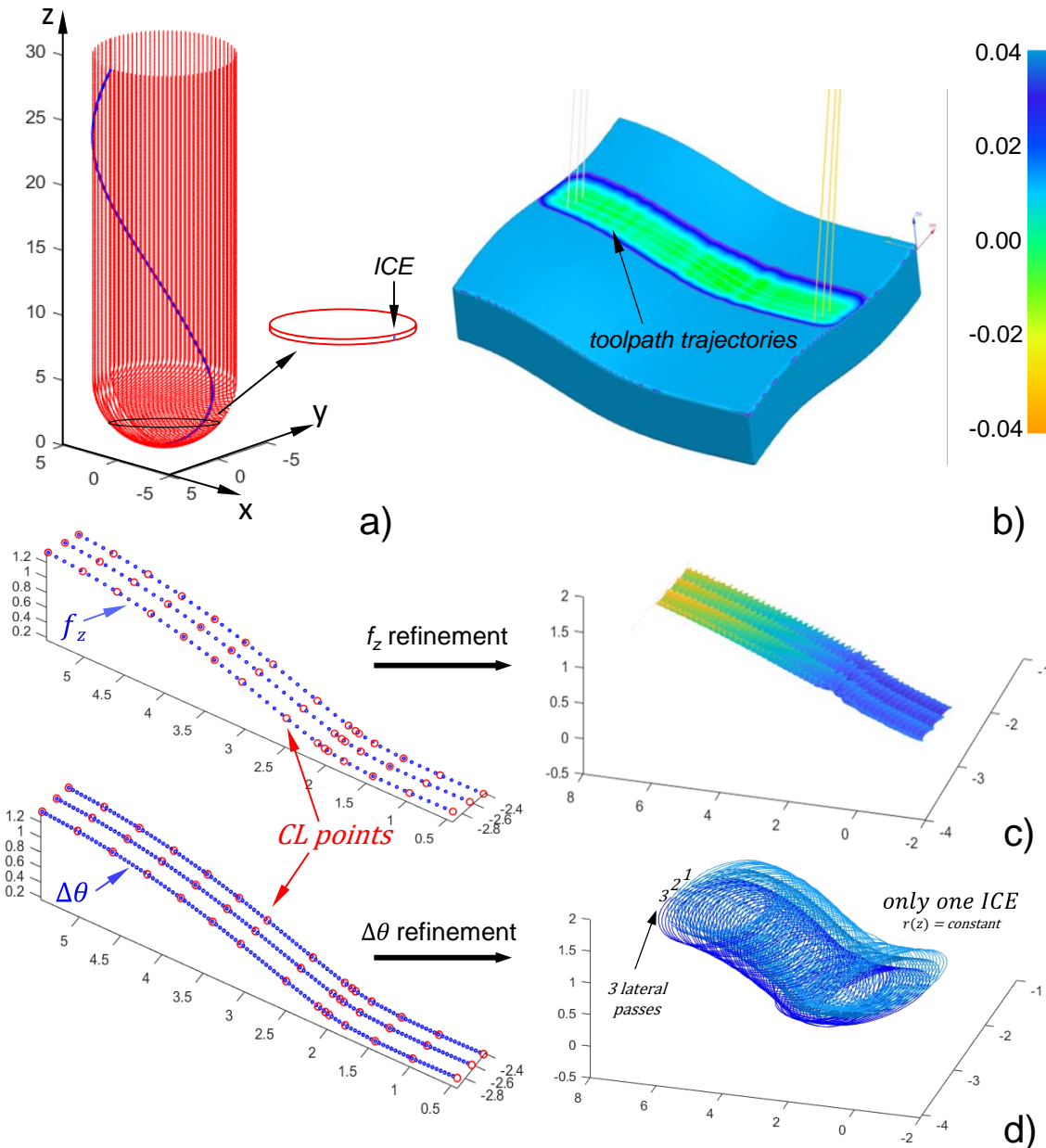


Figure IV-11. a) Ball-end tool dome and helix edge; b) 5-axis milling on a free-form surface simulated by the cam software; c) Toolpath data treatment for instantaneous surface modelling and application; d) Toolpath data treatment for ICE trochoidal movement and application.

Even though it presents only results with a single radius ball-end tooltip, the same procedure is valid for double radii tooltips because of the discrete modelling of the tool dome and ICE element as a function of the tool's height. Two case studies were conducted on a part containing free-form surfaces to demonstrate and evaluate the

developed modelling approaches. The first evaluates a conventional ball-end mill (Section IV. 8), while the second assesses the results of a double radii tooltip lens shape (Section IV. 9).

## IV. 8. Study Case 1 – Conventional ball-end tooltip

This study case aims to help overcome the limitations of CAM software in simulating the real texture of the machined surface, which does not consider crisp heights in the tool feed direction. The developed methodology (sections IV. 3 to IV. 6) is applied on a blade workpiece containing free-form surfaces designed, manufactured, and finished with single radius ball-end tools. Then, the routine was applied to obtain information directly from the software about the CAD geometry of the part and the toolpath calculated by the CAM (CC and CL data) to simulate the milled texture of the blade surface.

### IV. 8. 1. Materials and Methods

To evaluate the proposed methodology, a bladed workpiece containing free-form concave and convex surfaces was first designed using the software Siemens® NX, and the manufacturing process was investigated. The material used was a solid bulky cylinder with a nominal diameter of 46.5 mm of Waspalloy AMS 5706, with its nominal composition presented in Table IV-1. The machine used to manufacture the blade was a multitask machining centre Mazak i200, and the milling experiments were conducted using the machine tailstock.

Table IV-1. Composition of Waspalloy AMS 5706.

Ni	Cr	Co	Mo	Ti	Fe	Al	Zr	C	Mn
58.64	19.34	12.27	3.82	3.04	1.35	1.33	0.05	0.04	0.03
Si	Cu	B	Mg	P	N	S	Se	Pb	Ag
0.03	0.02	0.005	0.005			< 0.001			

The blade was finished using a ball-end tooltip with a 5 mm radius manufactured in micro grain solid carbide with 10% Co coated with multilayer TiSiN (3800 HV 0.05) with four flutes and a 30° helix angle. The tool was mounted on a high-torque toolholder with a 40 mm cantilever, and a presetter Zoller® SmartCheck 600 was used to measure tool length and the static run-out, as depicted in Figure IV-12b.

The milling trajectories were programmed on the software Siemens® NX, considering rough, semi-finishing, and finishing operations. A spiral toolpath with 0.4 mm of  $a_e$  was used in the semi-finishing operation, leaving the part with 0.4 mm stock for the finishing operation. The finishing process was conducted in down-milling with constant  $a_p$

(0.04 mm),  $a_e$  (0.2 mm),  $f_z$  (0.05 mm/tooth), and cutting speed of 80 m/min (parameters recommended by the tool maker).

Then, three different regions with 10 mm lengths were evaluated using, in all of them, a 5-axis spiral strategy (with a 0.01 mm tolerance band). This strategy avoids tool entrances and exits that damage the surface and compromise its integrity. Also, the direct action of the tooltip was avoided by tilting the tool in the feed direction. Three cutting engagements were assessed, one in each region, 5, 15, and 25 degrees, respectively. Figure IV-12a depicts the toolpath strategies.

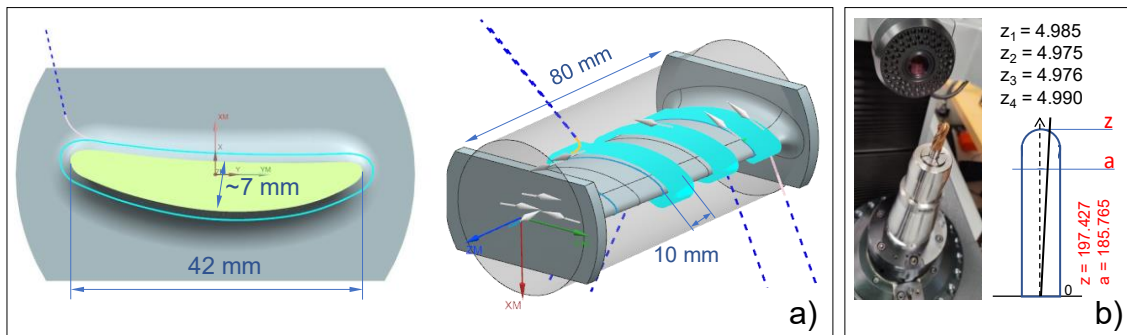


Figure IV-12. a) Part model and machining strategies. b) Tool with holder presetting.

The procedure presented in Section IV. 6.2. *Surface prediction using the mesh data cloud* was applied to simulate the texture of the machined surfaces. Then, the results were compared to the one measured using a confocal microscope Leica® DCM3D, with software Leica® Map 6.2, where the surface and the roughness were analysed within data cloud exportation. The surface data was treated using Matlab® 2021 software to compare the values with the simulation predictions using the proposed model. During the data treatment, the surface was analysed as scanned and without form, where a 5th-order polynomial regression was used to ease the roughness and model evaluation.

### IV. 8. 2. Results and modelling evaluation

The manufacture of a blade in Waspalloy AMS 5706 using continuous 5-axis milling with a ball-end tooltip and the inspection regions, respectively, to the lead angles of 5, 15, and 25 is presented in Figure IV-13, together with the measured machined surface by confocal microscopy.

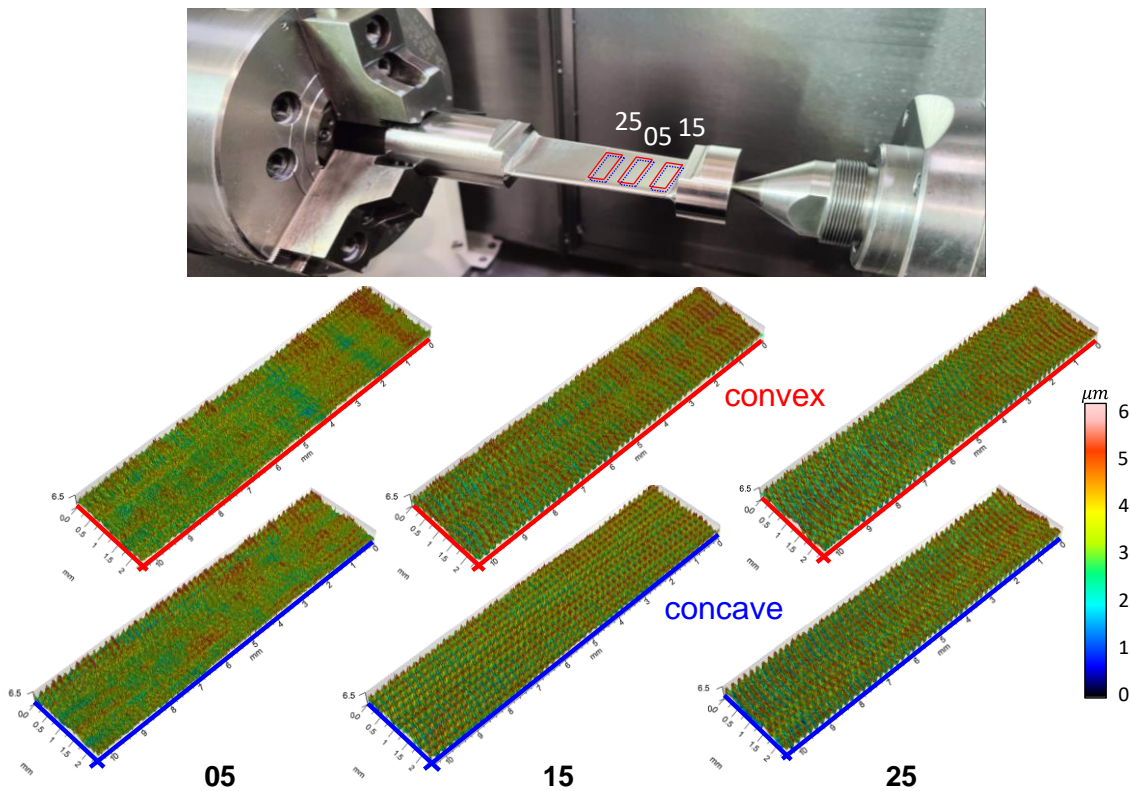


Figure IV-13. Machined blade and topography inspection of the central part.

Figure IV-14a and Figure IV-14b presents the roughness profile results measured for all cases evaluated with two samples for each condition obtained by confocal microscopy, allowing the evaluation of the cusp marks on the feed direction, respective roughness, and characteristic noise that comes from tool scratches (tool wear or imperfection), plastic deformations, and tool run out.

Table IV-2 summarizes the results of the roughness  $R_a$  and  $R_z$  of the profiles measured by confocal microscopy depicted in Figure IV-14a. It can be seen that the roughness is higher on the convex side for all cases evaluated, a fact directly related to geometrical factors of the surface curvature of the part and CWE, which contributes to convex and reduces on concave surfaces. Also, it was observed that the roughness increases with the increase of the lead angle.

Taking into account that only the ball dome acts in the cut (the same geometry for all tilts) and evaluating the surface texture, it can be inferred that the plastic deformation and elastic recovery of the milling process were the main causes of roughness increase with lead, corroborating with reported by some authors (Basso et al., 2022; Batista et al., 2017). It is also important to add that a higher lead angle and, consequently, higher effective cutting speed promotes ploughing reduction (de Souza et al., 2015). The different effective cutting speeds are presented in Table IV-3 and help support the hypothesis of the roughness increase with lead.

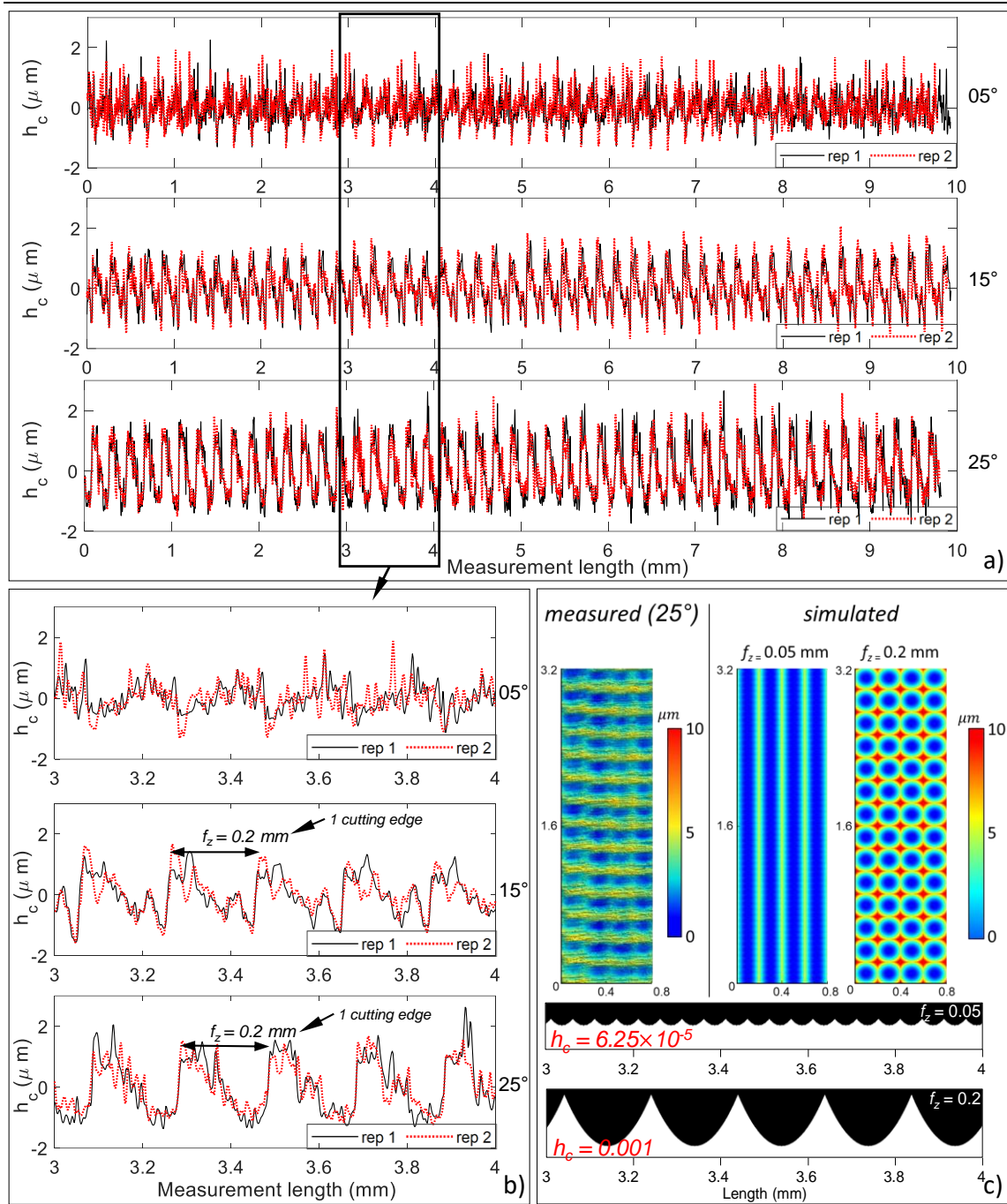


Figure IV-14. Roughness and topographical analysis. a) measured roughness profile; b) profile evaluation; c) comparison between simulated and measured with 25° lead angle.

Table IV-2. Surface roughness obtained by confocal microscopy.

Lead angle (°)	Concave			Convex			
	5	15	25	5	15	25	
$R_a$ ( $\mu\text{m}$ )	S1	0.314	0.418	0.596	0.403	0.499	0.625
	S2	0.333	0.437	0.513	0.459	0.441	0.502
	$\bar{x}_{Ra}$	0.324	0.428	0.555	0.431	0.470	0.564
	$\sigma_{Ra}$	0.013	0.013	0.059	0.040	0.041	0.087
$R_z$ ( $\mu\text{m}$ )	S1	2.07	2.20	2.65	2.55	2.77	2.82
	S2	2.29	2.59	2.60	2.36	2.43	2.67
	$\bar{x}_{Rz}$	2.18	2.40	2.63	2.46	2.60	2.75
	$\sigma_{Rz}$	0.16	0.28	0.04	0.13	0.24	0.11

The Roughness  $Rz$  presented in Table IV-2 was used to evaluate the simulated topography obtained with the instantaneous position procedure. The simulated surface presents repetitive marks that lead to repetitive samplings during  $Rz$  calculation, and its mean is equal to the crisp height ( $Rz = h_c$ ). So, the roughness  $Rz$  of the blade surface without form was compared with the  $h_c$  of the idealized surface on the feed direction, as presented in Figure IV-14c. The theoretical and simulated  $h_c$  of  $0.0625 \mu\text{m}$  obtained for a feed-per-tooth of  $0.05 \text{ mm/tooth}$  was much lower than the measured (about  $2.5 \mu\text{m}$ ), indicating the presence of more problems like tool run-out and plastic deformations.

Table IV-3. Lead angle effect on the effective radius and cutting speed ( $a_p$  of  $0.4 \text{ mm}$ ).

	Lead angle (°)		
	5	15	25
<b>V<sub>cef</sub> max(%)</b>	47.1	61.7	74.4
<b>R<sub>ef</sub> max (5 mm)</b>	2.353	3.083	3.720
<b>R<sub>ef</sub> max (z1) – 4.990 mm</b>	2.3501	3.0788	3.714
<b>error (%)</b>	0.0012	0.1479	0.1634
<b>R<sub>ef</sub> max (z2) – 4.985 mm</b>	2.3487	3.0765	3.7109
<b>error (%)</b>	0.1853	0.2219	0.2451
<b>R<sub>ef</sub> max (z3) – 4.976 mm</b>	2.3461	3.0724	3.7054
<b>error (%)</b>	0.2966	0.3551	0.3922
<b>R<sub>ef</sub> max (z4) – 4.975 mm</b>	2.3458	3.0720	3.7048
<b>error (%)</b>	0.3089	0.3699	0.4085

The evaluation of the milling surface (Figure IV-13) and the roughness profiles (Figure IV-14) of the six surfaces (3 concaves and three convexes) allowed identifying that 5 degrees lead angle did not produce the characteristic intermittent marks of the milling process related to the feed-per tooth. In this specific case, the surface has several scratches and random marks that characterize plastic deformation, probably due to low effective cutting speed (Table IV-3). Surprisingly, it was also the one with lower roughness, with crisp highs of about  $2.5 \mu\text{m}$  on the concave side and  $1.9 \mu\text{m}$  on the convex side. Probably, a combination of factors such as high feed per tooth, lower run-out at the tool centre (and its oscillation on a plane close to the surface normal), and stable clamping systems propitiate a smoother surface. Moreover, it highlights that even though the centre does not participate in the cut, its nearby region and reduced cutting speed supposedly propitiate a controlled plastic field that improves the final milled surface. However, concerns about the tool wear and higher forces on the z direction must be deeply addressed.

The surfaces manufactured with 15 and 25 lead angles presented clear peaks and valleys. However, the marks were not as distant as the programmed feed-per-tooth ( $0.05 \text{ mm/tooth}$ ) but by  $0.2 \text{ mm/tooth}$ , implying that the run-out was present in the process. This resulted in a deep investigation of the tool run-out. Hence, to improve the surface prediction, the methodology to identify and correct the feed-per-tooth that generates the surface was applied (Eq. 49 and Eq. 50).



First, the difference in the effective cutting radius was calculated for all cases evaluated. Table IV-3 presents the computed maximum effective cutting speed according to the lead angle and run-out. It can be seen that the difference between the radius is bigger than the theoretical crisp height, implying that only the major tool edge will directly generate the final surface. Thus, a feed-per-tooth correction was done to improve the surface prediction, increasing the simulation parameter  $f_z$  to 0.2 mm/tooth. The improved result of the surface prediction is depicted in Figure IV-15c. It is important to highlight that even though only one tooth generates the final surface, the others act in the cut (if  $a_p > \text{teeth run out}$ ), promoting a gradual removal that can affect the cutting process and surface topography.

As presented in Table IV-3, the proportional cutting speed in the case of a  $5^\circ$  lead angle is reduced by more than half, affecting the cinematic energy that propitiates shearing and increasing the ploughing phenomena, gradually lowering at 15 and 25 degrees, respectively. Furthermore, it was also observed that the lead angle tends to magnify the difference between the radius increasing the tool run-out together with the effective cutting speed. As tilting increases, the difference increases, affecting the roughness, which is one of the main factors that justify the roughness increase from 15 to 25.

Still, with the simulated topography for 0.2 mm/tooth, the crisp height observed was about four times lower than the measured by confocal microscopy independently of the surface curvature (concave or convex region). This can be attributed to the ploughing effect and elastic recovery of the surface, which cannot be predicted by the geometrical models of the surface. Figure IV-15 compares at six different tool heights the trochoidal movement of 4 different ICE elements with the equivalent diameter measured on the Zoller presenter (Figure IV-12b), allowing the evaluation of the effect of the three different levels of tilting 5, 15, and 25 lead angle degrees together with the tool run-out present on the machining process.

Figure IV-15b presents a top perspective of the cutting, grouping the ICE by the tool height ( $r(z) = l_i$ ). The first that can be noted is that the lateral cusp height decreases as the tool height increases. Secondly, the difference between the lateral crisp height using two feed-per-tooth ( $f_z$ ) levels, 0.05 and 0.2 mm/tooth, can be observed. The four times magnification of the feed-per tooth produced a significative decrease in the roughness, from about 19 to 14 times with the lateral crisp height in the first three levels presented ( $l_2$ ,  $l_3$ , and  $l_4$ ), respectively, 10, 20 and 30% of the theoretical crisp height on the feed direction (considering the effective  $f_z = 0.2$  mm/tooth), highlighting the importance of measuring the tool run-out for a correct estimation of the effective  $f_z$  on the surface roughness evaluation with ball-end tooltips.

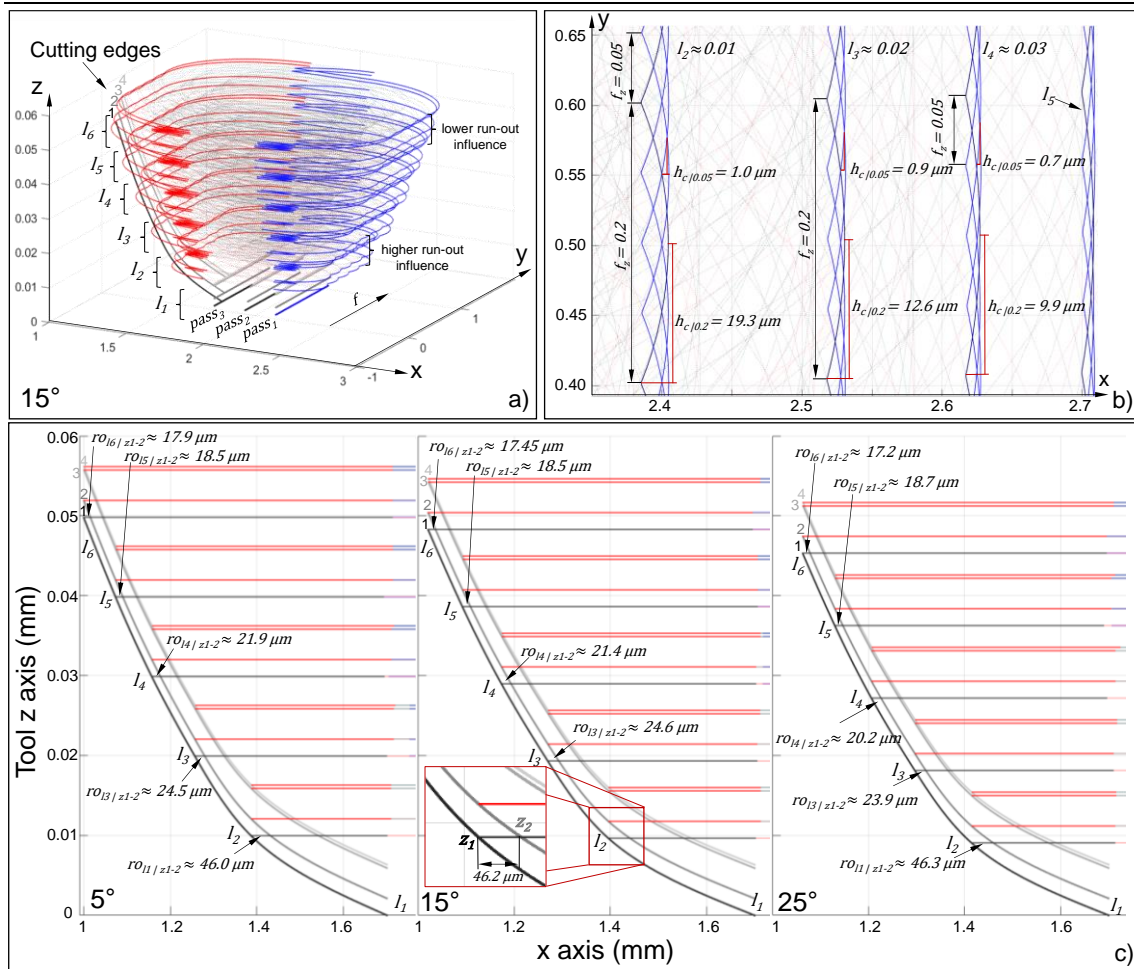


Figure IV-15. a) Simulation of the ICE trochoidal movement: a) isometric view of 3 passes with 15° lead angle; b) top view and theoretical lateral roughness using two levels of feed-per-tooth; c) lateral tool run-out on six tool heights considering 5, 15, and 25 lead angles.

Hereafter, Figure IV-15c presents the effect of the tool run-out. It is depicted that the effect of the lead angle on the lateral run-out is non-linear, with a bigger run-out at the centre of the tool, increasing with the tool tilting, corroborating with the higher roughness found with a tilting increase (Table IV-3). It also can be seen that even run-out decreases with the tool height, it is still higher than the difference in magnitude of the measured tooth in the Zoller presetter (~15 μm), supporting the idea that only one tooth of the tool generates the final surface.

Lastly, the application of the proposed methodology is presented on a section of the machined blade, locally evaluating the spiral toolpath used in the manufacture. The results depicted in Figure IV-16 allow the visualization of the very uneven CL points distribution (red dots) calculated by the CAM software. A significant number are located on surface regions with high curvature (small surface local radius), indicating the necessity of data normalization for a proper prediction. Therefore, the developed routine facilitates the data output with a more even distribution and considers the feed-per-tooth marks of 5-axis profiles over the hole surface, as can be seen in Figure IV-16b.

However, the data cloud generated and the complexity of generating the intersections or contours in highly curvy free-form surfaces limit the direct implementation of the trochoidal movement of the ICE element. Still, the developed model is a powerful tool that allows for obtaining texture aspects and the theoretical roughness of the machined surface locally by an infinitesimal approach, as presented in Figure IV-16c.

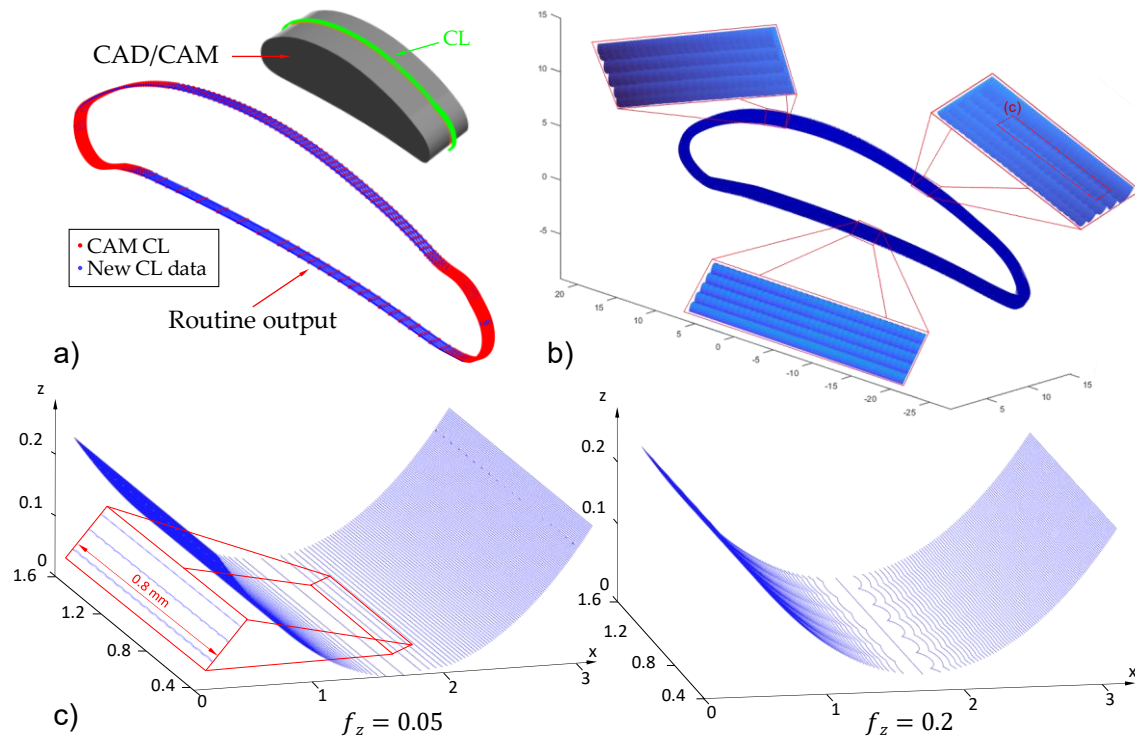


Figure IV-16. a) CAM programming and refined data obtained by the routine for a blade profile; b) Simulation of the surface using the treated data; c) ICE trochoidal movement on an infinitesimal plane.

### IV. 8. 3. Conclusions

In this work, it was observed that the CAM simulation does not provide a real estimation of the surface because it did not consider the crisp height in the feed direction. Thus, the instantaneous contact of the ball-end tool with the surface was mathematically modelled to identify the final topography and the trochoidal movement of the instantaneous cutting-edge element along the toolpath. A routine for data acquisition using CAD/CAM software with an open interface was developed to support the modelling, providing information on the instantaneous positions of the tool and surface. The proposed routine and model were evaluated through roughness prediction on a blade of Ni-Cr-based alloy manufactured in 5-axis milling with different tool inclinations. The main conclusions are:

- The developed model allowed the simulation of the crisp height in the direction of the lateral depth of cut ( $a_e$ ) and on the feed direction ( $f$ ), which the commercial CAM software does not compute, and also provides the identification of the number of the tooth that generates the final surface for a more accurate topography prediction.

- In the ball-end milling with a lead angle of 5 degrees, even with the tooltip centre not participating in the cut, its nearby region and low effective cutting speed affected the final surface, propitiating a plastic deformation dominance, making it hard to identify the characteristic cusp marks of the process, and propitiating a higher discrepancy to the simulated surface. In this specific case, the ploughing modelling is still necessary for improved surface prediction. Nevertheless, this combination resulted in lower roughness due to a lack of crisp highs.
- In cases of 15 and 25 lead angles due to the tool run-out, only an edge of the tool generates the final surface, a fact proved through the crisp height modelling, run-out measuring, and confocal imaging analysis. The modelling process showed the capability of adjusting and improving the topography prediction with the input of the measured run-out and the calculated crisp height.
- The developed routine propitiates a discretized output file for an arbitrary toolpath generated in a 5-axis CAM with automatic selection of the features involved, providing important data for modelling using both CL, CC with its respective vectors related to the tool and surface in a given instant.
- The evaluation of crisp height showed that the lead angle affects the run-out and the effective cutting speed, influencing the surface texture. Also, the simulation of the movement of the ICE elements allowed the identification of the higher the element position in relation to the tool reference system, the lower the effect of the tool run-out.
- Even though the modelling results presented a good correlation between the feed marks and the measured topography, the errors associated with the theoretical crisp height were still significant (about four times), and the effects of the effective cutting speed of the tooltip, feed rate oscillation, tool run-out, and cutting parameters which can be addressed in future works toward robust free-form surface modelling.

#### **IV. 8. 4. Future works**

Even though it has been possible to quantify the local crisp height marks with the free-form surface discretization, the proposed model cares for a graphical representation of the surface considering the movement of the ICE elements of the tooltip, which is the focus of future work.

Also, the proposed method can be expanded to simulate more complex problems of the free-form milling process, predicting the tool-workpiece contact and, consequently, the components of the cutting forces, enabling the estimation of tool deflection, geometric deviation, and tool wear, among others. Also, the model can be improved by addressing

other factors, such as the material properties, the effective cutting speed of the tooltip (ploughing), and the feed rate oscillation during the milling process towards a robust surface texture modelling with ball-end tooltips.

## **IV. 9. Study Case 2 – Comparison of the surface finishing with different tooltips**

Study case 2 advances into simulating the texture of machined free-form surfaces considering ball-end tooltips. In this study, a blade workpiece containing free-form surfaces is finished with different types of ball-end tooltips and cutting contact conditions. The finishing process is investigated using a conventional ball-end tooltip and a more recent lens-shape barrel tooltip. The different CWE conditions are evaluated through the surface texture inspection, and the developed methodology (sections IV. 3 to IV. 6) is applied to evaluate and improve the understanding of the process.

### ***IV. 9. 1. Materials and Methods***

To evaluate the effect of different CWE on the milling process of free-form geometries, a blade manufactured in Waspalloy AMS 5706 was finished using two ball-end mills and cutting conditions. The blade's central region was split into 9 regions (Figure IV-16a), machined under different cutting contact conditions, and the different surface textures produced were evaluated.

A multitask machining centre Mazak i200 was used to machine the blade together with Siemens® NX software to program the milling trajectories considering rough, semi-finishing, and finishing operations. All finishing and semi-finishing experiments undergo 80 m/min cutting speed, feed-per-tooth of 0.05 mm/tooth, HPC (80 bar), downmilling cutting conditions, and 3D spiral strategy using the machine tailstock. The blade was milled from the tailstock to the clamp chunk, increasing the set rigidity (9 to 1) using the concept presented in Figure II-30. To semi-finish, a lateral pass ( $a_e$ ) of 0.4 mm was used to mill half of the part until left 0.4 mm stock and the other half until 0.6 mm stock for the finishing operation, as depicted in Figure IV-17b.

For the finishing operation, two different types of tools (Figure IV-18a), 3 levels of lead angle, 2 levels of depth of cut, and constant lateral pass were evaluated. The three levels of lead angles were 5, 15, and 25 degrees, chosen to obtain different dominances of the radius on the chip formation according to the lens-shaped ball-end tooltip. The depth of cut were 0.4 mm and 0.6 mm, and the constant lateral pass was 0.2 mm. Table IV-4 presents the experimental matrix.

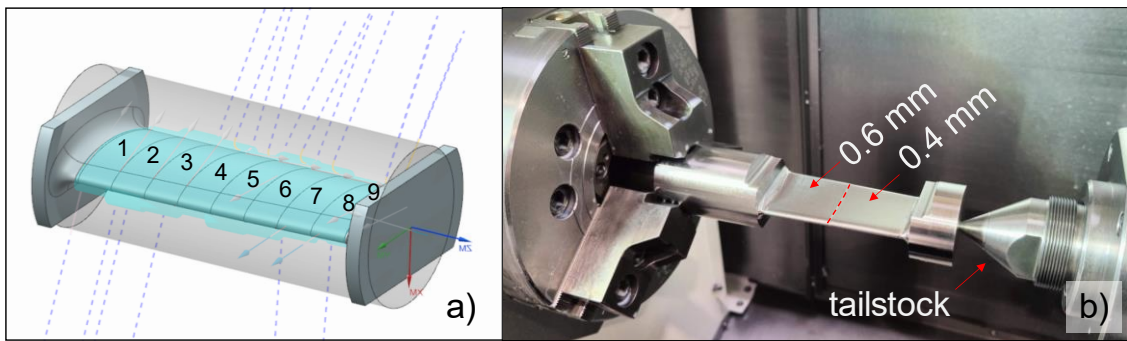


Figure IV-17. Blade geometry: a) CAM finishing toolpath evaluated; b) semi-finished.

Table IV-4. Experimental matrix.

Region	1	2	3	4	5	6	7	8	9
<b>Tooltip</b>	Ball-end	Lens	Lens	Lens	Lens	Lens	Lens	Ball-end	Ball-end
<b>Lead angle (°)</b>	25	25	15	05	25	15	05	05	15
<b>a<sub>p</sub> (mm)</b>	0.6	0.6	0.6	0.6	0.4	0.4	0.4	0.4	0.4

The tools used were a ball-end tooltip with a 5 mm radius and a barrel lens tool, with a major radius of 25 mm, a minor of 2 mm, and a body of 5 mm, thus with proportional angular speed. Both tools were manufactured by the same toolmaker in micro grain solid carbide with 10% Co coated with multilayer TiSiN (3800 HV 0.05) with four flutes, a 30° helix angle, and a chisel edge (CE) at the tooltip uniting two edges, like a drill bit. They were mounted on a high-torque toolholder with about 40 mm cantilever and presetted in a Zoller® SmartCheck 600 machine, where the tool length and the static run-out were measured, depicted in Figure IV-17b.

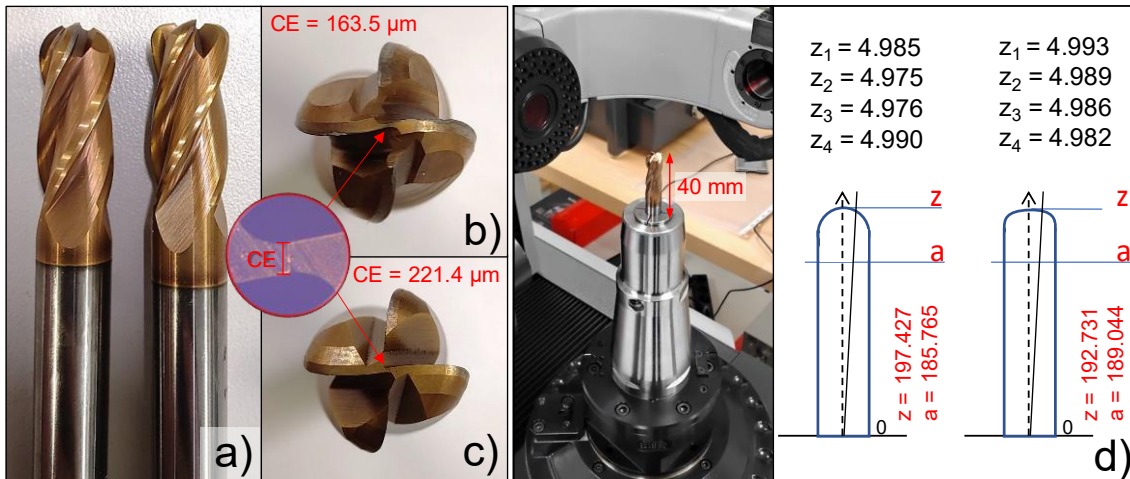


Figure IV-18. Ball-end tooltips: a) frontal view; b) single radius top view; c) lens shape top view; d) Presetting procedure and cutting edges measures.

All these cutting conditions seek the machining best practices and the toolmaker's recommendations to obtain the best results possible for the quite new barrel ball-end tooltip lens shape.

The inspection of the milled surfaces was conducted using a confocal microscope Leica® DCM3D, with software Leica® Map 6.2, where the surface and the roughness were

analysed as scanned and without form. Then, the procedure presented in Section IV. 6.2. *Surface prediction using the mesh data cloud* was applied to simulate the texture of the machined surfaces.

After that, the machined blade was portioned, and the cross sections perpendicular to the feed direction were evaluated. The samples were embedded, sanded, polished, and etched to evaluate, by optical imaging microscopy, the microstructural deformations of the surface under different ball-end tooltips and tilting conditions were evaluated using the software Quantikov v23.97. The samples were also evaluated by microhardness Vickers (HV 1) assays. The tests undergo 10 seconds of loading time in a durometer INNOVATEST Falcon 500, where each milled condition and surface side (concave or convex) of the embedded samples were measured in 2 rows of 4 indentations, and the hardness was compared with the central region of the sample.

Furthermore, the machining time was measured and compared with the time estimated by the CAM software, evaluating the machine response with different ball-end tooltips and correlating it to dynamic defects observed in the surface topography analysis and microstructural assays.

## ***IV. 9. 2. Results and Discussions***

The results and discussions are presented as follows: preliminary investigation of cutting contacts (IV. 9.2.1); milled part microstructure and hardness evaluations (IV. 9.2.2); surface topography measurements (IV. 9.2.3); iv) machine response (IV. 9.2.4); and finally, the modelling of the trochoidal movement of ICE elements with double radii ball-end tooltips (IV. 9.2.5).

### ***IV. 9. 2. 1. Preliminary investigation of cutting contacts***

Figure IV-19 presents all the relations of the tilt angle with the region of formation of the chip for both tooltips, different cutting contact conditions, and depth of cut evaluated, respectively 0.4 mm (yellow filled) and 0.6 mm (blue plus yellow fill).

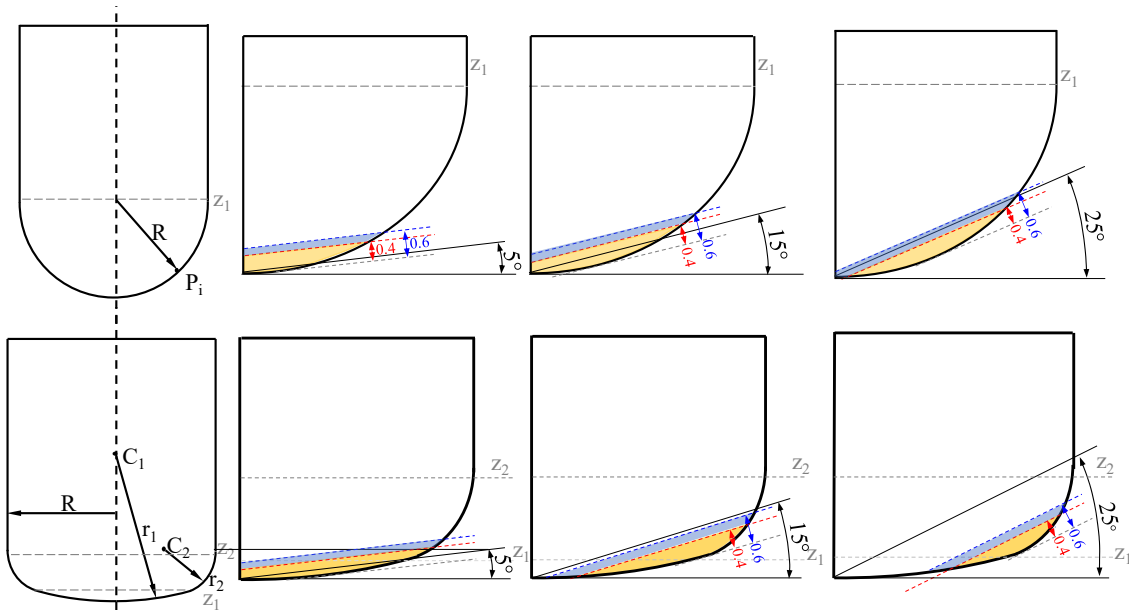


Figure IV-19. Different cutting contact engagements.

Figure IV-18 shows that under the tilt angles evaluated, a more balanced removal section was produced for the conventional ball-end tooltip, while for the lens tooltip, the dominant radius and area in-cut changes with tilting. With a 5° lead angle, the actuation of the major radius of the tooltip (25 mm) is dominant. With 15 degrees, it is more balanced between radii, and with 25 degrees, there is a dominance on the minor radius (2 mm). This combination of factors modifies the instantaneous geometry in-cut and allows the assay of different windows of cutting speed, besides geometrical aspects, on the final texture of the milled part. Table IV-5 summarizes the effective cutting radius and the proportional cutting speed for each condition evaluated.

Table IV-5. Variation of the effective cutting speed under different cutting tool tilts.

	Ball-end tool lead angle (°)			Barrel lens shape lead angle (°)		
	5	15	25	5	15	25
<b>R<sub>ef</sub> min 0.4</b>	0.000	0.000	0.268	0.000	1.070	2.304
<b>R<sub>ef</sub> min 0.6</b>	0.000	0.000	0.000	0.000	0.215	1.731
<b>R<sub>ef</sub> max 0.4</b>	2.353	3.083	3.720	4.307	4.573	4.764
<b>R<sub>ef</sub> max 0.6</b>	2.749	3.433	4.012	4.525	4.742	4.886
<b>V<sub>Cef</sub> 0.4 (%)</b>	<b>0 - 47.1</b>	<b>0 - 61.7</b>	<b>5.4 - 74.4</b>	<b>0 - 86.1</b>	<b>21.4 - 91.5</b>	<b>46.1 - 95.3</b>
<b>V<sub>Cef</sub> 0.6 (%)</b>	<b>0 - 55.0</b>	<b>0 - 68.7</b>	<b>0 - 80.2</b>	<b>0 - 94.84</b>	<b>4.3 - 94.8</b>	<b>34.6 - 97.7</b>

It is important to highlight that the final volume removed is maintained independent of the cutting condition once the semi-finished part and the final geometry don't change. The balance of effective cutting speed (Table IV-5) with the instantaneous area in-cutting changes the chip formation and affects the process. By correlating Figure IV-19 with the results depicted in Table IV-5, it can be seen that the null results for the minimum effective cutting speed can be correlated to the transitions of the cusp, which always occur at the centre of the tooltip that has a null effective radius and cutting speed. This should be responsible for producing more damage related to ploughing on the machined



surface. Conversely, it facilitates controlling the tooltip centre interaction with the final surface or part stock during the cut.

Also, the results depicted in Table IV-5 permit inferring that the maximum effective cutting speed is more influenced by the tool tilting and depth of cut than the minimum effective cutting speed. However, these initial assumptions can also be influenced by the feed per tooth used and other tool and surface geometrical parameters, requiring a deeper investigation of the trajectory of the ICE element. This investigation is better discussed in subsection (v) – modelling the trochoidal movement of ICE elements.

#### IV. 9. 2. 2. Milled part microstructure and hardness evaluations

Figure IV-20 presents OM images of the sections perpendicular to the feed direction for all conditions evaluated. No significant difference in the milled skin (~0.15 mm depth) between the lens shape and the conventional ball-end tooltip can be directly noted, nor can the presence of stretched grain, which is characteristic of severe plastic deformation.

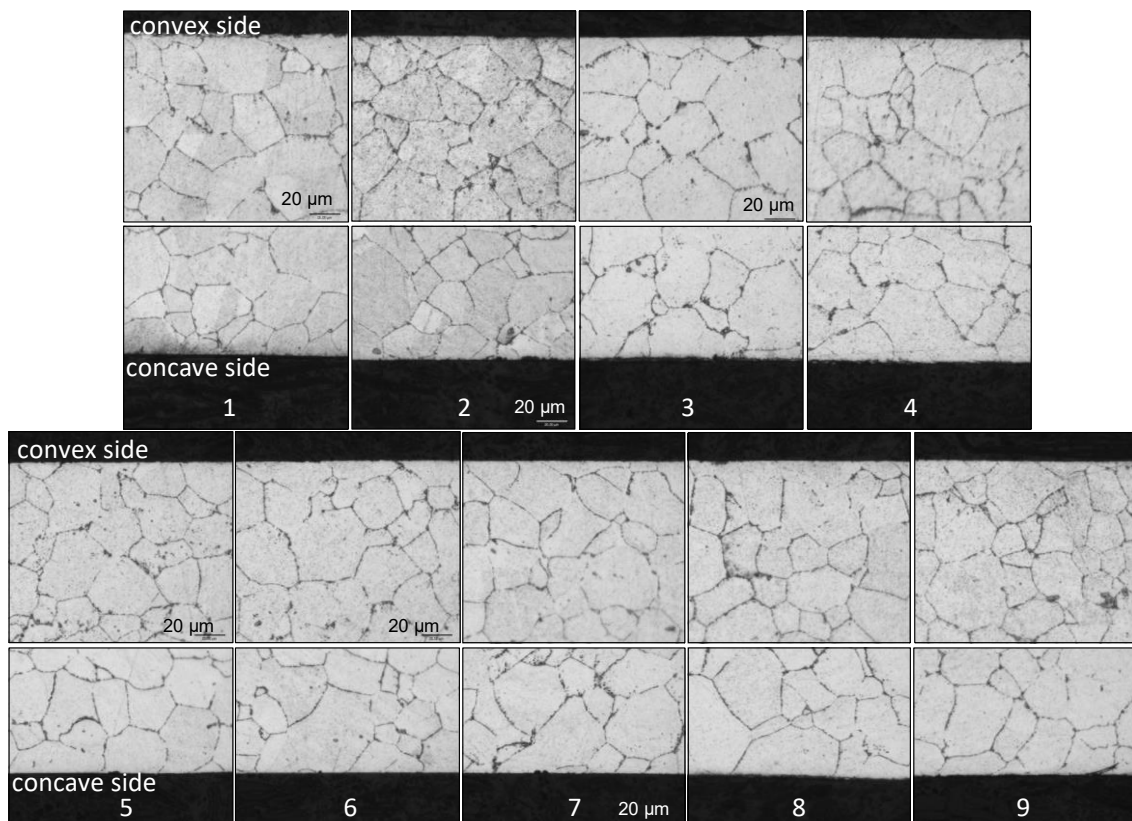


Figure IV-20. Metallographic images of the milled surface with 50x magnification.

Thus, a deeper investigation was conducted using the imaging analyser software. Figure IV-21 presents the images pre-treated (negative image + erosion filter) and marked to evaluate the grain boundary of each milled region plus one of the centres of the blade. Figure IV-22 presents the results of the average area and equivalent diameters per region, and Figure IV-22 presents the roundness analysis performed.

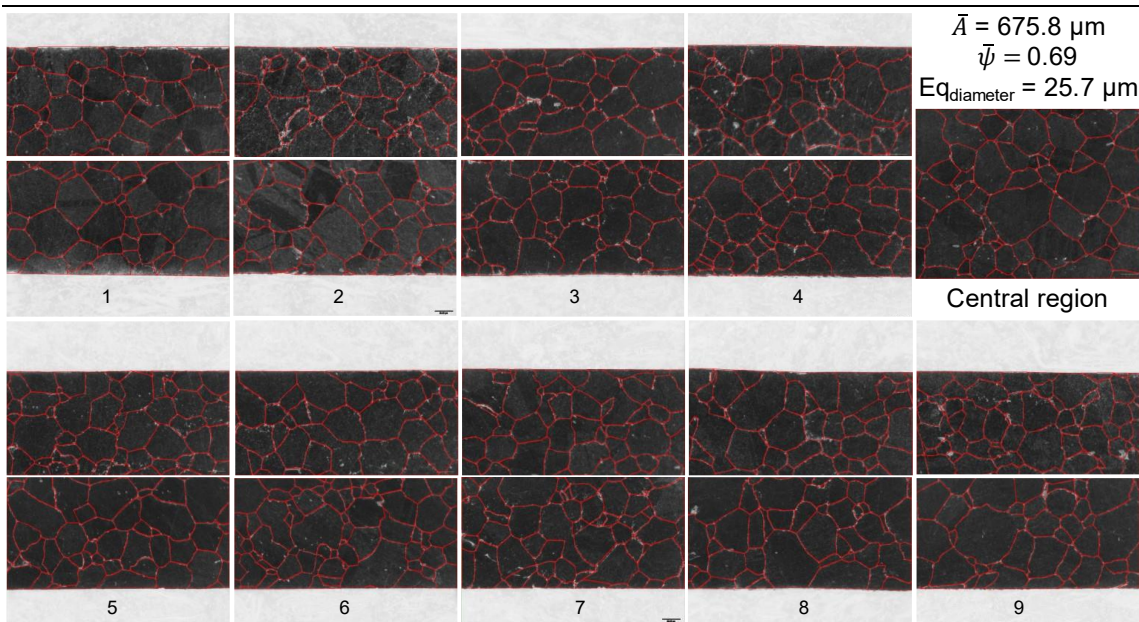


Figure IV-21. Post-processed optical images of the milled surfaces and central region.

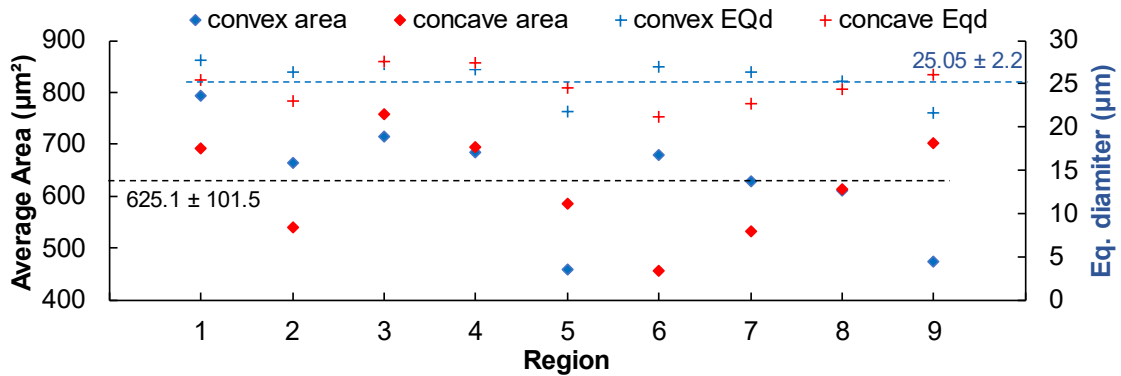


Figure IV-22. The average area of the grains and the equivalent diameter for each region.

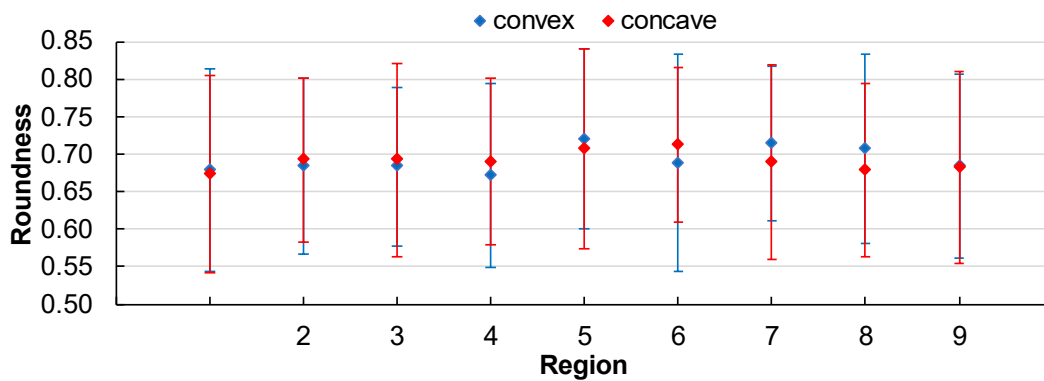


Figure IV-23. Roundness analysis of the grains.

The first it can be note is that the grains in the border of the machined blade are slightly lower ( $625.1 \mu\text{m}^2$ ) than the average measured on the centre of the part ( $675.8 \mu\text{m}^2$ ), about 7.5%, similar to the equivalent diameter that reduced by about 2.5%, from  $25.7 \mu\text{m}$  to  $25.05 \mu\text{m}$ . Supposedly, the high-pressure coolant used and the cutting parameter window evaluated, in all cases, helped maintain similar processing temperatures and microstructural modifications (without significative plastic deformations). Also, the milling process can be statistically influenced by the partial removal of some parts of the grains

during the milling process, justifying the slight grain size and roundness reduction on the borders. Hence, a microhardness investigation could provide additional information for a malicious investigation.

The roundness analysis depicted in Figure IV-22 shows a variation from 0.67 to 0.72 (average of  $0.69 \pm 0.15$ ), with a similar uniformity over all samples. It also can be inferred that the grains are mostly equiaxial, a characteristic of the polycrystalline microstructure of material used and produced by the conventional cold-rolled manufacturing process.

It also can be seen that the milling process did not significantly modify the internal microstructure (Figure IV-20 and Figure IV-21 depict the first 0.15 mm depth of the surface) with any tooltip or effective cutting speed investigated, giving a first indication that the new ball-end tooltip (lens shape) can produce surfaces with the same quality of the conventional ball-end tooltip. To strengthen this assumption a deep investigation was conducted addressing the microhardness profile of the samples. The microhardness results are depicted in Figure IV-24.

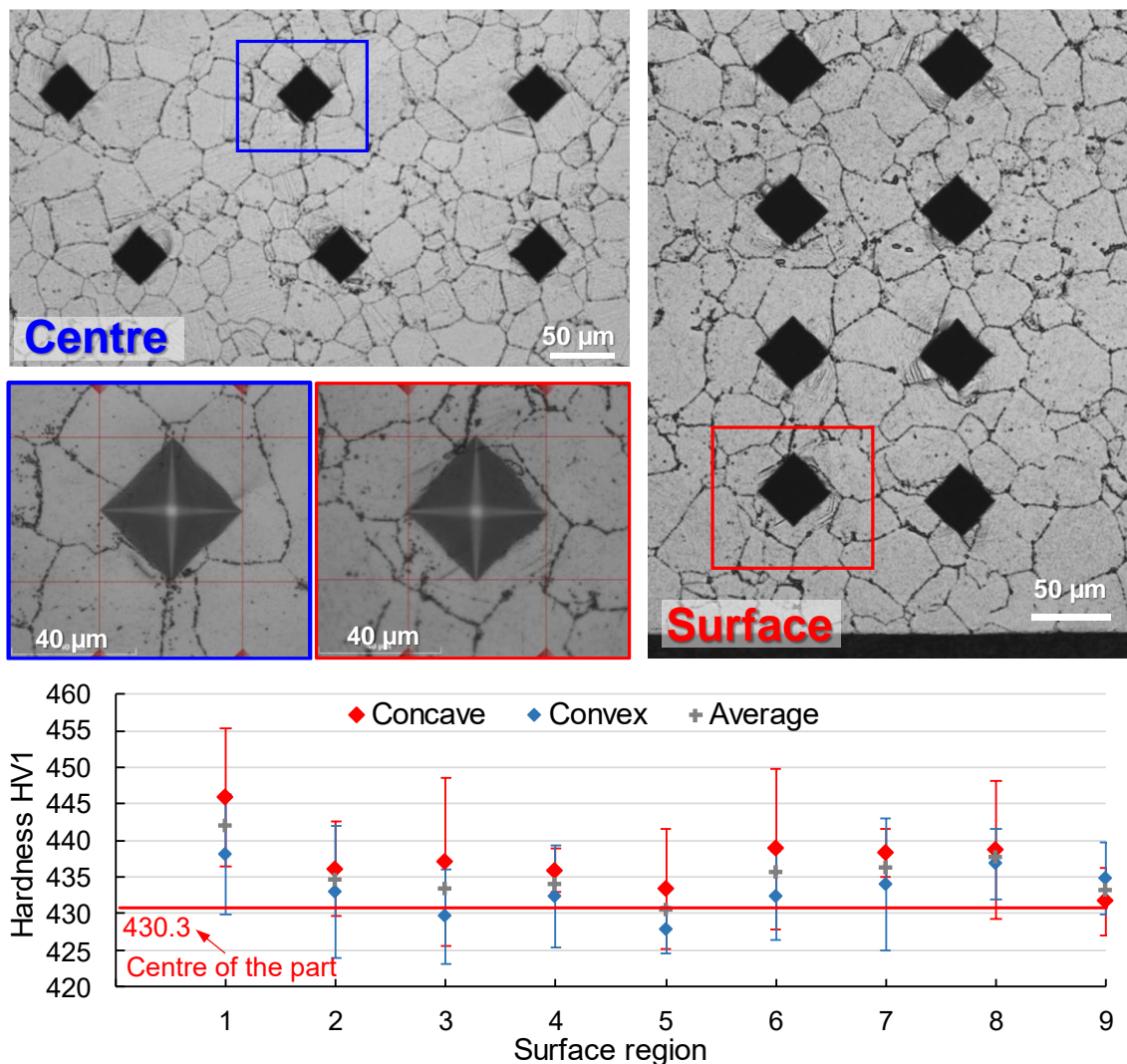


Figure IV-24. Surface hardness after the milling process on the concave and convex sides.

The hardness results show that even though there is no significant difference between the cutting conditions, there is a slight increase in the average hardness on the regions manufactured with cutting conditions 1 (442.1 HV1) and 8 (437.7 HV1), both manufactured with the conventional ball-end tooltip and, respectively, the extreme lead angles (5 and 25), suggesting the use of 15° lead angle for conventional ball-end tooltips.

Also, the average results of hardness with lens shape tools (433.5 HV1) were lower than with a conventional ball end tooltip (437.7 HV1) but higher than the central region (430.3 HV1), suggesting that this new kind of tooltip produces lower plastic deformations during milling fact that can be related to the tool geometry and its higher effective cutting speed. It also can be inferred that the concave side tends to present a higher hardness than the convex side except for region 9, which could be related to a higher instantaneous CWE produced with a negative surface curvature along the toolpath.

Even the grain size evaluation showed no significant difference in the milled surface and a slight reduction in the surface hardness; the results depict that it is possible to obtain very similar mechanical properties with the new ball end tooltip. So, deviations, milling time, and surface damages must be addressed to optimize the finishing process. Additionally, the evaluation of parts containing surfaces with higher instantaneous curvatures is suggested together with modelling of the process to gain a deeper insight into the process window results toward statistically significant outcomes of the finishing process with these tools.

#### ***IV. 9. 2. 3. Surface topography measurements***

Figure IV-25 presents the damages observed with the tool swing to machining the blade in a spiral toolpath. It can be seen that according to the tool inclination on the feed direction (lead angle), there is a tendency for overcutting material or undercutting. In this aspect, the more neutral results were observed within a lower inclination angle (5° lead angle). Besides the possible CWE deviations, the machine dynamics could influence the marks pattern, and special caution must be taken using lens shape tools.

Even though the error observed was minor, less than 10 µm, under the tolerance for most applications, this damage was sufficient to make visual marks damage to the workpiece that could reduce the attractiveness of this kind of tool for most applications, especially for optics purposes. The evaluation of aerodynamical losses under this magnitude remains unknown and could be addressed in future research lines.

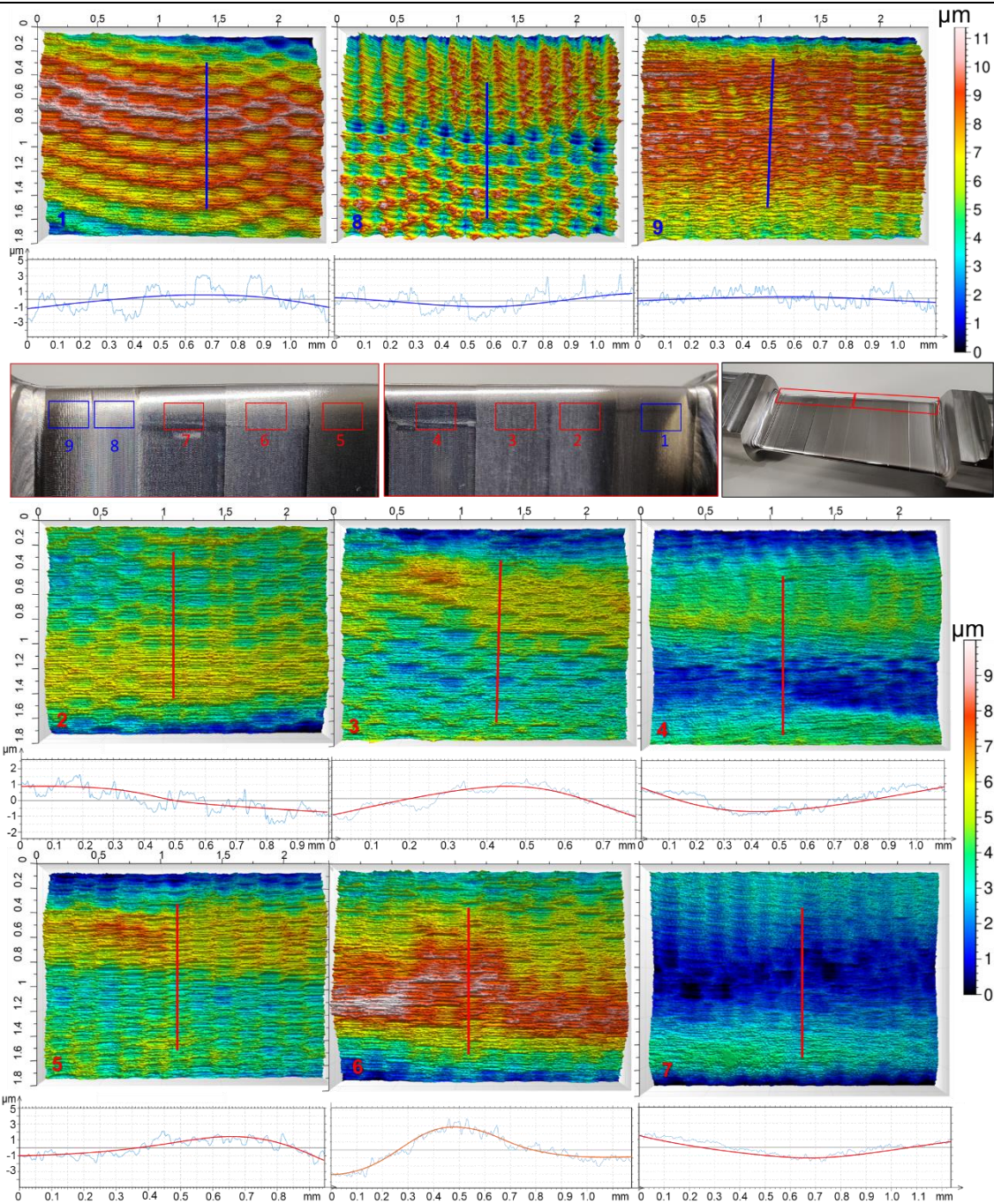


Figure IV-25. Surface damage after blade inversion according to the cutting condition.

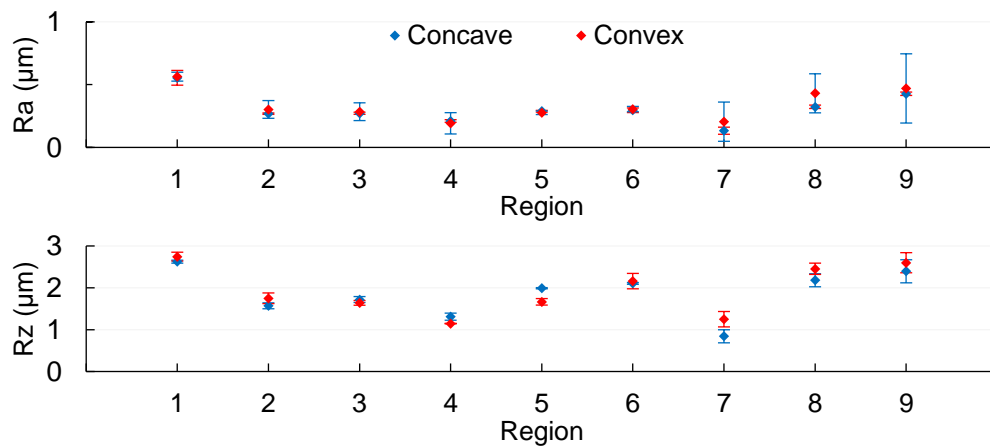


Figure IV-26. Roughness Ra and Rz according to the milled region.

As presented in Figure IV-26, the regions machined with conventional ball-end tooltips produced a higher roughness, a fact related to the geometrical constraints involved. Among all the results, the lower roughness measured was obtained with the lens shape tooltip under a 5° lead angle (regions 4 and 7).

Figure IV-27 presents the optical images of the topography of the milled surfaces for both tooltips evaluated under different tool inclinations. The first remark is the marks produced in both concave and convex regions by the ball-end tooltip under 5° lead angle, region 8. The conical-shaped mark with arbitrary oscillation typically indicates a higher plastic deformation that occurred during the material removal, which could be related to the influence of the centre actuation and its lower effective cutting speed with 5° lead angle.

Secondly, it can be seen that regions 4, 7, and also region 8, produced marks with a more uneven pattern. Also, a more significant pattern variation within the surface curvature can be observed in regions 4 and 7. In both cases, the different tool tilting and the angle formed between the tool and the instantaneous surface curvature may be the factors that caused the pattern variation once the material and other machining conditions are maintained. In these cases, the tilting level was the lower (5° lead angle).

As depicted in Figure IV-27, the metal debris become present on the milled region 8, which should mean that the broken chips in the machining process are extruded and bonded to the machined surface, indicative of the start of the actuation of plastic deformation mechanisms, also, in regions 4 and 7 present uneven smearing at the feed borders, which is another indication of plastic deformation. In both cases, the lead angle involved was 5°; these assumptions lead to the recommendation of, when possible, not using lead angles inferior to 5°; otherwise, more severe plastic deformations will dominate the cutting phenomenon, damaging the finished surface.

Correlating the better roughness obtained with the marks found in regions 4 and 7, supposedly, the lower instantaneous tooltip curvature produced by bigger radius and low tilting resulted in lower geometrical crisp heights on the feed and cross-direction. Also, using the centre of the tooltip with inferior cutting speed could be one of the factors that were improved by the controlled smash (under lower cutting speed) of the final surface obtained that presented uneven and bulged crisp heights, as depicted in Figure IV-27. These deformations were more pronounced on the convex side, where supposedly the engagement is lower.

Another assumption that could be made by using a tooltip with a higher radius, such as the lens shape, was about damages during the chip formation by insufficient chip thickness (initial or final). It is identified by smashed marks or deformed materials, which

were not observed. Also, no hardness increase was observed on the surface skin, indicating that this phenomenon was minimal.

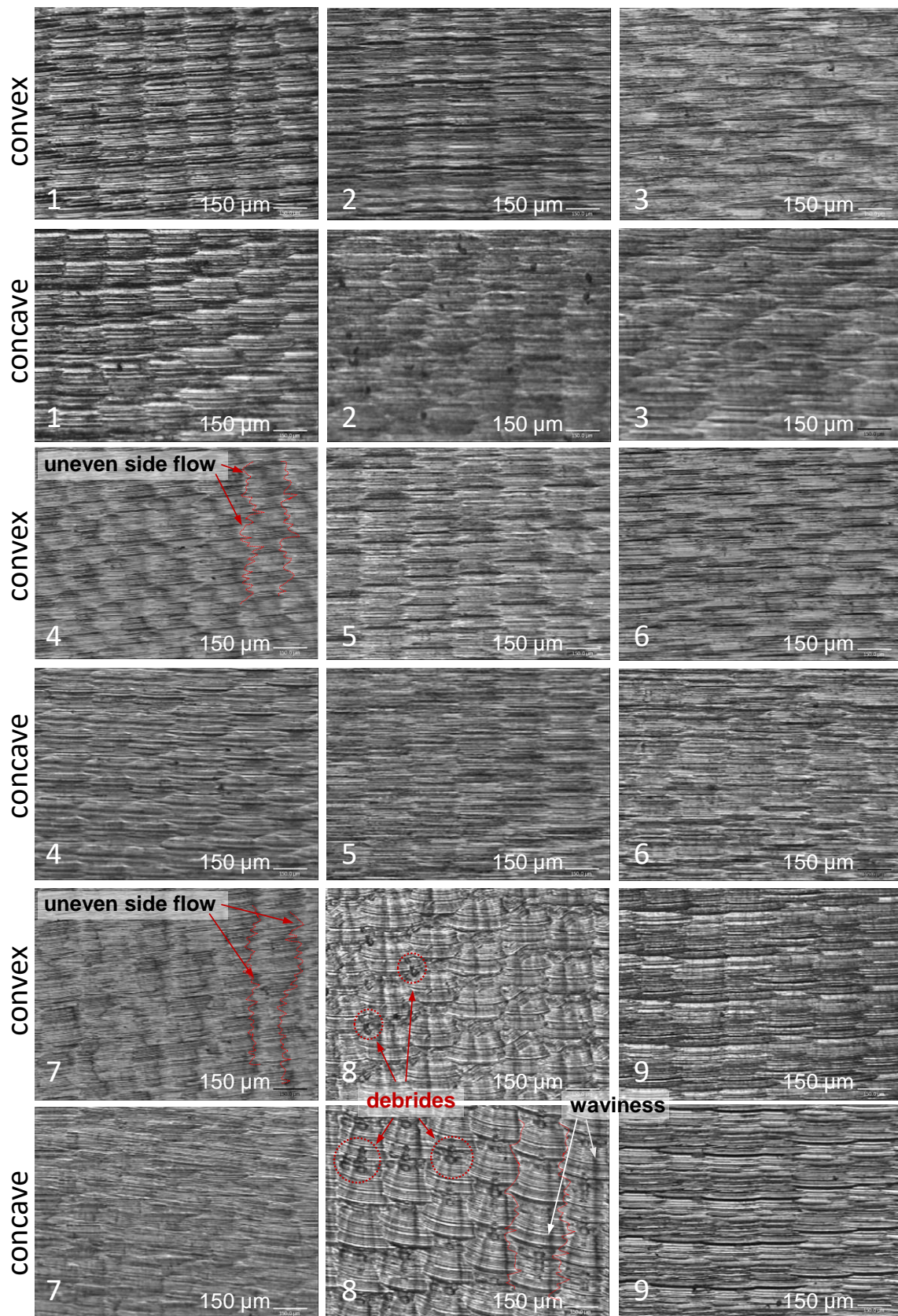


Figure IV-27. Milling texture under different tooltips and tool tilt.

**IV. 9. 2. 4. Machine Response**

Table IV-6 presents the results predicted by the CAM software for the milling time, the total time consumed, and the error between them. It also presents the number of lines of the NC file and the average machining time per segment, information directly correlated to the machine's kinematic, tool tilting, and geometrical factors (instantaneous CWE).

Table IV-6. Milling time predicted by the CAM versus real.

Region	1	2	3	4	5	6	7	8	9
<b>Lead angle</b>	<b>25</b>	<b>25</b>	<b>15</b>	<b>05</b>	<b>25</b>	<b>15</b>	<b>05</b>	<b>05</b>	<b>15</b>
<b>NC lines</b>	33613	56171	56157	34779	57132	55945	34635	5554	11400
<b>Machining time (s)</b>	646	689	655	621	672	644	617	332	320
<b>Time estimated by the CAM (s)</b>	600	653	624	571	632	602	557	269	276
<b>% Error</b>	<b>7.7</b>	<b>5.5</b>	<b>5.0</b>	<b>8.8</b>	<b>6.3</b>	<b>7.0</b>	<b>10.8</b>	<b>23.4</b>	<b>15.9</b>
<b>Average time per NC line (ms)</b>	<b>17.9</b>	<b>11.6</b>	<b>11.1</b>	<b>16.4</b>	<b>11.1</b>	<b>10.8</b>	<b>16.1</b>	<b>48.4</b>	<b>24.2</b>

By correlating the number of lines presented in Table IV-6 with the tool engagement depicted in Figure IV-19, it can be inferred that a higher number of tool position changes occurs with the increase of the tool tilt, which can be one of the factors apart of geometrical ones that compromise the surface and increases its roughness. Also, milling with the lens shape ball-end tooltip requires that the CAM software compute a higher number of CL positions for the same tolerance band used (0.01 mm).

The average error of the prediction time observed was about 7% for the lens shape tool, with a slight increase to about 10% for the 5° lead angle, contradicting the pattern of the number of segments computed. For the conventional ball-end tooltip, the error increases, reaching more than double. Supposedly, it can be correlated to the fast movement of the machine (G01 segment) and geometrical constraints on the start and final of the blade face, respectively, at regions 1 and 9. Still, region 8 (5° lead angle) presented a bigger error compared to other internal faces machined with the lens shape. It can be correlated to the worst roughness measured and also to the different conical shapes observed by OI microscopy.

**IV. 9. 2. 5. Modelling of the milling process**

The process was modelled to gain better insights into the milling process, considering different cutting conditions and tooltips. Hence, the methodologies of instantaneous position and the trochoidal movement of the ICE elements of the tooltip previously presented in section IV. 6 Surface prediction were applied.



Figure IV-28 presents the results of the modelling of the tooltip milling a flat surface considering the instantaneous position of the tooltip under the tilt angle evaluated, comparing the lens shape against the conventional ball-end tooltip. The result is proportional to the variation in the effective cutting radius.

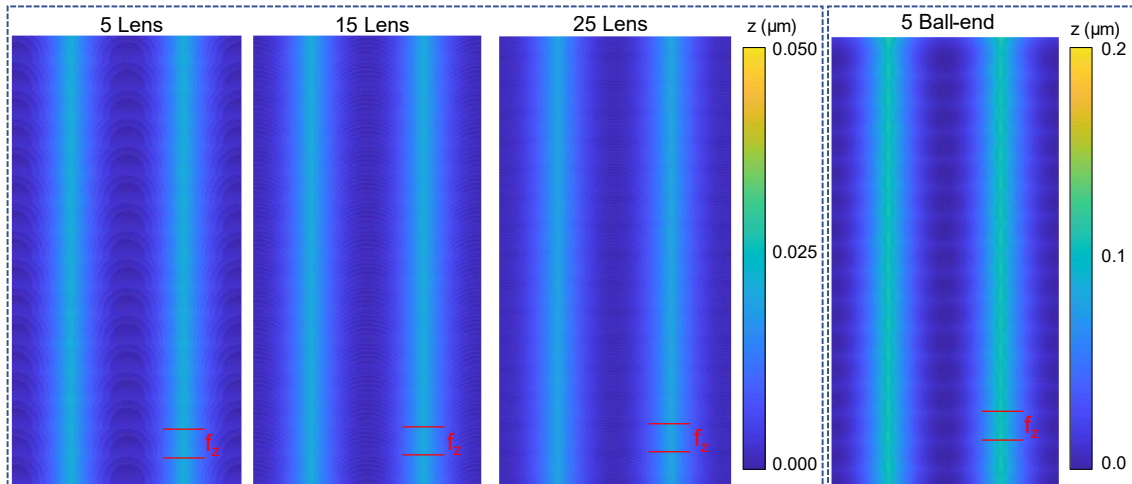


Figure IV-28. Simulated pattern of the surface texture with different tooltips and tool inclinations.

Comparing the results, the first that can be seen is that the effect of the tool tilting on the lens shape tooltip changes the theoretical lateral roughness even maintaining the same lateral pass ( $a_e$ ), an effect not seen with the single radius tooltip once there is no variation of the engagement of the surface with the dome produced by a single radius. It is observed that increasing the lead angle reduces the lateral roughness, which is justified by the lens tooltip domain change from the major to the minor radii of the tooltip. Also, it was possible to note that the variation in the average effective radius with the lead angles, which is about 4%, is inversely proportional to the crisp height variation.

Secondly, the crisp height using a conventional lens tooltip is about five times higher than using barrel tools with a lens tooltip; this means that for the same finishing quality, the program length and, thus, the machining time can be significantly reduced. This highlights the importance of the previous results observed regarding similar finishing quality regarding grain size, roughness, and hardness assays.

### IV. 9. 3. Conclusions

Study Case 2 evaluated the finishing process of a thin-walled blade containing free-form surfaces using 2 different ball-end tooltips and tool tilting. The main conclusions are depicted ahead:

- The metallographic assay of the milled surface (0.15 mm depth) with different tooltips and cutting conditions showed no significant variation in the grain size and the roundness. However, for all cases, a light decrease was identified compared to the

central region of the blade, about 7.5%. On the other hand, the microhardness evaluation showed lower values on the surface milled with lens shape tools (433.5 HV1) than with a conventional ball end tooltip (437.7 HV1) but still are higher than the central region (430.3 HV1).

- The hardness results also showed that in the conventional ball-end tooltip, the 15° lead angle produces a better surface finishing, supposedly in extreme cases, with angles of 5 and 25 degrees, resulting in higher efforts that increased the superficial hardness by about 3%. The concave side tends to present a higher hardness than the convex side except for region 9, which could be related to a higher instantaneous CWE produced with a negative surface curvature along the toolpath.
- The combination of machine kinematics with the calculated 3D spiral toolpath for the different tooltips used shows surface marks/damages after swiping from the concave to convex inferior to 10 µm, a value acceptable for this kind of component that also allows removal by post-processing, such as polishing.
- The better roughness results were obtained with the lens shape tooltip under 5°, probably due to higher plastic deformation under lower cutting speed and a higher circle segment in-cut. However, it was the one that presented the most severe marks after sweeping from concave-convex surfaces. Therefore, in parts with abrupt curvature changes, the lens shape should be programmed with a higher lead angle (over 5°) to minimize the problems related to machine kinematics; otherwise, regions of the part could be compromised.
- The simulation of surface topography and the analysis of the crisp heights left in the lateral direction of the feed rate showed that the height does not change for the ball-end tooltip. However, for the barrel lens shape, due to the presence of two circle segments at the tooltip, it does change. Furthermore, it was identified that the crisp height left is inversely proportional to its average effective cutting radius.

#### **IV. 9. 4. Future works**

- Increase the lateral depth of cut ( $a_e$ ) to improve productivity with the lens ball-end tooltip once the roughness obtained is lower with the same  $a_e$ .
- Evaluate the finishing process of both ball-end tooltips on a machine with a different dynamic response, addressing the productivity and the deviations obtained on a continuous milling toolpath on a geometry with abrupt inversions like the presented blade, and if possible, increase the variations of the instantaneous radii of the surfaces (concave and convex) to address more severe cases.
- Investigate the cutting force and the problems that come with that, such as tool deflection and final part deviations in materials with different mechanical properties.

---

**Chapter V. Manufacture of blades by PBF-LB  
containing microstructures**

---



## Chapter V. Manufacture of blades by PBF-LB containing microstructures

*This chapter presents the evaluation of parts finished by ball-end milling previously produced by the additive manufacturing process, more specifically, the PBF-LB. It has been addressed from the initial quality of components produced by this additive process to the design optimization towards reliable parts with good surface finishing.*

### V. 1. Introduction

This chapter presents a study case using additive manufacturing to propose a new blade concept containing internal microstructures (Figure V-1). As in the application of these components related to sectors with safety and high-efficiency concerns, the AM process, the final concept, the manufacturing process, and the final surface are evaluated. The chapter is split into two main studies. The first study is based on the paper published in the International Journal of Precision Engineering and Manufacturing-Green Technology entitled “Energy density effect on the interface zone in parts manufactured by laser powder bed fusion on machined bases”, where the effect of the AM process on the manufacture is investigated, more specifically, porosity control and its effect on the rupture pattern (V. 2). Then, a study case evaluating both the design and the finishing process in 5-axis machining with ball-end tooltips of this kind of component is accomplished (V. 3).

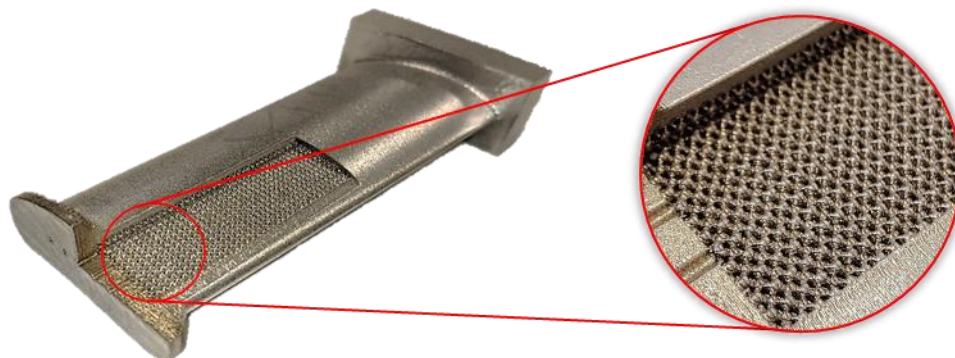


Figure V-1. Blade manufactured by PBF-LB with internal microstructures.

### V. 2. Evaluation of the PBF-LB process for manufacturing critical engineering components

This topic presents a study case manufacturing hybrid samples for mechanical properties evaluation with two main objectives. The first consists of evaluating the effect of the porosity on the mechanical properties of parts manufactured by PBF-LB. The second

objective is to evaluate the hybrid part manufacture and the mechanical properties progression from the bulky machined part, the melted interface zone, to the portion manufactured by PBF-LB. Furthermore, this initial study introduces the use of PBF-LB processes in hybrid manufacturing or for the repair of special components.

### ***V. 2. 1. Materials and methods***

Two different hybrid workpieces were manufactured to evaluate the properties of PBF-LB parts for critical engineering applications and the capacity to manufacture hybrid manufactured parts using PBF-LB and machined substrates. The first geometry evaluated was a cuboid sample manufactured over the machined block, evaluating the depth of interaction, hardness profile, and porosity of the PBF-LB process. The second geometry was a cylindrical shape and was applied to assess the tensile strength. Both samples were used to understand the influence of the heat-affected zone (HAZ) and porosity on the mechanical properties of the hybrid pieces for critical application. The materials and methods are divided into the following sections: experimental procedure of the hybrid PBF-LB and characterization of the hybrid samples.

#### ***V. 2. 1. 1. Experimental procedure of the hybrid PBF-LB manufacturing***

Half of the workpieces manufactured to evaluate the PBF-LB hybrid manufacturing were obtained using PH13-8Mo stainless steel (Villares Metals N4534QA) cold-rolled and machined – portion named substrate. The substrate was screwed into the manufacturing plate, and the other half was printed by PBF-LB processes using gas-atomized Uddeholm Corrax<sup>®</sup> powder with nominal particle sizes distributed in the range of 5-50  $\mu\text{m}$ . Spherical powder particles are revealed from the morphology obtained using scanning electron microscopy (FEG ZEISS SUPRA V55), Figure V-2a. The particles presented a small number of sintered particles and satellite formation, with an average particle size of about 12  $\mu\text{m}$  (Figure V-2b); particle size distribution limits the layer thickness and, together with the packing factor, affects the porosity and the part surface roughness. The chemical composition and the mechanical properties of the materials used in the hybrid manufacturing process are presented in Table V-1 and Table V-2.

A Concept Laser<sup>®</sup> machine model CL50WS with a YAG fibre laser (400W), a spot size of 100  $\mu\text{m}$ , and a 1064 – 1070 nm wavelength. Nitrogen with residual oxygen lower than 1% was used in the PBF-LB process. The scanning speed was modified by  $\pm 15\%$  and  $\pm 30\%$  to alter the energy of density. Its parameter has more significance on the Yield strength and porosity together with the laser power (Xu et al., 2018b), a parameter already set to the maximum value for production purposes. The other reference

parameters were selected according to the PBF-LB industrial service provider recommendation (optimized for 400 W). PBF-LB process parameters are listed in Table V-3. A chess scanning strategy with a 45° rotation between layers was selected. It favours the formation of equiaxial grains, providing higher isotropy and low-intensity texture, and increasing crystallographic isotropy (Pham et al., 2020). Hence, it presents properties closer to traditional manufacturing methods according to Voigt-Reuss-Hill (VRH) theory (Pérez-Ruiz et al., 2021).

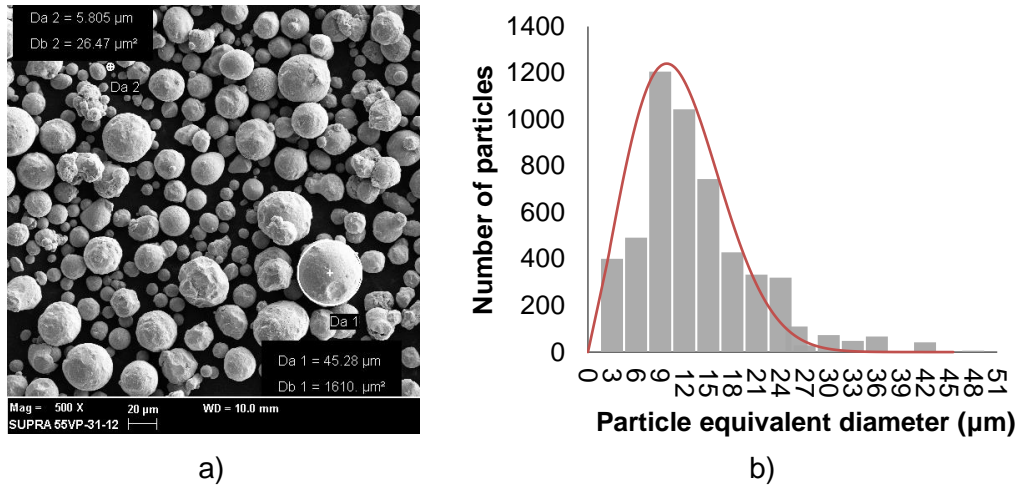


Figure V-2. Corrax® powder analysis: a) SEM scan 500x magnify; b) size distribution (Marin et al., 2023).

Table V-1. Chemical composition of the substrate and powder (Marin et al., 2023).

Material	C	Si	Mn	Cr	Ni	Mo	Al
Uddeholm Corrax®	0.03	0.30	0.30	12.00	9.20	1.40	1.60
Ph13-8Mo	0.05	0.10	0.10	13.25	8.50	2.50	1.35

Table V-2. Uddeholm Corrax® properties solution treated (Marin et al., 2023).

Material	Tensile strength (MPa)	Heat conductivity (W/m°C)	Heat expansion coefficient (μm/ m°C)
Uddeholm Corrax®	1100	18	11.7
Ph13-8Mo	1105	14	10.6

Table V-3. Parameters used for the manufacture of the samples (Marin et al., 2023).

Sample	Laser Power (W)	Layer thickness (μm)	Hatch (μm)	Scanning Speed (mm/s)	Variation	Energy density (J/mm³)
A	400	45	105	2300	+30%	36.8
B				2035	+15%	41.6
C				1770	Reference	47.8
D				1505	-15%	56.2
E				1240	-30%	68.3

Figure V-3 presents the samples manufactured to evaluate the hybrid process. Figure V-3a shows the cuboid samples with 10 mm edges with one replication for each parameter. Cylindrical specimens were printed with 10 mm diameter and 20 mm height using parameters A, C, and E with one replication each. Figure V-3b presents the machined tensile test specimen prepared according to ASTM 370.

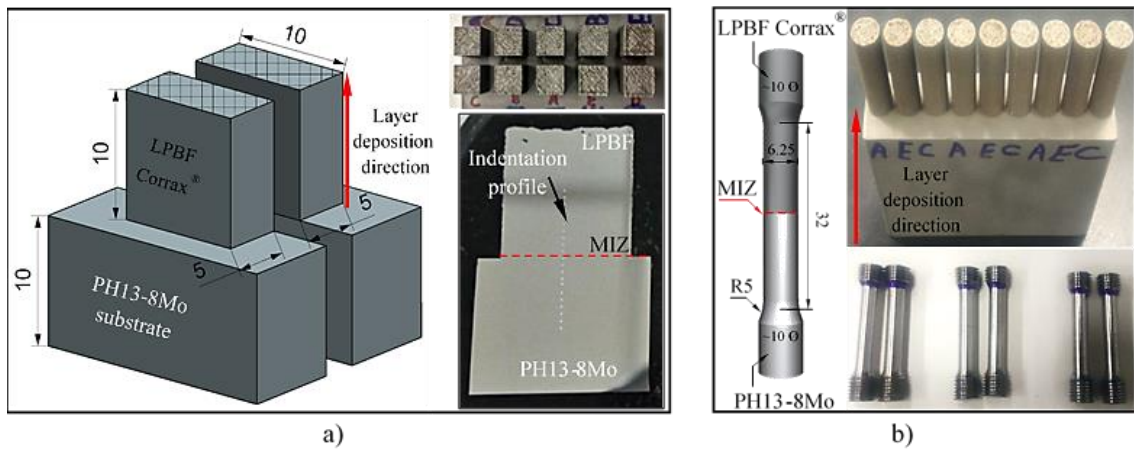


Figure V-3. Hybrid samples manufactured by PBF-LB over the PH13-8Mo substrate: a) CAD of the cuboid sample, as-built and indentation schematic; b) tensile test samples as-built and machined (Marin et al., 2023).

### V. 2. 1. 2. Characterization of the hybrid samples

The hybrid manufactured samples were evaluated in four aspects: i) metallography, ii) hardness, iii) tensile strength, and iv) pore size and distribution.

#### i) Metallography

The cuboid samples were prepared to analyse the microstructures and the depth of interaction of the melting interphase zone. Samples were sectioned using wire EDM, mounted in Bakelite, polished, and etched with a solution of 10 ml of  $H_2SO_4$  + 10 ml of  $HNO_3$  + 20 ml HF diluted in 50 ml of distilled water. The microstructure present in each region was accessed using SEM (VEGA 3, TESCAN) and evaluated on an Olympus BX61 optical microscope. Five images were taken, two at the milled component, one at the melting interface zone (MIZ), and two at the PBF-LB portion, thus evaluating the microstructure progression with the building direction. The MIZ depth was measured in a Stereoscope Zeiss Discovery V8 aided by software AxioVision Release 4.9.1 SP1 using 25x magnification images.

#### ii) Hardness

The hybrid sample's hardness was measured in both materials and at MIZ using a micro-durometer Vickers Wilson Instruments 402MVD with a  $136^\circ$  pyramidal edge. Eleven indentations HV0.5 (ISO 6507-1:2018) in line with a distance of 1 mm were made to obtain the hardness profile. The first was defined in the centre of the melting interface zone with five indentations in the PBF-LB portion and five in the machined portion (Figure V-3).

In addition, to address the optimal mechanical properties required in some applications, the samples manufactured with a higher energy density (D and E) were heat-treated to



evaluate hardness enhancement on hybrid samples. The heat treatment conditions were used according to the Uddeholm Corrax® manufacturer recommendation (Uddeholm, 2016). The process consisted of solubilization (850°C for 2 hours), quenching (1020°C for 30 min followed by cooling in a salt bath), and ageing (525°C for 2 hours). Then, the same procedure for hardness evaluation passed by the samples as built was carried out, with a posterior comparison with the previous results.

iii) Tensile strength analysis

The tensile strength analysis was conducted using the cylinders manufactured with A, C, and E parameters. The cylinders were machined according to ASTM 370 with the MIZ in the middle of the samples (Figure V-3b). The samples were tested in an INSTRON 5988 Universal Testing Systems, measuring the ultimate tensile strength (UTS) and elongation.

iv) Pore size and distribution

Observing that the variation in the hardness of the samples is not as significant as in the tensile test results, pore distribution and its morphology were analysed to address the changes in the mechanical properties according to scanning speed. The porosity of each sample was analysed in an optical microscope ZEISS IMAGER M2M. 28 images with 50x magnification were taken in distinct regions of the samples, always discarding 50 µm from the borders. The data were post-processed by Multiphase Grains Graphite software, where an analysis was carried out to identify the number of pores and their size through the pixel processing technique. The melting interphase zone of samples manufactured with parameters A (+30%), E (-30%), and C (reference parameter) was also evaluated using a tomograph ZEISS METROTOM 1500 with a minimum focal spot size of 7 µm, which limits the use of this technique to relative density measurement (Samei et al., 2021). The voxel data were treated using the software myVGL with Porosity/Inclusion analysis toolset, inspecting pore size, shape, number, and distribution. It is important to note that even a single voxel identifies a pore with at least three for realizing measurements.

To better understand the effects of the porosity on the mechanical behaviour of hybrid manufactured components, were calculated the number of pores (Eq. 61), modulus of tenacity (Eq. 62), ultimate tensile strength (Eq. 63), percentual strain (Eq. 64), and relative density (Eq. 65).

$$N_p = \sum_{i=1}^n N_i \quad \text{Eq. 61}$$

$$K_U = \int_0^{\varepsilon_f} \sigma d\varepsilon \quad \text{Eq. 62}$$

$$UTS = \sigma_{max} = \frac{F_{max}}{A_0} \quad \text{Eq. 63}$$

$$\%_{strain} = \frac{\Delta L}{L_0} 100\% = \frac{(L_f - L_0)}{L_0} 100\% \quad \text{Eq. 64}$$

$$\%_{R. density} = 1 - \frac{V_p}{V_t} 100\% = \frac{V_t - V_p}{V_t} 100\% \quad \text{Eq. 65}$$

Where  $N_p$  is the number of the pores,  $N_i$  is the  $i$  pore element,  $K_U$  is the modulus of tenacity,  $\varepsilon_f$  is the final elongation,  $UTS$  is the ultimate tensile strength,  $\sigma_{max}$  is the maximum stress,  $F_{max}$  is the maximum force,  $A_0$  the initial area of the cross-section of the tensile specimen,  $L_f$  is the final length,  $L_0$  is the initial length,  $V_t$  is the total volume of the body, and  $V_p$  is the pores volume (Eq. 66), which can be expressed in terms of sphere equivalent diameter ( $d_{seq}$ ). The sphericity ratio  $\psi$  is presented in Eq. 67 as a ratio between the area of an equivalent sphere ( $A_{seq}$ ) and the pore area ( $A_p$ ).

$$V_p = \frac{\pi d_{seq}^3}{6} \quad \text{Eq. 66}$$

$$\psi = \frac{A_{seq}}{A_p} = \frac{\pi^{1/3} (6V_p)^{2/3}}{A_p} \quad \text{Eq. 67}$$

In parts fabricated by additive manufacturing, the presence of pores reduces the mechanical properties mainly by two effects: the lower equivalent cross-section to hold out the load (plastic field) and creaking propagation. Figure V-4a presents an infinitesimal body with a single pore in load to aid the comprehension of these effects. The load is settled by the limit of all the resistive forces inside the body and equivalent to the stress applied per area unit (Eq. 69). From the equilibrium equation (Eq. 68), and considering the effect of the area reduction with a strain, expressed in terms of elongation (Eq. 70), is obtained in Eq. 71.

A body with multiple pores can be represented by the sum of infinitesimal elements within and without pores (Figure V-4b). Applying the equilibrium condition (Eq. 72), it is possible to express the force for additive manufactured components (Eq. 73). However, in an infinitesimal body, the area  $A_i$  of one element with one pore is expressed as a fraction of the area without pores  $A_i = A_0(1 - f)$ , in porous bodies, this fraction becomes a probability distribution function ( $g_{(d,\psi,o)}$ ) dependent on the distance between pores ( $d$ ), sphericity ( $\psi$ ), and orientation of the pores ( $o$ ).

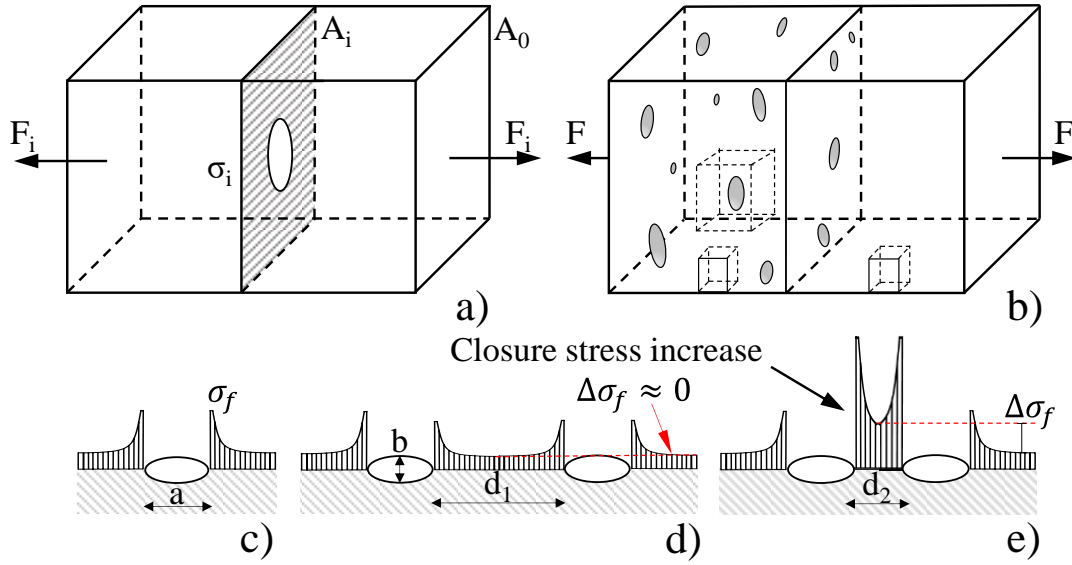


Figure V-4. Porous material representation: a) infinitesimal element; b) hybrid material; c) single pore strain; d) pores without stress concentration; e) pores with stress concentration interaction (Marin et al., 2023).

$$F_i = \sigma_i A_i \quad \text{Eq. 68}$$

$$F = \int \sigma dA = \frac{\sigma_i}{A_i} \quad \text{Eq. 69}$$

$$\varepsilon = \ln\left(\frac{A_0}{A_i}\right) \quad \text{Eq. 70}$$

$$F_i = \sigma_i A_i e^{-\varepsilon_i} \quad \text{Eq. 71}$$

$$\sum F = 0 \quad \text{Eq. 72}$$

$$\sigma_{AM} A_{AM} e^{-\varepsilon_{AM}} = \sum_{i=1}^n \sigma_i A_i e^{-\varepsilon} = \sum_{i=1}^n \sigma_{i_n} A_0 (g_{(d,\psi,o)}) e^{-\varepsilon_n} \quad \text{Eq. 73}$$

The crack propagation happens when the closure stress reaches a level where the strain concentration is higher than supported by the material, as depicted in Figure V-4e. For a single pore, it can be calculated considering the stress concentration effect of flaws  $k_t$ , where  $k_t = \sigma_f/\sigma$ . Using Eq. 74 and assuming a single pore with equivalent diameter, much smaller than part length ( $l$ ), is obtained a stress concentrator  $k_t = 3$  (Anderson, 2017). Meaning that the force required to propagate a crack and generate a fracture is three times lower than a solid body with the same dimension. Westergaard's stress function at the pore crack plane (Eq. 75) can be considered to calculate the crack propagation on a porous material. Considering only the real solution ( $\mathbb{R}$ ),  $|x| > |a|$  and the distance  $d$  between pores ( $d = x - a$ ) is obtained Eq. 76 (Anderson, 2017). Evaluating the equation is observed that for  $\lim_{d \rightarrow 0} \sigma_{xx} = +\infty$  otherwise for higher values of  $d$  will converge to  $\sigma$  as can be inferred in Fig. 3d.

$$\sigma_f = \sigma \left( 1 + \frac{d_{seq}}{l} \right) \quad \text{Eq. 74}$$

$$Z_{(z)} = \frac{\sigma z}{\sqrt{z^2 - a^2}} \quad \text{Eq. 75}$$

$$\sigma_{xx} = \sigma_{yy} = \frac{\sigma \sqrt{a}}{\sqrt{2}d} \quad \text{Eq. 76}$$

Also, all samples manufactured with one replication were evaluated using the coefficient of variance (CV, Eq. 77), verifying the heterogeneity of the results according to the mean data and the dispersion. Uniform distribution was used to calculate the dispersion of the samples with two replications (Eq. 78). As the CV is lower than 30%, it can be inferred that the results are in control (Brown, 1998), and there is no necessity for extra assessments.

$$CV\% = \frac{\sigma}{\mu} 100\% \quad \text{Eq. 77}$$

$$\sigma_u = \frac{b - a}{\sqrt{12}} \quad \text{Eq. 78}$$

## V. 2. 2. Results and discussion

The results of the hybrid manufacturing of samples are presented in terms of: melting interface zone (V.2.2.1), hardness profile (V.2.2.2), tensile strength (V.2.2.3), and porosity distribution and its influences on the mechanical properties (V.2.2.4).

### V. 2. 2. 1. Melting interface zone

Figure V-5 presents the analysis of the hybrid manufactured samples A, C, and E using metallographic images. For analysis, the samples were evaluated into five regions. Regions 1 and 2 depict the microstructure of the PBF-LB portion. Region 3 presents the MIZ, and regions 4 and 5 the metallography of the machined portions.

The OM images of Region 3 allow observing a transition region in hybrid manufacturing with a characteristic microstructural change. This transitional region has been identified as the melting interphase zone (MIZ). Highlights the presence of refined grains in the central zone, a region that also changes in length with the PBF-LB parameters used. On the substrate side (right), a transition in the grain size due to the laser power source can be noted. However, only the PBF-LB side (left) presents a critical columnar formation with needle-shaped grains. This type of microstructure is expected in the first layers of PBF-LB manufacturing due to the substrate's fast cooling and polycrystalline equiaxial matrix. Besides the compositions of the different materials, the microstructure was clearly affected by the nature of the process used, with different shapes and smaller grains in the PBF-LB portion.

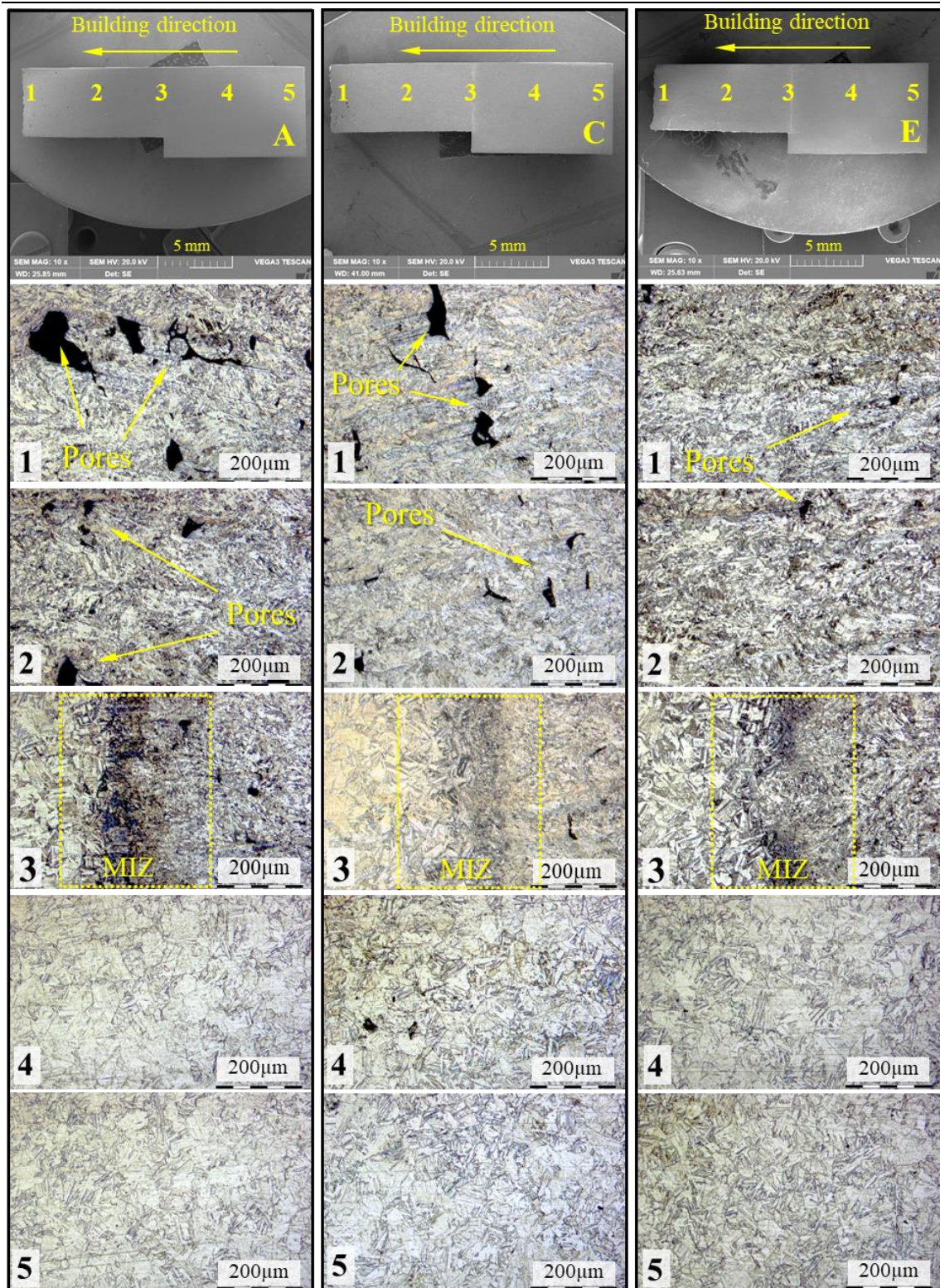


Figure V-5. Optical microscopy images of samples manufactured using PBF-LB parameters A, C, and E (Marin et al., 2023).

As expected, in regions 4 and 5, there is a great similarity for all samples, within the presence of a martensitic phase (BCC) and an austenitic phase (FCC), characteristics of the PH13-8Mo (Li et al., 2017). Regions 1 and 2 show the impacts of the use of different scanning speeds. The increase of the scanning speed and its distance from the MIZ increased the presence of pores, with a clear presence of bigger pores in sample A

than in sample C and almost none in sample E. A more detailed analysis of the grain growth of the hybrid samples can be observed in the SEM scan results presented in Figure V-6.

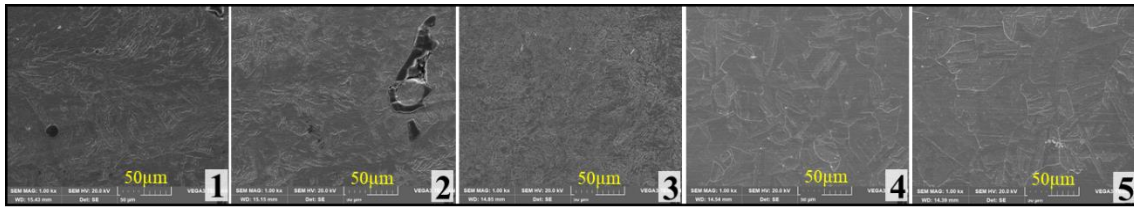


Figure V-6. SEM images of regions 1 to 5 of sample E (Marin et al., 2023).

The SEM images allow identifying the dominance of equiaxial grain in the substrate with a gradual refinement of the grain close to the MIZ promoted by the laser source. The images helped to identify the grain coarsening phenomenon as the main mechanism of microstructure shaper in hybrid manufacturing, characterizing the transaction of the substrate MIZ to the PBF-LB portion.

The gradual transition of the equiaxial grains presents in the substrate (regions 4 and 5) to a fine equiaxial grain (centre of region 3) to columnar grains structure (regions 1 and 2). As seen in regions 3 and 2, the first layers of PBF-LB manufacture present a mixed structure with an equiaxial formation that disputes the preferred columnar formation of PBF-LB. A more directional structure is observed in region 1, with a higher distance from the MIZ. The alignment of the columnar grains growths between layers (grain swallowing), forming a bigger columnar structure oriented in the preferred cubic crystallographic structure, in the building direction ( $0^\circ$ ) and oblique ( $90^\circ$ ), corroborating with found by Ji, Chen and Chen (Ji et al., 2018).

The stereoscope analysis of the melting interface zone using different scanning speeds is presented in Figure V-7. The region is delimited between the red line (support plane) and the yellow line. It can be seen that as the scanning speed increases, the MIZ decreases. It can be correlated to the longer laser interaction time that causes a deeper melting puddle. In sample A, the low energy density resulted in a weak bonding of 0.125 mm, while the slowest scanning speed (parameter E) resulted in 0.295 mm.

The stereoscope analysis detected no pores on the MIZ (Figure V-7). However, some pores can be noted near the MIZ in samples E (2300 mm/s) and D (2035 mm/s). A deeper investigation of this region was conducted by tomography analysis and SEM scan. Figure V-8 shows the distance of pores to the MIZ and its morphology according to the PBF-LB scanning speed.

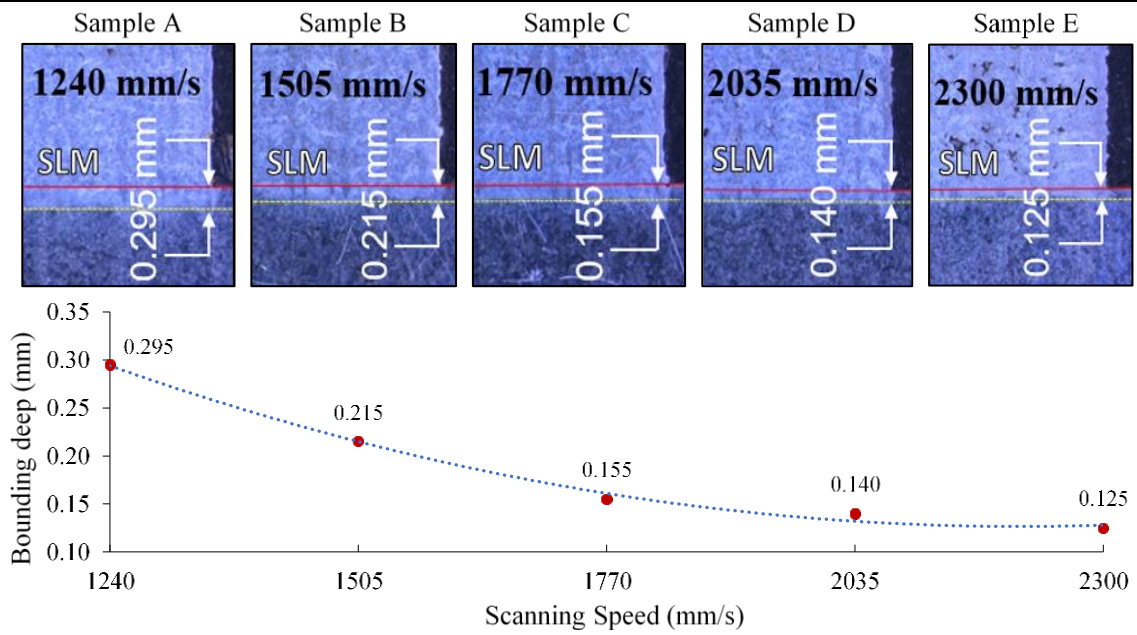


Figure V-7. Laser scanning speed versus MIZ (Marin et al., 2023).

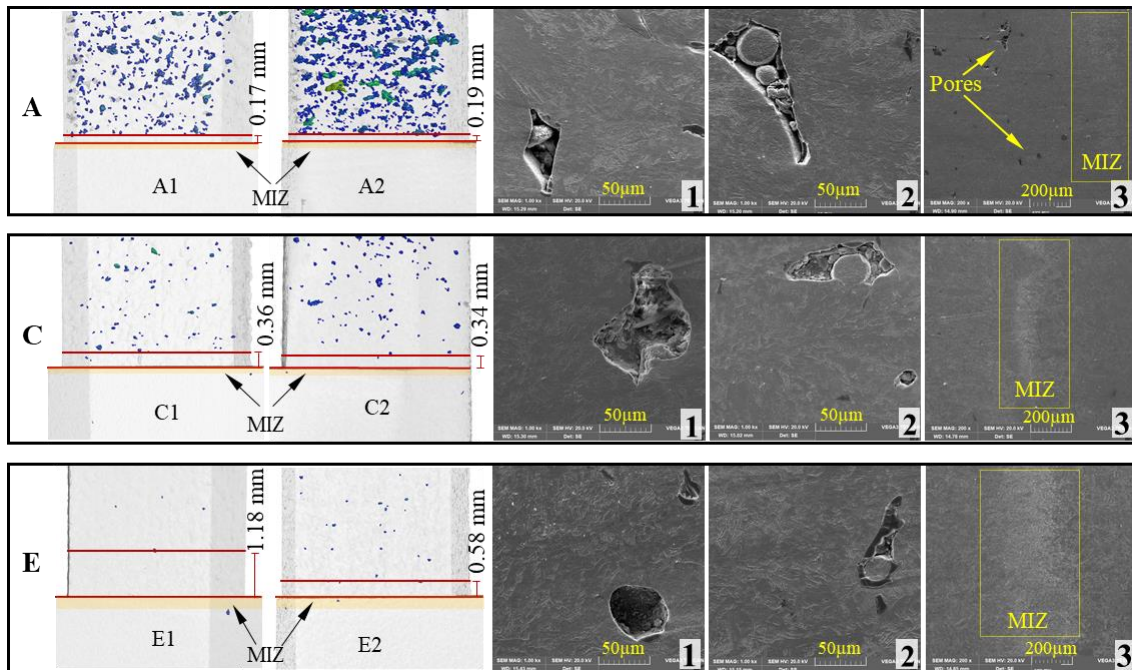


Figure V-8. Pore distance to MIZ of samples A, C, and E measured by tomography (left) and SEM scans of regions 1, 2, and 3 (right) (Marin et al., 2023).

The tomographic analysis shows that the melting interface zone does not present any significant pore, neither in quantity nor size, even for the more porous samples. It is noted that even for the fastest scanning speed, the distance of the pores to the substrate is at least 0.17 mm. Summing the bounding depth distance, at least 0.3 mm interaction region is obtained considering the fast scanning speed (parameter A). It was also observed that besides pores increasing in shape with the scanning speed, there is an increase in its randomness, favouring the entrapment of powder particles partially fused or completely unfused (depicted in region 2 of sample A). Furthermore, sample A was the only one that presented pores next to the MIZ.

### V. 2. 2. 2. Hardness profile

The average hardness profiles of the samples are presented in Figure V-9. As expected, the hardness on the machined portion showed to be independent of the manufacturing parameter, with almost the same value for all samples evaluated ( $344.7 \pm 4.4$  HV0.5). Whereas, in the region manufactured by PBF-LB, a higher variation is observed due to the PBF-LB parameters change (mean of  $340.9 \pm 8.8$  HV0.5).

Evaluating the hardness difference in the same sample according to the material, samples A, B, and C presented a lower hardness on the PBF-LB portion than the machined substrate (about 7.4 HV0.5). On samples D and E (slower scanning speeds), slightly higher hardness than the machined substrate was observed (about 1.4 HV0.5). Thus, as the scanning speed increases, the hardness decreases, influencing the hardness of the hybrid samples and modifying the elastic rigidity of the part.

Figure V-10 shows the results of solubilized and aged hybrid samples compared with the same sample as built. No cracks on the zone manufactured by PBF-LB or in the MIZ were found, indicating that hybrid manufacturing with these materials accepts heat treatment for a wide range of PBF-LB manufacturing parameters.

An increase of about 40% ( $\sim 150$  HV0.5) of hardness was obtained after the heat treatments. The hybrid sample D presented  $515.0 \pm 10.5$  HV0.5 at PBF-LB Corrax<sup>®</sup> and  $474.0 \pm 9.2$  HV0.5 on the PH13-8Mo (8% difference), while the hybrid sample E presented  $504.0 \pm 8.9$  at PBF-LB Corrax<sup>®</sup> and  $460.7 \pm 8.2$  HV0.5 at PH13-8Mo (8.6% difference). The difference in the hardness using the same parameters between additive Corrax<sup>®</sup> and the cold-rolled PH13-8Mo is correlated to the different material compositions and precipitation of components. Corrax<sup>®</sup> has a higher percentual of Ni, Si, and Al, elements that favour carbide formation. Furthermore, there is a slight difference in the hardness of the PBF-LB portion using parameters D and E after the heat treatments. The increase in the scanning speed propitiates more intergranular defects, facilitating intergranular austenite transformation into martensite.

In the specific case of the hybrid sample E, it is possible to observe a tendency of slight increment of the hardness in the first 3 mm of the deposited layers, probably due to a pre-tempering phenomenon, lowered after the heat treatments as depicted in Figure V-10. The Hall-Petch effect helps to explain this hardness increase. Using a high amount of energy (like laser processes) in materials with high grain contours can change the granular growth direction and increase internal tensions and material hardness.



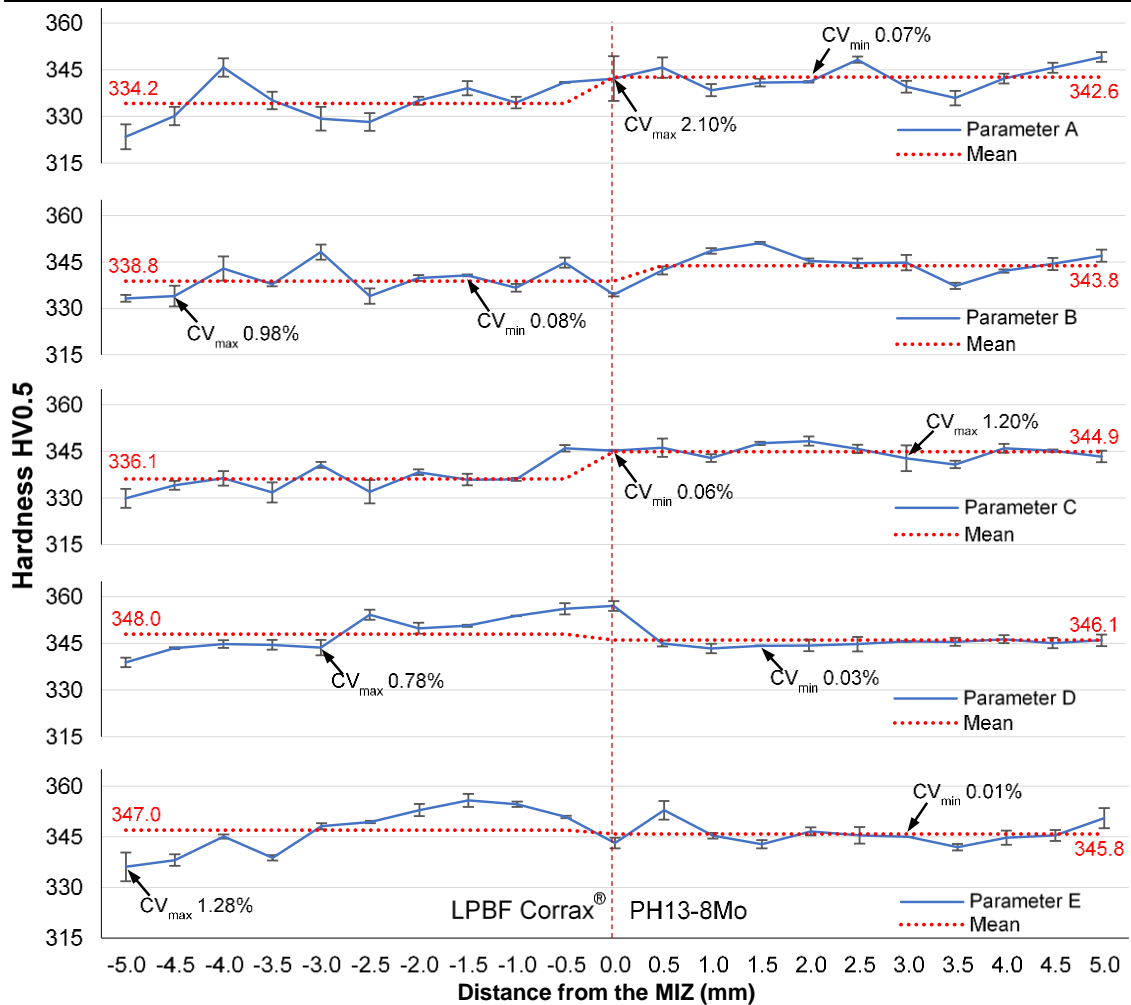


Figure V-9. Hardness profiles of the hybrid samples (Marin et al., 2023).

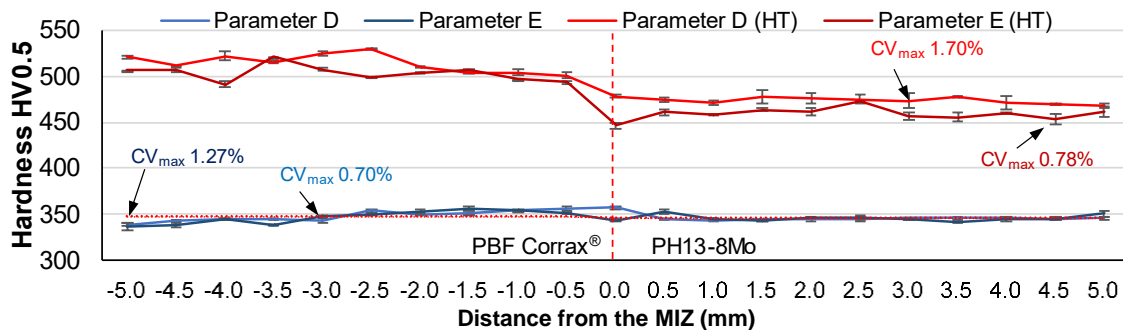


Figure V-10. Hardness profiles of the samples D and E solubilized and aged versus as built (Marin et al., 2023).

### V. 2. 2. 3. Tensile strength

Figure V-11 presents the images of samples A, C, and E after the tensile strength as well as its stress-strain diagrams. Notably, all hybrid samples tested broke in the PBF-LB portion. Even with a lower depth of interaction (0.125 mm), the rupture did not occur in the MIZ. Although the tensile test does not break in the MIZ, the depth of interaction affects the rupture distance and its pattern. The rupture distance from MIZ for the specimens manufactured with the parameters A and C were about 5 mm, while parameter E was about 15 mm.

Figure V-11 also shows that the rupture of the parts manufactured with higher scanning speed (parameter A; 2300 mm/s) presents only an elastic zone with brittle fracture (close to 0°). Manufacturing with parameter A resulted in an ultimate tensile strength (UTS) of  $663 \pm 1$  MPa and elongation of 2.06%. Using the reference parameter (C; 1740 mm/s), the fracture angle was about 20° with a total plastic elongation of 3.7%, UTS of  $960 \pm 6$  MPa, and 2.6% elastic elongation. Decreasing the scanning speed and increasing the energy density (parameter E; 1240 mm/s) is observed yielding, indicating a significant ductile gain, with about a 22% reduction in the diameter. For these samples, the total elongation was about 8%, UTS of  $1030 \pm 3$  MPa, and elastic elongation of 2.42%; mechanical property close to the Corrax® solution treated (1100 MPa) (Uddeholm, 2016). Furthermore, parameter E was the only one that produced necking and a cleavage angle of about 45°, characteristic of PH steels with a martensitic matrix.

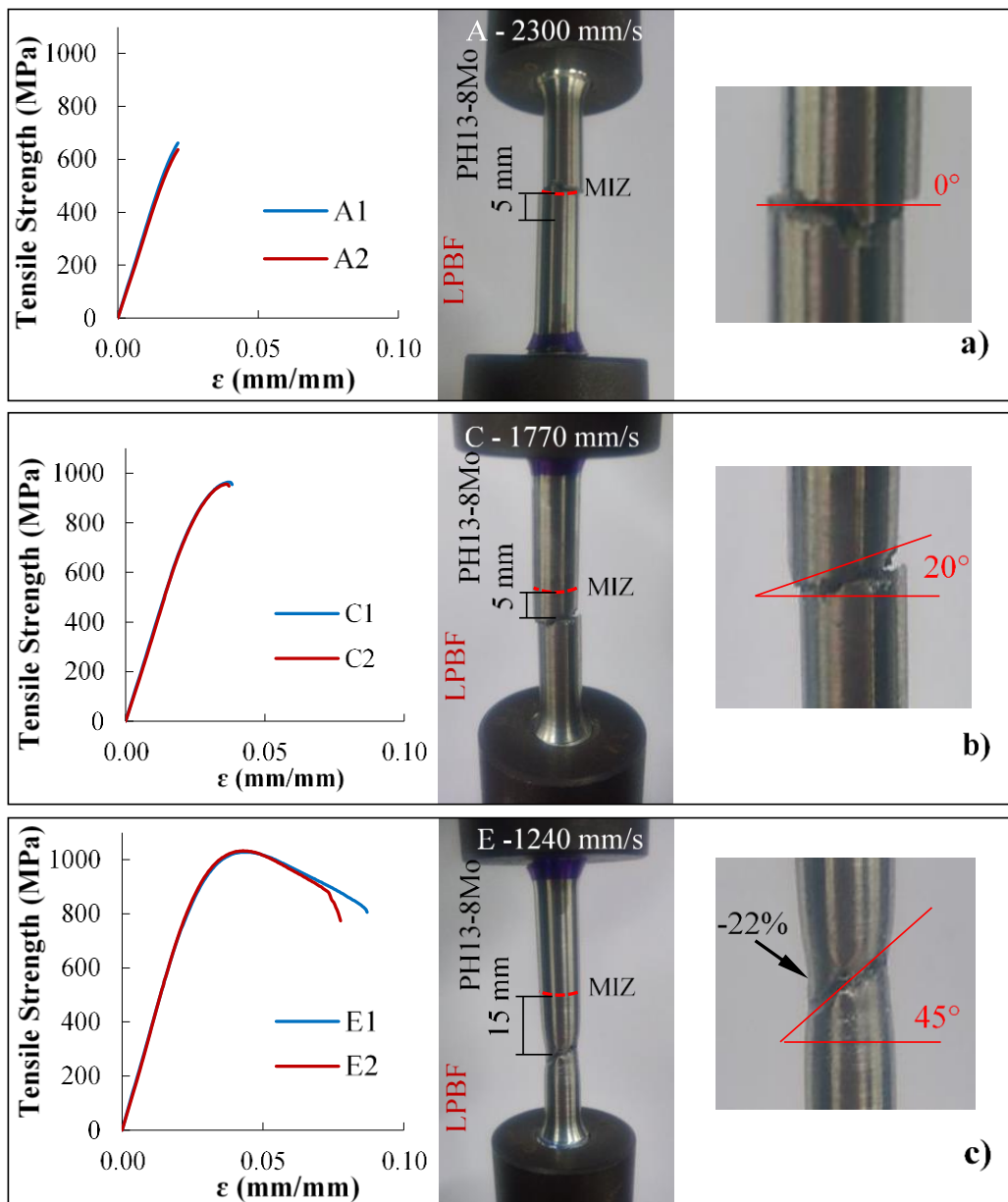


Figure V-11. Tensile strength test using ASTM 370 hybrid samples: a) samples A; b) samples C; c) samples E (Marin et al., 2023).

Besides, the energy absorbed in the fracture and the modulus of the toughness of each hybrid sample can be calculated by integrating the curves of tensile strength versus elongation (Figure V-11). The higher value was obtained with parameter E, slower scanning speed (3.933 J·m<sup>-3</sup>, CV 13.6%). Using scanning speed C it decreases 80% (0.816 J·m<sup>-3</sup>, CV 5.7%) and 93% with parameter A (0.280 J·m<sup>-3</sup>, CV 1.9%). Thus, the use of different densities of energy resulted in different break compartments. The reduction of about 6% in the mechanical component using parameter E and the higher cleavage angle suggest a ductile fracture with decreased local cross-section due to pores (Eq. 74).

In contrast, the cleavage angle and the higher UTS reduction on samples A and C suggest fragile fracture due to crack propagation (Eq. 18). The increase in the number, size, and distribution of the pores near the MIZ can be related to these effects. For this reason, they were deeply investigated in the next section.

#### V. 2. 2. 4. Porosity distribution and its influences on the mechanical properties

A concise analysis was conducted to understand the correlation between porosity and the patterns of fracture observed in the tensile test samples (Figure V-11). Figure V-12 presents one representative image of each sample (Figure V-12a) together with the relative density using post-processed OM images (Figure V-12b). The OM image presented was selected according to the closest average relative density, presenting the raw picture in half of the image and another half with the software pores notation (in red). Figure V-12c shows the direct correlation of the relative density with the average hardness and scanning speed.

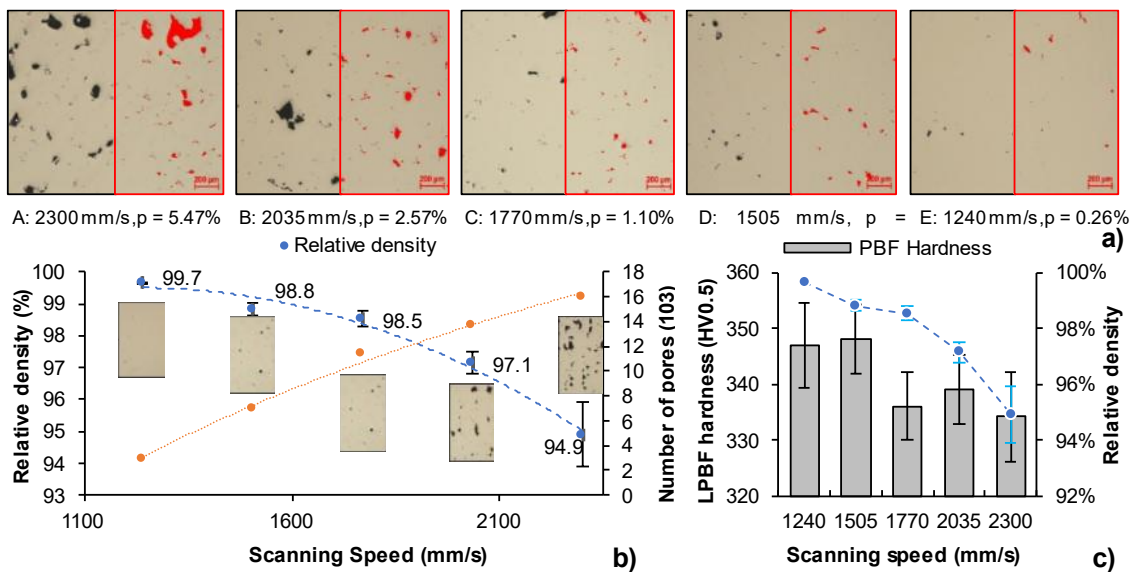


Figure V-12. Relative density: a) OM image according to scanning speed; b) relation with the scanning speed and the number of pores; c) relation with the average hardness of the samples (Marin et al., 2023).

The parts manufactured with higher scanning speed presented a reduction in the relative density and bigger pores with random shapes. The OM images showed a relative density of 99.7% for a scanning speed of 1240 mm/s, similar to those obtained by Asgari and Mohammadi (Asgari and Mohammadi, 2018). By increasing the scanning speed from 1770 to 2300 mm/s (+30%), the number of pores increased by about 39%, with relative density decreasing only by 3.6%. Decreasing the scanning speed to 1240 mm/s (-30%), the number of pores decreased by 74%, and the density increased by 1.2%. Hence, it is clear the decrease in pores number and size with scanning speed reduction.

Apart from the different fracture types (Figure V-11) and the direct correlation of the hardness with the scanning speed, the relation between the pore number and porosity factor is presented in Figure V-13a. Figure V-13b shows the toughness modulus and the strain according to the scanning speed, and Figure V-13c shows the UTS and the relative density.

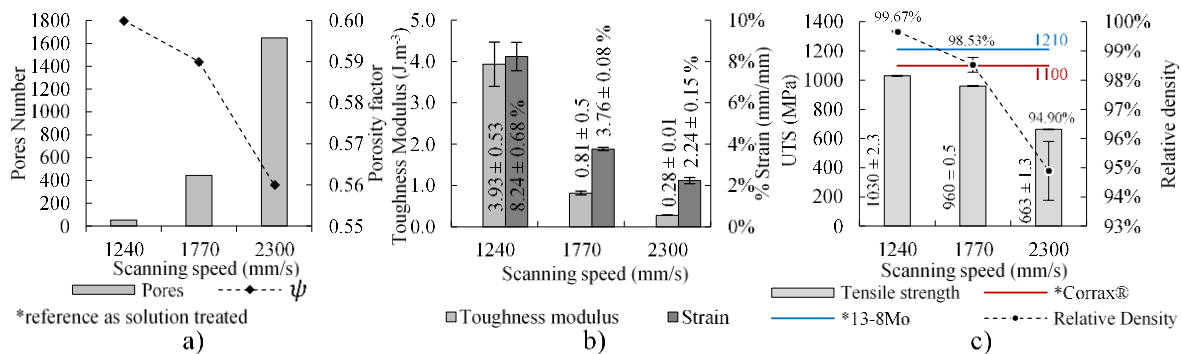


Figure V-13. Scanning speed porosity relation with tensile strength results: a) Pore number and sphericity; b) toughness modulus and strain; c) UTS and relative density (Marin et al., 2023).

The relative density has been examined to understand its influence on the UTS, fracture strain, and toughness modulus. Toughness modulus directly increased with UTS due to higher ductility and percentage elongation obtained at lower scanning speed. Furthermore, the porosity and UTS do not follow a linear pattern; for about 0.8% change in relative density (99.7 to 98.5%), UTS changes by 6%. For a reduction in the relative density of 5%, the UTS reduces by 35% (1030 MPa to 663 MPa). These observations lead to a detailed understanding and prediction of the porosity distribution, shapes, and their influence on crack propagation and fracture.

The results of the tomography analysis show the volume of the pores and their volumetric distribution over the samples manufactured with parameters A, C, and E (Figure V-14). In all cases, the pore's random shape and porosity tend to increase with the number of layers fabricated, probably due to the heat build-up. When manufacturing with a higher scanning speed, the low energy density can also result in partial melting bonding between layers during PBF-LB manufacturing, supporting pore formation.

Analysing Figure V-14, a higher number of irregular pores can be detected from higher scanning speed to lower, respectively, A, C, and then parameter E. From 1770 mm/s to 2300 mm/s, the number of pores significantly increased. Supposedly, the energy density was marginal to completely molten the powder, resulting in higher porosity. The entrapment of gases during the solidification of the molten pool can explain the presence of pores in the specific case where high energy density is involved (Fergani et al., 2017). The reduction of porosity with the volumetric energy increase leads to the conclusion that, with the selected parameters, the energy input was not excessive to generate pores by gas entrapment.

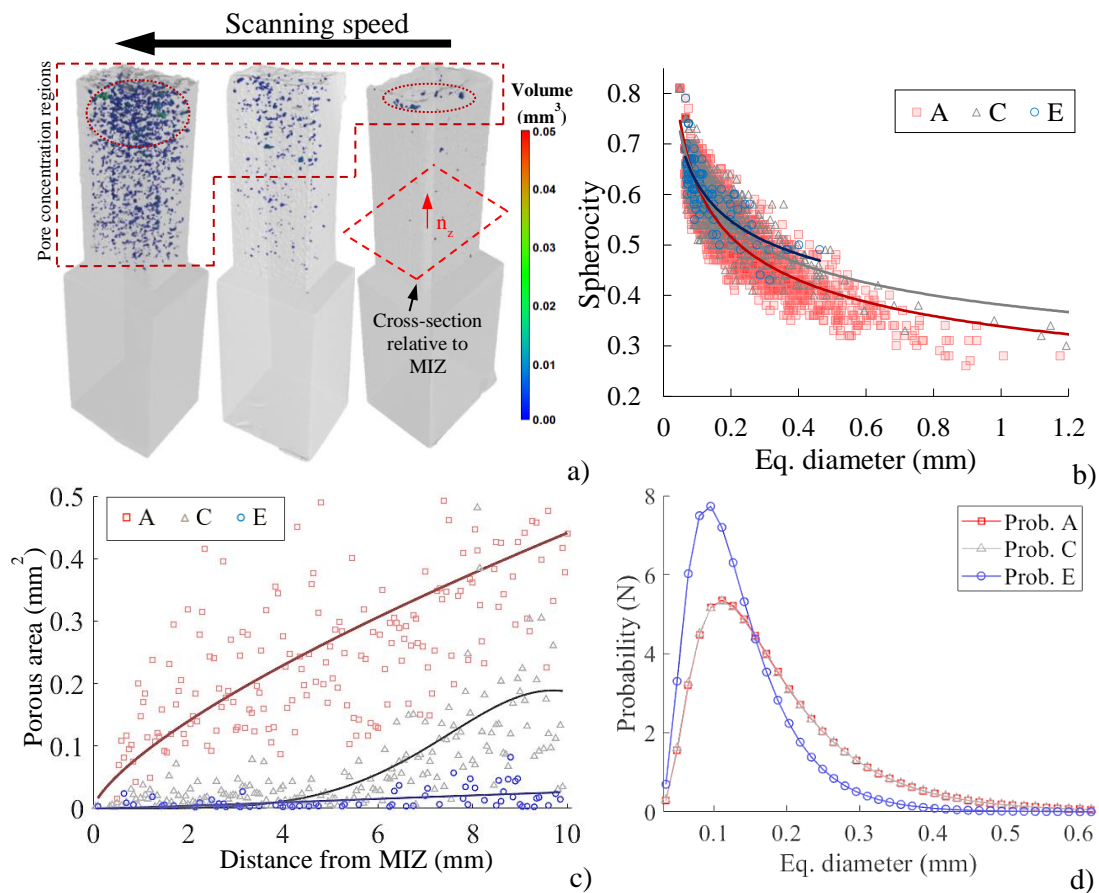


Figure V-14. Porosity analysis of the samples by tomography: a) sample schematic; b) sphericity versus equivalent diameter; c) pore area XY plane (normal to the building direction); d) pore size distribution (Marin et al., 2023).

The pore size distribution (Figure V-14d) shows a pore equivalent diameter of about 100  $\mu\text{m}$  independent of the scanning speeds utilized. Figure V-14b shows the sphericity versus the equivalent diameter. A lower influence of pores number than size was observed on the sphericity, with better sphericity obtained at lower scanning speeds. The porous parts (A and C) presented a wide sphericity range, varying from 0.2 to 0.8, while sample E showed variations between 0.5 to 0.8 (Figure V-14b). The higher volume of pores presented in sample A resulted in a higher reduction of the area at plane XY (Figure V-14c), a plane normal to the tensile test load, which can be one of the causes

of low UTS results presented in Figure V-11. Besides increasing the number of pores, the scanning speed increases non-linearly the volume of pores and shape irregularities, corroborating with findings Hague, Mansour, and Saleh (Hague et al., 2004).

Regions with more pores facilitate the crack due to a reduced effective area that increases the stress locally. Figure V-15a shows Westergaard's Stress Intensity Factor ( $K_t$ ) calculated considering the distribution of pores obtained by tomography analysis. A critical distance of 0.8 mm for crack propagation is found using the probabilistic pores size value (100  $\mu\text{m}$ ) and a stress superposition factor of 30% (equivalent to about  $2\sigma$  of the Gaussian distribution). It is also observed that the critical distance is reduced by increasing the reliability. Figure V-15b presents the minimum pores distance measured in the XY plane according to MIZ distances.

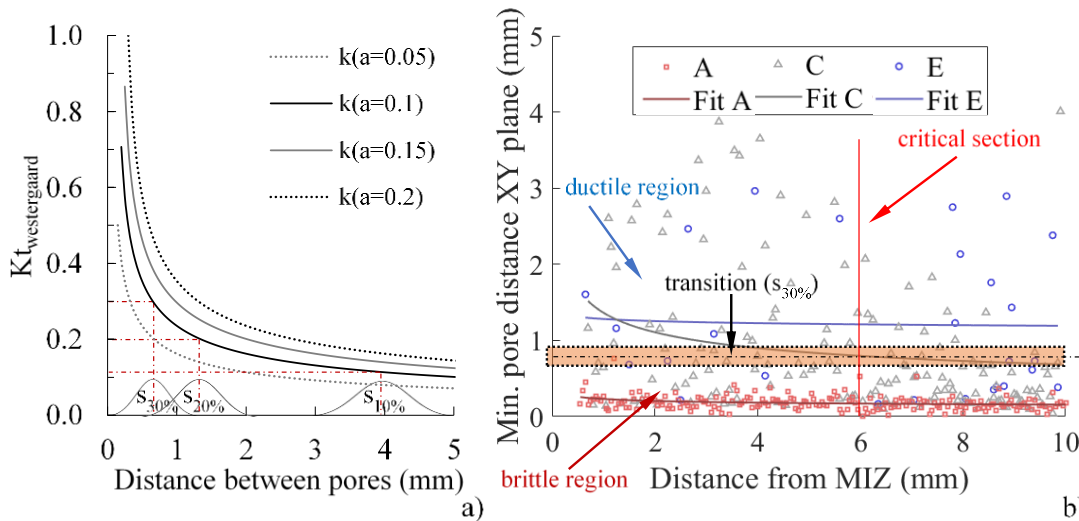


Figure V-15. Ductile to brittle fracture transition with porosity: a) stress concentrator factor; b) minimum pore distance versus the distance from MIZ (Marin et al., 2023).

The critical distance calculated shows that A and E are stationary zones, and the distance from MIZ should not affect the rupture pattern. Besides having a high number of pores, the sample manufactured with a higher scanning speed (parameter A) presents pores very close to each other (average distance of 0.2 mm). Thus, it is expected brittle compartment in the whole part. Compared to sample E, the low presence of pores and good dispersion leads to constant plastic compartment expected over all the parts. In sample C, the gradual increment in pore number (Figure V-14a) maintains the same particle distribution (Figure V-14d) and lower sphericity (Figure V-14b) with increased porous area from the 4 mm distance of the MIZ (Figure V-14c). That way, for this sample, is expected a transitional compartment before the 6 mm far from MIZ. Results that match the presented in Figure V-11, where sample C broke fragile close to 5 mm and with about 20% cleavage angle, and the difference of rupture pattern observed on samples A and E.

It was observed that the presence of pores changed the fracture pattern non-linearly. In the critical cases (with 1.5% and 5% pore volume), tomography porosity analysis data and mechanics (Eq. 73) and fracture mechanics equations (Eq. 76) predicted the fragile comportment that resulted in an expressive UTS reduction of up to 35%.

### **V. 2. 3. Conclusions**

The manufacturing process investigation using machining and PBF-LB showed that the melting interphase zone formed using different materials and processing parameters is not a limitation for the hybrid manufacturing process with PBF-LB. Besides, selecting the PBF-LB manufacturing parameters allowed control of the porosity, changing both productivity and mechanical properties. The main conclusions of the study case are:

- Varying the PBF-LB scanning speed from 1240 to 2300 mm/s, the depth of interaction between the Corrax<sup>®</sup> and PH13-8Mo was from 0.12 to 0.30 mm. The MIZ did not present pores and had good mechanical properties, not the hybrid part's weak portion.
- The hardness of the hybrid samples had a low influence by the scanning speed, varying less than 5% (about 15 HV0.5). The hardness variation increased to more than 8% with solubilization and the ageing process, showing the effects of the different material compositions. No fractures were observed after the heat treatment, demonstrating that hybrid parts with dissimilar materials can accept heat treatment.
- The laser scanning speed influenced the PBF-LB portion's porosity, affecting the mechanical properties of hybrid components. Reducing the scanning speed by 30% reduced the number of pores by 74%. An increase of 30% in the scanning speed increases the number of pores by 34%, reducing the sphericity factor, the distance between pores, and the pores cross-section area at the PBF-LB portion.
- The porosity mostly impacted the tensile strength results, reducing the UTS from 6% to 45% compared to the normalized Corrax<sup>®</sup>. The mitigation in pore size and distribution allowed the correlation of the rupture pattern, from plastic to fragile fracture, due to crack propagation. The samples with a low presence of pores presented ductile fracture, with a cleavage angle close to 45°. Increasing the scanning speed, the number of pores increased, and its distance was reduced, modifying the cleavage angle and the fracture pattern to brittle.
- The study of the hybrid manufacturing process method involving multi-materials is extremely promising, and the mechanical properties obtained can be extrapolated to repair or remanufacture engineering components in multiple steps using hybrid manufacturing methods.

### V. 3. Manufacture of a blade with Lattice structures

This subsection presents the study case of the manufacture of a blade containing lattice structures by PBF-LB and their machining influences in 5-axis with ball-end tooltips.

#### V. 3. 1. Materials and methods

##### V. 3. 1. 1. Part design and AM manufacturing procedure

To evaluate the influence on the finishing process of slender parts containing internal microstructure, two blades with different geometries, one with internal lattice structures and the other one solid, were designed and manufactured.

For the design process, Siemens NX 1953<sup>®</sup> was used. The part was designed with a wall thickness of 2 mm and fulfilled with lattice structures with a 1 mm edge of cell size and sprout of 0.2 mm. Figure V-16 shows the CAD of the blade and the distribution of the microstructures.

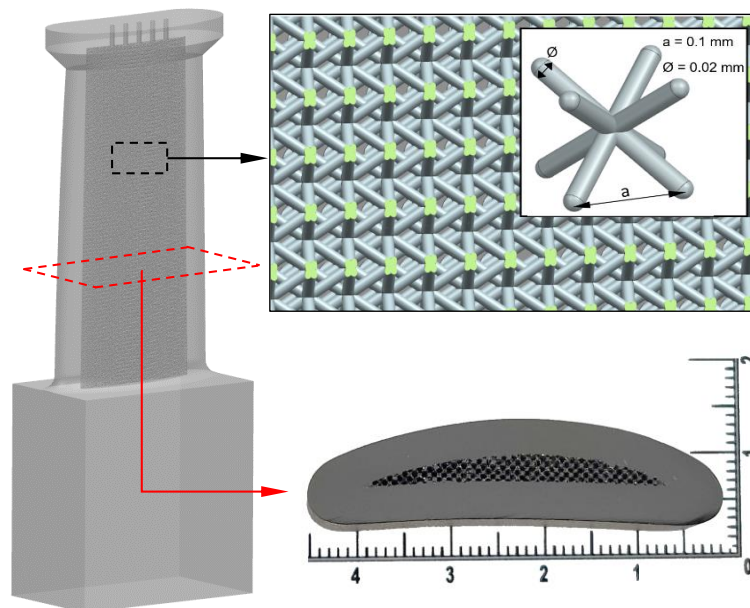


Figure V-16. Blade with lattice structures and dimensions.

The blades were manufactured in one production batch on a Renishaw<sup>®</sup> AM400 with an Yttrium fibre laser with 400 W maximum power. The material used in the process was a gas-atomised powder of Inconel<sup>®</sup> 718. The particle size distribution was analysed according to ISO 13320. The cumulative percentage of the gas atomised powder was  $d1 = 10.0 \mu\text{m}$ ;  $d10 = 17.1 \mu\text{m}$ ;  $d50 = 32.5 \mu\text{m}$  and  $d90 = 54.8 \mu\text{m}$ , which indicates the size distribution to the specified volume percentage. The PBF-LB manufacturing strategy used was raster with a rotation of  $67^\circ$  between layers (10 mm stripe). The blades were printed in the same batch and in a vertical position to reduce deviations by residual stresses inherent in the process. Besides, a stock of 1.5 mm was added to avoid



geometrical deviation issues, guaranteeing dimensional accuracy after machining. The manufacturing parameters are presented in Table V-4, and the nominal composition of the powder is presented in Table V-5.

Table V-4. PBF-LB manufacturing parameters.

PBF-LB manufacturing process	
Laser Power (W)	200
Scanning speed (mm/s)	1000
Hatching (mm)	0.09
Layer thickness (μm)	60
Laser HAZ size (μm)	70

Table V-5. Chemical composition of the Inconel® 718 powder (in weight %).

	Ni	Cr	Nb	Mo	Ti	Co	Al	Mn	Si	C	Fe
Inconel® 718	54.1	18.4	4.85	2.8–3.3	0.65–1.2	≤1.0	0.2–0.8	≤0.35	≤0.35	≤0.08	Balance

A hardness analysis was also conducted on an embedded sample from the blade to evaluate the anisotropy of the blades manufactured using PBF-LB. To do so, a durometer INNOVATEST Falcon 500 with micro Vickers indenter and 1 kg of load were used to make five evaluations on a cross-section normal to the building direction and another five on the transversal to the building direction, spaced by 1 mm from each other, starting from the border to the centre of the embedded sample. The result depicted in Figure V-17 shows no significant difference in the part anisotropy.

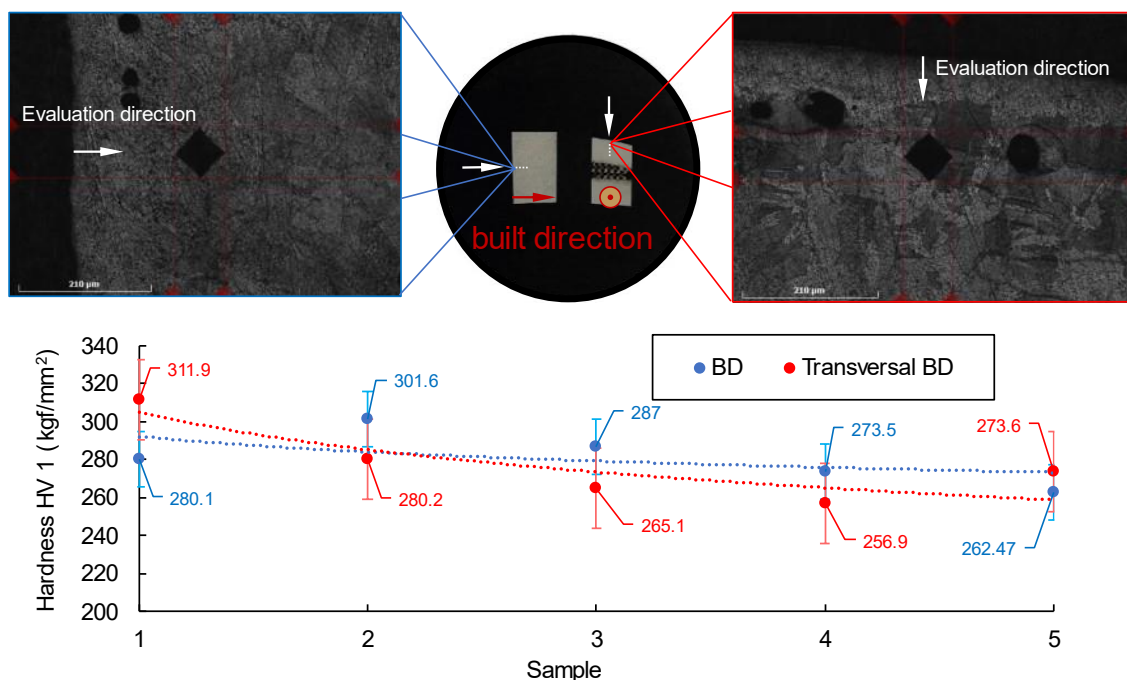


Figure V-17. Evaluation of the hardness on the blades manufactured by PBF-LB.

### V. 3. 1. 2. Machining procedure

The manufactured blades were machined on a multitasking 5-axis Mazak INTEGREX® i200 smooth. The parts were clamped in the machine with a 5-axis Makro-Grip Lang 48120-77 (clamp chuck with clamping force up to 14.000 N) without tailstock. In the

machining process of some complex thin-walled components, the use of tailstock is not possible due to geometrical limitations, and, in some cases, the pressure can add unexpected deformations to the final blade (Zha et al., 2023). Thus, in this case, no tailstock was used to simulate the most critical conditions and the damping performance of internal lattice structures.

The same strategies were used on both blade types to compare the effects of lattice structures on the finishing operation. The blade surface was split into eight sections with equal lengths (10 mm) to evaluate four different finishing conditions with one replication each. Two tool geometries, with different tooltips, a ball-end, and a barrel lens shape (both with 10 mm nominal diameter, 30 helix angle, micro grain solid carbide with 10% Co, and coated using multilayer TiAlN / TiSiN with 3800 HV 0.05) were selected. In addition, two levels of lead angle were used to obtain different cutter workpiece engagements (CWE). The selected lead angles of 15 and 25 degrees were based on the dominance of the lens shape tool minor radii ( $r_2$ ) or major radii ( $r_1$ ), as depicted in Figure V-18. For the ball-end tooltip, defined lead angles can produce a machined surface with good integrity, as reported by (Guillemot et al., 2013).

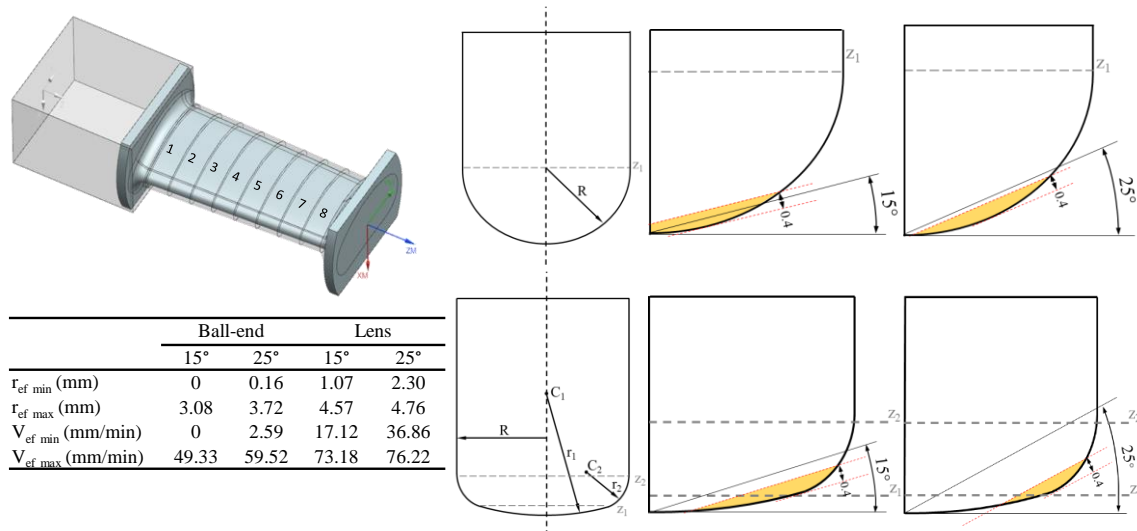


Figure V-18. Manufacturing regions and tool engagement schematics.

Milling tools were mounted in a high-torque toolholder with a 40 mm cantilever. The static run-out of the tools was below 5  $\mu\text{m}$ , and the precise length was verified using a Zoller® SmartCheck 600 tool presetter. The blades were semi-finished using a ball-end tooltip in a spiral strategy with 0.4 mm step over and letting 0.4 mm overstock. The manufacturing parameters utilised for finishing both blades are presented in Table V-6. They were carefully selected based on a previously machined blade using cold-rolled CrNi alloy.

Table V-6. Test definitions and manufacturing parameters.

<b>Cutting conditions</b>								
Region	Tool type	Lead angle (°)	$a_e$ (mm)	$a_p$ (mm)	Strategy	$V_c$ (m/min)	$f_z$ (mm/z)	Material
1	Ball-end	15						
2	Barrel	25						
3	Ball-end	25						
4	Barrel	15	0.2	0.4	spiral	80	0.05	PBF-LB Inconel® 718
5	Barrel	25						
6	Ball-end	15						
7	Barrel	15						
8	Ball-end	25						

### V. 3. 2. Results analysis procedure

Manufactured blades were analysed according to machining behaviour (V. 3.2.1), power consumption (V. 3.2.2), and dynamic behaviour (V. 3.2.3). Also, the surface quality was evaluated through roughness (V. 3.2.4) and dimensional analysis (V. 3.2.5), and Blade internal structure analysis by SEM and computer tomography (V. 3.2.6).

#### V. 3. 2. 1. Machining behaviour

In this section, blade machining behaviour was analysed taking into account the machining power consumption dependent on workpiece geometry, cutting parameters, and strategies. Moreover, workpiece dynamic behaviour was also analysed and compared.

#### V. 3. 2 .2. Machining power consumption

The spindle power consumption was monitored in all finishing passes using a Power Cell Model UPC-E®. As can be seen in Figure V-19, the power consumption mean value is obtained for each blade (solid and lattice microstructured one) and for each blade region (1-8) manufactured according to machining conditions in Table V-6. It can be observed that the tendency is maintained for all the regions and workpieces; this is, higher power consumption values were obtained for the blade with an internal lattice structure. These values are around 7% higher than the ones for the solid blade.

The part with internal microstructure presented higher values of power consumption, and this can be correlated to a higher specific rigidity of the blade with internal microstructures, presenting less deflection than the solid one, with higher values of shear resistance and, therefore, higher values of cutting forces.

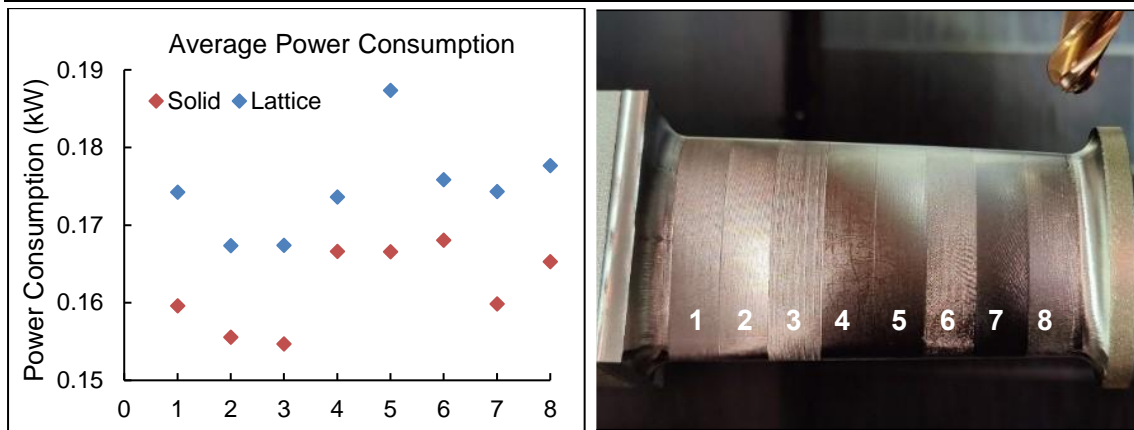


Figure V-19. Power consumption according to blade machining regions (1-8).

### V. 3. 2. 3. Dynamic behaviour

Just after the machining, hammer testing was conducted (Figure V-20a and Figure V-20b) in locus to consider the effects of the machine and clamping systems on the harmonic response of the machined blades (the solid one and the lattice structure). Two monoaxial accelerometers (PCB Piezotronics 352C22) and a Hammer (PCB Piezotronics 3425 with load sensor PCB 0865C03) were used to evaluate the blade's harmonic response.

The structural properties of both blades were experimentally tested, obtaining static stiffness, internal damping, and dynamic stiffness. Both solid and lattice blades presented very similar static stiffness (Figure V-20e) values, with a slightly higher value for the lattice blade with  $0.2 \text{ N}/\mu\text{m}$  in comparison to the solid blade with  $0.15 \text{ N}/\mu\text{m}$ .

On the other hand, the dynamic stiffness of both blades is shown in Figure V-20c and Figure V-20d. For the response of the first excitation, hammering position 1 with accelerometer on 3 (Figure V-20b), the receptance amplitude indicates that both blades are also very similar in terms of natural frequency ( $437.5 \text{ Hz}$ ) and damping ( $0.45\%$ ). For the response with the second excitation mode, which is hammering the part on position 2 with a sensor on position 4, it can be seen that the lattice blade presented higher dynamic stiffness, with a natural frequency of  $998.75 \text{ Hz}$  and damping of  $0.89\%$ , in comparison to the solid blade with  $966.25 \text{ Hz}$  and  $0.53\%$  damping.

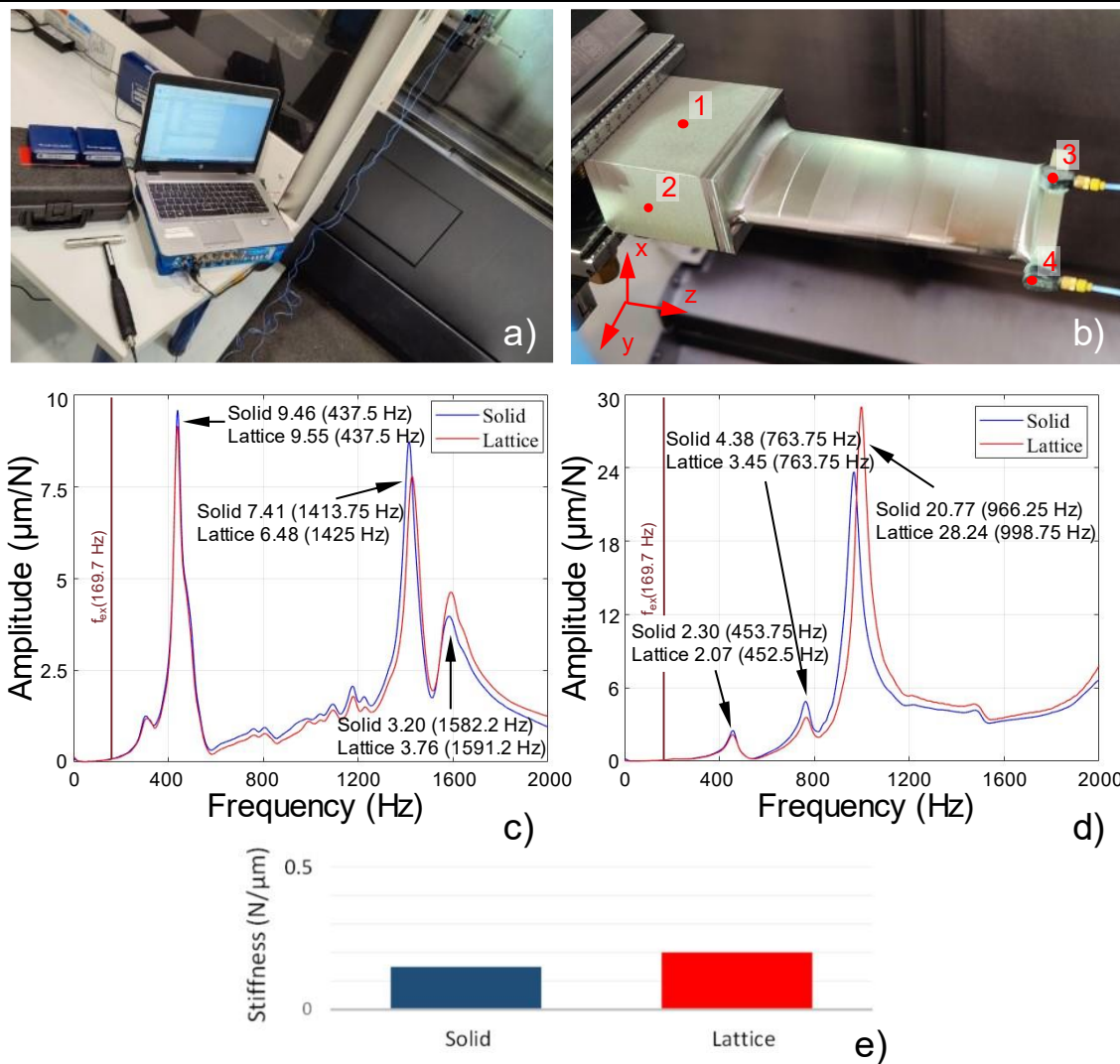


Figure V-20. Hammer test assay: a) Experimental apparatus; b) monoaxial sensors position and excitation points; c) first mode response; d) second mode response; e) static stiffness.

Therefore, the lattice blades are superior both in static stiffness and internal damping properties. This effect translated into a more rigid lattice blade, confirming the results obtained in the previous section for power consumption. The lattice blade absorbs and distributes the cutting force, being more rigid and presenting less vibrations.

### V. 3. 2. 4. Roughness results

Roughness values were measured with an optical microscope Leica<sup>®</sup> DCM3D for both components and both concave and convex surfaces of the 1-8 regions. Figure V-21 shows concave and convex topographies for both blade geometries and regions (1-8). The general tendency observed for both blades shows that concave surfaces have a maximum error of 30 µm, whereas the maximum error in convex surfaces is 60 µm. In relation to the region analysis, regions 2 and 4 (barrel tooltip and 25 and 15 lead angle values, respectively) are the ones with better results for concave surfaces. For convex surfaces, the tendency is maintained.

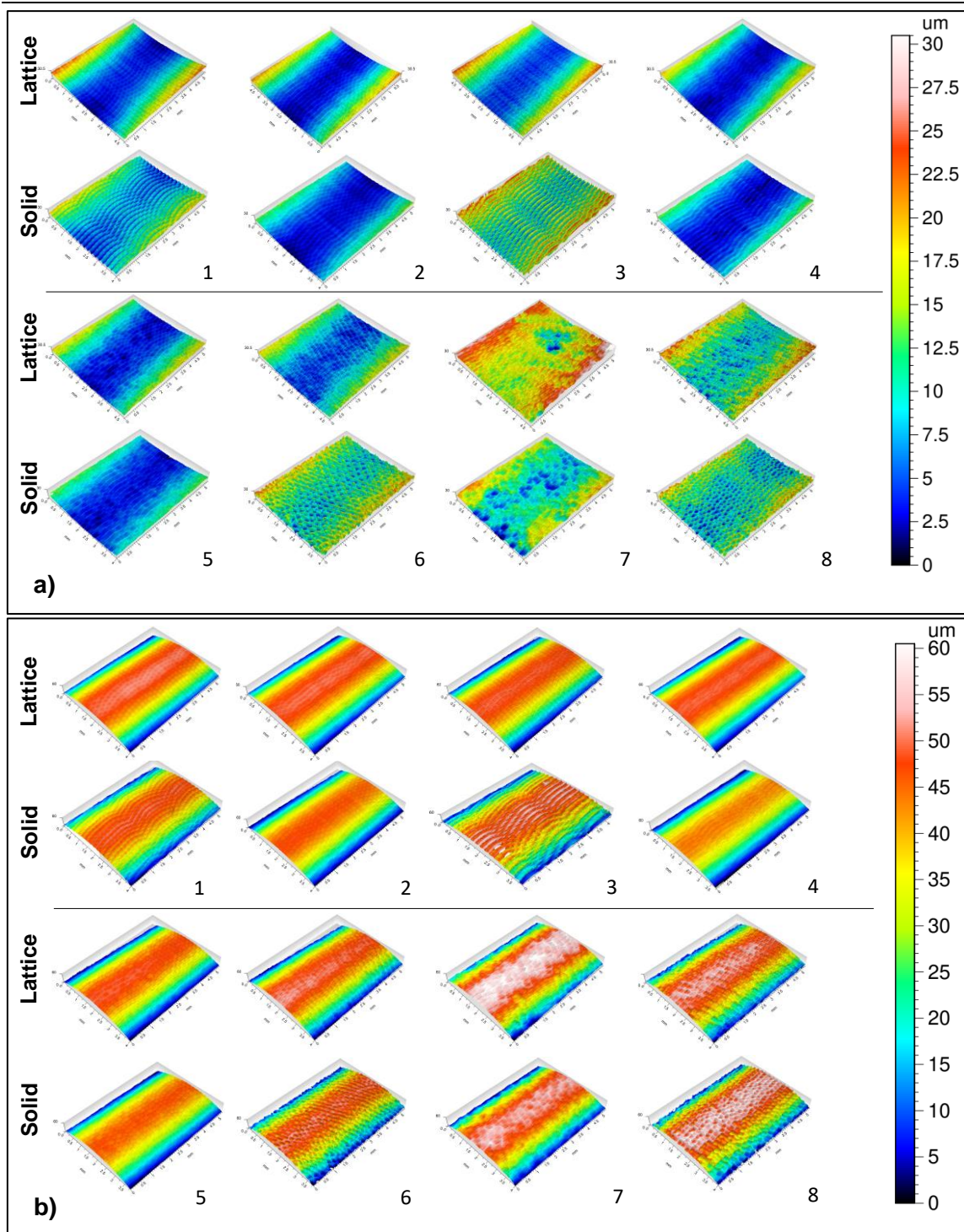


Figure V-21. Comparison of the surface topography of solid and latticed blades: a) concave; b) convex regions.

Figure V-22 shows  $Ra$  and  $Rz$  values for both geometries, both surfaces (concave and convex) and ball-end milled sections (1, 3, 6, 8) and barrel tool sections (2, 4, 5, 7). As can be seen, sections 2, 4, 5, and 7 (sections machined with barrel tool geometry) presented very good results for both blade geometries and surfaces (convex and concave) being both  $Ra$  and  $Rz$  results very similar, and  $Ra$  around  $0.2 - 0.3 \mu\text{m}$  and  $Rz$   $1 - 2 \mu\text{m}$ . For sections 1, 3, 6, and 8 (sections machined with ball-end tool), blade geometry with internal lattice microstructure presented better results than the solid blade.

Blade geometry with internal microstructure presented  $Ra$  values 0.2 - 0.6  $\mu\text{m}$  for the convex surface and  $Rz$  values 1 – 2  $\mu\text{m}$  for the concave surface. Solid blade geometry presented  $Ra$  values 0.3 – 1  $\mu\text{m}$  for convex surface and  $Rz$  values 1.8 -5  $\mu\text{m}$  for concave surface.

For both tool geometries, the minimum surface roughness was obtained with a lead angle of 15°.

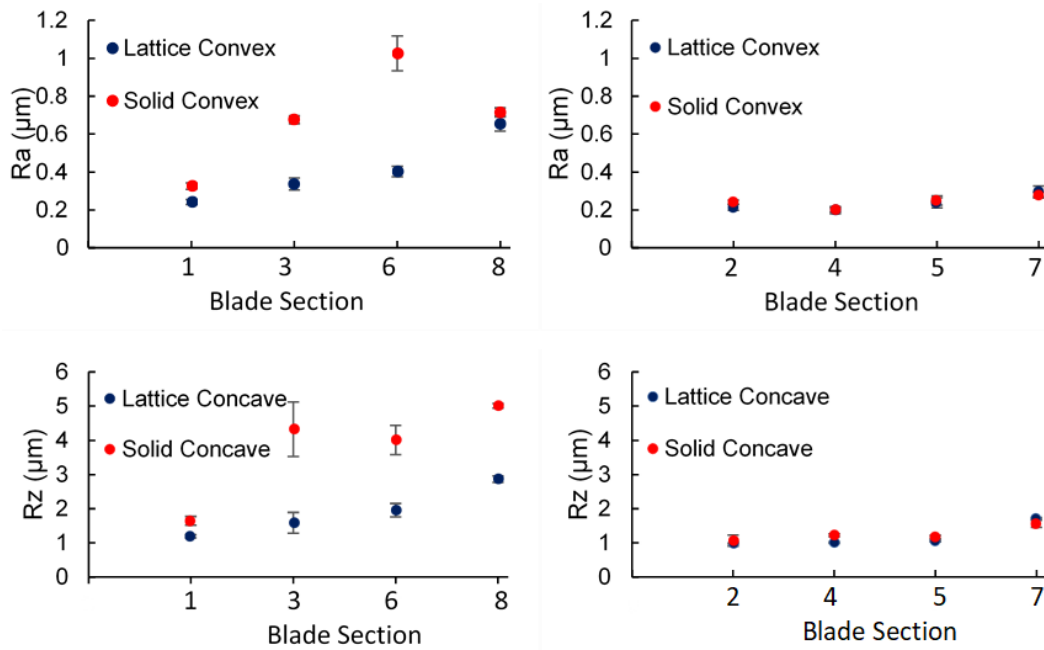


Figure V-22. Roughness  $Ra$  and  $Rz$  values.

### V. 3. 2. 5. Dimensional analysis

Dimensional analysis of both blade geometries was carried out with a Scanning head from Mitutoyo Crysta Apex S 9106. As it can be seen in Figure V-23, both blades present values under 300  $\mu\text{m}$ . However, better results are obtained on the lattice blade, with the entire geometry under 50  $\mu\text{m}$ , admissible for these components (Klocke et al., 2015).

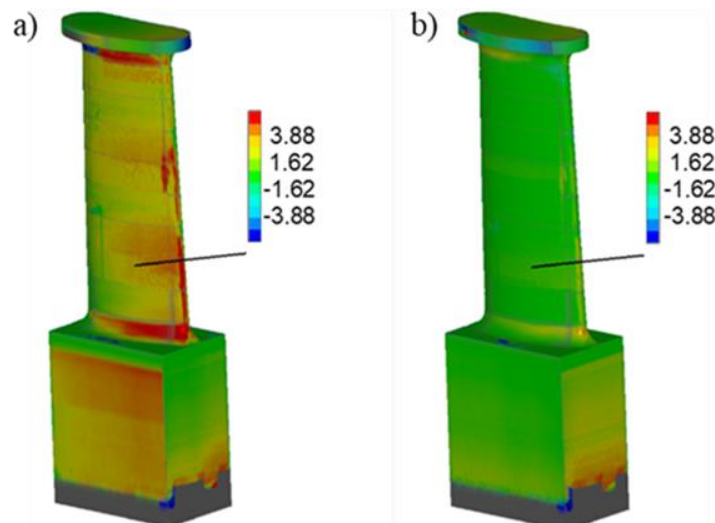


Figure V-23. Dimensional analysis: a) Solid blade; b) Lattice blade.

V. 3. 2. 6. Blade internal structure analysis by SEM and computer tomography

In this section, the internal structure of the blade is analysed through SEM (Scanning Electron Microscope) and computer tomography analysis. SEM analysis was performed for both blade geometries. Figure V-24 shows SEM images and energy spectrum with respect to the alloy elements. It can be observed that the internal microstructure presented some defects due to the lack of fusion of all the powder particles or the sintering of satellite particles.

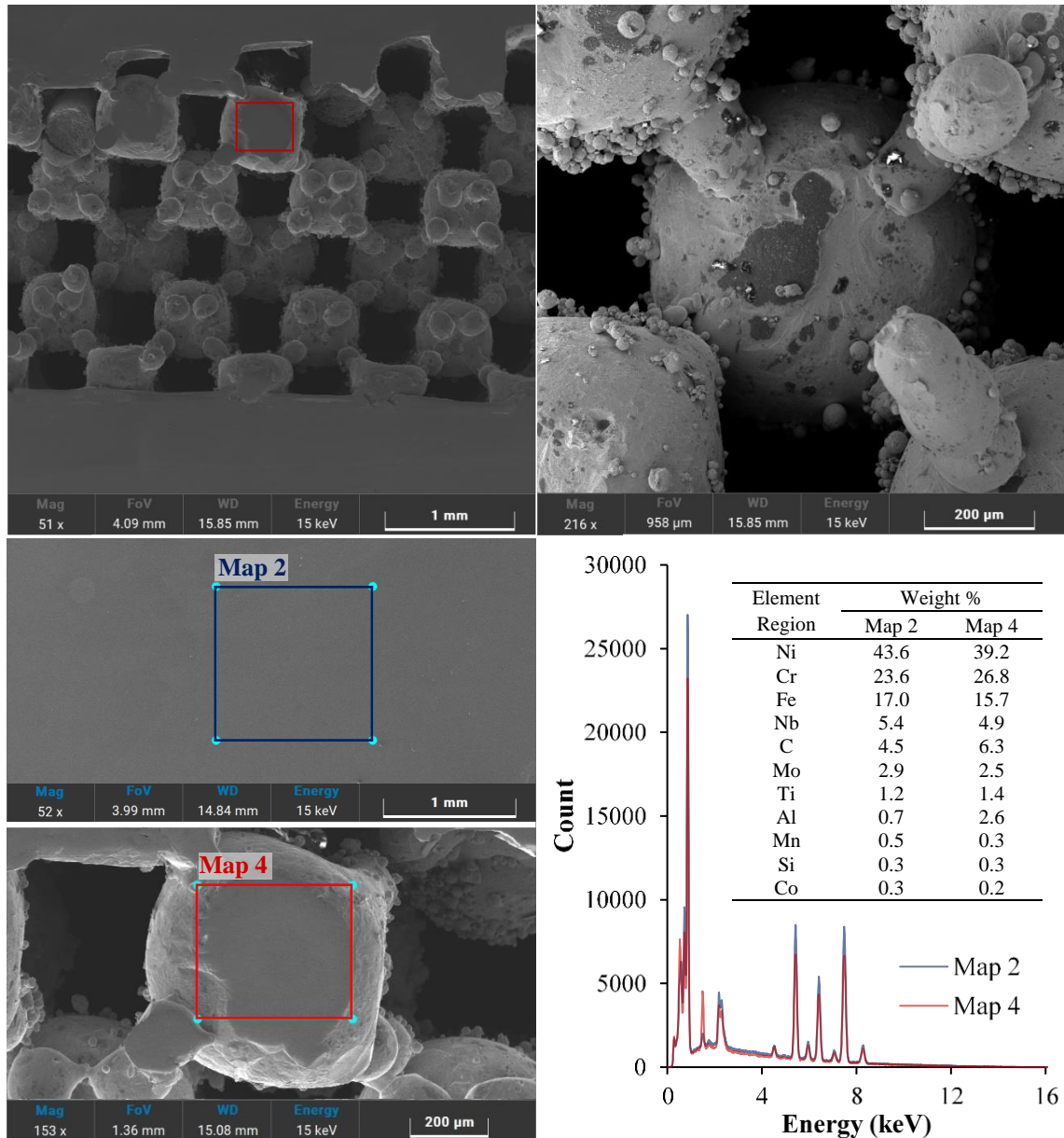


Figure V-24. Blade with internal microstructure SEM analysis and energy spectrum in relation to the alloy composition.

Regarding tomography, the analysis was used to evaluate the internal structure after the milling process. The equipment used was an X-Ray on a GE SEIFERT X-CUBE compact 195 KV tomography with a minimum voxel size of 90 μm.



Analysing the most critical cross-section (Figure V-25c), located at the extreme of the cantilever position and on the other side used for referencing the blade machining, the average distance from the machined face to the internal wall was  $2.244 \pm 0.325$  mm, a nominal error of about 12%. The same analysis showed a deviation of 1.8% on the convex face against 26% on the concave face. This deviation is a sum of the PBF-LB manufacturing uncertainties, tomography measurement and machining positioning (referencing, presenting and deflections).

About the PBF-LB manufacturing: Internal stresses, the blade's geometry also favours the bending to the concave part; thus, the deviation on this region was significantly higher.

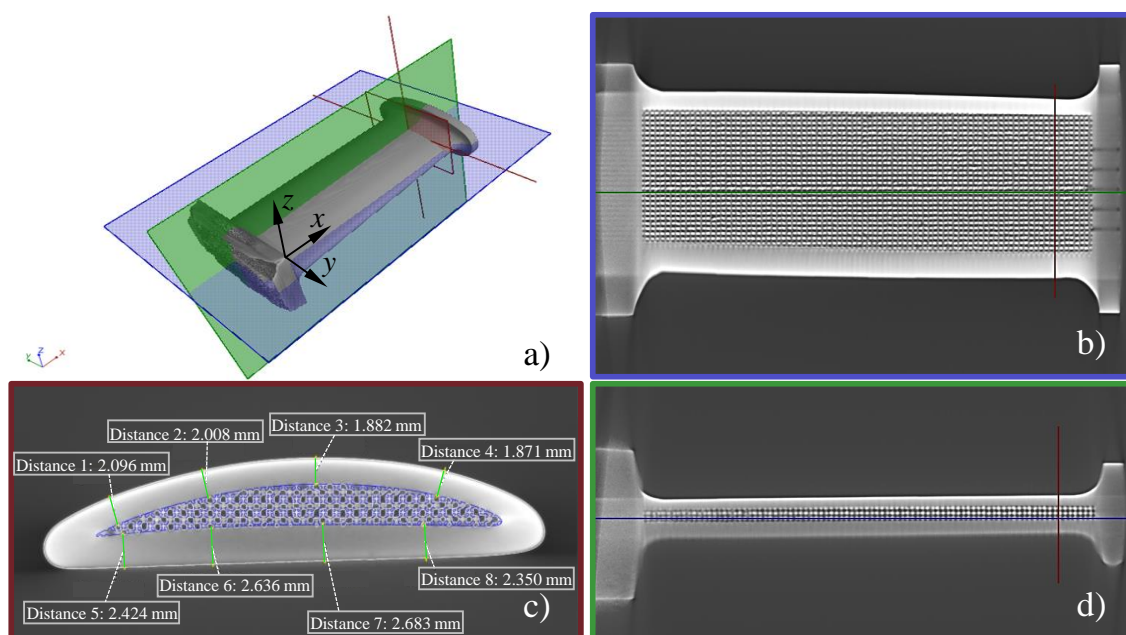


Figure V-25. Blade with internal microstructure tomography analysis: a) Analysed sections; b) Top section; c) Measured distances; d) Lateral section.

### V. 3. 3. Conclusions

The study case presented a comparison of the manufacture of blades by PBF-LB, proposing an optimal design using lattice structures. These designs are challenging from the conception, design, and manufacturing stages. For this purpose, the tomography, machining behaviour, surface quality, and PBF-LB formed integrity were analysed. The presented study case reaches to the following conclusions:

- In internal structured blades, the mass of the blade was reduced by 11.2% due to the design optimisation using cubic cells on the side as internal meshing. This reduction has an influence on the natural frequency of the final component. Moreover, it was observed that the stiffness is similar for both cases. So, the

proposed optimisation implies less cost of material and, in the case of the aeronautical sector, also an increase in efficiency in the buy-to-fly ratio.

- Lattice structures can be used to absorb mechanical vibrations. For the evaluated geometries, it was possible to improve the roughness by approximately 40% by including lattice structures. Additionally, the latticed blades presented superior static stiffness and damping properties. This effect translates into a more rigid lattice blade, confirming the results for power consumption. The lattice blade absorbs and distributes the cutting force, being more rigid, damping and vibrating less.
- From the surface integrity point of view, it is worth mentioning that the modification of the core of the piece does not affect the roughness obtained, achieving similar results both in solid blades and in lattice blades. Furthermore, the dimensional deviation presented in the proposed blade with lattice structures is lower.
- From the point of view of machining strategies, it was observed that the barrel milling cutter significantly improved the final roughness under the same cutting parameters, so it can also be used to improve the productivity of the process.

Several research endeavours are focused on analysing the lattice structure's behaviour from a mechanical point of view. However, these structures imply several challenges from the manufacturing point of view. In this line, this work shows the mechanical analysis of AM lattice structured blade compared to solid AM blade. However, further investigations are required to deeply comprehend these behaviours and explore the possibility of using different structural designs suitable for other applications.

---

## **Chapter VI. Contributions and future works**

---



## Chapter VI. Contributions and future works

*This last chapter summarises the main results obtained during the Ph.D. thesis investigation. Also, future lines and ideas for future works in the field of manufacturing complex parts, surface finishing with ball-end tools, and the development of smart CAM software are presented.*

### VI. 1. Contributions

This Ph.D. thesis investigated the manufacturing process of complex parts, focusing on the finishing process of free-form surfaces. During the development of the research work, an extensive literature review was conducted supporting the investigation of several aspects of the field, from machine responses, workpiece materials, manufacturing process, and geometrical modelling of the finishing process with ball-ended tooltips with up to double radii, more specifically conventional ball-end tooltip, oval barrel, and lens shape barrel tools. Besides, it extrapolates by investigating the manufacture of complex parts with internal microstructures, which are only possible by additive manufacturing, that modify the component design and mechanical properties and affect the finishing process.

In this line, the main contributions of the present Ph.D. thesis as a response to the specific objectives presented in 0 are summarized hereafter:

1. The state-of-the-art review aiming at the manufacture of complex parts with free-form surfaces was accomplished, identifying challenges and the main opportunities. It was identified that the aeronautical market requires several parts, most of them in hard-to-cut materials manufactured from bulk materials with a high buy-to-fly ratio due to safety means, being research of interest in both academic and industrial fields. Still, new additive manufacturing processes, which allow much more freedom in design, can not achieve the expected quality required in mechanical properties and surface finishing, requiring a conventional manufacturing process by removing material for finishing critical structural components and parts of the turbofan engine. Besides the challenges related to materials and tight tolerances, geometrical aspects of the components related to the big size, low thickness, and surface curvatures of the components increase manufacturing difficulties. Tools with a single contact are required to machine the free-form surfaces, leading to more complex problems related to surface roughness and deviations that come with the toolpath selection. It is affected by the machine control loop and the variation in the components of the cutting force that injures milled surfaces. Several advances have been made over the years with the development of tools,

software, and NC machines capable of performing the finishing of several shapes, but still, several advances and software implementation are possible. Furthermore, the use of new types of tools, like the arc-segment end mill, cares for development, being necessary research related to tool contact, toolpath optimization, and surface signature to widen its application in high-performance components.

2. The NC machining response in multiaxis milling was investigated through the machine response. Simple experiments were conducted to saturate the machine control loop and obtain its characteristics to obtain the machine response. It was executed in linear and angular motions, characterizing the machine response time (MRT) of the linear and angular axes, and it was observed that it did not always follow a linear pattern. The developed methodology and knowledge generated allowed the identification of critical regions in manufacturing a complex thin-walled part with concave and convex sides, highlighting that for this type of geometry, the machine's kinematic characteristics should be taken into account. It also assists the CAM user by giving an idea of the kinematics response of the CNC centre, and recommending specific tool orientations that do not generate surface damage or parts out of tolerances by the feed-rate oscillation.

3. The cutting workpiece engagement of ball-end tooltips was evaluated, and a programming routine was developed correlating the cutting location, cutting contact, and respective vectors of the tool and the surface with CAD/CAM software implementation. Predicting the cutting process is not trivial when it comes to free-form surfaces. Discretizing the complex surface in well-known segments can be a key solution to improve modelling and understanding of the milling process. A routine was developed on a high-end CAD/CAM software with an open interface, Siemens® NX, to obtain solutions for surface finishing with ball-end tooltips. The developed programming routine allowed for obtaining surface data and the tool orientation directly from the CAD/CAM software, usually protected by the core of the software. First, only 3-axis milling with a ball-end tool was considered, easing parameters for process analysis, like effective radius and cutting speeds. After that, the development of an API was expanded to 5-axis milling, considering the use of different shapes of tooltips, facilitating information on the NC file output for modelling of the process, taking into account the model present in this Ph.D. thesis and future developments, besides allowing rapid modifications on the tool positions and orientation.

4. To predict the free-form milled surfaces with ball-end tooltips, a geometrical model was developed together with the programming routine. The model of the process allows for identifying the instantaneous engagement of the tool with the surface and predicting the ideal surface, giving insights into the toolpath selection and avoiding trial-and-error

programming. First, the coordinate system was selected at the end of the tooltip to modelling the ball-end tools. Then, the infinitesimal elements that compose the tool dome were calculated and parametrized in the function of the tool height. To model the cutting edge, a constant helix angle was considered, with mathematical representation also in relation to the tool's height. This procedure made modelling different tooltips and cutting edges easy, facilitating future developments. With the geometrical model linked with the developed routine, with the surface and tool orientation data directly on the CAD/CAM software, the modelling of the process was conducted. The tools that were modelled were specifically ball-end tooltips with up to two cutting radii, as lens shape and oval barrel tooltips. The first output was the ideal surface texture that was modelled considering the instantaneous positions and the tool dome. Then, the trochoidal movement of the instantaneous cutting edge element of the tooltip was considered, including the helix angle and the tool run-out, obtaining the position of the cutting edge throughout the milling process and improving analysis. The integration of the refined programming routine with the geometric modelling has facilitated the analysis and comprehension of process phenomena, encompassing effective radius and cutting speeds. Moreover, it enables modelling any free-form surface patterns that lead to alterations in crisp highs and roughness patterns but still cares about development and processing optimizations for a commercial purpose. These insights can significantly impact the workpiece's final quality, supporting the manufacture of components with improved surface and performance.

5. The influence of the ball-end tooltip centre and workpiece material on the milling process was investigated. One of the factors contributing to the high complexity of the milling process for free-form surfaces is the vast possible combinations of geometric interactions and materials. Consequently, simplifying studies to comprehend more intricate cases has been employed for several decades and still cares for development. The cutting parameters can be easily adapted to the material according to the toolmaker's recommendation, but the tool tilting effects are unknown, which can make the cutting parameters selection not optimal or even wrong. Conversely, it is well known that the tooltip centre damaged the final surface due to its null cutting speed. In this particular case, the ploughing-shear pair significantly influences mechanical, dimensional, and surface aspects, and understanding the effect of the nearby regions on the cutting phenomena remains to resort to material-related aspects. This Ph.D. thesis investigated several kinds of materials, being milled copper, aluminium alloy, and steel alloys to Ni-Cr alloys with ball-end tooltips under different engagements. It was observed that even removing the centre of the tooltip, the nearby regions or even the centre can pass fractioning with the final surface, damaging it. Another important fact to highlight is

that sometimes, due to tool run-out, the final surface is generated by only some of the tool edges, increasing roughness. Another contribution of the Ph.D. thesis addresses surface formation and process classification. The geometrical modelling, effective cutting radius, cutting speed, force measurements, and accumulated energy gave insights into the chip and the surface formation. The process study led to the recommendation of a new classification of the free-form milling process with a ball-end tooltip, not in terms of the chip thickness variation, but according to the generation of the surface: up-milling when the machined surface is generated at the beginning of the cutting action and down-milling when it is produced at the end.

6. The tool rigidity and surface deflection according to tool tilting were investigated using a non-conventional ball-end tooltip with double radii, also classified as a circle-segment end mill with application on the manufacture of blades and BLISKs. A bulk material of forged Inconel® 718 (50 HRC) was milled under peripheral milling conditions to address the effect of the tool rigidity. This tool has a higher cutting radius; however, it presents a lower rigidity than a conventional ball-end mill due to higher section variation, which can damage the milled surface and compromise the performance of the manufactured component. That way, the cutting force, the surface deviation, and the topography were addressed together with the CAE simulation, considering the real geometry of the tooltip. The simulation results depicted that not considering the real geometry of the tooltip or using a linear stiffness for the component, as used in conventional end mills, results in significant errors, especially under higher tilt angles. In general, the oval barrel tool presents very good surface finishing, even varying the cutting speed and feed per tooth. The results show that for oval barrel tools machining under recommended conditions (with dominance of the major radius), the main force component is normal to the part, followed by the force component on the feed direction and with a minor influence of forces on the tool axis. Furthermore, the milling process results with this tool depicted a strong significance of the tool tilting on the cutting force, surface deviation, and surface roughness, being recommended its reduction to minimize deviations and extend the tool's life.

7. To investigate the manufacture of complex thin-walled parts and the effects of the part rigidity and clamping system on the form error, a big-sized part was designed and manufactured in AISI XM-12 stainless steel. The machined part is a mid-size aeronautical casing with 8 mm to 13 mm wall thickness in a part with 900 mm in diameter and 400 mm in height. The first remark regards the manufacturing time of this kind of component, which could exceed about 43% in relation to the planned by the CAM software. Besides, in this kind of component, a bulk of raw material is required, leading



to a high amount of material removed and a high buy-to-fly ratio with incremental changes in the part stiffness over the manufacturing process, resulting in several hours of machining. In this direction, a second contribution highlights the effect of some geometrical features of the part, flanges, and honeycomb iso grid lightning features shown to modify the part stiffness locally, contributing to roundness deviations, which could have a higher contribution and depth of actuation (over than 150 mm after the flange milled) than the clamp system. In the same direction, the honeycomb design showed a low influence on the form deviation and can be used successfully to reduce part weight; however, its manufacture is difficult due to regions with higher tool engagement, which requires manufacturing with a non-conventional manufacturing strategy that can mark the component and increase milling time. Still, the measuring results showed that it is possible to produce one big-size component with a conventional clamping system under a roundness error inferior to 0.02%, an amount under the specifications of aeronautical components.

8. To design and manufacture a part containing free-form surfaces with internal microstructures by PBF-LB and compare performance on the posterior finishing process by milling against a solid one. First, the PBF-LB process was studied with a focus on the mechanical properties obtained, taking into account the porosity intrinsic to the parts manufactured by this process. Then, the mechanical properties and fracture by crack propagation were analysed using the porosity data, which can be statistically obtained by destructive metallographic assays or computer tomography images, limited to small samples. It was possible to infer that the additive manufacturing process by PBF-LB can be used to manufacture parts where high performance is required, making it possible to obtain mechanical properties close to those obtained by conventional processes with raw materials, about 95%. At the same time, the hybrid manufacture of components was investigated using the PBF-LB process over a machined base with dissimilar material composition. The mechanical results showed that hybrid manufacturing is promising and capable of reducing manufacturing time and costs, with the melted region not the weakest zone, even when low energy densities are applied. However, the surface aspect of parts produced by PBF-LB is poor, requiring post-processing to accomplish dimensional tolerances and surface finishing. In this direction, the finishing process of components manufactured by PBF-LB containing free-form surfaces was investigated by ball-end milling. Two blade workpieces were designed and printed, one solid and another with internal microstructures, modifying its rigidity. The use of internal latticed structures resulted in a direct reduction of 11.2% of the blade mass, which is important for some sectors such as aeronautical. Also, the lattice structures gave the part a higher specific stiffness at the same time that propitiates a reduction of about 40% in the milling

energy consumed, lowering dimensional deviation and maintaining the same roughness quality. Thereby, contributing to the field with novel approaches towards the design and manufacturing of parts with improved surface finishing and tolerances.

Overall, this research Ph.D. thesis aimed to address the manufacture of complex parts by shape, material, size, or rigidity. Despite the research being conducted in an aeronautical background, the findings offered valuable contributions to both the academic and industrial fields of manufacturing, more specifically on the finishing milling employing ball-end tooltips.

## **VI. 2. Future works**

During the development of the Ph.D thesis, solid knowledge was developed and acquired, contributing to the understanding of the research field. Additionally, various challenges and limitations were encountered. Hereafter, detailed thoughts for future research on this line are provided:

1. The study of machine response time, as presented in section III. 2. 1, found a non-linear behaviour for the angular axis in 4-axis milling. For future developments, it is recommended to expand this knowledge to 5-axis milling, taking into account the dynamics of both rotary axes. However, it is necessary to handle the challenges related to multiple tool positioning and spatial movements with one degree of freedom. Understanding the inverse kinematics of the CNC machine when programming with Tool Centre Point Control (TCP) is a barrier to overcome.
2. The investigation in the Ph.D. thesis demonstrated that the finishing process of a free-form surface by milling is complex and influenced by several parameters. The results of the modelling of the tool-surface contact, forces, and cutting energy with conventional ball-end milling provided valuable insights into understanding the milling process on three materials with completely different characteristics. However, since the modelling is specific to the geometries involved, it is necessary to develop models for new types of tools, such as circle segment end mills. Furthermore, there is a need to enhance the complexity of the milling models to address more complex cases, improving solutions for parts with low rigidity and free-form surfaces, thereby improving the milling process of aeronautical components.
3. The Ph.D thesis findings also revealed that the manufacturing process of complex parts is complex, and the current CAM software are not capable of helping the user in several tasks, requiring external programming. The development of SMART CAM software is a tendency with external developments to ease the CAM user in programming the

manufacturing process, improving productivity, and avoiding losses related to non-quality parts. Besides, the context of Industry 4.0 has been showing an incredible potential for improvement through API. Some developed API helps the used on the tool selection, optimize strategies, predict tool wear, compute deflections, and compensate deviations. But still, besides taking into account databases containing the history of the process, it is necessary to develop solid mathematical models for obtaining high-quality parts. Thus, continuing to the modelling of 5-axis milling using ball-end tooltips and circle segment end mills is required for future implementations in CAD/CAM software with an open interface. The real signature left by the milling process on an API is still for do, being necessary to continue the modelling of the ICE element movement for surface prediction considering dynamical issues, real geometries, tool wear, and deflections.

4. Another branch investigated in the Ph.D thesis addresses the manufacture of mechanical parts by additive manufacturing, more specifically PBF-LB. Two new research lines are suggested. The first is the manufacture of hybrid parts or the use of this process for part repair, mainly because the mechanical properties obtained by PBF-LB are superior to other AM processes. Hybrid manufacturing with PBF-LB has the potential to improve costs, properties, and lead times, and it can be applied to critical aeronautical components. The second research line concerns the manufacture of mechanical parts with internal microstructures. The initial investigation using lattice structures shows promising potential to improve the finishing process and provide internal functional features for the PBF-LB parts, such as channels for fluids or weight reduction. It was clear that this process can modify the macro properties of the parts. Thus, new investigations into the morphological optimisation of lattice structure design and selection are suggested as a new research line. Additionally, performing mechanical assays on the parts containing internal microstructures is still necessary for ensuring the long-term usability of such parts in critical engineering applications, such as the aeronautic sector.

5. Finally, it was identified that the manufacture of big-sized thin-walled parts is influenced by the design of their features and clamping system. The lack of information on its application for the design of the part, devices, and clamping systems configuration on real-scale parts could be a research line of interest for academics such as industrial applications. Additionally, several of the big-sized aeronautical components are manufactured from hard-to-cut materials, such as Ti and NiCr alloys, which are critical in terms of manufacturing costs due to the consumption of various resources such as raw materials, time, cutting tools, and high-cost machines. The use of these materials increases the cutting loads and can amplify form errors due to the clamping system and its geometrical features, deserving attention.



---

## References

- Abrantes, I., Ferreira, A. F., Silva, A., and Costa, M. (2021). Sustainable aviation fuels and imminent technologies - CO<sub>2</sub> emissions evolution towards 2050. *Journal of Cleaner Production*, 313, 1–14.
- Abrari, F., and Elbestawi, M. A. (1997). Closed form formulation of cutting forces for ball and flat end mills. *International Journal of Machine Tools and Manufacture*, 37, 17–27.
- Abrari, F., Elbestawi, M. A., and Spence, A. D. (1998). On the dynamics of ball end milling: Modeling of cutting forces and stability analysis. *International Journal of Machine Tools and Manufacture*, 38, 215–237.
- Aguiar, M. M., Diniz, A. E., and Pederiva, R. (2013). Correlating surface roughness, tool wear and tool vibration in the milling process of hardened steel using long slender tools. *International Journal of Machine Tools and Manufacture*, 68, 1–10.
- Ahn, D.-G. G. (2011). Applications of laser assisted metal rapid tooling process to manufacture of molding & forming tools - state of the art. *International Journal of Precision Engineering and Manufacturing*, 12, 925–938.
- Albrecht, P. (1960). New developments in the theory of the metal-cutting process: Part I. the ploughing process in metal cutting. *Journal of Manufacturing Science and Engineering, Transactions of the ASME*, 82, 348–356.
- Almond, E. A. (1981). Towards improved tests based on fundamental properties. *Proceedings of the International Conference on Improved Performance of Tool Materials, The National Laboratory and the Metals Society, Teddington, Middlesex*, 161–169.
- Altintas, Y., and Lee, P. (1998). Mechanics and dynamics of ball end milling. *Journal of Manufacturing Science and Engineering, Transactions of the ASME*, 120, 684–692.
- Amigo, F. J., Urbikain, G., López de Lacalle, L. N., Pereira, O., Fernández-Lucio, P., and Fernández-Valdivielso, A. (2023). Prediction of cutting forces including tool wear in high-feed turning of Nimonic® C-263 superalloy: A geometric distortion-based model. *Measurement: Journal of the International Measurement Confederation*, 211, 1–21.
- Anderson, T. L. (2017). *Fracture mechanics: fundamentals and applications*. CRC press.
- Arizmendi, M., Fernández, J., Lacalle, L. N. L. de, Lamikiz, A., Gil, A., Sánchez, J. A., Campa, F. J., and Veiga, F. (2008). Model development for the prediction of surface topography generated by ball-end mills taking into account the tool parallel axis offset. Experimental validation. *CIRP Annals - Manufacturing Technology*, 57, 101–104.
- Arnaiz-González, Á., Fernández-Valdivielso, A., Bustillo, A., and López de Lacalle, L. N. (2016). Using artificial neural networks for the prediction of dimensional error on inclined surfaces manufactured by ball-end milling. *International Journal of Advanced Manufacturing Technology*, 83, 847–859.
- Arrazola, P. J., Özel, T., Umbrello, D., Davies, M., and Jawahir, I. S. (2013). Recent advances in

## References

---

- modelling of metal machining processes. *CIRP Annals - Manufacturing Technology*, 62, 695–718.
- Arunachalam, R. M., Mannan, M. A., and Spowage, A. C. (2004). Surface integrity when machining age hardened Inconel 718 with coated carbide cutting tools. *International Journal of Machine Tools and Manufacture*, 44, 1481–1491.
- Asgari, H., and Mohammadi, M. (2018). Microstructure and mechanical properties of stainless steel CX manufactured by Direct Metal Laser Sintering. *Materials Science and Engineering A*, 709, 82–89.
- Aspinwall, D. K., Dewes, R. C., Ng, E. G., Sage, C., and Soo, S. L. (2007). The influence of cutter orientation and workpiece angle on machinability when high-speed milling Inconel 718 under finishing conditions. *International Journal of Machine Tools and Manufacture*, 47, 1839–1846.
- Axinte, D. A., and Dewes, R. C. (2002). Surface integrity of hot work tool steel after high speed milling-experimental data and empirical models. *Journal of Materials Processing Technology*, 127, 325–335.
- Bai, T., Liu, J., Zhang, W., and Zou, Z. (2014). Effect of surface roughness on the aerodynamic performance of turbine blade cascade. *Propulsion and Power Research*, 3, 82–89.
- Balázs, B. Z., Jacsó, Á., and Takács, M. (2020). Micromachining of hardened hot-work tool steel: effects of milling strategies. *International Journal of Advanced Manufacturing Technology*.
- Basso, I., Voigt, R., Rodrigues, A. R., Marin, F., de Souza, A. F., and de Lacalle, L. N. L. (2022). Influences of the workpiece material and the tool-surface engagement (TSE) on surface finishing when ball-end milling. *Journal of Manufacturing Processes*, 75, 219–231.
- Batista, M. F., Rodrigues, A. R., and Coelho, R. T. (2017). Modelling and characterisation of roughness of moulds produced by high-speed machining with ball-nose end mill. *Proceedings of the Institution of Mechanical Engineers, Part B: Journal of Engineering Manufacture*, 231, 933–944.
- Baumers, M., Beltrametti, L., Gasparre, A., and Hague, R. (2017). Informing additive manufacturing technology adoption: total cost and the impact of capacity utilisation. *International Journal of Production Research*, 55, 6957–6970.
- Benardos, P. G., and Vosniakos, G. C. (2003). Predicting surface roughness in machining: a review. *International Journal of Machine Tools and Manufacture*, 43, 833–844.
- Beňo, J., Maňková, I., Ižol, P., and Vrabel, M. (2016). An approach to the evaluation of multivariate data during ball end milling free-form surface fragments. *Measurement*, 84, 7–20.
- Bi, J., Wu, L., Li, S., Yang, Z., Jia, X., Starostenkov, M. D., and Dong, G. (2023). Beam shaping technology and its application in metal laser additive manufacturing: A review. *Journal of Materials Research and Technology*, 26, 4606–4628.
- Bobzin, K., Wietheger, W., Knoch, M. A., Schacht, A., Reisgen, U., Sharma, R., and Oster, L. (2020). Comparison of Residual Stress Measurements Conducted by X-ray Stress Analysis and Incremental Hole Drilling Method. *Journal of Thermal Spray Technology*, 29, 1218–1228.

- Boivie, K., Karlsen, R., and Ystgaard, P. (2012). The concept of hybrid manufacturing for high performance parts . *South African Journal of Industrial Engineering* , 23, 106–115.
- Boschetto, A., Bottini, L., and Veniali, F. (2018). Surface roughness and radiusing of Ti6Al4V selective laser melting-manufactured parts conditioned by barrel finishing. *International Journal of Advanced Manufacturing Technology*, 94, 2773–2790.
- Brooks, Z., Nath, C., and Kurfess, T. R. (2016). Investigating surface metrology of curved wall surface during milling of SS304 with different tool path strategies. *The International Journal of Advanced Manufacturing Technology* 2016 86:5, 86, 1963–1972.
- Brown, C. E. (1998). Coefficient of Variation. *Applied Multivariate Statistics in Geohydrology and Related Sciences*, 155–157.
- Budak, E., and Altintas, Y. (1995). Modeling and avoidance of static form errors in peripheral milling of plates. *International Journal of Machine Tools and Manufacture*, 35, 459–476.
- Budak, E., Altintaş, Y., and Armarego, E. J. A. (1996). Prediction of milling force coefficients from orthogonal cutting data. *Journal of Manufacturing Science and Engineering, Transactions of the ASME*, 118, 216–224.
- Budak, E., Ozlu, E., Bakioglu, H., and Barzegar, Z. (2016). Thermo-mechanical modeling of the third deformation zone in machining for prediction of cutting forces. *CIRP Annals - Manufacturing Technology*, 65, 121–124.
- Bushlya, V., Gutnichenko, O., Zhou, J., Avdovic, P., and Ståhl, J. E. (2013). Effects of cutting speed when turning age hardened inconel 718 with PCBN tools of binderless and low-CBN grades. *Machining Science and Technology*, 17, 497–523.
- Cao, Q., Zhao, J., Li, Y., and Chen, X. (2012). Tool deflection modeling in ball-end milling of sculptured surface. *Key Engineering Materials*, 516, 7–12.
- Cao, Y., Bai, Y., Tian, J., Fan, Q., and Wang, Z. (2015). Multi-axis NC spiral milling of thin-walled aluminium 7075/T651 blade with spiral tool path generation algorithm. *Materials Research Innovations*, 19, 445–447.
- Carter, D. (2013). Confocal microscopy. *Current Protocols in Essential Laboratory Techniques*, 1, 1–10.
- Caruso, S., Outeiro, J. C., Umbrello, D., and M'Saoubi, R. (2010). Modeling and experimental validation of the surface residual stresses induced by hard machining of AISI H13 tool steel. *International Journal of Material Forming*, 3, 515–518.
- Cauí, Y., Xi, G., and Wang, S. (2003). Efficient tool path planning for five-axis surface machining with a drum-taper cutter. *International Journal of Production Research*, 41, 3631–3644.
- Chen, W. Y., Zhang, X., Li, M., Xu, R., Zhao, C., and Sun, T. (2020). Laser powder bed fusion of Inconel 718 on 316 stainless steel. *Additive Manufacturing*, 36, 1–9.
- Chiang, S. T., Tsai, C. M., and Lee, A. C. (1995). Analysis of cutting forces in ball-end milling. *Journal of Materials Processing Tech.*, 47, 231–249.
- Choi, J. P., Shin, G. H., Yang, S., Yang, D. Y., Lee, J. S., Brochu, M., and Yu, J. H. (2017).

## References

---

- Densification and microstructural investigation of Inconel 718 parts fabricated by selective laser melting. *Powder Technology*, 310, 60–66.
- Chouhan, A., Aggarwal, A., and Kumar, A. (2021). Role of melt flow dynamics on track surface morphology in the L-PBF additive manufacturing process. *International Journal of Heat and Mass Transfer*, 178, 1–17.
- Chuan, S. P., Ghani, J. A., Tomadi, S. H., and Hassan, C. H. C. (2012). Analysis of Ti-base hard coating performance in machining process: a review. *Journal of Applied Sciences*, 12, 1882–1890.
- Chung, C., and Ma, T. C. (2018). Implementation of CAM programming with machinability database. *SII 2017 - 2017 IEEE/SICE International Symposium on System Integration, 2018-Janua*, 236–240. Institute of Electrical and Electronics Engineers Inc.
- Coelho, R. T., de Souza, A. F., Roger, A. R., Rigatti, A. M. Y., and Ribeiro, A. A. de L. (2010). Mechanistic approach to predict real machining time for milling free-form geometries applying high feed rate. *International Journal of Advanced Manufacturing Technology*, 46, 1103–1111.
- Coelho, Silva, L. R., Braghini, A., and Bezerra, A. A. (2004). Some effects of cutting edge preparation and geometric modifications when turning INCONEL 718™ at high cutting speeds. *Journal of Materials Processing Technology*, 148, 147–153.
- Dávila, J. L., Neto, P. I., Noritomi, P. Y., Coelho, R. T., and da Silva, J. V. L. (2020). Hybrid manufacturing: a review of the synergy between directed energy deposition and subtractive processes. *The International Journal of Advanced Manufacturing Technology 2020 110:11*, 110, 3377–3390.
- de Lacalle, L. N. L., Lamikiz, A., Sánchez, J. A., and Salgado, M. A. (2004). Effects of tool deflection in the high-speed milling of inclined surfaces. *International Journal of Advanced Manufacturing Technology*, 24, 621–631.
- de Lacalle, L. N., Lamikiz, A., Sánchez, J. A., and Salgado, M. A. (2007). Toolpath selection based on the minimum deflection cutting forces in the programming of complex surfaces milling. *International Journal of Machine Tools and Manufacture*, 47, 388–400.
- de Oliveira, E. L., de Souza, A. F., and Diniz, A. E. (2018). Evaluating the influences of the cutting parameters on the surface roughness and form errors in 4-axis milling of thin-walled free-form parts of AISI H13 steel. *Journal of the Brazilian Society of Mechanical Sciences and Engineering*, 40, 1–10.
- de Souza, A. F., Al-Rubaie, K. S., Marques, S., Zluhan, B., and Santos, E. C. (2019a). Effect of laser speed, layer thickness, and part position on the mechanical properties of maraging 300 parts manufactured by selective laser melting. *Materials Science and Engineering: A*, 767, 1–13.
- de Souza, A. F., Berkenbrock, E., Diniz, A. E., and Rodrigues, A. R. (2015). Influences of the tool path strategy on the machining force when milling free form geometries with a ball-end cutting tool. *Journal of the Brazilian Society of Mechanical Sciences and Engineering*, 37, 675–687.
- de Souza, A. F., Camargo, L. G., Gaspar, H. da S., Marin, F., Ochoa, A. C., and de Lacalle, L. N.



- 
- L. (2021). New mechanistic model to predict machining time for milling free form geometries using 4-axis milling. *Procedia CIRP*, 101, 34–37. Elsevier.
- de Souza, A. F., and Coelho, R. T. (2007). Experimental investigation of feed rate limitations on high speed milling aimed at industrial applications. *International Journal of Advanced Manufacturing Technology*, 32, 1104–1114.
- de Souza, A. F., Diniz, A. E., Rodrigues, A. R., and Coelho, R. T. (2014a). Investigating the cutting phenomena in free-form milling using a ball-end cutting tool for die and mold manufacturing. *International Journal of Advanced Manufacturing Technology*, 71, 1565–1577.
- de Souza, A. F., Käsemödel, R. B., Arias, M., Marin, F., and Rodrigues, A. R. (2019b). Study of tool paths calculated by different commercial CAM systems and influences on the real machining time and surface roughness for milling free-form geometries. *Journal of the Brazilian Society of Mechanical Sciences and Engineering*, 41, 363.
- de Souza, A. F., Machado, A., Beckert, S. F., and Diniz, A. E. (2014b). Evaluating the roughness according to the tool path strategy when milling free form surfaces for mold application. *Procedia CIRP*, 14, 188–193.
- Del Sol, I., Rivero, A., de Lacalle, L. N., and Gamez, A. J. (2019). Thin-Wall Machining of Light Alloys: A Review of Models and Industrial Approaches. *Materials*, 12, 2012.
- Denkena, B., Böß, V., Nesper, D., Gilge, P., Hohenstein, S., and Seume, J. (2015). Prediction of the 3D surface topography after ball end milling and its influence on aerodynamics. *Procedia CIRP*, 31, 221–227. Elsevier.
- Denkena, B., Böß, V., Nesper, D., and Samp, A. (2011). Kinematic and Stochastic Surface Topography of Machined TiAl6V4-Parts by means of Ball Nose End Milling. *Procedia Engineering*, 19, 81–87.
- Desai, K. A., and Rao, P. V. M. (2012). On cutter deflection surface errors in peripheral milling. *Journal of Materials Processing Technology*, 212, 2443–2454.
- Devaux, A., Nazé, L., Molins, R., Pineau, A., Organista, A., Guédou, J. Y., Uginet, J. F., and Héritier, P. (2008). Gamma double prime precipitation kinetic in Alloy 718. *Materials Science and Engineering: A*, 486, 117–122.
- Dieter, G. E. (1988). *Mechanical metallurgy* (4th ed.). London: McGraw-Hill.
- Diez, E., Perez, H., Marquez, J., and Vizan, A. (2015). Feasibility study of in-process compensation of deformations in flexible milling. *International Journal of Machine Tools and Manufacture*, 94, 1–14.
- Dikshit, M. K., Puri, A. B., and Maity, A. (2017). Analysis of cutting force coefficients in high-speed ball end milling at varying rotational speeds. *Machining Science and Technology*, 21, 416–435.
- Dilberoglu, U. M., Gharehpapagh, B., Yaman, U., and Dolen, M. (2017). The Role of Additive Manufacturing in the Era of Industry 4.0. *Procedia Manufacturing*, 11, 545–554.
- Dittrich, M. A., and Uhlich, F. (2020). Self-optimizing compensation of surface deviations in 5-axis ball-end milling based on an enhanced description of cutting conditions. *CIRP Journal of*
-

## References

---

*Manufacturing Science and Technology*, 31, 224–232.

Dong, J., Wang, T., Li, B., and Ding, Y. (2014). Smooth feedrate planning for continuous short line tool path with contour error constraint. *International Journal of Machine Tools and Manufacture*, 76, 1–12.

Duan, X., Peng, F. Y., Yan, R., Zhu, Z., and Li, B. (2015). Experimental study of the effect of tool orientation on cutter deflection in five-axis filleted end dry milling of ultrahigh-strength steel. *International Journal of Advanced Manufacturing Technology*, 81, 653–666.

Dugas, A., Lee, J. J., Terrier, M., and Hascoët, J. Y. (2003). Development of a machining simulator considering machine behaviour. *Proceedings of the Institution of Mechanical Engineers, Part B: Journal of Engineering Manufacture*, 217, 1333–1339.

Dwivedi, P., Siddiquee, A. N., and Maheshwari, S. (2021). Issues and Requirements for Aluminum Alloys Used in Aircraft Components: State of the Art. *Russian Journal of Non-Ferrous Metals*, 62, 212–225.

El-Mounayri, H. A., Elbestawi, M. A., Spence, A. D., and Bedif, S. (1997). General geometric modelling approach for machining process simulation. *International Journal of Advanced Manufacturing Technology*, 13, 237–247.

Engin, S., and Altintas, Y. (2001). Mechanics and dynamics of general milling cutters. Part I: Helical end mills. *International Journal of Machine Tools and Manufacture*, 41, 2195–2212.

Ezugwu, E. O. (2005). Key improvements in the machining of difficult-to-cut aerospace superalloys. *International Journal of Machine Tools and Manufacture*, 45, 1353–1367.

Ezugwu, E. O., Bonney, J., and Yamane, Y. (2003). An overview of the machinability of aeroengine alloys. *Journal of Materials Processing Technology*, 134, 233–253.

Ezugwu, E. O., Da Silva, R. B., Bonney, J., and MacHado, Á. R. (2005). Evaluation of the performance of CBN tools when turning Ti–6Al–4V alloy with high pressure coolant supplies. *International Journal of Machine Tools and Manufacture*, 45, 1009–1014.

Ezugwu, E. O., Wang, Z. M., and Okeke, C. I. (1999). Tool life and surface integrity when machining inconel 718 with pvd- and cvd-coated tools. *Tribology Transactions*, 42, 353–360.

Feng, H. Y., and Menq, C. H. (1994a). The prediction of cutting forces in the ball-end milling process—I. Model formulation and model building procedure. *International Journal of Machine Tools and Manufacture*, 34, 697–710.

Feng, H. Y., and Menq, C. H. (1994b). The prediction of cutting forces in the ball-end milling process—II. Cut geometry analysis and model verification. *International Journal of Machine Tools and Manufacture*, 34, 711–719.

Fergani, O., Berto, F., Welo, T., and Liang, S. Y. (2017). Analytical modelling of residual stress in additive manufacturing. *Fatigue & Fracture of Engineering Materials & Structures*, 40, 971–978.

Fontaine, M., Devillez, A., Moufki, A., and Dudzinski, D. (2006). Predictive force model for ball-end milling and experimental validation with a wavelike form machining test. *International Journal*

---

of *Machine Tools and Manufacture*, 46, 367–380.

Furumoto, T., Koizumi, A., Alkahari, M. R., Anayama, R., Hosokawa, A., Tanaka, R., and Ueda, T. (2015). Permeability and strength of a porous metal structure fabricated by additive manufacturing. *Journal of Materials Processing Technology*, 219, 10–16.

Gangireddy, S., Komarasamy, M., Faierson, E. J., and Mishra, R. S. (2019). High strain rate mechanical behavior of Ti-6Al-4V octet lattice structures additively manufactured by selective laser melting (SLM). *Materials Science and Engineering: A*, 745, 231–239.

Geddes, B., Leon, H., and Huang, X. (2010). *Superalloys: alloying and performance*. Asm International.

Ghorbani, M., and Movahhedy, M. R. (2019a). An analytical model for cutter-workpiece engagement calculation in ball-end finish milling of doubly curved surfaces. *International Journal of Advanced Manufacturing Technology*, 102, 1635–1657.

Ghorbani, M., and Movahhedy, M. R. (2019b). Extraction of surface curvatures from tool path data and prediction of cutting forces in the finish milling of sculptured surfaces. *Journal of Manufacturing Processes*, 45, 273–289.

Godec, M., Malej, S., Feizpour, D., Donik, Balažic, M., Klobčar, D., Pambaguian, L., Conradi, M., and Kocijan, A. (2021). Hybrid additive manufacturing of Inconel 718 for future space applications. *Materials Characterization*, 172.

Gok, A., Gologlu, C., and Demirci, H. I. (2013). Cutting parameter and tool path style effects on cutting force and tool deflection in machining of convex and concave inclined surfaces. *International Journal of Advanced Manufacturing Technology*, 69, 1063–1078.

González-Barrio, H., Calleja-Ochoa, A., de Lacalle, L. N., and Lamikiz, A. (2022). Hybrid manufacturing of complex components: Full methodology including laser metal deposition (LMD) module development, cladding geometry estimation and case study validation. *Mechanical Systems and Signal Processing*, 179, 1–14.

Grandguillaume, L., Lavernhe, S., Quinsat, Y., and Tournier, C. (2015). Mold Manufacturing Optimization: A Global Approach of Milling and Polishing Processes. *Procedia CIRP*, 31, 13–18.

Grešová, Z., Ižol, P., Vrabel', M., Kaščák, L., Brindza, J., and Demko, M. (2022). Influence of Ball-End Milling Strategy on the Accuracy and Roughness of Free Form Surfaces. *Applied Sciences*, 12, 1–17.

Grigoriev, S., Vereschaka, A., Uglov, V., Milovich, F., Cherenda, N., Andreev, N., Migranov, M., and Seleznev, A. (2023). Influence of tribological properties of Zr-ZrN-(Zr,Cr,Al)N and Zr-ZrN-(Zr,Mo,Al)N multilayer nanostructured coatings on the cutting properties of coated tools during dry turning of Inconel 718 alloy. *Wear*, 512–513, 1–12.

Guillemot, N., Mawussi, B. K., Lartigue, C., and Billardon, R. (2013). A first approach to characterize the surface integrity generated by ball-end finishing milling. *International Journal of Advanced Manufacturing Technology*, 64, 269–279.

Guimaraes, A. A., and Jonas, J. J. (1981). Recrystallization and aging effects associated with the

## References

---

- high temperature deformation of waspaloy and inconel 718. *Metallurgical Transactions A*, 12, 1655–1666.
- Guo, M., Wei, Z., Wang, M., Li, S., and Liu, S. (2018a). An identification model of cutting force coefficients for five-axis ball-end milling. *International Journal of Advanced Manufacturing Technology*, 99, 937–949.
- Guo, Q., Zhao, B., Jiang, Y., and Zhao, W. (2018b). Cutting force modeling for non-uniform helix tools based on compensated chip thickness in five-axis flank milling process. *Precision Engineering*, 51, 659–681.
- Guo, Y. B., Li, W., and Jawahir, I. S. (2009). Surface integrity characterization and prediction in machining of hardened and difficult-to-machine alloys: A state-of-art research review and analysis. *Machining Science and Technology*, 13, 437–470.
- Gupta, A., Bennett, C. J., and Sun, W. (2022). An experimental investigation on the progressive failure of an additively manufactured Laser Powder Bed Fusion Ti-6Al-4V aero-engine bracket under Low Cycle Fatigue. *Engineering Failure Analysis*, 139, 1–21.
- Habibi, M., Arezoo, B., and Vahebi Nojehdeh, M. (2011). Tool deflection and geometrical error compensation by tool path modification. *International Journal of Machine Tools and Manufacture*, 51, 439–449.
- Habibi, M., Tuysuz, O., and Altintas, Y. (2019). Modification of Tool Orientation and Position to Compensate Tool and Part Deflections in Five-Axis Ball End Milling Operations. *Journal of Manufacturing Science and Engineering, Transactions of the ASME*, 141, 1–9.
- Hague, R., Mansour, S., and Saleh, N. (2004). Material and design considerations for rapid manufacturing. *International Journal of Production Research*, 42, 4691–4708.
- Han, X., and Tang, L. (2015). Precise prediction of forces in milling circular corners. *International Journal of Machine Tools and Manufacture*, 88, 184–193.
- Heo, E. Y., Kim, D. W., Kim, B. H., and Frank Chen, F. (2006). Estimation of NC machining time using NC block distribution for sculptured surface machining. *Robotics and Computer-Integrated Manufacturing*, 22, 437–446.
- Hiller, J., Maisl, M., and Reindl, L. M. (2012). Physical characterization and performance evaluation of an x-ray micro-computed tomography system for dimensional metrology applications. *Measurement Science and Technology*, 23, 18.
- Hosseini, A., and Kishawy, H. A. (2014). *Cutting Tool Materials and Tool Wear*. Springer, Berlin, Heidelberg.
- Hyer, H. C., and Petrie, C. M. (2022). Effect of powder layer thickness on the microstructural development of additively manufactured SS316. *Journal of Manufacturing Processes*, 76, 666–674.
- Ikuu, B. W., Tanaka, H., Obata, F., and Sakamoto, S. (2001). Prediction of cutting forces and machining error in ball end milling of curved surfaces -I theoretical analysis. *Precision Engineering*, 25, 266–273.

- Ikua, B. W., Tanaka, H., Obata, F., Sakamoto, S., Kishi, T., and Ishii, T. (2002). Prediction of cutting forces and machining error in ball end milling of curved surfaces -II experimental verification. *Precision Engineering*, 26, 69–82.
- Imani, B. M., Sadeghi, M. H., and Elbestawi, M. A. (1998). An improved process simulation system for ball-end milling of sculptured surfaces. *International Journal of Machine Tools and Manufacture*, 38, 1089–1107.
- ISO. (1989). ISO 8688-2:1989 Tool life testing in milling - Part 2: End milling. Accessed September 15, 2023, from <https://www.iso.org/standard/16092.html>
- Jafarian, F., Imaz Ciaran, M., Umbrello, D., Arrazola, P. J., Filice, L., and Amirabadi, H. (2014). Finite element simulation of machining Inconel 718 alloy including microstructure changes. *International Journal of Mechanical Sciences*, 88, 110–121.
- Jawahir, Attia, H., Biermann, D., Duflou, J., Klocke, F., Meyer, D., ... Umbrello, D. (2016). Cryogenic manufacturing processes. *CIRP Annals - Manufacturing Technology*, 65, 713–736.
- Ji, Y., Chen, L., and Chen, L. Q. (2018). Understanding Microstructure Evolution During Additive Manufacturing of Metallic Alloys Using Phase-Field Modeling. *Thermo-Mechanical Modeling of Additive Manufacturing*, 93–116.
- Jianxin, D., Lili, L., Jianhua, L., Jinlong, Z., and Xuefeng, Y. (2005). Failure mechanisms of TiB<sub>2</sub> particle and SiC whisker reinforced Al<sub>2</sub>O<sub>3</sub> ceramic cutting tools when machining nickel-based alloys. *International Journal of Machine Tools and Manufacture*, 45, 1393–1401.
- Jiménez, A., Bidare, P., Hassanin, H., Tarlochan, F., Dimov, S., and Essa, K. (2021). Powder-based laser hybrid additive manufacturing of metals: a review. *The International Journal of Advanced Manufacturing Technology*, 114, 63–96.
- Kamath, C., El-Dasher, B., Gallegos, G. F., King, W. E., and Sisto, A. (2014). Density of additively-manufactured, 316L SS parts using laser powder-bed fusion at powers up to 400 W. *International Journal of Advanced Manufacturing Technology*, 74, 65–78.
- Käsemödel, R. B., Souza, A. F., Voigt, R., Basso, I., and Rodrigues, A. R. (2020). CAD/CAM interfaced algorithm reduces cutting force, roughness, and machining time in free-form milling. *International Journal of Advanced Manufacturing Technology*, 107, 1883–1900.
- Kaynak, Y. (2014). Evaluation of machining performance in cryogenic machining of Inconel 718 and comparison with dry and MQL machining. *The International Journal of Advanced Manufacturing Technology* 2014 72:5, 72, 919–933.
- Ketcham, R. A. (2005). Three-dimensional grain fabric measurements using high-resolution X-ray computed tomography. *Journal of Structural Geology*, 27, 1217–1228.
- Khatri, A., and Jahan, M. P. (2018). Investigating tool wear mechanisms in machining of Ti-6Al-4V in flood coolant, dry and MQL conditions. *Procedia Manufacturing*, 26, 434–445. Elsevier.
- Kim, G. M., Cho, P. J., and Chu, C. N. (2000). Prediction of cutting force in ball-end milling of sculptured surface using improved Z-map. *International Journal of Advanced Manufacturing Technology*, 40, 277–291.

## References

---

- Kim, G. M., Kim, B. H., and Chu, C. N. (2003). Estimation of cutter deflection and form error in ball-end milling processes. *International Journal of Machine Tools and Manufacture*, 43, 917–924.
- Kishawy, H. A., and Hosseini, A. (2019). *Machining Difficult-to-Cut Materials: Basic Principles and Challenges* (1st ed.). Springer Cham.
- Klocke, F., Schmitt, R., Zeis, M., Heidemanns, L., Kerkhoff, J., Heinen, D., and Klink, A. (2015). Technological and Economical Assessment of Alternative Process Chains for Blisk Manufacture. *Procedia CIRP*, 35, 67–72. Elsevier.
- Kopac, J. (2009). Achievements of sustainable manufacturing by machining. *Journal of Achievements in Materials and Manufacturing Engineering*, 34, 180–187.
- Kops, L., and Vo, D. T. (1990). Determination of the Equivalent Diameter of an End Mill Based on its Compliance. *CIRP Annals - Manufacturing Technology*, 39, 93–96.
- Kurt, M., and Bagci, E. (2011). Feedrate optimisation/scheduling on sculptured surface machining: a comprehensive review, applications and future directions. *The International Journal of Advanced Manufacturing Technology* 2011 55:9, 55, 1037–1067.
- Lamikiz, A., De Lacalle, L. N. L., Sánchez, J. A., and Salgado, M. A. (2004). Cutting force estimation in sculptured surface milling. *International Journal of Machine Tools and Manufacture*, 44, 1511–1526.
- Lamikiz, A., Lopez De Lacalle, L. N., Sanchez, J. A., and Bravo, U. (2005). Calculation of the specific cutting coefficients and geometrical aspects in sculptured surface machining. *Machining Science and Technology*, 9, 411–436.
- Lasemi, A., Xue, D., and Gu, P. (2010). Recent development in CNC machining of freeform surfaces: A state-of-the-art review. *CAD Computer Aided Design*, 42, 641–654.
- Lavernhe, S., Quinsat, Y., Lartigue, C., and Brown, C. (2014). Realistic simulation of surface defects in five-axis milling using the measured geometry of the tool. *International Journal of Advanced Manufacturing Technology*, 74, 393–401.
- Layegh K, S. E., and Lazoglu, I. (2017). 3D surface topography analysis in 5-axis ball-end milling. *CIRP Annals - Manufacturing Technology*, 66, 133–136.
- Lazoglu, I. (2003). Sculpture surface machining: A generalized model of ball-end milling force system. *International Journal of Machine Tools and Manufacture*, 43, 453–462.
- Lazoglu, I., Boz, Y., and Erdim, H. (2011). Five-axis milling mechanics for complex free form surfaces. *CIRP Annals - Manufacturing Technology*, 60, 117–120.
- Lazoglu, I., and Liang, S. Y. (1997). Analytical modeling of force system in ball-end milling. *Machining Science and Technology*, 1, 219–234.
- Lazoglu, I., and Liang, S. Y. (2000). Modeling of Ball-End Milling Forces With Cutter Axis Inclination. *Journal of Manufacturing Science and Engineering*, 122, 3–11.
- Lee, P., and Altintas, Y. (1996). Prediction of ball-end milling forces from orthogonal cutting data.

- 
- International Journal of Machine Tools and Manufacture*, 36, 1059–1072.
- Lee, W. C., Lee, Y. tzu, and Wei, C. C. (2019). Automatic error compensation for free-form surfaces by using on-machine measurement data. *Applied Sciences*, 9, 1–13.
- Lerch, B. A., Jayaraman, N., and Antolovich, S. D. (1984). A study of fatigue damage mechanisms in Waspaloy from 25 to 800°C. *Materials Science and Engineering*, 66, 151–166.
- Li, B. (2012). A review of tool wear estimation using theoretical analysis and numerical simulation technologies. *International Journal of Refractory Metals and Hard Materials*, 35, 143–151.
- Li, S. J., Zhou, Y. F., Jin, R. C., and Ji, Z. (2001). Dynamic force modelling for a ball-end milling cutter based on the merchant oblique cutting theory. *International Journal of Advanced Manufacturing Technology*, 17, 477–483.
- Li, X., Zhang, J., Akiyama, E., Li, Q., and Wang, Y. (2017). Effect of heat treatment on hydrogen-assisted fracture behavior of PH13-8Mo steel. *Corrosion Science*, 128, 198–212.
- Li, Z., Xu, K., and Tang, K. (2019). A new trochoidal pattern for slotting operation. *International Journal of Advanced Manufacturing Technology*, 102, 1153–1163.
- Liang, X.-G., and Yao, Z.-Q. (2011). An accuracy algorithm for chip thickness modeling in 5-axis ball-end finish milling. *Computer-Aided Design*, 43, 971–978.
- Liang, X., and Liu, Z. (2017). Experimental investigations on effects of tool flank wear on surface integrity during orthogonal dry cutting of Ti-6Al-4V. *The International Journal of Advanced Manufacturing Technology* 2017 93:5, 93, 1617–1626.
- Liao, Y. S., Lin, H. M., and Wang, J. H. (2008). Behaviors of end milling Inconel 718 superalloy by cemented carbide tools. *Journal of Materials Processing Technology*, 201, 460–465.
- Liao, Y. S., and Shiue, R. H. (1996). Carbide tool wear mechanism in turning of Inconel 718 superalloy. *Wear*, 193, 16–24.
- Lin, X., Wu, G., Zhang, Y., Cui, T., Zhang, B., and Sun, P. (2019). The identification of the cutting force coefficients for ball-end finish milling. *International Journal of Advanced Manufacturing Technology*, 102, 4121–4135.
- Linling, L., Liming, S., and Xiaoyu, Z. (2022). Property analysis of periodic lattice structure with considering its size effect. *Advances in Astronautics Science and Technology*, 5, 251–259.
- Liu, F., Lin, X., Huang, C., Song, M., Yang, G., Chen, J., and Huang, W. (2011). The effect of laser scanning path on microstructures and mechanical properties of laser solid formed nickel-base superalloy Inconel 718. *Journal of Alloys and Compounds*, 509, 4505–4509.
- Liu, G., Zou, B., Huang, C., Wang, X., Wang, J., and Liu, Z. (2016). Tool damage and its effect on the machined surface roughness in high-speed face milling the 17-4PH stainless steel. *International Journal of Advanced Manufacturing Technology*, 83, 257–264.
- Liu, X.-W., Cheng, K., Longstaff, A. P., Widiyanto, M. H., and Ford, D. (2005). Improved dynamic cutting force model in ball-end milling. Part I: theoretical modelling and experimental calibration. *The International Journal of Advanced Manufacturing Technology*, 26, 457–465.
-

## References

---

- Liu, Xiong, J., Zhou, L., Guo, Z., Wen, H., You, Q., Li, X., Liu, J., and Zhao, W. (2021). Properties of TiN–Al<sub>2</sub>O<sub>3</sub>–TiCN–TiN, TiAlN, and DLC-coated Ti(C,N)-based cermets and their wear behaviors during dry cutting of 7075 aluminum alloys. *International Journal of Applied Ceramic Technology*, 18, 792–802.
- Lobov, A., and Tran, T. A. (2020). Object-oriented approach to product design using extended NX Open API. *Procedia Manufacturing*, 51, 1014–1020.
- Lu, Y. A., Ding, Y., Wang, C., and Zhu, L. (2019). Tool path generation for five-axis machining of blisks with barrel cutters. *International Journal of Production Research*, 57, 1300–1314.
- Luo, M., Yan, D., Wu, B., and Zhang, D. (2015). Barrel cutter design and toolpath planning for high-efficiency machining of freeform surface. *The International Journal of Advanced Manufacturing Technology* 2015 85:9, 85, 2495–2503.
- M'Saoubi, R., Axinte, D., Soo, S. L., Nobel, C., Attia, H., Kappmeyer, G., Engin, S., and Sim, W. M. (2015). High performance cutting of advanced aerospace alloys and composite materials. *CIRP Annals*, 64, 557–580.
- Ma, J., Hu, G., Jia, Z., Zhang, N., and Wang, F. (2018). Effect of geometric feature and cutting direction on variation of force and vibration in high-speed milling of TC4 curved surface. *The International Journal of Advanced Manufacturing Technology*, 95, 2207–2218.
- Ma, W., He, G., Zhu, L., and Guo, L. (2015). Tool deflection error compensation in five-axis ball-end milling of sculptured surface. *The International Journal of Advanced Manufacturing Technology*, 84, 1421–1430.
- Mahesh, K., Philip, J. T., Joshi, S. N., and Kuriachen, B. (2021). Machinability of Inconel 718: A critical review on the impact of cutting temperatures. *Materials and Manufacturing Processes*, 36, 753–791.
- Mali, R. A., Gupta, T. V. K., and Ramkumar, J. (2021). A comprehensive review of free-form surface milling—Advances over a decade. *Journal of Manufacturing Processes*, 62, 132–167.
- Marin, F., de Souza, A. F., Mikowski, A., Fontanella, L. H. G., Soares, P., and de Lacalle, L. N. L. (2023). Energy Density Effect on the Interface Zone in Parts Manufactured by Laser Powder Bed Fusion on Machined Bases. *International Journal of Precision Engineering and Manufacturing - Green Technology*, 10, 905–923.
- Meinzer, C. E., and Seume, J. R. (2020). Experimental and numerical quantification of the aerodynamic damping of a turbine blisk. *Journal of Turbomachinery*, 142.
- Meng, F. J., Chen, Z. T., Xu, R. F., and Li, X. (2014). Optimal barrel cutter selection for the CNC machining of blisk. *CAD Computer Aided Design*, 53, 36–45.
- Mhamdi, M.-B., Boujelbene, M., Bayraktar, E., and Zghal, A. (2012). Surface Integrity of Titanium Alloy Ti-6Al-4 V in Ball end Milling. *Physics Procedia*, 25, 355–362.
- Mia, M., Rahman, M. A., Gupta, M. K., Sharma, N., Danish, M., and Prakash, C. (2022). Advanced cooling-lubrication technologies in metal machining. *Machining and Tribology: Processes, Surfaces, Coolants, and Modeling*, 67–92.



- Mignanelli, P. M., Jones, N. G., Pickering, E. J., Messé, O. M. D. M., Rae, C. M. F., Hardy, M. C., and Stone, H. J. (2017). Gamma-gamma prime-gamma double prime dual-superlattice superalloys. *Scripta Materialia*, 136, 136–140.
- Miller, S. (1996). Advanced materials mean advanced engines. *Interdisciplinary Science Reviews*, 20, 117–129.
- Minsky, M. (1988). Memoir on inventing the confocal scanning microscope. *Scanning*, 10, 128–138.
- Mitsubishi. (2023). Mitsubishi materials corporation - Product VQT6UR. Accessed September 24, 2023, from [https://www.mmc-carbide.com/sea/products/rotating\\_tools/solid\\_end\\_mills/vqt6ur](https://www.mmc-carbide.com/sea/products/rotating_tools/solid_end_mills/vqt6ur)
- Mitutoyo. (2010). Quick guide to surface roughness measurement. In *Mitutoyo America Corporation* (Vol. 1, pp. 1–8).
- Mou, W., Zhu, S., Zhu, M., Han, L., and Jiang, L. (2020). A Prediction Model of Cutting Force about Ball End Milling for Sculptured Surface. *Mathematical Problems in Engineering*, 2020.
- Narasimharaju, S. R., Zeng, W., See, T. L., Zhu, Z., Scott, P., Jiang, X., and Lou, S. (2022). A comprehensive review on laser powder bed fusion of steels: Processing, microstructure, defects and control methods, mechanical properties, current challenges and future trends. *Journal of Manufacturing Processes*, 75, 375–414.
- Ning, J., and Zhu, L. (2019). Parametric design and surface topography analysis of turbine blade processing by turn-milling based on CAM. *International Journal of Advanced Manufacturing Technology*, 104, 3977–3990.
- Oblak, J. M., Duvall, D. S., and Paulonis, D. F. (1974). An estimate of the strengthening arising from coherent, tetragonally-distorted particles. *Materials Science and Engineering*, 13, 51–56.
- Ochoa, A. (2015). *Método de fabricación de componentes de alto valor añadido por combinación de mecanizado multieje y aportación láser*. (Doctoral thesis, University of Basque Country).
- Oliveira, A. J., and Diniz, A. E. (2009). Tool life and tool wear in the semi-finish milling of inclined surfaces. *Journal of Materials Processing Technology*, 209, 5448–5455.
- Ortega, N., Martínez, S., Cerrillo, I., Lamikiz, A., and Ukar, E. (2017). Computed tomography approach to quality control of the Inconel 718 components obtained by additive manufacturing (SLM). *Procedia Manufacturing*, 13, 116–123.
- Ozturk, B., and Lazoglu, I. (2006). Machining of free-form surfaces. Part I: Analytical chip load. *International Journal of Machine Tools and Manufacture*, 46, 728–735.
- Ozturk, B., Lazoglu, I., and Erdim, H. (2006). Machining of free-form surfaces. Part II: Calibration and forces. *International Journal of Machine Tools and Manufacture*, 46, 736–746.
- Ozturk, E., and Budak, E. (2007). Modeling of 5-axis milling processes. *Machining Science and Technology*, 11, 287–311.
- Ozturk, E., Tunc, L. T., and Budak, E. (2009). Investigation of lead and tilt angle effects in 5-axis ball-end milling processes. *International Journal of Machine Tools and Manufacture*, 49, 1053–1062.

## References

---

- Pechenin, V. A., Rusanov, N. V., and Bolotov, M. A. (2018). Model and software module for predicting uncertainties of coordinate measurements using the NX OPEN API. *Journal of Physics: Conference Series*, 1096, 012162. IOP Publishing.
- Peng, Z., Jiao, L., Yan, P., Yuan, M., Gao, S., Yi, J., and Wang, X. (2018). Simulation and experimental study on 3D surface topography in micro-ball-end milling. *International Journal of Advanced Manufacturing Technology*, 96, 1943–1958.
- Perea-Moreno, A.-J., Meloni, E., Vilardi, G., Carlos, J., Pires, M., Skov, I. R., and Belikov, J. (2022). Use of Sustainable Fuels in Aviation—A Review. *Energies* 2022, Vol. 15, Page 2440, 15, 2440.
- Pereira, O., Rodríguez, A., Calleja-Ochoa, A., Celaya, A., de Lacalle, L. N. L., Fernández-Valdivielso, A., and González, H. (2022). Simulation of Cryo-cooling to Improve Super Alloys Cutting Tools. *International Journal of Precision Engineering and Manufacturing - Green Technology*, 9, 73–82.
- Pereira, O., Rodríguez, A., Fernández-Abia, A. I., Barreiro, J., and de Lacalle, L. N. (2016). Cryogenic and minimum quantity lubrication for an eco-efficiency turning of AISI 304. *Journal of Cleaner Production*, 139, 440–449.
- Pérez-Ruiz, J. D., de Lacalle, L. N. L., Urbikain, G., Pereira, O., Martínez, S., and Bris, J. (2021). On the relationship between cutting forces and anisotropy features in the milling of LPBF Inconel 718 for near net shape parts. *International Journal of Machine Tools and Manufacture*, 170, 1–27.
- Pérez-Ruiz, J. D., Marin, F., Martínez, S., Lamikiz, A., Urbikain, G., and López de Lacalle, L. N. (2022). Stiffening near-net-shape functional parts of Inconel 718 LPBF considering material anisotropy and subsequent machining issues. *Mechanical Systems and Signal Processing*, 168, 1–18.
- Pervaiz, S., Rashid, A., Deiab, I., and Nicolescu, M. (2014). Influence of tool materials on machinability of titanium- and nickel-based alloys: A review. *Materials and Manufacturing Processes*, 29, 219–252.
- Pham, M. S., Dovggy, B., Hooper, P. A., Gourlay, C. M., and Piglione, A. (2020). The role of side-branching in microstructure development in laser powder-bed fusion. *Nature Communications*, 11.
- Pleta, A., and Mears, L. (2016). Cutting Force Investigation of Trochoidal Milling in Nickel-based Superalloy. *Procedia Manufacturing*, 5, 1348–1356.
- Polvorosa, R., Suárez, A., de Lacalle, L. N. L., Cerrillo, I., Wretland, A., and Veiga, F. (2017). Tool wear on nickel alloys with different coolant pressures: Comparison of Alloy 718 and Waspaloy. *Journal of Manufacturing Processes*, 26, 44–56.
- Pratheesh Kumar, S., Elangovan, S., Mohanraj, R., and Ramakrishna, J. R. (2021). Review on the evolution and technology of State-of-the-Art metal additive manufacturing processes. *Materials Today: Proceedings*, 46, 7907–7920.

- Qin, S., Hao, Y., Zhu, L., Wiercigroch, M., Yuan, Z., Shi, C., and Cui, D. (2023). CWE identification and cutting force prediction in ball-end milling process. *International Journal of Mechanical Sciences*, 239, 1–22.
- Quinsat, Y., Lavernhe, S., and Lartigue, C. (2011). Characterization of 3D surface topography in 5-axis milling. *Wear*, 271, 590–595.
- Quinsat, Y., Sabourin, L., and Lartigue, C. (2008). Surface topography in ball end milling process: Description of a 3D surface roughness parameter. *Journal of Materials Processing Technology*, 195, 135–143.
- Rajain, K., Sliusarenko, O., Bizzarri, M., and Bartoň, M. (2022). Curve-guided 5-axis CNC flank milling of free-form surfaces using custom-shaped tools. *Computer Aided Geometric Design*, 94, 1–14.
- Ratchev, S., Liu, S., and Becker, A. A. (2005). Error compensation strategy in milling flexible thin-wall parts. *Journal of Materials Processing Technology*, 162–163, 673–681.
- Ratchev, S., Liu, S., Huang, W., and Becker, A. A. (2004). A flexible force model for end milling of low-rigidity parts. *Journal of Materials Processing Technology*, 153–154, 134–138.
- Raza, S. (2015). Superalloys: an introduction with thermal analysis. *Journal of Fundamental and Applied Sciences*, 7, 364.
- Redonnet, J. M., Djebali, S., Segonds, S., Senatore, J., and Rubio, W. (2013). Study of the effective cutter radius for end milling of free-form surfaces using a torus milling cutter. *Computer-Aided Design*, 45, 951–962.
- Ren, Y., Yau, H. T., and Lee, Y. S. (2004). Clean-up tool path generation by contraction tool method for machining complex polyhedral models. *Computers in Industry*, 54, 17–33.
- Renhof, L., Kremaszky, C., Werner, E., and Stockinger, M. (2005). Analysis of microstructural properties of IN 718 after high speed forging. *The Minerals, Metals & Materials Society*.
- Rocca, G. La. (2012). Knowledge based engineering: Between AI and CAD. Review of a language based technology to support engineering design. *Advanced Engineering Informatics*, 26, 159–179.
- Rodríguez, R. J., García, J. A., Medrano, A., Rico, M., Sánchez, R., Martínez, R., Labrugère, C., Lahaye, M., and Guede, A. (2002). Tribological behaviour of hard coatings deposited by arc-evaporation PVD. *Vacuum*, 67, 559–566. Pergamon.
- Rolls-Royce. (2023). UltraFan. Accessed September 5, 2023, from <https://www.rolls-royce.com/innovation/ultrafan>
- Rosa, F., Manzoni, S., and Casati, R. (2018). Damping behavior of 316L lattice structures produced by Selective Laser Melting. *Materials and Design*, 160, 1010–1018.
- Ryu, S. H., and Chu, C. N. (2005). The form error reduction in side wall machining using successive down and up milling. *International Journal of Machine Tools and Manufacture*, 45, 1523–1530.
- Sai, L., Belguith, R., Baili, M., Dessein, G., and Bouzid, W. (2018). An approach to modeling the

## References

---

- chip thickness and cutter workpiece engagement region in 3 and 5 axis ball end milling. *Journal of Manufacturing Processes*, 34, 7–17.
- Salmon, S. C. (1992). Modern grinding process technology. *Journal of Manufacturing Systems*, 11, 379–380.
- Samei, J., Asgari, H., Pelligra, C., Sanjari, M., Salavati, S., Shahriari, A., Amirmaleki, M., Jahanbakht, M., Hadadzadeh, A., Amirkhiz, B. S., and Mohammadi, M. (2021). A hybrid additively manufactured martensitic-maraging stainless steel with superior strength and corrosion resistance for plastic injection molding dies. *Additive Manufacturing*, 45, 1–14.
- Scalzo, F., Totis, G., Vaglio, E., and Sortino, M. (2021). Experimental study on the high-damping properties of metallic lattice structures obtained from SLM. *Precision Engineering*, 71, 63–77.
- Scandiffio, I., Diniz, A. E., and de Souza, A. F. (2016). Evaluating surface roughness, tool life, and machining force when milling free-form shapes on hardened AISI D6 steel. *International Journal of Advanced Manufacturing Technology*, 82, 2075–2086.
- Sharma, V. S., Dogra, M., and Suri, N. M. (2009). Cooling techniques for improved productivity in turning. *International Journal of Machine Tools and Manufacture*, 49, 435–453.
- Shaw, M. C. (1996). *Principles of abrasive processing* (1st ed.). Clarendon: Oxford University Press.
- Shaw, M. C. (2005). *Metal cutting principles* (2nd ed.). New York: Oxford University Press.
- Shujuan, L., Dong, Y., Li, Y., Li, P., Yang, Z., and Landers, R. G. (2019). Geometrical simulation and analysis of ball-end milling surface topography. *International Journal of Advanced Manufacturing Technology*, 102, 1885–1900.
- Siller, H., Rodriguez, C. A., and Ahuett, H. (2006). Cycle time prediction in high-speed milling operations for sculptured surface finishing. *Journal of Materials Processing Technology*, 174, 355–362.
- Smith, G. T. (2008). *Cutting Tool Technology* (1st ed.). London: Springer London.
- Soori, M., Arezoo, B., and Habibi, M. (2014). Virtual machining considering dimensional, geometrical and tool deflection errors in three-axis CNC milling machines. *Journal of Manufacturing Systems*, 33, 498–507.
- Sortino, M., Totis, G., Scalzo, F., and Vaglio, E. (2019). Preliminary investigation of static and dynamic properties of SLM lattice structures for robotic applications. *Mechanisms and Machine Science*, 66, 260–267.
- Su, Y., He, N., Li, L., and Li, X. L. (2006). An experimental investigation of effects of cooling/lubrication conditions on tool wear in high-speed end milling of Ti-6Al-4V. *Wear*, 261, 760–766.
- Sun, Y., Ren, F., Guo, D., and Jia, Z. (2009). Estimation and experimental validation of cutting forces in ball-end milling of sculptured surfaces. *International Journal of Machine Tools and Manufacture*, 49, 1238–1244.

- 
- Suzuki, T., Okamoto, K., and Morishige, K. (2021). Tool Path Generation for Five-Axis Controlled Machining of Free-Form Surfaces Using a Barrel Tool Considering Continuity of Tool Postures. *International Journal of Automation Technology*, 15, 885–892.
- Tai, C. C., and Fuh, K. H. (1995a). Model for cutting forces prediction in ball-end milling. *International Journal of Machine Tools and Manufacture*, 35, 511–534.
- Tai, C. C., and Fuh, K. H. (1995b). The prediction of cutting forces in the ball-end milling process. *Journal of Materials Processing Tech.*, 54, 286–301.
- Tikhomirov, V. A. (2019). *The Method of Automatic Determination of the Types of Spatial Angles in 3D Models of CAD Systems*. 1–4.
- Toh, C. K. (2005). Design, evaluation and optimisation of cutter path strategies when high speed machining hardened mould and die materials. *Materials and Design*, 26, 517–533.
- Tsai, C. L., and Liao, Y. S. (2010). Cutting force prediction in ball-end milling with inclined feed by means of geometrical analysis. *International Journal of Advanced Manufacturing Technology*, 46, 529–541.
- Tunc, L. T. (2016). Rapid extraction of machined surface data through inverse geometrical solution of tool path information. *International Journal of Advanced Manufacturing Technology*, 87, 353–362.
- Tunc, L. T., and Budak, E. (2009). Extraction of 5-axis milling conditions from CAM data for process simulation. *International Journal of Advanced Manufacturing Technology*, 43, 538–550.
- Tuysuz, O., Altintas, Y., and Feng, H. Y. (2013). Prediction of cutting forces in three and five-axis ball-end milling with tool indentation effect. *International Journal of Machine Tools and Manufacture*, 66, 66–81.
- Uddeholm. (2016). Uddeholm Corrax. Accessed September 20, 2020, from [https://www.uddeholm.com/files/PB\\_Uddeholm\\_corrax\\_english.pdf](https://www.uddeholm.com/files/PB_Uddeholm_corrax_english.pdf)
- Uhlmann, E., Kersting, R., Klein, T. B., Cruz, M. F., and Borille, A. V. (2015). Additive Manufacturing of Titanium Alloy for Aircraft Components. *Procedia CIRP*, 35, 55–60.
- Ulutan, D., and Ozel, T. (2011). Machining induced surface integrity in titanium and nickel alloys: A review. *International Journal of Machine Tools and Manufacture*, 51, 250–280.
- Urbikain Pelayo, G., Olvera-Trejo, D., Luo, M., López de Lacalle, L. N., and Elías-Zuñiga, A. (2021). Surface roughness prediction with new barrel-shape mills considering runout: Modelling and validation. *Measurement*, 173, 1–10.
- Valle, L. C. M., Araújo, L. S., Gabriel, S. B., Dille, J., and De Almeida, L. H. (2013). The Effect of  $\alpha$  Phase on the Mechanical Properties of an Inconel 718 Superalloy. *Journal of Materials Engineering and Performance*, 22, 1512–1518.
- Ventura, C. E. H., and Hassui, A. (2013). Evaluation of static cutting forces and tool wear in HSM process applied to pocket milling. *International Journal of Advanced Manufacturing Technology*, 65, 1681–1689.
- Vetri Velmurugan, K., Venkatesan, K., Devendiran, S., and Mathew, A. T. (2019). Investigation of

## References

---

- Parameters for Machining a Difficult-to-Machine Superalloy: Inconel X-750 and Waspaloy. *Lecture Notes in Mechanical Engineering*, 199–215. Springer.
- Wang, B., Liu, Z., Cai, Y., Luo, X., Ma, H., Song, Q., and Xiong, Z. (2021a). Advancements in material removal mechanism and surface integrity of high speed metal cutting: A review. *International Journal of Machine Tools and Manufacture*, Vol. 166, pp. 1–32. Pergamon.
- Wang, D., Chen, W., Li, T., and Xu, R. (2009). Five-Axis Flank Milling of Sculptured Surface with Barrel Cutters. *Key Engineering Materials*, 407–408, 292–297.
- Wang, D., Ren, J., and Tian, W. (2020). A method for the prediction of cutting force for 5-axis ball-end milling of workpieces with curved surfaces. *International Journal of Advanced Manufacturing Technology*, 107, 2023–2039.
- Wang, M. H., and Sun, Y. (2014). Error prediction and compensation based on interference-free tool paths in blade milling. *International Journal of Advanced Manufacturing Technology*, 71, 1309–1318.
- Wang, M., Yang, C., Li, Z., Zhao, S., Zhang, Y., and Lu, X. (2021b). Effects of surface roughness on the aerodynamic performance of a high subsonic compressor airfoil at low Reynolds number. *Chinese Journal of Aeronautics*, 34, 71–81.
- Wang, R., Zhang, S., Ge, R., Luan, X., Zhang, Q., Wang, J., and Lu, S. (2021c). Modified iterative approach for predicting machined surface topography in ball-end milling operation. *The International Journal of Advanced Manufacturing Technology*, 115, 1783–1794.
- Wang, S., and Xu, B. (2021). Calibrated X-ray computed tomography for testing micro-scale pore defect in metallic powder particles for additive manufacturing. *Measurement: Sensors*, 18, 1–5. Elsevier.
- Wang, Z. J., Chen, W. Y., Zhang, Y. Du, Chen, Z. T., and Liu, Q. (2005). Study on the Machining Distortion of Thin-walled Part Caused by Redistribution of Residual Stress. *Chinese Journal of Aeronautics*, 18, 175–179.
- Wang, Z., Wang, B., and Yuan, J. (2019). Modeling of surface topography based on cutting vibration in ball-end milling of thin-walled parts. *International Journal of Advanced Manufacturing Technology*, 101, 1837–1854.
- Wei, Z. C., Guo, M. L., Wang, M. J., Li, S. Q., and Liu, S. X. (2018). Force predictive model for five-axis ball end milling of sculptured surface. *The International Journal of Advanced Manufacturing Technology* 2018 98:5, 98, 1367–1377.
- Wei, Z. C., Guo, M. L., Wang, M. J., Li, S. Q., and Wang, J. (2019). Prediction of cutting force for ball end mill in sculptured surface based on analytic model of CWE and ICCE. *Machining Science and Technology*, 23, 688–711.
- Wei, Z. C., Wang, M. J., Cai, Y. J., and Wang, S. F. (2013). Prediction of cutting force in ball-end milling of sculptured surface using improved Z-map. *International Journal of Advanced Manufacturing Technology*, 68, 1167–1177.
- Wei, Z. C., Wang, M. J., Zhu, J. N., and Gu, L. Y. (2011). Cutting force prediction in ball end

- 
- milling of sculptured surface with Z-level contouring tool path. *International Journal of Machine Tools and Manufacture*, 51, 428–432.
- Wojciechowski, S., Wiackiewicz, M., and Krolczyk, G. M. (2018). Study on metrological relations between instant tool displacements and surface roughness during precise ball end milling. *Measurement: Journal of the International Measurement Confederation*, 129, 686–694.
- Xie, X., Xu, C., Wang, G., Dong, J., Cao, W. Di, and Kennedy, R. (2005). TTT diagram of a newly developed nickel-base superalloy- Allvac® 718Plus™. *Proceedings of the International Symposium on Superalloys and Various Derivatives*, 718, 193–202.
- Xu, D., Liao, Z., Axinte, D., and Hardy, M. (2020). A novel method to continuously map the surface integrity and cutting mechanism transition in various cutting conditions. *International Journal of Machine Tools and Manufacture*, 151, 1–8.
- Xu, D., Liao, Z., Axinte, D., Hardy, M., and M'Saoubi, R. (2019). A quick method for evaluating the thresholds of workpiece surface damage in machining. *CIRP Annals*, 68, 61–64.
- Xu, F., Fang, F., and Zhang, X. (2017). Side Flow Effect on Surface Generation in Nano Cutting. *Nanoscale Research Letters*, 12, 359.
- Xu, J., Zhang, H., and Sun, Y. (2018a). Swept surface-based approach to simulating surface topography in ball-end CNC milling. *International Journal of Advanced Manufacturing Technology*, 98, 107–118.
- Xu, Z., Hyde, C. J., Tuck, C., and Clare, A. T. (2018b). Creep behaviour of inconel 718 processed by laser powder bed fusion. *Journal of Materials Processing Technology*, 256, 13–24.
- Xue, M., Chen, X., Ji, X., Xie, X., Chao, Q., and Fan, G. (2023). Effect of Particle Size Distribution on the Printing Quality and Tensile Properties of Ti-6Al-4V Alloy Produced by LPBF Process. *Metals*, 13, 604.
- Yan, B., Hao, Y., Zhu, L., and Liu, C. (2022). Towards high milling accuracy of turbine blades: A review. *Mechanical Systems and Signal Processing*, Vol. 170, p. 108727. Academic Press.
- Yan, X., Shirase, K., Hirao, M., and Yasui, T. (1999). NC program evaluator for higher machining productivity. *International Journal of Machine Tools & Manufacture*, 39, 1563–1573.
- Yang, M., and Park, H. (1991). The prediction of cutting force in ball-end milling. *International Journal of Machine Tools and Manufacture*, 31, 45–54.
- Yang, M. Y., and Choi, J. G. (1998). A Tool Deflection Compensation System for End Milling Accuracy Improvement. *Journal of Manufacturing Science and Engineering*, 120, 222–229.
- Yang, Y., Zhang, W. H., Ma, Y. C., and Wan, M. (2016). Chatter prediction for the peripheral milling of thin-walled workpieces with curved surfaces. *International Journal of Machine Tools and Manufacture*, 109, 36–48.
- Yao, C., Tan, L., Yang, P., and Zhang, D. (2018). Effects of tool orientation and surface curvature on surface integrity in ball end milling of TC17. *The International Journal of Advanced Manufacturing Technology*, 94, 1699–1710.
- YaoAn, L., QingZhen, B., BaoRui, D., ShuLin, C., LiMin, Z., Kai, H., ... Huang, K. (2014). Five-

## References

---

- Axis Strip Machining with Barrel Cutter Based on Tolerance Constraint for Sculptured Surfaces. *International Journal of Mechanical Aerospace, Industrial Mecatronic and Manufacturing Engineering*, 8, 1779–1784.
- Yin, P., Zhang, Y., Wu, Q., and Chen, S. (2019). A Conversion Platform for Multi-Software NC Programming. *IOP Conference Series: Earth and Environmental Science*, 252, 1–8. IOP Publishing.
- Zeroudi, N., Fontaine, M., and Necib, K. (2012). Prediction of cutting forces in 3-axes milling of sculptured surfaces directly from CAM tool path. *Journal of Intelligent Manufacturing*, 23, 1573–1587.
- Zha, J., Villarrazo, N., Martínez de Pisson, G., Li, Y., Zhang, H., and López de Lacalle, L. N. (2023). An accuracy evolution method applied to five-axis machining of curved surfaces. *International Journal of Advanced Manufacturing Technology*, 125, 3475–3487.
- Zhang, A., Liu, X., Yue, C., Li, R., Liang, S. Y., and Wang, L. (2022). Velocity effect sensitivity analysis of ball-end milling Ti-6Al-4 V. *International Journal of Advanced Manufacturing Technology*, 118, 3963–3982.
- Zhang, C., Guo, S., Zhang, H., and Zhou, L. (2013). Modeling and predicting for surface topography considering tool wear in milling process. *The International Journal of Advanced Manufacturing Technology*, 68, 2849–2860.
- Zhang, X., Zhang, J., Zheng, X., Pang, B., and Zhao, W. (2017). Tool orientation optimization of 5-axis ball-end milling based on an accurate cutter/workpiece engagement model. *CIRP Journal of Manufacturing Science and Technology*, 19, 106–116.
- Zhou, J. M., Bushlya, V., and Stahl, J. E. (2012). An investigation of surface damage in the high speed turning of Inconel 718 with use of whisker reinforced ceramic tools. *Journal of Materials Processing Technology*, 212, 372–384.
- Zhou, R., and Chen, Q. (2021). An analytical prediction model of surface topography generated in 4-axis milling process. *International Journal of Advanced Manufacturing Technology*, 115, 3289–3299.
- Zhu, R., Kapoor, S. G., and DeVor, R. E. (2001). Mechanistic modeling of the ball end milling process for multi-axis machining of free-form surfaces. *Journal of Manufacturing Science and Engineering, Transactions of the ASME*, 123, 369–379.
- Ziółkowski, G., Gruber, K., Tokarczyk, E., Roszak, R., and Ziegenhorn, M. (2021). X-ray Computed Tomography for the ex-situ mechanical testing and simulation of additively manufactured IN718 samples. *Additive Manufacturing*, 45, 1–21.
- Zoya, Z. A., and Krishnamurthy, R. (2000). The performance of CBN tools in the machining of titanium alloys. *Journal of Materials Processing Technology*, 100, 80–86.